ISSN 0424-7116 | DOI 10.3285/eg.62.2
Edited by the German Quaternary Association
Editor-in-Chief: Holger Freund

E&G

Eiszeitalter und Gegenwart
Quaternary Science Journal

Vol. 62
No 2
2013

ENVIRONMENT – MAN – GEOHAZARDS IN THE QUATERNARY

GUEST EDITORS Ludwig Zöller, Holger Freund

GEOZON

E&G

Eiszeitalter und Gegenwart
Quaternary Science Journal

Volume 62 / Number 2 / 2013 / DOI: 10.3285/eg.62.2 / ISSN 0424-7116 / www.quaternary-science.net / Founded in 1951

AIMS & SCOPE
The *Quaternary Science Journal* publishes original articles of quaternary geology, geography, palaeontology, soil science, archaeology, climatology etc.; special issues with main topics and articles of lectures of several scientific events.
MANUSCRIPT SUBMISSION
Please upload your manuscript at the online submission system at our journal site www.quaternary-science.net. Please note the instructions for authors before.
FREQUENCY
2 numbers per year

SUBSCRIPTION
Free for DEUQUA-Members! Prices for standing order: single number 27,– Euro; double number 54,– Euro; plus shipping costs. We offer discounts for libraries and bookstores. Please subscribe to the journal at the publisher *Geozon Science Media*.
JOURNAL EXCHANGE
If you are interested in exchange your journal with the *Quaternary Science Journal*, please contact: Universitätsbibliothek Halle
Tauschstelle, Frau Winther
August-Bebel-Straße 13
D-06108 Halle (Saale), Germany
Tel. +49 (0)345-55 22 183
E-Mail: tausch (at) bibliothek.uni-halle.de
REORDER
Reorders are possible at the publishing house. See full list and special prices of available numbers on next to last page.
PUBLISHING HOUSE
Geozon Science Media UG (haftungsbeschränkt)
Postfach 3245
D-17462 Greifswald
Germany
Tel. +49 (0)3834-80 14 80
E-Mail: info (at) geozon.net
www.geozon.net

PRINT
Printed in Germany on 100% recycled paper climate neutral produced
COVER FIGURE
Extent of the August 2005-debris flow deposits in Antholz-Mittertal village (Fig. p. 141)

E&G Quaternary Science Journal
Volume 62 / Number 2 / 2013 / 83 / DOI 10.3285/eg.62.2.00
www.quaternary-science.net

GEOZON SCIENCE MEDIA
ISSN 0424-7116

Foreword

special issue

Ludwig Zöller

The present volume 62/2 of "E&G Quaternary Science Journal" contains contributions submitted to the 36th assembly of the "Deutsche Quartärvereinigung" (DEUQUA, German Quaternary Association), held at the University of Bayreuth from 16 to 20 September, 2012. Thanks to generous support from the Deutsche Forschungsgemeinschaft (DFG) substantial contributions by external scientists were made possible. The program included 45 oral and 53 poster presentations, a minor part of which are being published for the first time in the present volume. Nevertheless, the publications presented here reflect the broad scope of the scientific program under the principal theme "Umwelt – Mensch – Georisiken im Quartär" (Environment – Man – Geohazards in the Quaternary). This included geoarchaeologic research as well as studies in the sedimentary heritage of Quaternary processes influencing present-day and future geohazards.

The first article by *Solis-Castillo et al.* investigates the provenance of Holocene sediments in the Mayan Lowlands in Central America, their degree of weathering, palaeosols and pedostratigraphy, and their chronology.

The second article by *Tillmann et al.* deals with the historical processes and landscape evolution of the western coast of the island of Amrum in the German tidelands of the North Sea. The results are obtained by careful multidisciplinary work including historical maps and documents as well as geophysical and sedimentological methods.

The third and the fourth articles report on the state of the art in deciphering the Palaeolithic record at the Lower Gravettian open air site of Grub-Kranawetberg, Lower Austria. The contribution by *Antl* highlights recent and ongoing archaeological research, thereby focussing on Archaeological Horizons 4 and 3, which point to different groups of humans occupying the site within a short time under changing environmental conditions. The article by *Zöller et al.* (edited by Holger Freund) reports on a diachronic chronology of the site and discusses some unexpected problems with luminescence dating techniques (IRSL and OSL) in comparison with calibrated radiocarbon ages.

The relevance of Quaternary researchers dealing with present and near future geohazards in an Alpine environment is demonstrated in the article by *Damm & Felderer*. Based on intensive studies in the spatial distribution of debris flows since the Little Ice Age, the authors attempt to project their results into the middle of the 21st century for a scenario of 1 to 2 K atmospheric warming. The retrospective study by Jaeger et al. investigates a landslide from 1957 AD in the average mountain area built up from slightly dipping Mesozoic sedimentary rocks in Northern Bavaria, Germany. The area is very prone to landslides. The contribution is able to further differentiate some elements and processes of the landslide compared to earlier studies. With respect to ongoing climate change and possible change of precipitation patterns an endangered susceptible slope area is indicated in the future.

The last article by Diedrich deals with a famous cave in the northern Franconian Alb, Germany. The intermittent use of the cave by Pleistocene animals and humans is discussed with respect to the geomorphologic evolution of river terraces. The contribution boldly raises the question of a limited valley glaciation in the area during the Last Glacial Maximum at altitudes of around 5 00 m a.s.l., sedimentary remnants of which may only have been protected in caves from later erosion.

The editors are much obliged to the authors for submitting their manuscripts and hope for a comparatively wide range of contributions in future.

Bayreuth, 1st December 2013

E&G Quaternary Science Journal
Volume 62 / Number 2 / 2013 / 84–97 / DOI 10.3285/eg.62.2.01
www.quaternary-science.net

GEOZON SCIENCE MEDIA
ISSN 0424-7116

Holocene sequences in the Mayan Lowlands – A provenance study using heavy mineral distributions

Berenice Solís-Castillo, Christine Thiel, Héctor Cabadas Baez, Elizabeth Solleiro Rebolledo, Sergey Sedov, Birgit Terhorst, Bodo Damm, Manfred Frechen, Sumiko Tsukamoto

How to cite: Solís-Castillo, B., Thiel C., Cabadas Baez, H., Solleiro Rebolledo, E., Sedov, S., Terhorst, B., Damm, B., Frechen, M., Tsukamoto, S. (2013): Holocene sequences in the Mayan Lowlands – A provenance study using heavy mineral distributions. – E&G Quaternary Science Journal, 62 (2): 84–97. DOI: 10.3285/eg.62.2.01

Abstract: Heavy mineral analysis of alluvial sediments and paleosols on Holocene terraces of the Usumacinta River provided an effective tool to reconstruct sediment provenance in the Mayan Lowlands. Furthermore, the mineralogical data are useful for pedostratigraphic correlations in the region. Based on our observations from the Tierra Blanca profile, the ultrastable detrital heavy minerals assemblage (mostly zircon, tourmaline, and rutile) are the most promising mineral proxies to recognize the provenance of the sediments. Those minerals are accompanied by an intriguing variety of high density authigenic minerals (including titanite). Using the specific characteristics and the ages obtained for some layers, it may now be possible to develop a regional chronostratigraphy for the paleosols and alluvial sequences. Our data suggest that sediments were transported westward in river channels originating from the highlands of Guatemala. The studied materials also contain high amounts of volcanic minerals, most of them fresh and with angular shapes, thus indicating a proximal source, mostly likely from Tacana Volcano, Mexico/Guatemala.

Holozäne Sequenzen in den Tieflandgebieten der Mayas – Eine Untersuchung der Liefergebiete auf Basis von Schwermineralgesellschaften

Kurzfassung: Schwermineralanalysen an alluvialen Sedimenten und Paläoböden des Usumacinta-Flusses sind ein sehr effektives Werkzeug für die Rekonstruktion der relevanten Liefergebiete in den Tieflandgebieten der Mayas. Die mineralogischen Daten können für die pedostratigraphische Korrelation in der Region nützlich sein. Auf der Basis unserer Beobachtungen für Tierra Blanca ist die ultrastabile Schwermineralkomponente (zumeist Zirkon, Turmalin und Rutil) besonders erfolgversprechend für den Nachweis der Liefergebiete der Sedimente. Diese Minerale treten gemeinsam mit einer großen Vielfalt von sehr dichten authigenen Mineralen auf (u.a. Titanit). Unter Berücksichtigung der spezifischen Eigenschaften und der Alter von ausgewählten Horizonten, kann nun versucht werden, eine regionale Chronostratigraphie für Paläoböden und alluviale Sequenzen zu entwickeln. Unsere Daten deuten auf Sedimenttransport in Flussrinnen von den Hochländern Guatemalas gen Westen hin. Die untersuchten Schichten enthalten auch große Anteile an vulkanischen Mineralen mit frischen und eckigen Formen, was auf ein proximales Liefergebiet (wahrscheinlich Tacana Volcano, Mexico/Guatemala) hinweist.

Keywords: *heavy mineral assemblages, pedostratigraphy, micromorphology, alluvial sediments, Mayan Lowlands, Mexico*

Addresses of authors: **B. Solís-Castillo**, Posgrado en Ciencias de la Tierra. Instituto de Geología, UNAM. 04510, México, D.F., E-Mail: bsolisc.geologia@gmail.com; **C. Thiel**, Nordic Laboratory for Luminescence Dating, Department of Geoscience, Aarhus University, Risø Campus, Frederiksborgvej 399, 4000 Roskilde, Denmark; Center for Nuclear Technologies, Technical University of Denmark, Risø Campus, Frederiksborgvej 399, 4000 Roskilde, Denmark. E-Mail: chrth@dtu.dk; **H. Cabadas Baez**, Laboratorio de Geología, Facultad de Geografía, UAEM. 50110, Toluca Edo. México. hvcabadasb@uaemex.mx; **E. Solleiro Rebolledo**, **S. Sedov**, Instituto de Geología, UNAM. 04510, México, DF. E-Mail: solleiro@geologia.unam.mx; serg_sedov@yahoo.com; **B. Terhorst**, Institute of Geography and Geology, University of Würzburg, Am Hubland, 97047 Würzburg, Germany. birgit.terhorst@uni-wuerzburg.de; **B. Damm**, Institut für Strukturforschung und Planung in agrarischen Intensivgebieten (ISPA), Vechta University, 49364 Vechta. E-Mail: bdamm@ispa.uni-vechta.de; **M. Frechen**, **S. Tsukamoto**, Leibniz Institute for Applied Geophysics Section, S3: Geochronology and Isotope Hydrology, Stilleweg 2, 30655 Hannover, Germany. E-Mail: manfred.frechen@liag-hannover.de; E-Mail: sumiko.tsukamoto@liag-hannover.de

1 Introduction

The reconstruction of the environmental and landscape changes in Mexico for the Late Quaternary is based on numerous data. The majority of data is derived from lacustrine sediments, glacial and paleopedological records; however, due to the fragmentary character of glacial records, hiatuses in lake cores, and low temporal resolution of tephra-paleosols sequences these records are still contradictory (Sedov et al. 2007). With respect to this problem, new insights might be obtained by studying alluvial sequences. Until now the alluvial and fluvial archives in Mexico have not received sufficient attention as a source to understand short-term changes in the landscape; only very few detailed studies deal specifically with flu-

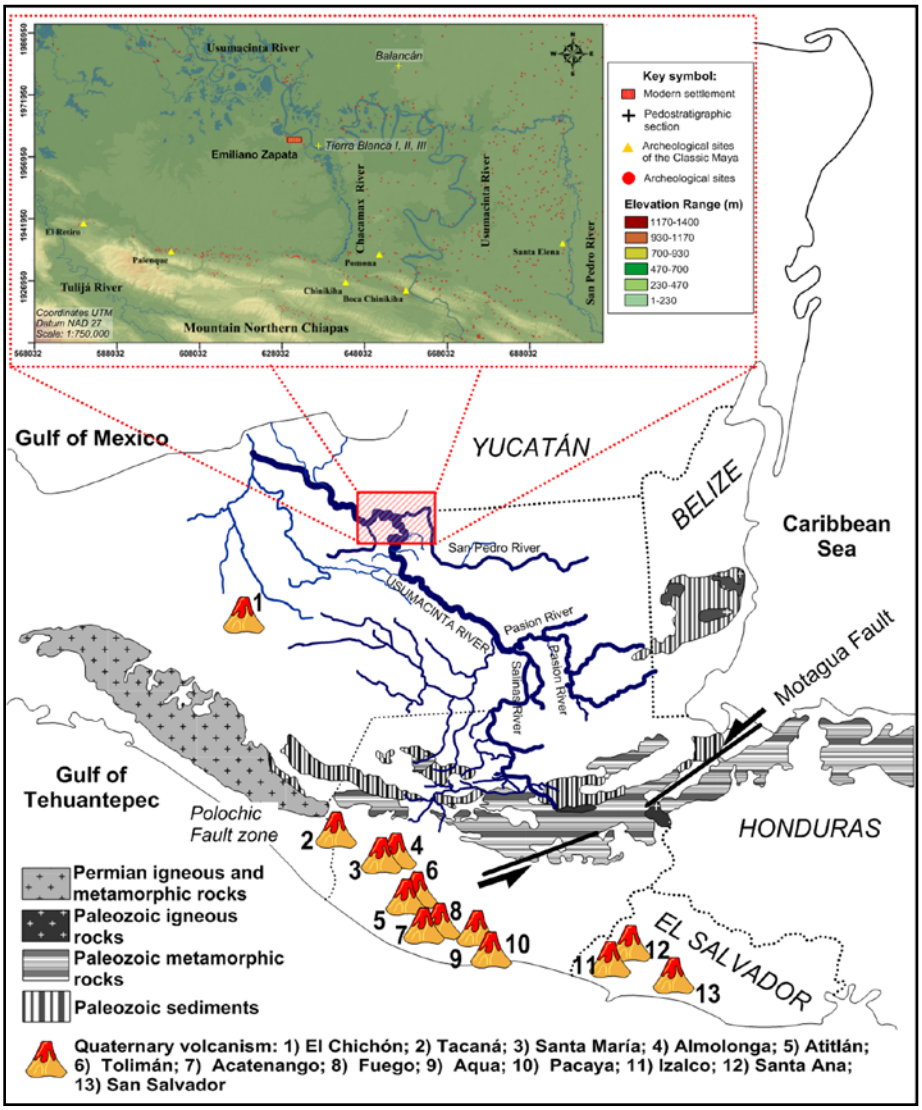

Fig. 1: Location of the study area and simplified geological map showing the boundary between the Maya and the Chortis blocks. Modified after Ortega-Gutiérrez *et al. (1992), and* French & Schenk *(1997).*

Abb. 1: Lage des Untersuchungsgebiets und vereinfachte Darstellung der regionalen Geologie mit der Grenze zwischen der Maya- und der Cortis-Platte. Verändert nach Ortega-Gutiérrez *et al. (1992)und* French & Schenk *(1997).*

vial Late Pleistocene-Holocene sequences (cf. Solleiro-Rebolledo et al. 2011).

Particularly, the alluvial-paleosol sedimentary sequences in the Southeast of Mexico are highly sensitive to the environmental changes and are rich and detailed Holcene archives (Solís-Castillo et al. 2013). However, river systems are very complex due to the dynamics involved in their formation, thus controlling the different phases of aggradation, degradation, and pedogenesis. Aggradation phases can be recognized by selective sorting of particles due to differential entrainment and transport. This is especially seen in the characteristics of heavy minerals, such as densitiy, grain size and shape. In general, the sorting may be a result of ancient depositional environments and provenance of sediments (Komar 2007). In rivers with high sedimentation rates, heavy minerals are affected by considerable sorting before they reach the alluvial plain (Pirkle et al. 2007).

Alluvial landscapes are very complex due to the presence of discontinuities in vertical successions, being controlled by several forces (climatic, geologic, geomorphic, anthropogenic), and interpretation of the successions can be problematic. Similar sediments can be produced in different and distant areas or periods; this makes paleoenvironmental reconstruction difficult. In consequence, paleosols are important records for the environmental history and can help to unravel the alluvial stratigraphy (Hughes 2010). Alluvial soils exhibit characteristics of both sedimentary and soil formation processes. Such soils are characterized by the textural and mineralogical composition of the material transported across the drainage basins (Kraus 2002). Traditionally, analyses of mineral composition have been applied to paleosols on surfaces of different ages to establish morphostratigraphical units (Schatzl & Anderson 2005). In particular, heavy minerals in soils are used as indicators for sediment provenance. Furthermore, heavy minerals have been used to determine weathering degrees, thus being useful as relative dating tools (Mikesell et al. 2004). In sequences where paleosols show contrasting differences, weathering indices are commonly used to evaluate the intensity of the process and their relation to environmental conditions.

The Usumacinta River in Tabasco, Mexico (Fig. 1) has carried vast quantities of sediments from Chiapas and Guatemala since the Plio-Pleistocene and therefore exhibits a great potential for the application of heavy mineral analyses. At present, detailed information on the heavy mineral assemblages in soils are very scarce for the Mayan Lowlands. This area is known for its high cultural diversity since the Mid-Holocene, which is probably related to the river-channel stability and soil formation on the Holocene terraces, thus

providing space for settlements in the alluvial plain (Solís-Castillo et al. 2013).

Altogether, the analysis of mineral provenance is of great importance to better understand the river dynamics and climatic changes in this region, which is reflected in different weathering intensities. Unraveling the changes in the landscape and in the soils will contribute to a better understanding of human migration along the Mayan Lowlands.

It is surprising that most of the information about the climate history of the Maya region comes from studies in Yucatan (Rosenmeier et al. 2002; Hodell et al. 2005; Sedov et al. 2007; Fredick et al. 2008; Cabadas et al. 2010), as well as from Guatemala and Belize (Dahlin et al. 1980; Beach et al. 2003; Fernandez et al. 2005; Dunning et al. 2002, 2006). Until now, for the Maya Lowlands, only Solís-Castillo et al. (2013) provided data on the reconstruction of Holocene climatic changes in the Usumacinta River region on the base of paleopedology.

The authors found that the Late Pleistocene-Early Holocene paleosols show strong weathering and gleyzation related to more humid climatic conditions. These conditions were only observed in the paleosols with gleyic features, while in the alluvial sediments only few oxide-reduction characteristic were found. Mid-Holocene paleosols are characterized by the presence of carbonate concretions combined with vertic features, which indicate a major drying trend as well as fluctuations between wet and dry conditions. Late Holocene paleosols show vertic properties and lack gleyic features; this corresponds to dryer conditions. Further, Middle and Late Holocene paleosols are observed at the base of other sequences located on the younger terraces; these paleosols do not show any signs of oxide-reduction conditions.

In this study we use heavy minerals to detect the weathering degree of alluvial sediments and paleosols; these data serve as proxy for the relative stability during the Late Pleistocene and the Holocene. Some samples were selected for micromorphology in order to investigate the bulk mineral composition.

Furthermore, the composition of the heavy minerals from the alluvial sediments of the Usumacinta River helped to reconstruct the provenance. In addition, radiocarbon and luminescence ages provide a numerical chronology for the sediments under study.

2 Regional setting and the Usumacinta River

The Mayan Lowlands are characterized by active volcanoes, rugged terrain of the Sierra de Chiapas and the Central Cordillera, and faulting as well as extensive karst systems in the northern lowlands (Figure 1). Volcanism and tectonics are a result of the highly variable spatial and temporal evolution of plate boundaries between Cocos, North American, and Caribbean Plates (Donnelly et al. 1990).

The Sierra de Chiapas is mainly formed by Tertiary folded, northwest-southeast oriented limestones. The limestones show extensive karstic features with abundant subterranean drainage and ephemeral surface streams. The highlands of the Chiapas region are composed of extrusive igneous rocks (andesites, dacites, and pyroclastic products) and sedimentary rocks (shales, sandstones, and limestones). Their ages range from Late Cretaceous to Tertiary, and Quaternary (Hernandez et al. 2012). The Paleozoic geology in Chiapas is characterized by metamorphic rocks, which consist of granitic gneiss and gneiss of biotite and orthoclase, sedimentary rocks, and biotite schists. In the western part of Guatemala, gneiss and schists of quartz are present. The Paleozoic Granitic Massif of Chiapas is composed of pink granite of biotite with graduation to granodiorite (Monografia Geologica-Minera del Estado de Tabasco 1999).

The Usumacinta River is one of the larger fluvial systems in Mexico with a drainage area of 63,804 km^2 (West et al. 1969), which flows through both the highlands of Chiapas and Guatemala and the coastal plains of the southern Gulf of Mexico.

The latter are formed by Late Tertiary (Pliocene) and Quaternary deposits, which are mainly composed of alluvium, lacustrine and marsh sediments, as well as coastal bars and residual soils. During the Holocene, three tributary channels (San Pedro in the east, Chakamax in the center, and Tulijá in the west) flew across the terraces of the Central Usumacinta and discharged into the Lower Usumacinta (Solís-Castillo et al. 2013).

Starting in Guatemala, the Usumacinta River runs northeast to the Bay of Campeche in the Gulf of Mexico (Figure 1). This vast region has been subdivided into two main areas: the Upper Usumacinta (from the rivers Salinas and Passion in Guatemala to Boca del Cerro, Chiapas), and the Lower Usumacinta (from Boca del Cerro to the Gulf of Mexico). In pre-Hispanic times, several population centers were located in these areas. Until now, there is evidence of 2,300 archeological sites with different characteristics; they are preferably located in the plains of Tabasco. The number of occupation sites in the numerous side valleys along the Usumacinta River in the mountainous region is still unknown (Liendo et al. 2012). The archeological research has revealed a long sequence of occupation for the region ranging from the Middle Preclassic period (800–300 B.C.) to the Terminal Classic period (850 A.D.) (Liendo et al. 2012, and references therein).

In the north, the Usumacinta River flows through the State of Tabasco in an alluvial valley composed of Plio-Pleistocene to Holocene terraces (Ortiz-Perez et al. 2005); these are affected by Neogene tectonic activity with a set of normal faults causing a horst-graben system (Padilla & Sanchez 2007). The main tributaries follow normal fault planes. The oldest terraces are located in the areas more distant from the sea. In contrast, Holocene terraces are formed by incisions and floodplain deposits along the main channel. Three levels of Holocene terraces have been recognized by Solís-Castillo et al. (2013), referred to as HT2 (at 15–10 m asl), HT1 (at 10–5 m asl) and HT0 (at <5 m asl), from the oldest to the youngest.

3 Materials

In Tierra Blanca (Figure 1), the studied sequence is composed of alluvial sediments intercalated with paleosols. Three profiles were studied (Figure 2): Tierra Blanca (TB) I, TB II and TB III. Solís-Castillo et al. (2013) have

presented soil morphologic data, archeological and cultural evidence, as well as radiocarbon ages for TB I and TB II (amongst other sections from the same region). Here, we present new data for TB III and compare them to TB I and II in order to get a more complete understanding of the landscape formation and paleoenvironmental changes. A composite profile is shown in Figure 3. The pedological and sedimentological survey is complemented by micromorphology. Furthermore, three alluvial layers were dated using optically stimulated luminescence (OSL); these ages can be compared with the radiocarbon ages presented in Solís-Castillo et al. (2013). Heavy mineral analysis is used to trace the provenance. In addition to the Tierra Blanca site, data from a sequence in Balancán (Figure 1) are presented; the section in Balancán is also located on a Pleistocene terrace of the Usumacinta River.

The TB I, II and III sequences are located on the oldest Holocene terrace (HT2), and represent the most complete stratigraphic section of the area. In TB I and TB II two types of paleosols are present, gleyic at the base and vertic at the top. They are clearly separated by alluvial sediments (TB III) (Figure 3).

On top of a sandy Pleistocene alluvium the lower part of the composite profile (TB I) contains four paleosols (numbered 6, 7, 8, 9). This section with a total thickness of 267 cm, is characterized by the following horizons: 6G, 7Bg, 8G, 8Gk, 9G, 9Bkg, 9BCgk (Figure 3). A horizons are not preserved due to erosional processes; there is no separation of the individual paleosols by C horizons. All horizons show strong gleyic features expressed as grayish brown colors with reddish-yellowish-greenish mottles, coarse subangular blocky structure, Fe concretions and/or spots, and dendritic Mn. In the paleosols of unit 9 the gleyic features decrease with depth, and at the base of horizon 9BCgk the oxide-reduction characteristics are less. The strongest gleyic features are observed in paleosol 6, where also slickensides are present. One of the most remarkable features in the gleyic unit in horizon 9Bkg is the presence of hard carbonate concretions, around 5 to 10 cm in diameter. These concretions were radiocarbon dated to 5450–5380 cal. B.P. (3240–3110 B.C.) (Solís-Castillo et al. 2013).

The upper paleosols (section TB II; Figure 3) formed on top of silty sediment (i.e. on top of section TB III; Figure 3). The paleosols in section TB II (labeled as paleosols 2, 3, 4, 5) show evidence of human occupation in three different periods (according to the Mesoamerican chronology): Formative (800 B.C. – A.D. 150), Classic (A.D. 150–1000) and Post-classic (A.D. 1000–1500). Paleosols 2 and 3 are weakly developed. Horizon 4Bk is a pedosediment, composed of soil fragments and broken carbonate concretions. Paleosol 5 bears the strongest pedogenic features of all paleosols, and can be subdivided in 5Ass, 5Bss and 5BC, with a total thickness >1 m. This paleosol shows strong vertic features: slickensides, hard angular blocky structure, and vertical cracks. Carbonates in the form of white spots and filling fractures and pores are found throughout the entire profile. The modern surface is made up of ~100 cm of alluvial sediment little affected by pedogenesis (C horizon).

The chronology of these paleosols has been previously established by radiocarbon dating (Table 1) and archeological evidence (Solís-Castillo et al. 2013). The soil organic matter (SOM) in 5Ass was dated to 2340–2300 cal. B.P. (390–350 B.C.) The carbonates disseminated in 5Bss horizon gave a much younger age, 720–660 cal B.P. (1230–1290 A.D.). However, artifacts found in this paleosol belong to the Formative Period (1800 B.C.–150 A.D.), which confirms its stratigraphic position. Clearly, the carbonates must have formed later. Charcoal from the 3A horizon yielded an age of 1140–970 cal. B.P. (810–980 A.D.). Classic ceramic fragments (A.D. 150–1000) recovered from this paleosol support this date. The upper paleosol 2 has not been dated with any numerical technique; however it contains Post-classic artifacts (A.D. 1000–1500) and thus allows for assigning an age to it.

The alluvial sediments were best expressed in profile TB III located only 10 m to the east of TB I. At the contact to

Tab. 1: Summary of the dating results. Blue OSL data are from quartz, $pIRIR_{290}$ are from K-feldspar. For sample 2464, the quartz is in saturation, i.e. a minimum dose and correspondingly age are given. The radiocarbon ages are taken from Solís-Castillo et al. (2013).

Tab. 1: Zusammenfassung der Datierungsergebnisse. Blaue OSL-Daten stammen von Quarz, $pIRIR_{290}$ von K-Feldspat. Der Quarz für Probe 2464 ist in Sättigung, d.h. es kann nur eine Mindestdosis und ein -alter angegeben werden. Die Radiokarbonalter stammen aus Solís-Castillo et al. (2013).

Lab code	Horizon	Dose rate [Gy/ka]		Equivalent dose [Gy]		Age [ka]		Radiocarbon age
		quartz	feldspar	blue OSL	$pIRIR_{290}$	blue OSL	$pIRIR_{290}$	cal. BP [2σ]
BETA-300447	3A	-	-	-	-	-	-	1140-970 [3]
2462	3C	2.90 ± 0.11	-	6.1 ± 1.4 [1]	-	2.1 ± 0.5	-	
BETA-300448	5Ass	-	-	-	-	-	-	2340-2300 [4]
BETA-300449	5Bss	-	-	-	-	-	-	720-660 [5]
2463	TB3_07	3.27 ± 0.11	-	29 ± 6 [1]	-	9 ± 2	-	-
BETA-277572	9Bkg	-	-	-	-	-	-	5450-5380 [5]
2464	9BCgk	1.98 ± 0.10	2.61 ± 0.11	> 130 [2]	322 ± 10 [2]	> 65	123 ± 6	-

[1] *>24 aliquots measured.*
[2] *9 aliquots measured.*
[3] *Charcoal dated.*
[4] *Soil organic matter dated.*
[5] *$CaCO_3$ nodules dated.*

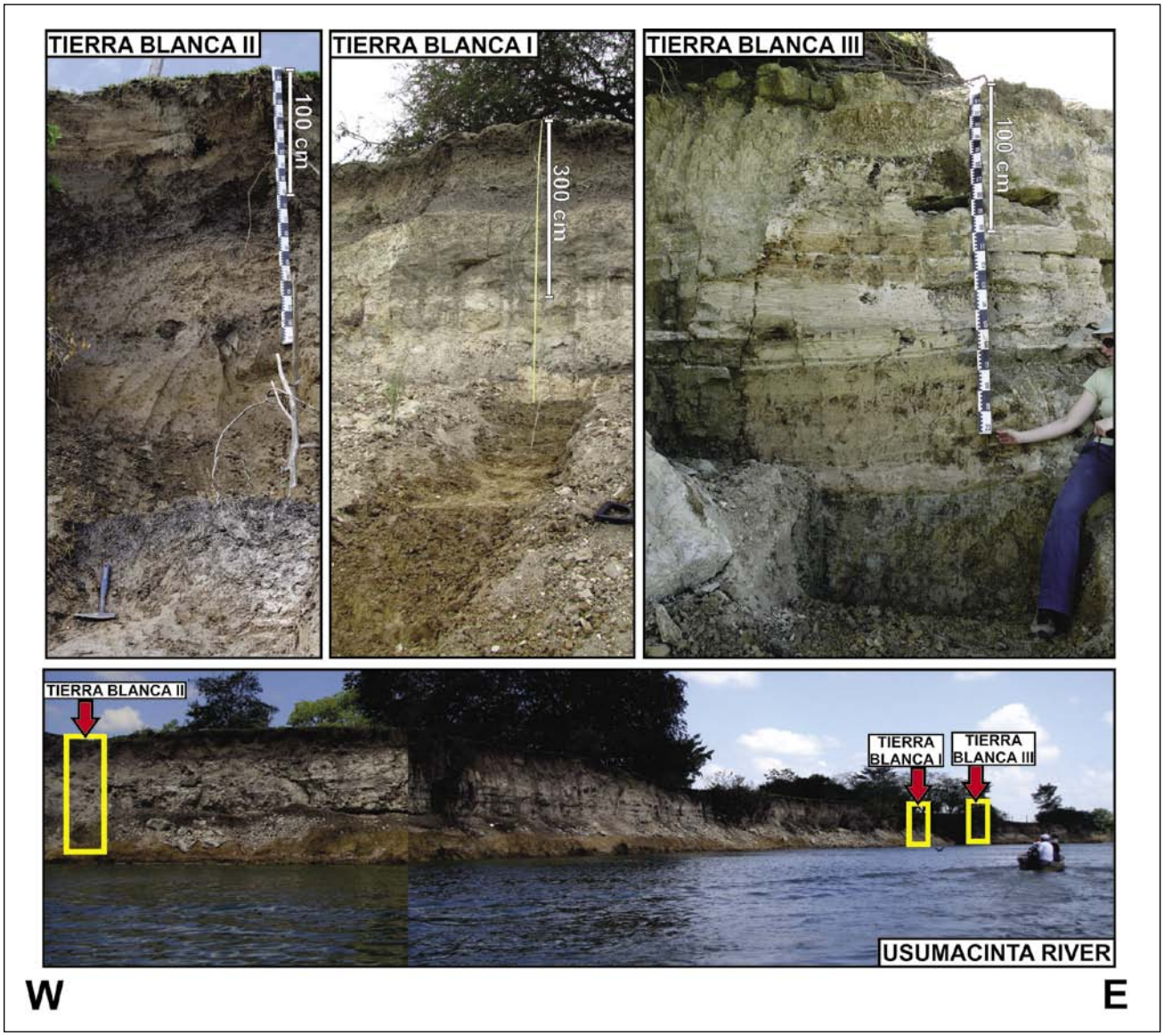

Fig. 2: Photograph showing the positions of the individual profiles in Tierra Blanca.

Abb. 2: Übersichtsaufnahme von Tierra Blanca und einzelne Profile.

paleosols with evidence of human occupation, the overlying sediment is laminated and shows a wavy boundary and has a total thickness of 10 cm. The middle part alternates from lamination to crossed stratification and is characterized by a sand texture, reductomorphic features and carbonate concretions. In this section, two phases representing slow water flow or even standing water can be found (as shown by clayey material with some reductomorphic features and root traces).

The upper part is also laminated, with vertical cracks up to 40 cm in length cutting through the sediment layer (cf. Figure 3). The material of all laminated strata reacts intensively with HCl. We refer to this material as silt sediment due to the dominance of this fraction (62%); however, it also has a high proportion of clay (32%) (Solís-Castillo et al. 2013).

Another profile situated on top of a Pleistocene terrace is found in the Balancán section (Figure 4). It is characterized by a monogenetic soil ($A/Bg/G_1/G_2$) with strong gleyic features (grayish brown colors with reddish-yellowish-greenish mottles, Fe concretions and dendritic Mn). The soils at Balancán are morphologically similar to the ones at the base of the Tierra Blanca sequence. However, the Balancán soils are more intensely weathered as shown by the larger amount of clay, and the more compact and pronounced oxide-reduction features (Figure 4).

4 Methods

4.1 Mineralogy and micromorphology

Thirty-two samples were taken for heavy mineral analyses (cf. Figure 5). The fine sand (63–125 µm) was separated by sieving and pretreated with 10% hydrocholoric acid (HCl) to dissolve carbonates, and subsequently with 30% hydrogen peroxide (H_2O_2) to remove organic matter. The sands were dried and then floated in sodium polytungstate liquid with a density of 2.82 ± 0.02 g/cm³. Heavy minerals were collected in filters and after drying dispersed in Mountex resin with a refraction index of N=1.67. The identification of the minerals was conducted under a polarization microscope after Mange & Maurer (1992). Two hundred mineral grains were counted for each sample.

We furthermore took three samples representative for the

E&G / Vol. 62 / No. 2 / 2013 / 84–97 / DOI 10.3285/eg.62.2.01 / © Authors / Creative Commons Attribution License

three types of materials found: the gleyic paleosols at the base (9Bgk horizon, TB I); the paleosols with signs of human occupation (3A horizon, TB II), and the top of the silty sediment (TB3_00, TB III; cf. Figure 3). Using micromorphology the bulk mineral composition was applied, focusing on the light minerals. The thin-sections (30 µm thick) were prepared from undisturbed soil samples, impregnated at room temperature with resin Cristal MC-40. They were studied under a petrographic microscope, and described following the terminology of Bullock et al. (1985). Additionally, the thin section of the silty sediment was scanned with high resolution, 4800 and 9600 dots per inch (DPI) in order to investigate its overall structure.

4.2 Luminescence dating

Luminescence samples were taken by hammering metal tubes into the freshly cleaned profile (cf. Figures 2 and 3); the tubes were sealed to prevent any light intrusion. Additional samples for dose rate determination (dosimetry) were taken from immediately around the tube samples. The luminescence samples were treated under subdued orange light. The material from the outer ends of the tubes was discarded, and the samples were then dried prior to sieving. The fraction 100–150 µm was treated with 30% HCl, 10% H_2O_2, and sodium oxalate prior to density separation using sodium polytungstate (quartz: $\rho < 2.7$ g/cm³ but > 2.62 g/cm³; potassium (K)-rich feldspar $\rho < 2.58$ g/cm³). The quartz grains were subsequently etched at least once in 30% hydrofluoric acid (HF) for 1 hour, while the feldspar grains only got a short (20 minutes) HF etch (10%) to remove the outer layer of the grains. Finally all fractions were treated with 30% HCl to destroy any fluorides that might have build up during HF etching.

The equivalent doses (D_e) were measured with automated Risø TL/OSL readers as small (samples 2463 and 2464) or medium (sample 2462) aliquots mounted on stainless steel cups. Both infrared (IR) light emitting diodes (LED) and blue LEDs were used. For the quartz extracts the luminescence was detected through a Hoya U340 filter, whilst feldspar detection was through a Schott BG39/Corning 7–59 filter (IR stimulation). All measurements procedures are single aliquot regenerative (SAR) protocols (Murray & Wintle 2000).

Quartz purity checks showed that some aliquots of samples 2462 and 2463 exhibited contamination from IR sensitive material (most likely feldspar), even though the average IR depletion ratio (Duller 2003) was within 10% of unity. To ensure a quartz signal as pure as instrumentally possible from all aliquots, a double SAR (Banerjee et al. 2001) was applied using a preheat of 200°C (10 s) and a cutheat of 180°C. IR and blue stimulation were for 100 s at 125°C. At the end of each cycle, a high temperature blue clean-out (280°C for 40 s) was inserted. The quartz of 2464 was measured without the IR step as it was found to be clean (IR depletion within 2% of unity); the preheat temperature was 260°C and the cutheat temperature 220°C, respectively. Early background subtraction (Cunningham & Wallinga, 2010) was used to calculate the equivalent doses.

Because the quartz for sample 2464 was found to be in saturation (cf. results section and Table 1), equivalent

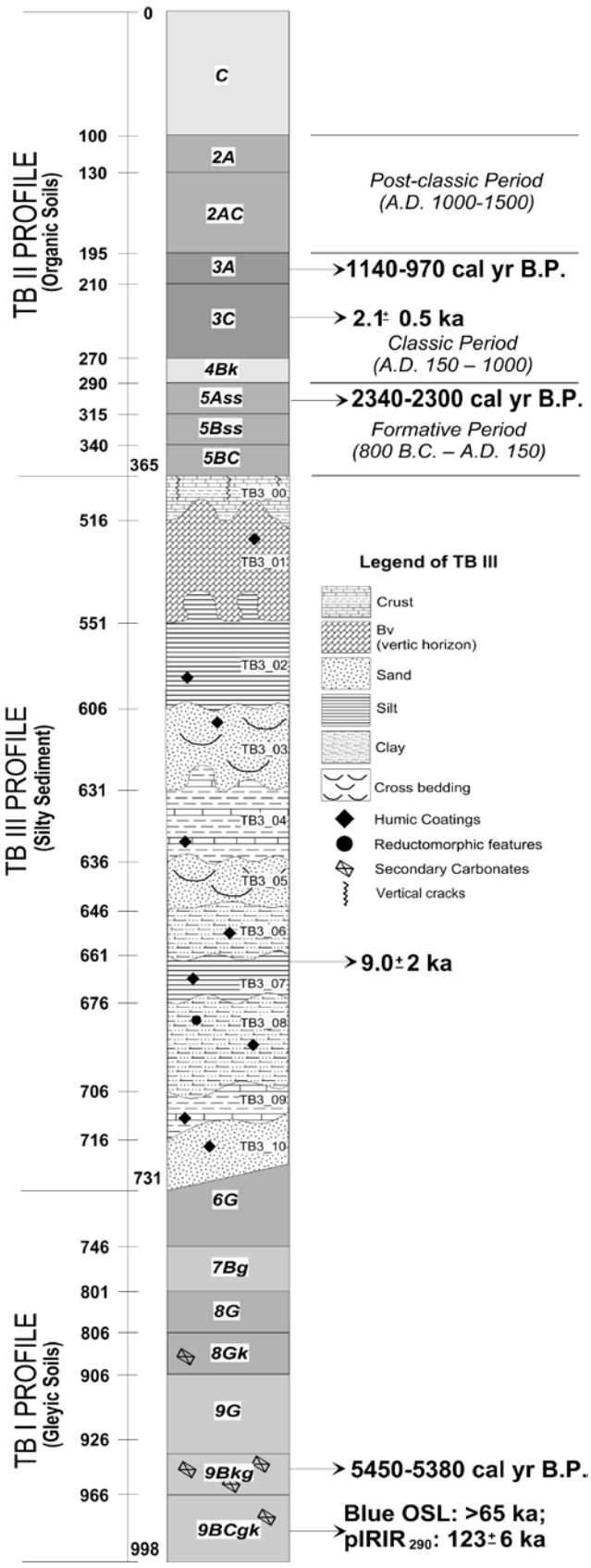

Fig. 3: Tierra Blanca: composite profile and ages.

Abb. 3: Gesamtprofil und Alter für Tierra Blanca.

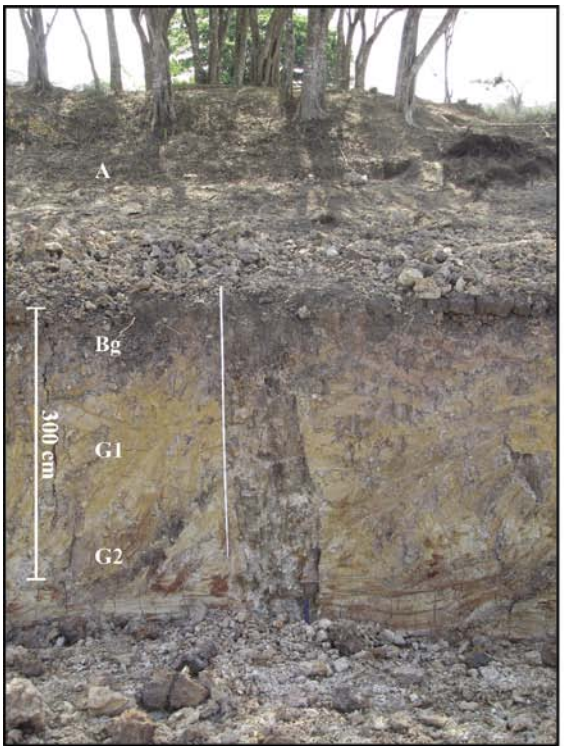

A Horizon (0-10 cm): Sandy material, with very friable subangular blocky structure; dark gray. This horizon is strongly affected by recent human activities, i.e. agriculture and cattle.

Bg Horizon (10-104 cm): Sandy silt with very compact subangular blocky structure. The matrix is gray with red and yellow mottles; slickensides are present. The matrix is free of carbonates and contains traces of large roots (90 cm-lenght) filled of reddish-yellow material. The horizon is moderately friable.

G1 Horizon (104-153 cm): Silty sand and very hard subangular blocky structure that breaks into columns; grayish-green with yellowish and reddish mottles. The matrix is free of carbonates. Slickensides are present.

G2 Horizon (153-260 cm): Silty material with angular blocky structure, which is clearly more friable than G1. It has a green color with mottles in the ped surfaces. On the surfaces of soil fractures there is reddish material, which is friable and silty. The yellowish color is more intense at a depth of 210 cm; where, also Fe concretions and Mn mottles appear

Fig. 4: Balancán: composite profile and field description.

Abb. 4: Gesamtprofil und Geländeaufnahme für Balancán.

doses were also derived from the K-feldspar fraction. A post-IR IRSL protocol was applied using a preheat and cutheat temperature of 320°C, IR stimulation at 50°C (200 s) and post-IR IR stimulation at 290°C (200 s; referred to as $pIRIR_{290}$) (Thiel et al. 2011; Buylaert et al. 2012). An IR clean-out at 325°C (100 s) complemented the measurement cycle. The initial 2 s minus a background of the last 40 s were used for equivalent dose calculation.

Dosimetry samples were dried and homogenized prior to packing ~50 g into N-type beakers. High-resolution gamma-counting was conducted at the Leibniz Institute for Applied Geophysics (Hannover, Germany). Conversion to dose rates is based on the values given in Guérin et al. (2011). The cosmic ray contribution was calculated using the data given in Prescott & Hutton (1994), and for all samples a water content of 25 ± 5% was used. Equivalent doses, dose rates and ages are listed in Table 1.

4 Results

4.1 Heavy minerals

An overview of the heavy minerals found is shown in Figures 6 and 7. The heavy mineral composition of the paleosols and river sediments of the Usumacinta shows a clear pattern for all studied samples (Figure 5): There is a dominance of opaque minerals. These show signs of weathering (Table 2), indicated by leucoxene whitish rings. These observations are specifically pronounced in the alluvial sediments with concentrations ranging from 14.5% to 59.6%. The samples from the TB II section (the youngest paleosols with strong evidence of human occupation; see Table 2) have the lowest concentration of fresh opaque minerals for all studied samples (including Balancán). The smallest amount is found in horizons 3A and 3C, where it is about 4.5%. The underlying horizons show values between 22% and 33%. Epidote is the second most abundant mineral (1% to 21%), with a notable increase in the lowest horizons (5Bss, 5BC, 5C). Interestingly, there are high concentrations of pyroxene in the three uppermost horizons (AC-2A-2AC) with values between 12% and 22%; these are the highest concentration of all studied profiles (Table 2). Furthermore, these horizons show the highest concentrations of green (11%) and brown amphibole (5% to 9%). In general green amphibole has greater abundance than brown hornblende. The presence of calcite is more or less constant throughout the profile, with the exception of the uppermost horizons (AC-2A-2AC-3A), where the content ranges from 18% to 55%. Chlorite and zoisite were also found; they do not exceed 4.5%, again with the highest concentrations in the uppermost horizons. The lower part of the profile (4Bk-5As-5Bss-5BC-5C) shows remarkable heavy mineral patterns with relatively high concentrations of rutile (1.3% to 2.5%), chromospinel (3.0% to 5.8%), turmaline (1.1% to 4.0%), kyanite (1.4% to 2.0%) and monazite (2.0% to 2.8%). It is interesting to note that the 4Bk horizon is the only layer with well-rounded minerals, including coarse silt size, and the presence of volcanic glass on the surface of amphiboles.

For the alluvial units, the most striking aspect is the high concentration of volcanic material represented by amphibole, which is coated by volcanic glass and pyroxenes with dissolution surfaces. However, is not possible to identify a general pattern throughout the sequence except for the presence of calcite in percentages between 1% and 59% (the major part located in the middle of the sedimentary sequence). The accumulation of minerals is less homogene-

E&G / Vol. 62 / No. 2 / 2013 / 84–97 / DOI 10.3285/eg.62.2.01 / © Authors / Creative Commons Attribution License

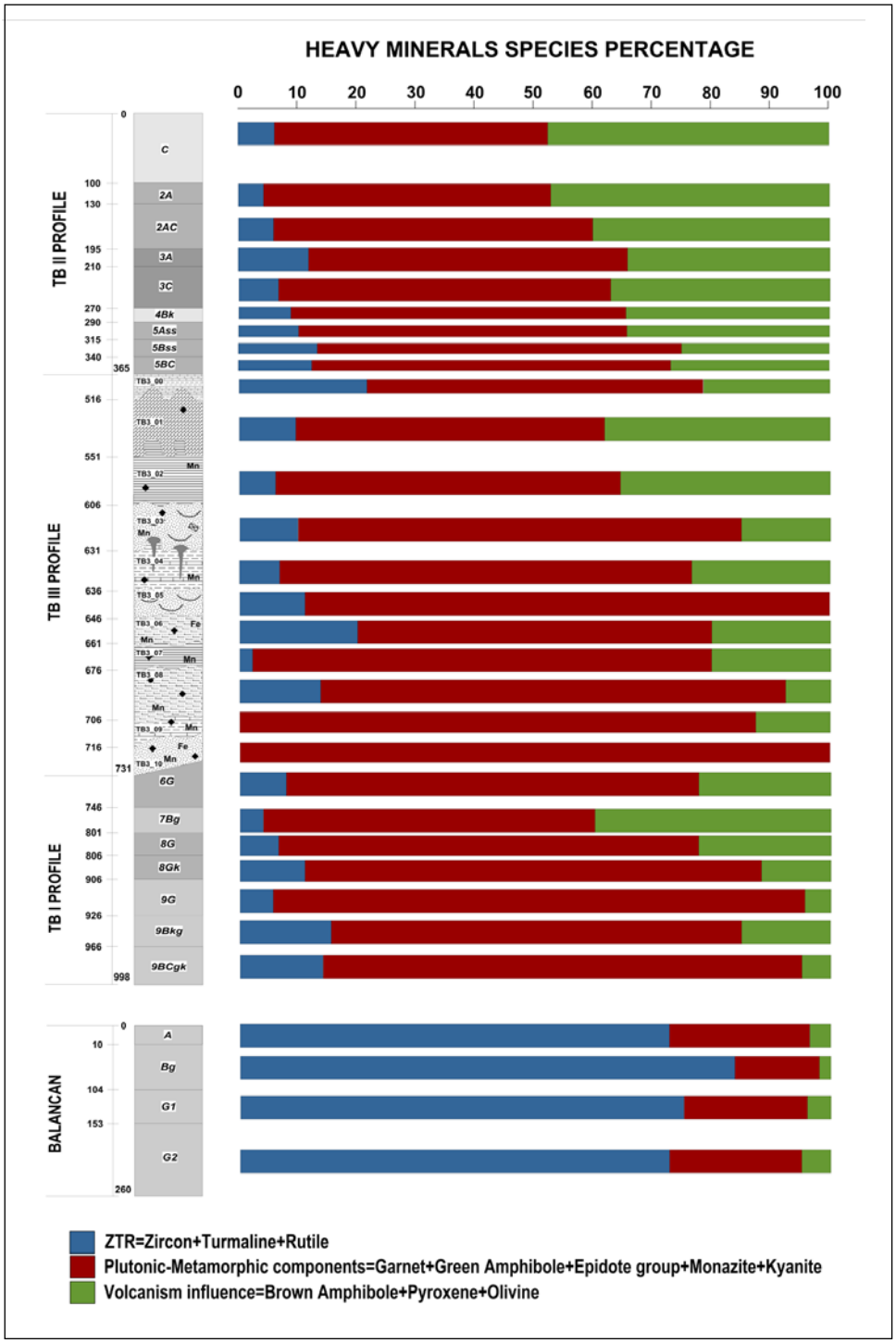

Fig. 5: Tierra Blanca and Balancán profiles and relative abundance of heavy minerals.

Abb. 5: Zusammenstellung der Profile und relative Vorkommen der Schwerminerale für Tierra Blanca und Balancán.

ous compared to the soil profiles. There seems to be a weak tendency of enhanced concentrations for green amphibole, epidote, and pyroxene in the bottom of the profile. Garnet is only of importance in the middle part of the profile (3.4% to 6.0%).

The lower part of the TB profile (TB I; Figure 3) shows a more regular pattern in the mineral concentration. The most important characteristic is the highest presence of epidote ranging from 20.8% to 28.3%, and the concentration of stable minerals (garnet, titanite, zircon, zoisite, rutile, chromospinel, monazite, and kyanite) with a decrease of less stable minerals (like amphibole). Many of these minerals have a metamorphic source (from moderate to high grade metamorphic phases). The influence of the volcanic source is less evident, however, pyroxene and olivine show large concentrations (mainly in the upper part of the profile, i.e. 6G-7Bg-8G-8Gk). Horizons 6G and 9G show the largest abundance of opaque minerals (Table 2). There is clearly a change in the mineral composition at the boundary between 6G and the lowermost part of the silty sediment (Figure 3), where the metamorphic components dominate. The amount of calcite is much smaller than for TB II and TB III (0.2% to 3.5%).

The Balancán profile shows clear differences in comparison to the Tierra Blanca sections; there ultrastable minerals are present (Figure 5). The sequence shows very high contents of zircon (17% to 25.5%), rutile (3.4% to 8.4%), and titanite (2.0% to 5.3%). There is only very little epidote and hardly any calcite present (Table 2).

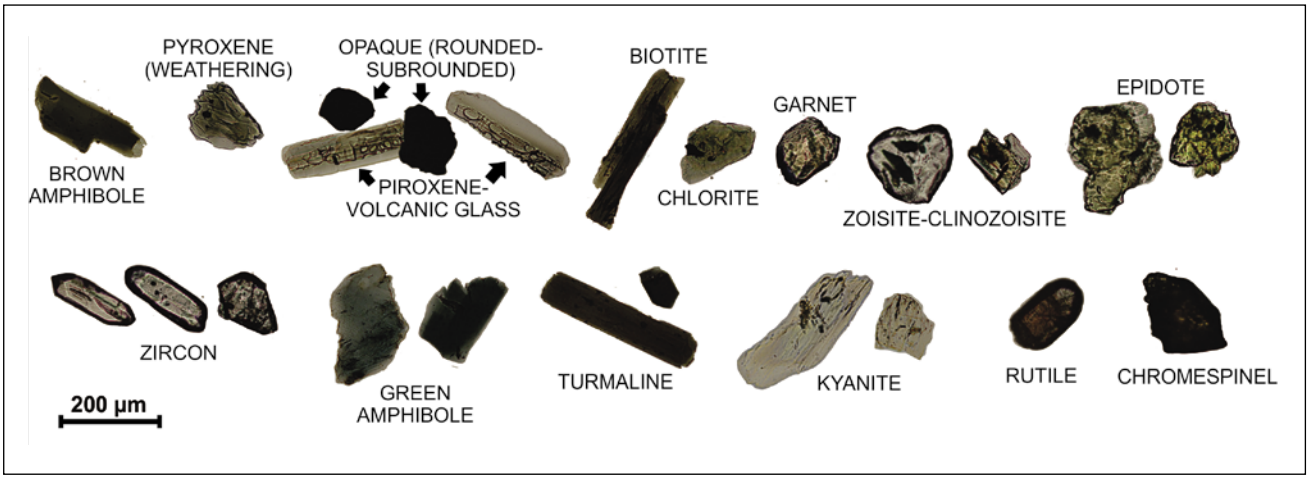

Fig. 6: Heavy minerals under the petrographic microscope using plane polarized light.

Abb. 6: Ausgewählte Schwerminerale unter dem petrograpischen Mikroskop unter der Verwendung von eben-polarisiertem Licht.

4.2 Micromorphology of selected horizons

Horizon 3A (TB I) is dominated by a clayey-silty texture; there are only a few sand grains. The structure evidences vertic features (angular blocky structure with porostriated b-fabric; Figure 7a). Weathered volcanic glass is also present (Figure 7b). 9Bkg horizon is very clayey but contains some sand grains, which are mainly composed of quartz (Figures 7c and 7d). A few micas are also present; these are all highly weathered. Clay coatings are frequent. In TB III the most remarkable feature in the silty sediment is the strong lamination that is clearly shown not only in the profile (Figure 2c) but also in the scanned section (Figure 7e). This laminated sediment is dominated by volcanic glass which is angular (Figure 7f).

5 Discussion

5.1 Ages of the paleosol units and pedostratigraphy

The gleyic paleosols (horizons 6 to 9) found in TB I are clearly much older than the overlying succession (TB III and TB II). Horizon 9BCgk was luminescence dated to >65 ka (quartz OSL; sample 2464); the feldspar ($pIRIR_{290}$) yielded an age of 123 ± 6 ka (Table 1). This age represents the age of the parent material of paleosol 9, i.e. the paleosols are younger. One might argue that alluvial sediments are not well-bleached prior to deposition, i.e. the luminescence signal is not reset, which would result in an age overestimate. It is very unlikely that the alluvial sediments at this site carry a large residual dose, which is shown by the youngest sample (horizon 3C; sample 2462): Its luminescence age is in very good agreement with the radiocarbon ages of the over- and underlying layers (Table 1). The radiocarbon age of 5450–5380 cal. B.P. for the lowermost paleosol (horizon 9Bkg; Table 1) was derived from neoformed carbonates; they postdate the age of the sediments. The gleyic paleosols show strong redoximorphic features, leaching (carbonates are absent in the groundmass) and intense clay accumulation (including well preserved clay coatings). All these characteristics point to pedogenesis in a moist environment, sometimes accompanied by water-logging that is hardly compatible with the formation of calcite. Thus, carbonates precipitated much later, after environmental conditions changed. As a consequence, the age of the carbonate concretions (5450–5380 cal. B.P.) cannot be interpreted as the age of the first intensive pedogenetic phase. According to the luminescence ages of the parent material and of the overlying alluvial sequence (sample 2463; cf. Table 1) the soils formed after 123 ± 6 ka but prior to 9 ± 2 ka.

The latter age is the only age estimate for the silt sediment between the two pedocomplexes (TB I and TB II) (cf. Figure 3). The deposition thus took place during the Holocene. The underlying pedocomplex had a very long time for its development (i.e. from 123 ± 6 ka until the Holocene). The presence of several phases of sedimentation and soil formation (to constitute each paleosol in the pedocomplex) take a considerable time span, especially if one takes into account the weathering degree of each paleosol, which is higher than for the soils of the overlying sequence.

However, one has to consider that the migration of the river system might have caused erosion of parts of the Late Pleistocene sequence. Evidence of such erosional phases are as follows: None of the Gleysols have A horizons, and there are changes in the heavy mineral distribution, which clearly reflects discontinuities (Figure 5). Such discontinuities are obvious between 8G/7Bg; 7Bg/6G, and 6G/silty sediment (the latest is the most contrasting).

Solís-Castillo et al. (2013) have presented a chronological framework based on radiocarbon and archeological evidence for the younger paleosols (TB II). They presented an age of 2340–2300 cal B.P. for soil horizon 5Ass (Figure 3), and they found ceramic belonging to the Formative culture, which agrees with the dating result. The presence of Vertisols, which formed during the same period, has been documented in other areas of the Mayan Lowlands (Dahlin et al. 1980; Pope & Dahlin 1989, 1993; Dunning & Beach 2004; Beach et al. 2006; Dunning et al. 2006).

Horizon 3A was radiocarbon dated to 1140–970 cal. B.P (Solís-Castillo et al. 2013). The luminescence age of 2.1 ± 0.5 ka for horizon 3C fits well into this chronological framework, and can give some insights about the period of relative landscape stability. The age from the 3C horizon represents the time when the sediment was deposited, that is the maxi-

E&G / Vol. 62 / No. 2 / 2013 / 84–97 / DOI 10.3285/eg.62.2.01 / © Authors / Creative Commons Attribution License

Tab. 2: Summary of the heavy mineral analysis results (in percentage).

Tab. 2: Zusammenfassung der Ergebnisse der Schwermineralanalyse (angegeben in Prozent).

Horizon	Volcanic		Plutonic-Metamorphic					ZTR (ultra stable)			Opaque Minerals	
	Brown amphibole	Pyroxene	Garnet	Green amphibole	Epidote group	Monazite	Kyanite	Zircon	Turmaline	Rutile	Weathered	Fresh
Tierra Blanca II												
C	8.95	17.02	2.28	11.05	8.07	0.00	0.00	2.28	0.00	1.05	25.26	0.00
2A	5.32	22.20	1.28	11.19	13.03	0.00	0.00	0.73	0.73	1.10	22.02	0.00
2AC	6.52	11.86	7.31	2.17	12.85	0.00	0.59	1.38	0.20	1.19	26.68	0.99
3A	0.00	0.00	0.25	0.75	1.01	0.00	0.00	0.25	0.00	0.00	4.52	5.03
3C	1.67	0.83	0.83	3.33	2.92	0.00	0.00	2.08	0.42	0.00	4.58	0.83
4Ck	1.42	3.30	6.60	5.19	10.85	0.00	0.47	2.36	0.94	0.00	33.02	3.30
5Ass	7.17	7.89	2.15	2.15	10.04	2.51	1.43	6.45	3.94	0.72	27.60	6.09
5Bss	6.31	4.32	1.99	1.33	20.60	1.99	1.99	3.99	1.66	1.33	24.25	6.31
5BC	6.20	5.43	4.65	1.94	17.83	1.94	0.00	3.49	1.16	1.16	29.07	4.26
5C	4.13	6.06	3.31	2.20	20.94	2.75	0.83	6.61	3.31	2.48	27.00	2.75
Tierra Blanca III												
TB3_0	11.01	12.50	0.89	7.74	20.83	1.79	1.19	2.68	2.38	1.19	24.40	1.49
TB3_1	1.74	6.67	2.32	2.32	7.83	0.58	0.00	1.16	0.00	0.29	19.13	7.83
TB3_2	2.54	0.00	1.69	4.24	5.93	0.00	0.00	1.69	0.00	0.00	50.00	16.10
TB3_3	0.78	7.03	1.56	4.69	14.06	0.78	0.00	2.34	0.00	0.00	30.47	17.19
TB3_4	0.00	0.00	0.81	2.42	3.23	0.00	0.00	0.81	0.00	0.00	14.52	16.13
TB3_5	6.78	3.39	3.39	13.56	11.86	0.00	0.00	8.47	1.69	0.00	18.64	3.39
TB3_6	7.69	3.85	8.97	19.23	15.38	0.00	0.00	1.28	0.00	0.00	23.08	2.56
TB3_7	1.82	1.82	5.45	12.73	18.18	0.00	0.00	3.64	3.64	0.00	14.55	1.82
TB3_8	1.75	1.75	0.00	3.51	21.05	0.00	0.00	0.00	0.00	0.00	59.65	7.02
TB3_9	0.00	0.00	3.09	0.00	6.79	0.00	0.00	0.00	0.00	0.00	61.11	27.16
TB3_10	3.55	8.28	2.37	18.93	14.20	1.79	0.00	1.78	2.37	0.00	37.87	4.14
Tierra Blanca I												
6G	2.49	7.21	2.62	0.98	22.62	0.00	0.00	2.30	1.49	0.50	25.87	0.50
7Bg	0.66	2.53	2.11	0.84	28.27	0.00	0.33	2.11	0.33	0.33	37.70	4.92
8G	0.84	2.70	1.96	0.25	26.72	0.98	0.00	2.45	0.00	0.42	38.40	9.28
8Gk	1.96	1.22	6.40	1.22	28.96	1.69	0.00	0.91	0.25	1.96	44.61	0.98
9G	0.00	5.38	6.01	0.95	20.89	1.72	0.00	5.70	0.30	1.22	36.89	10.37
9Bkg	1.90	0.70	6.32	1.75	23.51	0.61	2.85	5.26	0.32	1.58	25.63	13.29
9BCgk	1.05	7.21	2.62	0.98	22.62	0.95	0.35	2.30	0.00	1.05	32.28	4.56
Balancan												
A	1.55	0.00	0.00	7.75	1.55	0.78	0.00	24.42	0.39	7.36	44.96	3.88
Bg	0.62	0.00	0.00	0.62	2.80	0.93	0.62	20.81	0.00	8.39	25.16	30.12
G_1	0.76	0.38	0.00	1.14	2.28	1.14	1.14	19.77	0.00	3.42	46.77	10.27
G_2	1.06	0.53	0.00	3.19	2.66	1.06	0.53	17.02	1.60	6.38	48.40	6.38

mum age of the soil. In contrast, the date obtained from the bulk organic matter of 3A represents the minimum age of the paleosol, just prior to its burial. These ages show that the soil formed within 1000 years (the difference between the age of 3C and 3A horizons: beginning and end of pedogenesis).

5.2 Provenance and landscape evolution: Mineralogical evidences

Mineralogical assemblages are similar among all studied profiles (Figure 5). However, in the upper units, higher amounts of volcanic minerals can be detected. It is clear

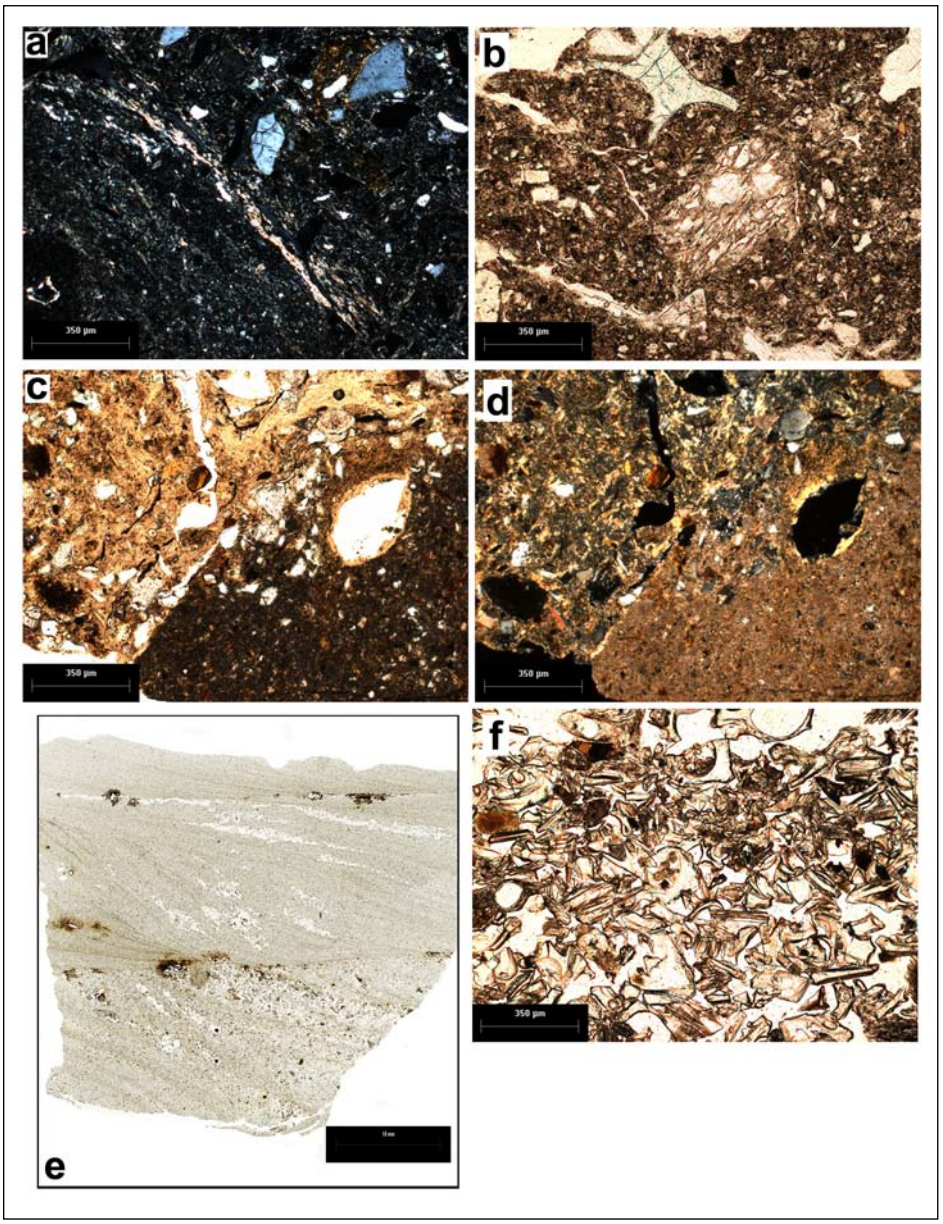

Fig. 7. Micromorphology of selected horizons: (a) porostriated b-fabric in horizon 3A TB I, cross polarized light (XPL); (b) weathered pumice in horizon 3A TB I, plane-polarized light (PPL); (c) Clay coatings and pedogenetic carbonates in 8Bkg horizons (PPL); (d) Clay coatings and pedogenetic carbonates in 8Bkg horizons (XPL); (e) silty sediment from TB III; (f) volcanic glass in the silty sediment of TB III (PPL).

Abb. 7: Mikromorphologie von ausgewählten Horizonten: (a) poro-streifiges b-Fabric aus Horizont 3A TBI, gekreuztploarisiertes Licht (XPL); (b) verwitterter Bims aus Horizont 3A TB1, ebenpolarisiertes Licht (PPL); (c)Toncutane und pedogenes Karbonat aus Horizont 8Bkg (PPL); (d) Toncutane und pedogenes Karbonat aus Horizont 8Bkg (XPL); (e) silitiges Sediment aus TB III; (f) vulkanisches Glas im siltigen Sediment aus TB III (PPL).

that the active volcanism in the Central America Volcanic Arc can provide such minerals to the alluvial plain of Tabasco (Figure 1). It is interesting to note that these minerals have angular and subangular shapes suggesting transport by slow river flow. It is likely that they originate from ash falls coming directly from the primary source.

One of the most intriguing materials is the silty sediment in the upper part of TB III (TB3_00). Its sand fraction contains a mixture of volcanic, metamorphic, and plutonic minerals, but in the thin sections, we clearly observe the dominance of laminated volcanic materials, particularly, volcanic glass (Figure 7). Based on the mineralogical data and an age of 9 ± 2 ka of the sediment, in which the minerals were found, we attempt to correlate the mineral assemblage to a possible eruption in the surrounding area. According to Arce (personal communication), it is likely that the Tacana volcano (Figure 1) provided the volcanic material found in the sediment. This volcano had large voluminous eruptions during the Late Pleistocene (Arce et al. 2012). This material can subsequently be reworked over short distances by the river. However, a detailed analysis is needed to draw any final conclusions on the provenance of this sample.

The heavy mineral associations (Figure 8) of the investigated sediments imply a broad range of metamorphic source rocks, suggesting the influence of different tectonic environments. Zircon-Turmaline-Rutile (ZTR) suit minerals (Hubert 1962) are common in acidic to intermediate granitoid rocks as well as in mature siliciclastic sediments and some metamorphic rocks (e.g. von Eynatten & Gaupp 1999). The highest concentrations of ZTR in the Balancán profile can be interpreted as originating from an ancient sedimentary recycling phase, where the dissolution and pedogenesis reduces the less stable minerals (Garzanti & Ando 2007). It is interesting to draw attention to the origin of the rutile phases: The majority of detrital rutile comes from medium to high grade metamorphic rocks (Force 1980; 1991) and recycled sediments. The same mineralogical evidence is found in the metamorphic complex of Southeast Guatemala (garnet, kyanite, rutile schists, and abundant ortho-gneisses, which range from mafic to granitic); this is where the Usumacinta River starts. In consequence, our data suggest that the river transported material from this region.

E&G / Vol. 62 / No. 2 / 2013 / 84–97 / DOI 10.3285/eg.62.2.01 / © Authors / Creative Commons Attribution License

Additionally, the dominance of euhedral tourmaline indicates proximity to the source rocks and short transport from a predominantly low-grade metamorphic source (Singh et al. 2004). Chlorite and epidote were also derived from low-grade metamorphic series, whereas gneisses, granitoid rocks and recycled sedimentary rocks are possible sources of (ultra) stable minerals like zircon, tourmaline and rutile. Kyanite indicates the presence of high-pressure metamorphic rocks in the catchment; it has to be noted that it is not a dominant mineral in the assemblage. Solari et al. (2011) have documented areas in Central Guatemala with high-pressure metamorphic rocks. As this area is cut northwards by the Chixoy River until it joins with the Passion River (a tributary of the Usumacinta; Figure 1), it is very likely that this is the sediment source for the alluvial plain.

The presence of chromspinel and epidote group minerals are indicative for a source area with ophiolite complexes associated with suture zones. The most important suture zone near the study area is in Guatemala where the Usumacinta River springs (Figure1). At present, this suture zone is part of a major left lateral strike slip boundary between the North American plate to the north (locally known as the Maya block) and the Caribbean plate (locally the Chortís block) to the south (Brueckner et al. 2009).

The units in the Mayan block include the Chuacús metamorphic complex, recently shown to include eclogitic lenses that record a Late Cretaceous event (Ortega-Gutierrez et al. 2007; Martens et al. 2007, 2010), Paleozoic sedimentary rocks of the Santa Rosa Group, low-grade meta-sediments (white mica-chlorite schists, quartzite, and minor marble) associated with antigorite schist/mélange and deformed granites. The Chortís block contains the green schist facies, San Diego phyllite, the amphibolites facies Las Ovejas complex, and relatively undeformed granitoids. Numerous U-Pb zircon ages from granites and their host gneisses north of the fault resulted in Late Proterozoic (Grenville), Carboniferous, and Triassic ages as well as a metamorphic event at c. 70 Ma (Martens et al. 2007, 2010).

5.3 Implication for human land use

Our data can provide some insight into the land use of the region, especially with respect to fluctuations of human occupation and to the ceramic production. It is obvious that the presence of well-drained soils in Tierra Blanca (TB II) favored human occupation. These paleosurfaces were not inundated and represented stable areas for human activities, which were more or less continuous throughout the last 2–3 millennia. In contrast, other archeological sites such as Palenque, even though bigger in size, had less continuous occupation (for details see Liendo et al. 2013).

Further, is interesting to note that the suite of heavy minerals in paleosols and sediments found in Tierra Blanca has also been documented in petrographic studies about the pottery of the region (Obando et al. 2011). It can therefore be deduced that the material at Tierra Blanca is very suitable for the manufacturing of the pottery. The gleyic paleosols at the base provided clay for the clay matrix of the ceramic, while the volcanic glass found in the silty sediment (TB III) could be used as temper. Thus, this area has been of great importance to the humans at this time.

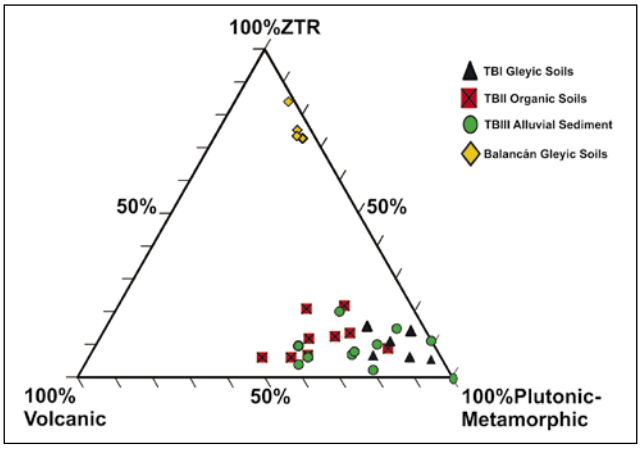

Fig. 8: Ternary diagram with the relative mineralogical suites of heavy minerals. ZTR = zircon + turmaline + rutile; Plutonic-Metamorphic = garnet + green amphibole + epidote group + monazite + kyanite; Volcanic = brown amphibole + pyroxene + olivine.

Abb. 8: Phasendiagramm für die mineralogischen Charakter der Schwerminerale. ZTR = Zirkon + Turmalin + Rutil; plutonisch-metamorph = Granat + grüner Amphibol + Epidotgruppe + Monazit + Kyanit; Vulkanisch = brauner Amphibol + Pyroxen + Olivin.

6 Conclusions

The alluvial terrace system of the Usumacinta River reflects the Late Quaternary pedostratigraphy of the region. On the alluvial Pleistocene terrace, soils with gleyic features are present. On the oldest Holocene terrace (HT2), we found the remnants of the gleyic paleosols in sediment dated to 123 ± 6 ka ($pIRIR_{290}$), while on the younger terraces (HT1, HT0) only less developed paleosols are present.

Metamorphic and plutonic terrains of the south of Mexico and Guatemala were identified as the main source of sediments for the Tierra Blanca area. However, the heavy mineral assemblages reflect some changes in provenance throughout time. Soils located on the older terraces, as in Balancán, show the presence of ultra-stable minerals; these reflect prolonged landscape stability and soil formation. In consequence, this mineralogical set can be used for pedostratigraphic correlation and tracing the oldest terraces in the area.

Larger amounts of volcanic minerals in the younger paleosols may allow for pointing out areas which were affected by eruptions. Further, the mineral compositions, if compared with those of ceramics might make it possible to trace the source regions for ceramic production.

Acknowledgement

This research has been funded by PAPIIT, (grants no. IN117709 and IN110710; E. Solleiro-Rebolledo), a bilateral project (no. CONACYT-DLR J010/0705/09 and CONACYT 166878; E. Solleiro-Rebolledo), and Coordinación de Estudios de Posgrado (UNAM). Funding from the Bundesministerium für Bildung und Forschung, Internationales Büro (German Ministery for Education and Research, International office) in form of the bilateral project MEX 08/002 is very much appreciated. We thank Christina Wiesbeck, Daniel Jäger, Jaime Díaz and Serafín Sánchez for assistance during field work.

References

Arce, J.L., Macías, J.L., Gardner, J.E., Rangel, E. (2012): Reconstruction of the Sibinal Pumice, an andesitic Plinian eruption at Tacaná Volcanic Complex, Mexico–Guatemala. – Journal of Volcanology and Geothermal Research 217–218: 39–55.

Banerjee, D., Murray, A.S., Bøtter-Jensen, L., Lang, A. (2001): Equivalent dose estimation using a single aliquot of polymineral fine grains. – Radiation Measurements, 33: 73–94.

Beach, T., Luzzadder-Beach, S., Dunning, N. & Scarborough, V. (2003): Depression soils in the lowland tropics of northwestern Belize. – In: Gomez-Pompa, A., Allen, M., Fedick, S.L., Jimenez-Osornio, J.J. (eds.): Lowland Maya Area: Three Millennia at the Human-Wildland Interface: 139–173; Binghamton, NY (Haworth Press).

Beach, T., Dunning, N., Luzzadder-Beach, S., Cook, D.E. & Lohse, J. (2006): Impacts of the ancient Maya on soils and soil erosion in the central Maya Lowlands. – Catena, 65: 166–178.

Brueckner, H.K. & Force, E.R. (1980): The provenance of rutile. – Journal of Sedimentary Petrology, 50: 485–488.

Brueckner, H.K., Avé Lallemant, H.G., Sisson, V.B., Harlow, G.E., Hemming, S.R., Artens, U., Tsujimori, T. & Sorensen, S.S. (2009): Metamorphic reworking of a high pressure–low temperature mélange along the Motagua fault, Guatemala: A record of Neocomian and Maastrichtian transpressional tectonics. – Earth and Planetary Sciences Letters, 284: 228–235.

Bullock, P., Fedoroff, N., Jongerius, A., Stoops, G., Tursina, T. & Babel, U. (1985): Handbook for Soil Thin Section Description. – 152 p.; Waine Research Publications, Wolverhampton, Ukraine.

Buylaert, J.-P., Jain, M., Murray, A.S., Thomsen, K.J., Thiel, C. & Sohbati, R. (2012): A robust feldspar luminescence dating method for Middle and Late Pleistocene sediments. – Boreas, 41: 435–451.

Cabadas-Baez, H., Solleiro-Rebolledo, E., Sedov, S., Pi, T. & Gama-Castro J. (2010): Pedosediments of karstic sinkholes in the eolianites of NE Yucatán: a record of Late Quaternary soil development, geomorphic processes and landscape stability. – Geomorphology, 122: 323–337.

Consejo de Recursos Minerales (1999): Monografía Geológico Minera del Estado de Tabasco. – 152 p.; Conabio, Mexico.

Cunningham, A.C. & Wallinga, J. (2010): Selection of integration time intervals for quartz OSL decay curves. – Quaternary Geochronology, 5: 657–666.

Dahlin, B.H., Chambers, M.E. & Foss, J.E. (1980): Project Acalches: Reconstructing the Natural and Cultural History of a Seasonal Swamp at El Mirador Guatemala; Preliminary Results. – In: Matheny R. (ed.): El Mirador, Peten, Guatemala: An Interim Report. Publication 45. New World Archaeological Foundation; Provo, Utah.

Donnelly, T.W., Horne, G.S., Finch, R.C. & Lopez, R.E. (1990): Northern Central America: The Maya and Chortis blocks. – In: Dengo, G., Case, J.E. (eds.): The Geology of North America, Vol. H: The Caribbean Region: 37–76; Geological Society of America.

Duller, G.A.T. (2003): Distinguishing quartz and feldspar in single grain luminescence measurements. – Radiation Measurements, 37: 161–165.

Dunning, N.P. & Beach, T. (2004): Fruit of the Lu'um: Lowland Maya Soil Knowledge and Agricultural Practices. – Mono y Conejo, 2: 1–25.

Dunning, N.P., Luzzadder-Beach, S.L., Beach, T., Jones, J.G., Scarborough, V. & Culbert, T.P. (2002): Arising from the Bajos: The Evolution of a Neotropical Landscape and the Rise of Maya Civilization. – Annals of the Association of American Geographers, 92: 267–283.

Dunning, N., Beach, T. & Luzzadder-Beach, S. (2006): Environmental variability among bajos in the southern Maya Lowlands and its implications for ancient Maya civilization and archaeology. – In: Lucero, L., Fash, B. (eds.): Pre-Columbian Water Management: 111–133; University of Arizona Press.

Einsele, G. (1992): Sedimentary Basins. – 648 p; Springer (Berlin).

Fedick, S.L., Flores-Delgadillo, M.L., Sedov, S., Solleiro-Rebolledo, E. & Palacios-Mayorga, S. (2008): Adaptation of Maya Homegardens by Container Gardening in Limestone Bedrock Cavities. – Journal of Ethnobiology, 28: 305–317.

Fernandez F., Johnson, K., Terry, R., Nelson, S. & Webster, D. (2005): Soil resources of the Ancient Maya at Piedras Negras, Guatemala. – Soil Science Society of America Journal, 69: 2020–2032.

Force, E.R. (1980): The provenance of rutile. – Journal of Sedimentary Petrology, 50: 485–488.

Force, E.R. (1991): Geology of titanium-mineral deposits. – Geological Society of America Special Paper, 259: 112.

Garzanti, E. & Ando, S. (2007): Heavy mineral concentration in modern sands: implications for provenance interpretation. – In: Mange, M.A. & Wright, D.T. (eds.): Heavy Minerals in Use: Developments in Sedimentology, 58: 517–545.

Guérin, G., Mercier, N. & Adamiec, G. (2011): Dose-rate conversion factors: update. – Ancient TL, 29: 5–8.

Hernandez Santana, J.R., Mendez Linares, A.P. & Bollo Manent, M. (2012): Análisis morfoestructural del relieve noroccidental del Estado de Chiapas, México. – Revista Geográfica Venezolana, 53: 57–75.

Hodell, D., Brenner, M. & Curtis, J.H. (2005): Terminal Classic drought in the northern Maya Lowlands inferred from multiple sediment cores in Lake Chichancanab (Mexico). – Quaternary Science Reviews, 24: 1413–1427.

Hubert, J.F. (1962): A zircon–tourmaline–rutile maturity index and the interdependence of the composition of heavy mineral assemblages with the gross composition and texture of sandstones. – Journal of Sedimentary Petrology, 32: 440–450.

Hughes, P.H. (2010): Geomorphology and Quaternary stratigraphy. The roles of morpho-, litho-, and allostratigraphy. – Geomorphology, 123: 189–199.

Komar, P.D. (2007): The entrainment, transport and sorting of heavy minerals by waves and currents. In: Mange, M.A. & Wright, D.T. (eds). Heavy Minerals in use. – Developments in Sedimentology, 58: 3–48.

Kraus, M.J. (2002): Basin-scale changes in floodplain paleosols: implications for interpreting alluvial architecture. – Journal of Sedimentary Research, 72: 500–509.

Martens, U., Mattinson, C.G., Wooden, J. & Liou, J.G. (2007): Protolith and metamorphic ages of gneiss hosting eclogite in the Chuacús complex, Central Guatemala. – American Geophysical Union (AGU), EOS Transactions, 88(23), Joint Assembly Supplement, Abstract: U53A-08.

Martens, U., Weber, B. & Valencia, V.A. (2010): U/Pb geochronology of Devonian and older Paleozoic beds in the southwestern Maya Block, Central America: its affinity with Peri-Gondwanan terranes. – Geological Society of America Bulletin, 122: 815–829.

Mikesell, L.R., Schaetzl, R. & Velbel, M.A. (2004): Hornblende etching and quartz/feldspar ratios as weathering and soil development indicators in some Michigan soils. – Quaternary Research, 62: 162–171.

Murray, A.S. & Wintle, A.G. (2000): Luminescence dating of quartz using an improved single-aliquot regenerative-dose protocol. – Radiation Measurements, 32: 57–73.

Ortega-Gutiérrez, F., Solari, L.A., Ortega-Obregón, C., Elías-Herrera, M., Morán-Ical, S., Chiquín, M., Keppie, J.D., Torres de León, R. & Schaaf, P. (2007): The Maya-Chortís boundary: a tectonostratigraphic approach. – International Geology Review, 449: 996–1024.

Ortiz Perez, M.A., Siebe, C. & Cram, S. (2005): Diferenciación ecogeográfica de Tabasco. In: Bueno, J., Álvarez, F. & Santiago, S. (eds.): Biodiversidad del Estado de Tabasco: 305–322; Instituto de Biología, UNAM- CONABIO (Mexico).

Padilla, R. & Sanchez, R.J. (2007): Evolución geológica del sureste mexicano desde el Mesozoico al presente en el contexto regional del Golfo de México. – Boletín de la Sociedad Geológica Mexicana, LIX: 19–42.

Pirkle, F.L., Pirkle, W.A. & Pirkle, E.C. (2007): Heavy Minerals Sands of the Atlantic and Gulf Coastal Plains, USA. – In: Mange, M.A. & Wright, D.T. (eds): Heavy Minerals in use. – Developments in Sedimentology, 58: 1145–1234.

Pope, K.D. & Dahlin, B.H. (1989): Ancient Maya Wetland Agriculture. New Insights from Ecological and Remote Sensing. – Journal of Field Archaeology, 16: 87–106.

Prescott, J.R. & Hutton, J.T. (1994): Cosmic ray contributions to dose rates for luminescence and ESR dating: large depths and long-term variations. – Radiation Measurements, 23: 497–500.

Retallack, G.J. (1990): Soils of the past. An introduction to paleopedology. – 404 p.; Blackwell Science (U. K.).

Rosenmeier, M.F., Hodell, D.A., Brenner, M. & Curtis, J.H. (2002): A 4000-Year Lacustrine Record of Environmental Change in the Southern Maya Lowlands, Petén, Guatemala. – Quaternary Research, 57: 183–190.

Sedov S., Solleiro-Rebolledo, E., Fedick, S.L., Gama-Castro, J., Palacios-Mayorga, S. & Vallejo Gomez, E. (2007): Soil genesis in relation to landscape evolution and ancient sustainable land use in the northeastern Yucatan Peninsula, Mexico. – Atti della Società Toscana de Scienze Naturali di Pisa, Serie A, 112: 115–126.

Schatzl, R. & Anderson, S. (2005): Soils: Genesis and Geomorphology. –791 p; New York.

Singh, B.P., Pawar, J.S. & Karlupia, S.K. (2004): Dense mineral data from the northwest Himalayan foreland sedimentary rocks and recent river sediments: evaluation of the hinterland. – Journal of Asian Earth Sciences, 23: 25–35.

Solís-Castillo, B., Solleiro-Rebolledo, E., Sedov, S., Liendo, R., Ortiz-Pérez, M.A., López-Rivera, S. (2013): Paleoenvironment and human occupation in the Maya lowlands of the Usumacinta River, Mexico. – Geoarchaeology, 28: 268–288.

Solleiro-Rebolledo, E., Sycheva, S., Sedov, S., McClung de Tapia, E., Rivera-Uria, Y., Salcido-Berkovich, C., Kuznetsova, A., (2011): Fluvial processes and paleopedogenesis in the Teotihuacan Valley, México: Responses to late Quaternary environmental changes. – Quaternary International, 233: 40–52.

Thiel, C., Buylaert, J.-P., Murray, A., Terhorst, B., Hofer, I., Tsukamoto, S. & Frechen, M. (2011): Luminescence dating of the Stratzing loess profile (Austria) – Testing the potential of an elevated temperature post-IR IRSL protocol. – Quaternary International, 234: 23–31.

Von Eynatten, H. & Gaupp, R. (1999): Provenance of Cretaceous synorogenic sandstones in the Eastern Alps: constraints from framework petrography, heavy mineral analysis and mineral chemistry. – Sedimentary Geology, 124: 81–111.

West R.C., Psuty, N.P. & Thom, B.G. (1969): The Tabasco lowlands of Southern Mexico. – 88 p.; Louisiana State University Press.

WRB, World Reference Base for soil resources (2006): A framework for international classification, correlation and communication: World Soil Resources Reports 103, Food and Agricultural Organization of the United Nations, Rome.

E&G Quaternary Science Journal
Volume 62 / Number 2 / 2013 / 98–119 / DOI 10.3285/eg.62.2.02
www.quaternary-science.net

GEOZON SCIENCE MEDIA
ISSN 0424-7116

Holozäne Landschaftsentwicklung an der Westküste der Nordseeinsel Amrum

Tanja Tillmann, Daniel Ziehe, Jürgen Wunderlich

How to cite: Tillmann, T., Ziehe, D., Wunderlich J. (2013): Holozäne Landschaftsentwicklung an der Westküste der Nordsee Amrum. – E&G Quaternary Science Journal, 62 (2): 98–119. DOI 10.3285/eg.62.2.02

Kurzfassung:

Barriereinseln und Außensände, geformt durch eine Kombination aus Wind, Wellen, Strömung und Küstenlängstransport gelten als morphologisch hoch aktive Küstenbereiche und variieren häufig in Ursprung, Genese und Entwicklung. Sie besitzen durch ihre dissipative Wirkungsweise eine bedeutende Schutzfunktion für rückwärtige Inseln, Halligen und Festlandbereiche und bilden vor der Küste Nordfrieslands die westliche Außengrenze des Wattenmeeres.
Ziel der nachfolgenden Studie ist es, anhand hochauflösender Georadarmessungen und sedimentologischer Daten aus Bohrungen die Landschaftsgeschichte an der Westküste Amrums sowie die Entstehung und interne sedimentäre Architektur des der Insel westlich angelagerten Kniepsandes zu untersuchen und die Prozesse, die zur Genese geführt haben, durch Datierungen zeitlich einzuordnen. Auf Grundlage der gewonnenen Daten wurden zwei stratigraphische Modelle entwickelt, welche die geologisch-geomorphologischen Prozesse und Sedimentationsbedingungen im Westküstenvorfeld erklären.
Ein Modell zeigt die Landschaftsentwicklung an der Westküste Amrums und beschreibt die Sedimentationsbedingungen, die im Vorfeld der Westküste herrschten, bevor der Kniepsand an die Insel heranwanderte. Auf der Landoberfläche des ertrinkenden saaleeiszeitlichen Geestkerns wurden zu Beginn der Flandrischen Transgression feinkörnige Sedimente eines Misch- und Schlickwatts abgelagert. Es ist davon auszugehen, dass der damals noch weit vor der Küste Amrums liegende Kniepsand eine Barriere bildete und so an der heute hochenergetischen Westküste für strömungsberuhigte Sedimentationsbedingungen sorgte. Durch Erosion am Geestkern bildeten sich in unterschiedlichen Höhenpositionen fossile Kliffs, die dem damaligen Meeresspiegelstand entsprechen.
Ein weiteres Modell beschreibt den Andockmechanismus des Kniepsandes an die Insel Amrum. Durch die Anlagerung des ehemaligen Außensandes und den damit einhergehenden Sedimentinput wurden die Bedingungen für eine großflächige Dünenbildung geschaffen.

Holocene landscape development in front of the west coast of Amrum (North Sea/ German Bight) – Insights from ground-penetrating radar surveys and sedimentological data

Abstract:

Barrier sandbars and barrier islands are geologically young, highly dynamic and represent a complex coastal system that includes a number of different but closely related sedimentary depositional environments with geomorphologic elements of varying origin, genesis and evolution. Barrier sandbars are exposed ridges of sand that are built offshore by wave action.
The so-called Kniepsand on the island of Amrum represents one of the widest beaches in Europe. The Kniepsand originally belongs to a system of sandbars lining the North-Frisian coast. Some of these sandbars are already attached to the mainland (e.g. St. Peter-Ording-Sand and Westerhever-Sand). The offshore sandbars of Japsand, Norderoogsand and Süderoogsand are located in front of the western coastline of the North-Frisian Island and the Halligen and fulfil the function of natural coastal defence dissipating the energy of the incoming deep-water waves of the North Sea.
Barrier sandbars are usually investigated through the use of aerial photos and borehole data. Therefore, the processes of evolution, migration and the internal structure of sandbars are often unknown. That is why this study chooses an integrated approach using high-resolution ground-penetrating radar (GPR) and sedimentological analyses of shallow sediment cores drilled at selected sites along the radar profiles. A geophysical Survey Systems Inc. radar system, SIR-2000 coupled with a 200 MHz antenna, was used.
Based on these data two sedimentary models were generated. One model describes the process of barrier sandbar migration and the attachment to the Pleistocene island core. According to historical maps and nautical charts of the sixteenth and seventeenth century, the Kniepsand used to be a solitary barrier sandbar located well in front of the island's west coast without any connection to its Pleistocene core consisting of Saalian moraine deposits. The presented model shows how the Kniepsand has welded onto the island core of Amrum.
Before the barrier sandbar was connected to the island, conditions for sedimentation had been quite different. Tidal flat deposits had been accumulated in a low energy environment. Tidal flat deposits show a general coarsening upward trend and turn into overlying coarser grained beach deposits. Old cliffs formed through several storm surges are also preserved in GPR data. The landscape evolution in front of the westcoast of Amrum was summarized in the second model.

Keywords: *Holocene landscape development, barrier sandbar migration, barrier island stratigraphy, ground-penetrating radar (GPR), Amrum, North Sea/German Bight*

Addresses of authors: **T. Tillmann**, Niedersächsisches Institut für historische Küstenforschung (NIhK), Viktoriastraße 26/28, 26382 Wilhelmshaven, E-Mail: tanja.tillmann@nihk.de; Carl von Ossietzky Universität Oldenburg, Institut für Chemie und Biologie des Meeres/ ICBM-Terramare, Schleusenstraße 1, 26382 Wilhelmshaven, E-Mail: tanja.tillmann@uni-oldenburg.de; **D. Ziehe**, Johann Heinrich von Thünen-Institut, Institut für Agrarrelevante Klimaforschung, Bundesallee 50, 38116 Braunschweig, E-Mail: daniel.ziehe@, vti.bund.de, **J. Wunderlich**, Goethe-Universität Frankfurt Institut für Physische Geographie, Altenhöferallee 1, 60438 Frankfurt, E-Mail: j.wunderlich@em.uni-frankfurt.de

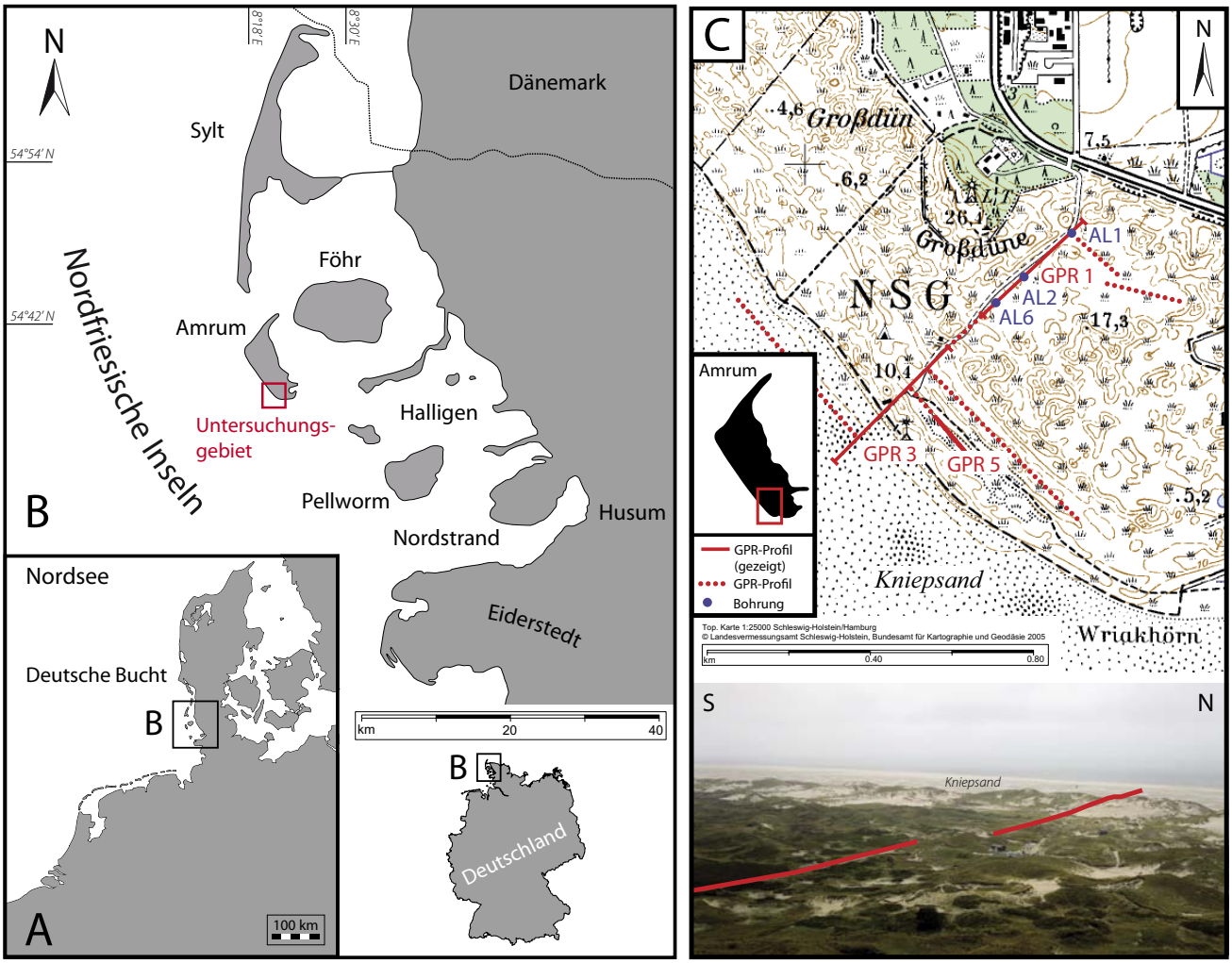

Abb. 1: Überblick über das Untersuchungsgebiet. A: Lage der Nordfriesischen Inseln innerhalb der Deutschen Bucht. B: Lage des Untersuchungsgebietes nahe des Leuchtturms der Insel Amrum. C: Position der GPR-Profile und Bohrungen im Untersuchungsgebiet.

Fig. 1: Overview of the study area. A: German Bight with the position of the Northfrisian Islands. B: Position of the study area next to the lighthouse of Amrum Island. C: Position of GPR-profiles and cores in the study area.

1 Einleitung

Barriereinseln und Außensände, geformt durch eine Kombination aus Wind, Wellen, Strömung und Küstenlängstransport gelten als morphologisch hoch aktive Küstenbereiche und variieren häufig in Ursprung, Genese und Entwicklung. Durch ihre dissipative Wirkungsweise besitzen sie eine bedeutende Schutzfunktion für die rückwärtigen Inseln, Halligen und Festlandbereiche und bilden so vor der Küste Nordfrieslands die Außengrenze des Wattenmeeres.

Bisherige Untersuchungen zur Stratigraphie dieser Sedimentationsräume basieren häufig allein auf Bohrungen. Daher sind die interne sedimentologische Struktur und die Prozesse, die zur Entwicklung und Wanderung von Barriereinseln und -sänden geführt haben, oftmals unzureichend untersucht.

Ziel der folgenden Studie ist es daher, anhand hochauflösender geophysikalischer und sedimentologischer Daten die Landschaftsgeschichte an der Westküste Amrums zu rekonstruieren sowie die interne sedimentäre Architektur des der Insel westlich angelagerten Kniepsandes zu untersuchen. Neben der Rekonstruktion der Landschaftsentwicklung sind vor allem die Sedimentationsbedingungen, die an der Westküste der Insel Amrum geherrscht haben, bevor sich der Kniepsand an die Insel anlagerte, von besonderem Interesse. Dabei stehen folgende Fragen im Vordergrund:

- Wie hat sich der Kniepsand als ehemaliger, weit vor der Westküste Amrums liegender Außensand, an die Insel anlagert?
- Welche Landschafts- und Sedimentationsbedingungen herrschten an der Westküste Amrums bevor der Kniepsand sich an die Insel anlagerte?
- Welche morphologischen Prozesse und Bedingungen haben zum Heranwandern und Andocken des ehemaligen Außensandes an den Inselgeestkern geführt?
- Inwieweit ist es möglich mit Hilfe hochauflösender Georadardaten die ursprüngliche Andockstelle des Kniepsandes an den Inselgeestkern zu definieren und rekonstruieren?

2 Untersuchungsgebiet

Die Insel Amrum in der südlichen Nordsee (Deutsche Bucht) bildet zusammen mit der nördlichen Nachbarinsel Sylt, den dänischen Inseln Fanø, Mandø, Rømø und den nordfriesischen Außensänden Japsand, Norderoog- und

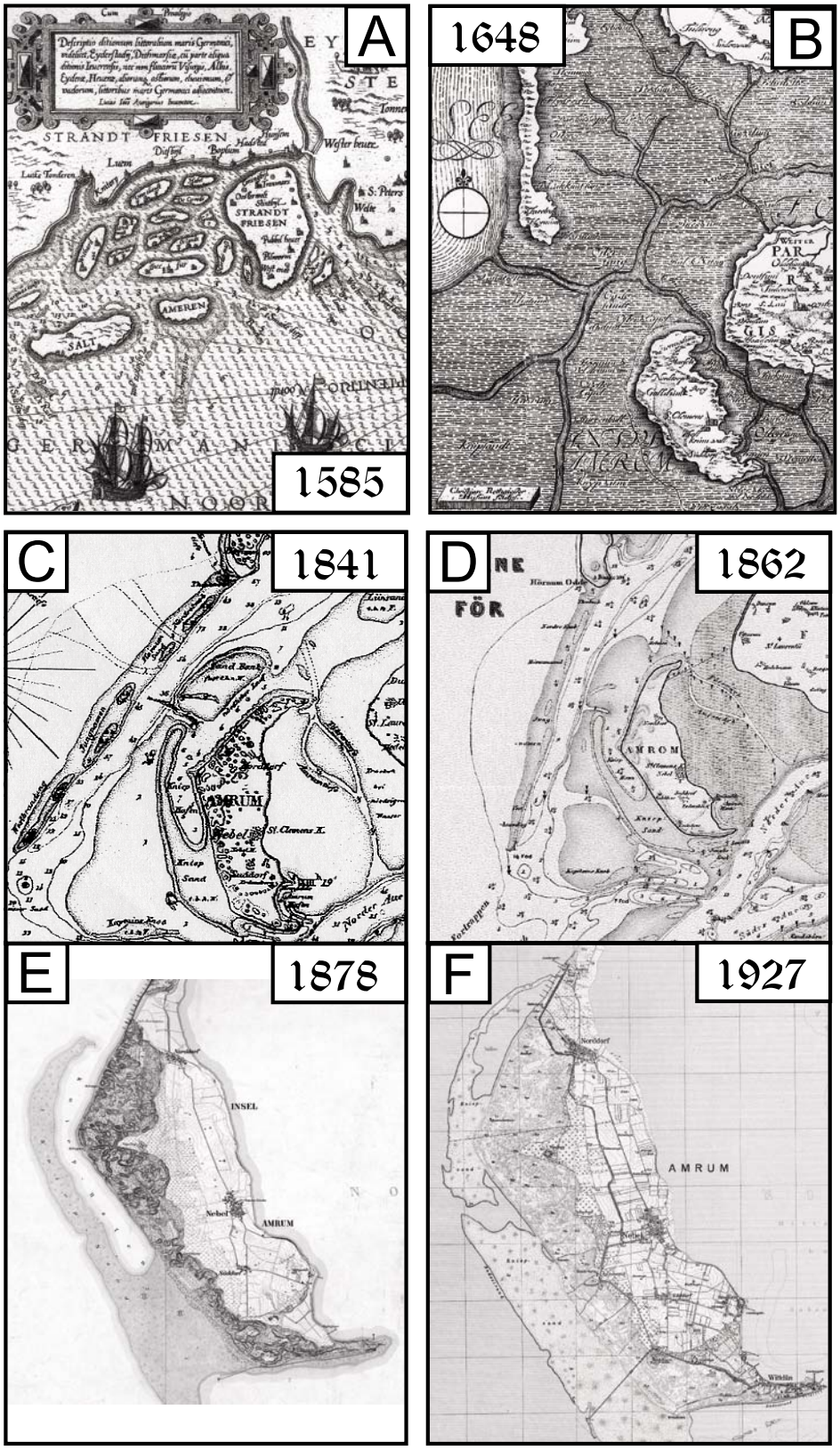

Abb. 2 A: Der Ausschnitt aus der Seekarte der Deutschen Bucht von W. J. Waghenaer aus dem Jahr 1585 mit Blickrichtung nach Osten zeigt die Insel Amrum mit vorgelagerter Sandbank „Ameren Bor". B: Ausschnitt aus der Landkarte des Amt Tondern aus dem Jahre 1648 nach Johannes Mejer verändert nach Danckwerth (1652). Westlich vor der Küste Amrum ist der „Kniepsandt" erstmals namentlich erwähnt. C: Ausschnitt aus einer Seekarte der Helgoländer Bucht von Zahrtmann aus dem Jahre 1841(aus Lang 1973). D: Ausschnitt aus einer Seekarte der Helgoländer Bucht von Zahrtmann aus dem Jahre 1862 (aus Lang 1973). E: Ausschnitt aus einer topographischen Karte der Königl. Preuss. Landes-Aufnahme (Maßstab 1:25000) aus dem Jahre 1878. F: Ausschnitt aus einer topographischen Karte (Meßtischb1att 199 im Maßstab 1:25000) aus dem Jahre 1927.

Fig. 2 A: The map section of the German Bight of 1585 from W. J. Waghenaer shows the island of Amrum with the sandbar „Ameren Bor". B: Map section of Tondern of 1648 from Johannes Mejer modified by Danckwerth (1652). The "Kniepsandt" is named to the west of Amrum's coast for the first time. C: Map section of the Helgoland Bight from Zahrtmann (1841) in Lang (1973). D: Map section of the Helgoland Bight from Zahrtmann (1862) in Lang (1973). E: Map section of a topographic map of the year 1878. F: Map section of a topographic map of the year 1927.

Süderoogsand im Süden eine Kette aus Barriereinseln, die als westliche Außengrenzen des Wattenmeeres der dänischen und schleswig-holsteinischen Festlandsküste vorgelagert sind. Von der Wortbedeutung leitet sich der Name Amrum von „Am Rem" ab, das soviel bedeutet wie „sandiger Rand" (Quedens 2008) und sich morphologisch auf den der Insel Amrum im Westen vorgelagerten Kniepsand bezieht.

Geologisch gehört Amrum zu den Nordfriesischen Geestkerninseln und weist als kleinste dieser Inseln eine Nord-Süd-Erstreckung von knapp 10 km und eine Fläche von rund 20 km² auf. Wird der Kniepsand, ein heute bis zu 1,5 km breiter Sandstrand, der sich als ehemaliger Außensand entlang der Westküste erstreckt, mit zu der Inselfläche gerechnet, misst die Gesamtfläche 30,5 km².

Das Untersuchungsgebiet befindet sich im Südwesten der Insel und umfasst das Dünengebiet südlich der 26,4 m ho-

E&G / Vol. 62 / No. 2 / 2013 / 98–119 / DOI 10.3285/eg.62.2.02 / © Authors / Creative Commons Attribution License

hen „Großdüne“ auf der 1875 der Leuchtturm (54°37’52,2’’ N/ 8°21’16,5’’ E) errichtet wurde (Abb. 1). An die Dünen schließt sich im Südwesten der Kniepsand an.

Der pleistozäne Geestkern der Insel Amrum nimmt heute mit 13,7 km2 etwa 2/3 der Inselfläche ein (Remde 1972). Im Zuge der Flandrischen Transgression zu Beginn des Holozäns griff die Brandung des ansteigenden Meeresspiegels den Geestkern Amrums von allen Seiten an und schuf durch Abrasion an der gesamten Westküste und an vorspringenden Teilen der Ostküste ein Kliff. Auf diese Weise entstand an der Westküste Amrums auf einer Strecke zwischen Wriakhörn und Norddorf das Littorina Kliff. Im Gegensatz zum Steenodder Kliff an der Wattseite ist das Littorina Kliff an der Westküste rezent durch den Kniepsand und die vorgelagerten Dünenketten vor der Brandung geschützt und so zum fossilen Kliff geworden.

Eine Besonderheit hinsichtlich der Morphologie der Insel Amrum stellt der Kniepsand dar, der auf 16,5 km Länge entlang der Westküste von Wittdün im Süden bis nach Norddorf im Norden reicht. Mit bis zu 1,5 km Breite zählt er heute zu den breitesten Stränden Europas. Die rund 10 km2 große Sandfläche weißt im Mittel eine Höhe von NN +1,75 m auf und wird nur noch während winterlicher Sturmfluten vom Meer überflutet.

Aus geologischer Sicht ist der Kniepsand kein echter Bestandteil der Insel Amrum. Im weitesten Sinne handelt es sich um eine ehemalige der Westküste Amrums vorgelagerte Sandbank, die sich als einstiger Außensand der Inselküste im Westen angeschlossen hat. Der Kniepsand gehört damit zu einer Reihe von Außensänden und Sandbänken, die den Inseln und Halligen der Nordfriesischen Küsten im Westen vorgelagert sind. Einige dieser ehemaligen Außensände wie beispielsweise der Sand vor St. Peter-Ording und der weiter nördlich gelegene Westerhever-Sand sind bereits komplett an die Küste heran gewandert und stellen die heutigen Strände der dortigen Festlandsküste dar. Andere Außensände wie zum Beispiel der Norderoog- und Süderoogsand oder der deutlich kleinere Japsand westlich der Hallig Hooge liegen noch heute im *offshore* Bereich und dienen so den rückwärtigen Inseln und Halligen während Sturmfluten als natürlicher Wellenbrecher.

Einzelheiten hinsichtlich der Entstehung sowie der Herkunft des Kniepsandes sind bis dato nicht bekannt. Als erster verzeichnete ihn Mejer in seiner Karte aus dem Jahre 1648 (Abb. 2 Bild B), wo einige Kilometer westlich der Insel Amrum ein „Kniepsandt“ eingetragen ist. Dieser stellte vermutlich zu dieser Zeit für die Seefahrt eine Untiefe dar.

In historischen Seekarten aus dem 16. und 17. Jahrhundert, wie z. B. der Waghenaer-Karte aus dem Jahr 1585, ist der Kniepsand als solitäre Sandbank mit der Bezeichnung „Ameren bor“ (Amrumer Barriere) eingetragen (vgl. Abb. 2 A), die der Westküste von Amrum vorgelagert ist. Nach Hassenpflug (1985) lag der Kniepsand auch im 17. Jahrhundert noch als Außensand weit westlich der Insel und ist erst im Laufe der letzten Jahrhunderte von Westen an die Küstenlinie Amrums herangewandert. Zausig (1939) stellte anhand alter Seekarten fest, dass der Kniepsand bei seiner Wanderung nach Osten einen alten Verlauf des Hörnum-Tiefs zuschüttete, das damals zwischen dem Kniepsand und Amrum verlief. Der mittlere und südliche Teil der Sandbank lagerte sich zuerst an Amrums Westküste an.

So wird der Kniepsand in den Karten in den Abbildungen 2 C bis 2 F als eine zu Amrum zählende Sandbank eingezeichnet, die auf der Höhe des Untersuchungsgebietes am Leuchtturm von Amrum bereits eine direkte Verbindung zum Inselkern aufweist. Deutlich erkennbar ist in den zwei Seekarten (Abb. 2 C und D) und in der topographischen Karte von 1878 (Abb. 2 E) der Kniephafen, der zu dieser Zeit einen beschiffbaren (Remde 1972; Quedens 2008) Hafen darstellte.

Das Andocken des Kniepsandes an die Insel erfolgte morphologisch als Sandbank. Nach der Anlagerung des einstigen Außensandes erfuhr der Kniepsand allmählich eine Modifikation, die primär durch eine nach Norden und Süden gerichtete Strömungskomponente des Küstenlängstransportes gesteuert wurde. Die Art und Weise seiner Weiterentwicklung charakterisieren den heutigen Kniepsand dementsprechend als Ablagerung einer Meeresströmung und somit eindeutig als Nehrungsbildung. Bereits Johannsen (1867) zitiert nach Müller & Fischer (1937: 93) wies auf diese morphologische Veränderung hin und schrieb über den Kniepsand „[…] diese zwei Stunden lange Sandbank verlängert sich nach Süden wie nach Norden und wird nur bei Springflut und außerordentlichen Sturmfluten überschwemmt“.

Die Wurzel der Nehrung bzw. ihr Aufhängerpunkt an der Küste ist nach Voigt (1969) westlich des Amrumer Leuchtturms zu suchen. Von seiner ursprünglichen Ansatzzone aus schob sich der Kniepsand dementsprechend nach Nordwesten vor. Durch eine nach Norden gerichtete Meeresströmung wuchs der Nehrungsstreifen allmählich von seinem Wurzelgebiet am Wriakhörn südlich des Leuchtturms zunächst nach Nordwesten und später nach Norden (Voigt 1969). Der nördliche Teil bewegte sich langsamer, sodass eine Bucht mit Nehrungscharakter und Lagune entstand in der sich bis 1890 (Quedens 2008) der Kniephafen befand. Dieser stellte in historischer Vergangenheit einen wichtigen Ankerplatz für Fischer- und Segelboote dar (Jessen 1932) und reichte in seiner äußersten Ausdehnung bis westlich der Satteldüne. Reste der ehemaligen Bucht waren noch 1913 zu erkennen (Krause 1913) und sind in der Karte von 1927 (Abb. 2 E) nördlich des Quermarkenfeuers abgebildet. Der Kniephafen verlandete allmählich von Süden her und wurde im Norden von dem langsam nachrückenden Teil des Kniepsandes geschlossen (Remde 1972).

Gemäß Johannsen (1861) war der Kniepsandhafen bereits um das Jahr 1860 nicht mehr für Lastensegler schiffbar. Nach Krause (1913) lagerte sich der Kniepsand zuerst in seiner Mitte an den Inselkörper an, sodass infolge seiner West-Ost-Wanderung die Strömung in dem parallel zur Küstenlinie verlaufenden Priel „Troode diep“ (Voigt 1969) unterbrochen und Stillwasserbereiche für die Akkumulation feinkörniger Sedimente geschaffen wurden. Zausig (1939) vermutete ferner, dass der nördliche Teil von einem anstehenden festeren Untergrund in seiner Wanderungsbewegung verlangsamt wurde. Dieser festere Untergrund ist in den historischen Karten als „Sylter Riff“ eingetragen. Heute hat der Kniepsand sich vollständig an die Westküste von Amrum angeschlossen und den ehemaligen Kniephafen mitsamt der Bucht zugeschüttet.

Demzufolge setzt sich der heutige Kniepsand morphologisch aus zwei ihrer Entstehung nach verschiedenen Tei-

len zusammen, nämlich der eigentlichen Nehrung und dem Kniephafen, den man als das zum Nehrungsstreifen gehörende Haff bezeichnen kann (Voigt 1969).

3 Methoden

Im Untersuchungsgebiet Amrumer Leuchtturm wurde eine Methodenkombination aus Georadarmessungen, Bohrungen, sedimentologischen Laboranalysen und AAR-Datierungen angewandt.

3.1 Georadar (GPR)

Das Georadar, engl. Ground-penetrating radar (GPR), ist ein hochauflösendes elektromagnetisches Impulsreflexionsverfahren, das eine hochauflösende und zerstörungsfreie Prospektion des oberflächennahen Untergrundes bietet (vgl. u. a. Annan 2001, 2009; Blindow et al. 2005). Elektromagnetische Wellen breiten sich im Untergrund aus und werden bei Änderungen elektrischer Materialeigenschaften reflektiert, gebrochen, gestreut und zum Teil absorbiert. Das reflektierte elektrische Feld der elektromagnetischen Welle wird aufgezeichnet und in einem Weg-Zeit-Diagramm, dem Radargramm, dargestellt. Durch die Reflexion an Schichtgrenzen oder Störkörpern erhält man ein quasi kontinuierliches Profil des Untergrundes in Abhängigkeit von dessen dielektrischen Eigenschaften (Annan 2009).

Die nachfolgenden Georadarmessungen wurden mit einem Georadarsystem SIR 2000 der Firma Geophysical Survey Systems Inc. (GSSI SIR-2000) in Kombination mit einer 200 MHz Antenne durchgeführt. Insgesamt wurden im Untersuchungsgebiet am Leuchtturm von Amrum 8 GPR-Profile auf natürlichem Untergrund gemessen (Abb. 1). Für die Georadarmessungen wurde ein 2-dimensionales und 2,5-dimensionales Survey Design gewählt. Eine 2,5 dimensionale Darstellung wird durch Kreuzungs- oder Berührungspunkte einzelner zweidimensionaler GPR-Profile gewährleistest und ermöglicht so eine pseudo-dreidimensionale Betrachtungsweise der Untergrundstrukturen im Arbeitsgebiet. Die Messungen erfolgten parallel und senkrecht zur heutigen Küstenlinie.

Die Transekte der GPR-Profile wurden bevorzugt auf ebenem Gelände und in den flachen Bereichen der Dünentäler gemessen. Dennoch führen auch schon geringe topographische Höhenunterschiede entlang der Georadar-Transekte zu Verzerrungen im Radargramm (z. B. Fisher et al. 1996; Jol & Bristow 2003; Tillmann & Wunderlich 2012) und wurden daher im unmittelbaren Anschluss an die Georadarmessungen mit Hilfe eines differentiellen GPS Systems (Ashtech ProMark 2) erfasst. Die Ausbreitungsgeschwindigkeiten der elektromagnetischen Welle im Untergrund wurden mit Hilfe von Diffraktionshyperbeln und durch die Korrelation mit Bohrungen ermittelt.

Das Processing der GPR-Rohdaten erfolgte mit der Software „Reflex-Win“ (Version 5.6) der Firma „Sandmeier Scientific Software, Karlsruhe“. So wurde ein Bearbeitungsverfahren aus *offset*-Korrektur, *dewow*-Filter, Bandpassfilter und *background removal*-Filter standardmäßig angewendet.

Eine mit zunehmender Tiefe verstärkte Signalabschwächung konnte mit Hilfe der gain-Funktion (*energy decay*) kompensiert werden. Die Migration der Radargramme erfolgte unter Verwendung des Migrations-Algorithmus nach Stolt (1978). Jedem einzelnen GPR-Profil wurde dabei eine einheitliche Durchschnittsgeschwindigkeit zugrunde gelegt. Durch die Migration wurden die Achsen von Diffraktionshyperbeln entfernt und die Reflexionen der Objekte auf einen punktförmigen Reflektor reduziert, der der tatsächlichen Objektlage und -größe entspricht. Wo Diffraktionshyperbeln im starken Maße zur Interpretation beitragen, wurde auf das Entfernen der Hyperbeln im Radargramm verzichtet.

3.2 Bohrungen und sedimentologische Laboranalysen

Im Untersuchungsgebiet am Leuchtturm von Amrum wurden Rammkern- und Pürkhauersondierungen durchgeführt. Die Rammkernsondierungen AL2 und AL6 sowie die Pürkhauersondierung AL1 wurden direkt in das Transsekt von GPR-Profil 1 eingebracht. Die Rammkernsondierungen AL2 und AL6 wurden mit einer Kombination aus Benzinschlagkopfbohrer (Wackerbohrer), Schlitzsonden und hydraulischem Ziehgerät durchgeführt und bis zu einer Tiefe von 8 m abgeteuft. In Abhängigkeit von der Eindringteufe kamen unterschiedliche, sich mit zunehmender Tiefe verjüngende Schlitzsonden (Ø = 80 mm, Ø = 60 mm, Ø = 30 mm), zum Einsatz.

Aus den Bohrkernen wurden ca. 90 Sedimentproben für granulometrische Laboranalysen (Nass- und Trockensiebung) entnommen. Zur Berechnung korngrößenstatistischer Parameter wurde das Programm Gradistat nach Blott & Pye (2001) verwendet. Die Auswertung nach korngrößenstatistischen Parametern erfolgte mit der Methode nach Folk & Ward (1957).

3.3 Datierung

Für die Datierung der Probe aus dem Untersuchungsgebiet Amrum Leuchtturm wurde die Aminosäure-Racemisierungs-Methode (AAR) herangezogen.

Die AAR-Datierung wurde im Jahre 2012 von Herrn Dr. Daniel Ziehe im Johann Heinrich von Thünen-Institut in Braunschweig durch die in Ziehe (2009) entwickelte Methode durchgeführt.

Die AAR-Datierung beruht auf der Bestimmung von Aminosäure-D/L-Verhältnissen in den organischen Matrices biogener Carbonate (vgl. Demarchi et al. 2011; Goodfriend 1987; Murray-Wallace & Belperio 1994; Ziehe 2009). Die Anwendbarkeit der AAR-Methode für geologisch sehr junge Ablagerungsräume wurde von Ziehe (2009) am Beispiel unterschiedlicher Standorte im Wattenmeer nachgewiesen.

Zur Datierung wurde eine Herzmuschel (*Cerastoderma edule*) herangezogen, die als intakte Schalenklappe aus einer Bohrtiefe von 728 cm gewonnen wurde. Aufgrund ihrer Einbettung in schillfreie, feinkörnige Wattsedimente ist davon auszugehen, dass es sich um den ursprünglichen Lebensraum der Muschel handelt, bzw. diese nicht in Form von Bruchschill verlagert wurde. Um etwaige Messungenauigkeiten zu minimieren, wurde die Probe 3-fach datiert. Aus abweichenden Messergebnissen wurde anschließend ein Mittelwert gebildet. Die zeitliche Einordnung mittels der AAR-Methode ist aufgrund der geringen Datendichte an datierbarem Mate-

E&G / Vol. 62 / No. 2 / 2013 / 98–119 / DOI 10.3285/eg.62.2.02

Radargramm	Interpretation	Radar-fazies	Ampli-tude	Form, Winkel, Kontinuität, Besonderheiten	Position, Tiefe	Sedimentologische Interpretation
A. Einfallende Reflexionen						
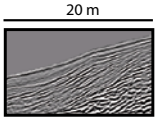	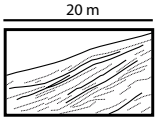	Rf-AL-A1	stark - mittel	kontinuierlich, subparallel - parallel	vorwiegend oberhalb von Rf-AL-B1	Dünen-Fazies, äolische Kreuz- und Schrägschichtung
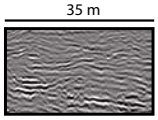	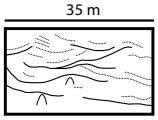	Rf-AL-A2	mittel	wellen- bis rinnenförmige konkave + konvexe Reflexionen, einzelne Diffraktionshyperbeln, mäßig kontinuierlich	im Bereich von Rf-AL-B1 bis unter Rf-AL-B1	intertidale Sedimentkörper/ swash bars und ridge-and-runnel-Topographie auf dem Strand
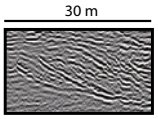	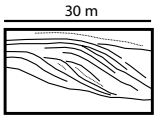	Rf-AL-A3	stark - mittel	sigmoidal - oblique tangential, kontinuierlich - mäßig kontinuierlich	ausschließlich unter Rf-AL-B1	Progradations-Fazies/ Kniepsand
B. Horizontale Reflexionen						
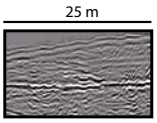	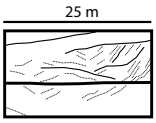	Rf-AL-B1	stark	planar kontinuierlich, horizontal - subhorizontal, linear		Grundwasserspiegel
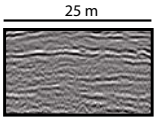	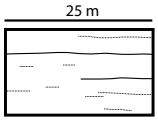	Rf-AL-B2	mittel-schwach	horizontal - planar, parallel, mäßig kontinuierlich - diskontinuierlich	ausschließlich unter Rf-AL-B1	Watt-Fazies
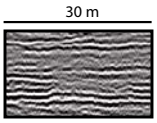	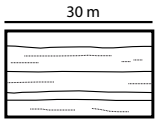	Rf-AL-B3	mittel - schwach	horizontal, planar, teilweise wellenförmig, parallel - subparallel, kontinuierlich - mäßig kontinuierlich	im Bereich von Rf-AL-B1 bis unter Rf-AL-B1	Strand-Fazies
C. Irreguläre Reflexionen						
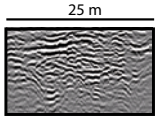	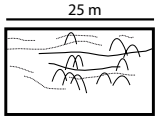	Rf-AL-C1	stark - mittel	mäßig kontinuierlich, wellenförmig, teilweise chaotisch, viele Diffraktionshyperbeln	unter Rf-AL-B1	Geschiebenester im Geestkern
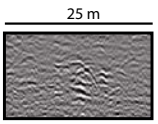	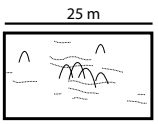	Rf-AL-C2	schwach	diskontinuierlich, chaotisch, Diffraktionshyperbeln	vorwiegend unter Rf-AL-B1	Geestkern-Fazies
D. Radar-Schichtflächen						
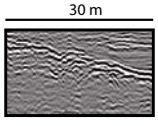	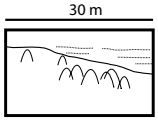	Rf-AL-D1	stark	nach Westen einfallende Schichtfläche mit Diffraktionshyperbeln, kontinuierlich	größtenteils unter Rf-AL-B1	Geestkernoberfläche, Grenze zwischen Watt/ Strand und Geestkern coastal onlap
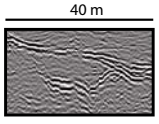	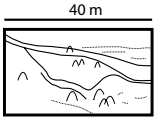	Rf-AL-D2	stark	steil einfallende Schicht-flächenkonfiguration, Diffraktionshyperbeln, kontinuierlich	unter Rf-AL-B1	fossile Kliffs entstanden durch sturmflutbedingte Erosion am Geestkern, Brandungshohlkehlen

Abb. 3: Radarfazies-Definition aus dem Untersuchungsgebiet Amrum Leuchtturm.

Fig. 3: Radarfacies-definition of the study area next to the lighthouse of Amrum.

rial sowie dem Fehlen von Vergleichsaltern lediglich als grober zeitlicher Anhaltspunkt zu sehen.

4 Ergebnisse

4.1 Radarfazies Analyse

Reflexionsmuster in GPR-Daten lassen auf Sedimentstrukturen im Untergrund schließen. Die Interpretation der gezeigten GPR-Profile basiert auf der Methode der Radarstratigraphie. Die Radarstratigraphie wurde erstmals durch Jol & Smith (1991) als eine Interpretationstechnik für Georadardaten eingeführt und basiert in ihren Grundzügen auf den Prinzipien der in den 1970er Jahren von der Erdölindustrie entwickelten Seismischen Stratigraphie nach Mitchum et al. (1977). Diese geht von sedimentären Sequenzen (speziell siliziklastischen Sequenzen) aus, die in eine Hierarchie der Sedimentationseinheiten von einzelnen Laminae bis hin zu sedimentären Beckenfüllungen unterteilt werden (Allen 1982; Campbell 1967; Miall 1991) und stellt damit die Grundlage der Sequenzstratigraphie dar (Payton 1977). Durch die Definition einer Radarfazies werden die Reflexionsmuster des Untersuchungsgebietes klassifiziert und entsprechend einer von Neal (2004) entwickelten Standardterminologie zusammengefasst. Auf diese Weise ist es möglich, die Radargramme in ihre stratigraphischen Einheiten zu unterteilen, und so in eine relative chronologische Reihenfolge einzuordnen. Im Untersuchungsgebiet am Leuchtturm von Amrum ließen sich insgesamt 10 unterschiedliche Radarfazien definieren. Die Benennung der Radarfazies erfolgte nach folgendem Schema. Eine erste Einteilung der Reflexionen erfolgte in Bezug auf das Untersuchungsgebiet und wird mit „AL“ für „Amrum Leuchtturm“ abgekürzt. Des Weiteren wird zwischen einfallende Reflexionen (Rf-AL-A), horizontale Reflexionen (Rf-AL-B), irreguläre Reflexionen (Rf-AL-C) und Radarschichtflächen (Rf-AL-D) unterschieden (Abb. 3).

Rf-AL-A1 Dünen-Fazies

Radarfazies

Die Radarfazies Rf-AL-A1 umfasst einfallende kontinuierliche bis moderat kontinuierliche Reflektoren von mittlerer bis starker Amplitude (vgl. auch Tillmann & Wunderlich 2011a, 2011b, 2013). Die einzelnen Reflektoren sind zueinander parallel bis subparallel orientiert und besitzen ein steiles bis mittleres Einfallen (10°–30°) in unterschiedliche Richtungen. Die Reflexionen sind in einzelne Radarschichtpakete unterteilt.

Sedimentfazies

In den Bohrkernen AL1, AL2 und AL6 besteht Rf-AL-A1 ausschließlich aus hellen Fein- und Mittelsanden. Die mittlere Korngröße bewegt sich im feinen Mittelsandbereich zwischen 2,11 φ und 1,73 φ. Die Sedimente von Rf-AL-A1 weisen eine mäßig gute (0,60 φ) bis mäßige Sortierung (0,81 φ) auf und zeigen dadurch nur geringe Abweichung innerhalb des Korngrößenspektrums.

Die Korngrößenverteilung von Rf-AL-A1 ist in der Regel unimodal bis bimodal mit dem größten Anteil an der Korngröße Mittelsand. Die Schiefe ist dementsprechend vorwiegend symmetrisch (0,067 φ bis -0,002 φ). Geringfügige Abweichungen zu einer positiven und negativen Schiefe sind dennoch festzustellen und abhängig davon, ob innerhalb der Sedimentprobe von Rf-AL-A1 gröbere oder feinere Mittelsande dominieren.

Die Sedimente von Rf-AL-A1 enthalten im Bohrkern keine makroskopisch erkennbaren Muscheln oder Schillanteile. Grobe Komponenten wie Kiese sind ebenfalls nicht nachzuweisen. Demgegenüber sind Wurzeln in Verbindung mit organischen Humushorizonten häufig.

Interpretation

Die Radarfazies Rf-AL-A1 wird als Dünen-Fazies interpretiert. Eine vergleichbare Radarfazies-Definition ist bereits aus früheren Arbeiten (z. B. Bristow et al. 1996, 2000a, 2000b, 2010a, 2010b; Botha et al. 2003; Girardi & Davis 2010; Harari 1996; Tillmann & Wunderlich 2012, 2013) bekannt. Im Untersuchungsgebiet bildet die Dünen-Fazies die jüngste stratigraphische Einheit und zeigt im Radargramm (Abb. 4) die für Küstendünen typischen äolischen Sedimentstrukturen der Schräg- und Kreuzschichtung, die durch kleinräumig wechselnde Windrichtungen bedingt sind (McKee 1966; Tucker 1985; van Overmeeren 1998).

Die interne Dünenschichtung setzt sich aus einzelnen sog. „foresets“ zusammen und ist von als „bounding surfaces“ (vgl. Bristow 2009; Bristow & Pucillo 2006) bezeichneten Schichtflächen unterbrochen. Generell resultiert die interne Struktur und Schichtung von Dünen aus Änderungen des vorherrschenden Windregimes bzw. einer dadurch bedingten Wanderungsbewegung (Davis 1992).

Ein Beispiel für die komplexe interne Geometrie der Dünen im Untersuchungsgebiet am Leuchtturm von Amrum zeigt die Vordüne aus GPR-Profil 5 in Abbildung 4. Das 130 m lange GPR-Transekt wurde im Weißdünengürtel parallel zur Küste mittels einer 200 MHz-Antenne gemessen und verläuft von Nordwesten nach Südosten. Der als Sedimentlieferant fungierende Strand (Kniepsand) befindet sich südwestlich der Vordünenkette. Die Düne zeigt zahlreiche einzelne *foresets*-Schichten, die in Sedimentpakete von bis zu 2 m Mächtigkeit zusammengefasst und durch zahlreiche *bounding surfaces* begrenzt werden. Unterschiedliche Einfallswinkel und Richtungen der bounding surfaces lassen kleinräumig wechselnde Windbedingungen vermuten. Diffraktionshyperbeln innerhalb des Dünenkomplexes und an den Oberflächen der *bounding surface* sind häufig und werden in Übereinstimmung mit Beiträgen von Giradi & Davis (2010) und van Dam (2012) als durch Dünensand überdeckte Vegetation (evtl. Strandhaferhorste) interpretiert.

Abbildung 4 (Bild D) zeigt einen Ausschnitt der internen Dünenschichtung im Kern einer in das GPR-Transekt eingebrachten Pürkhauersondierung. Die mittleren Korngrößen bewegen sich zwischen 1,092 φ und 1,719 φ. Demzufolge entsprechen alle Schichten Sanden der Mittelsandfraktion und zeigen somit nur geringe Variationen hinsichtlich der Korngröße.

Dennoch können schon minimale Änderungen von Korngröße und Kornzusammensetzung der Dünensande Änderungen im Wasserhaushalt der einzelnen Schichten hervorrufen und dadurch im Radargramm zu Reflexionen führen. Auch organische Boden- und Wurzelhorizon-

E&G / Vol. 62 / No. 2 / 2013 / 98–119 / DOI 10.3285/eg.62.2.02

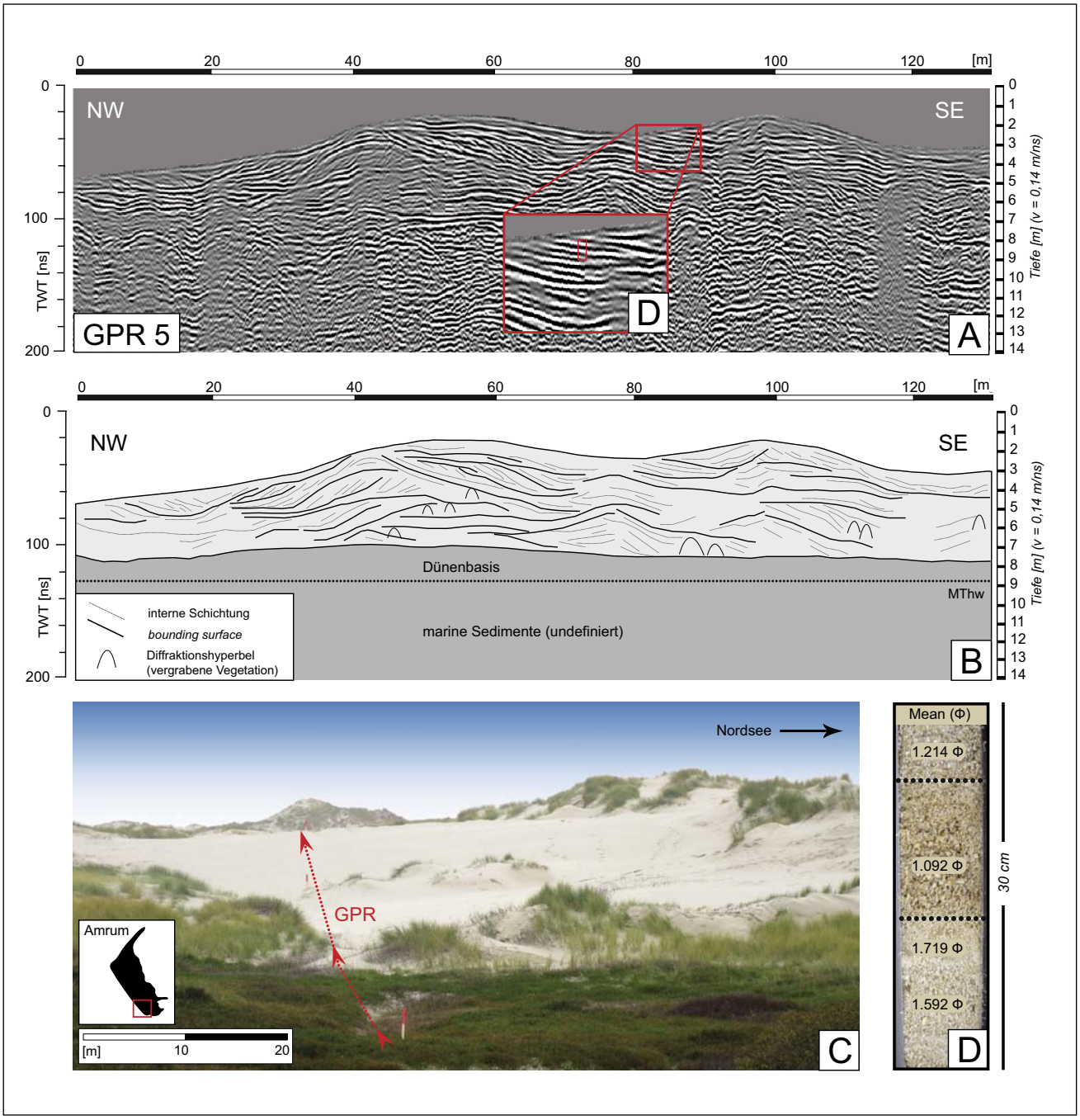

Abb. 4 A: Das Radargramm (200 MHz) zeigt einen Ausschnitt aus GPR-Profil 5. Die Lage von GPR-Profil 5 im Untersuchungsgebiet ist aus Abbildung 1 ersichtlich. Für die GPR-Daten wurde ein Basis-Processing aus (static correction, subtract-mean dewow, Bandpassfilter, background removal, gain) angewandt und die Topographie mit Hilfe von dGPS Koordinaten ausgeglichen. Für die trockenen Dünensande wurde eine Durchschnittsgeschwindigkeit von 0,14 m/ns ermittelt. B: Interpretation und Legende. Bounding surfaces sind durch starke Linien gekennzeichnet. Die interne Schichtung ist anhand feiner Linien zu erkennen. C: Foto der Düne mit Lage von GPR-Profil 5. D: Pürkhauer-Bohrung und Korngrößenverteilung innerhalb der Dünen-Fazies.

Fig. 4 A: The radargramm (200 MHz) shows a section of GPR-profile 5. Position of GPR-profile 5 in the study area is shown in figure 1. Processing (static correction, subtract-mean dewow, bandpassfilter, background removal, gain) and topographic correction of the radargramm were already applied. A velocity of 0.14 m/ns was determined for dry dune sand. B: Interpretation and legend. Bold lines represent bounding surfaces, fine lines display internal structures. C: Picture of the dune with position of GPR-profile 5. D: Core and grain size characteristic of the dune facies.

te konnten innerhalb der Dünenschichtung nachgewiesen werden. Sie verursachen im Radargramm ebenfalls verstärkte Reflexionen.

Rf-AL-A2 intertidale Sedimentkörper (swash bars)

Radarfazies

Die Reflexionen der Radarfazies Rf-AL-A2 kommen im Radargramm im direkten Verbund mit den Reflexionen der Radarfazies Rf-AL-B3 vor und umfassen den Tiefenbereich von 0 m NN bis -4 m NN. Dementsprechend ist Rf-AL-A2 ausschließlich unterhalb des Grundwasserspiegels nachzuweisen.

Im Radargramm bilden die Reflexionen von Rf-AL-A2 sowohl konkave, rinnenförmige Hohlformen als auch konvexe Vollformen aus. Hohlformen und Vollformen kommen in unmittelbarer Nachbarschaft zueinander vor und lassen auf einen morphologischen Zusammenhang schließen. Gelegentlich sind innerhalb der Radarfazies von Rf-AL-A2 ein-

zelne Diffraktionshyperbeln festzustellen, die allerdings kein eindeutiges Verteilungsmuster aufweisen.

Sedimentfazies
Hinsichtlich der Sedimentfazies bestehen keine oder nur geringfügige Unterschiede von Rf-AL-A2 und Rf-AL-B3. Dies deutet auf einen morphologischen Zusammenhang oder einen einheitlichen Sedimentationsraum hin. So dominieren schillführende Fein- und Mittelsande (1,00φ – 2,13φ), die eine mäßige bis mäßig gute (0,60 φ–0,97 φ) Sortierung aufweisen. Die Korngrößen sind vorwiegend unimodal und bimodal verteilt, besitzen eine beinahe symmetrische Schiefe und zeigen daher nur geringfügige Abweichungen.

Interpretation
Der direkte Verbund der Reflexionen von Rf-AL-A2 und Rf-AL-B3 im Radargramm deutet auf einen einheitlichen Sedimentationsraum sowie eine ähnliche Genese der durch Rf-AL-A2 und Rf-AL-B3 abgebildeten Sedimentstrukturen hin. Geomorphologisch handelt es sich bei den Radarfazien Rf-AL-A2 und Rf-AL-B3 um einen Strand, der den Tiefenbereich von 0 - 4 m unter NN umfasst.

Im Vergleich zu horizontal lagernden und in der Regel gut geschichteten Wattsedimenten bilden die als Strandsedimente interpretierten Reflexionen von Rf-AL-A2 und Rf-AL-B3 eine typisch unruhige Strandmorphologie aus. Primär wird diese durch die Radarfazies Rf-AL-A2 hervorgerufen, die aufgrund ihrer Reflexionsgeometrien sedimentologisch auf Voll- und Hohlformen hindeutet.

Der interne Aufbau der Vollformen ähnelt dabei der internen Schichtung intertidaler Sedimentkörper (*tidal bars, swash bars*) wie sie heute im Strandbereich vieler Nordseeinseln zu finden sind. Intertidale Sedimentkörper (*intertidal bars* und *swash bars*) zählen nach FitzGerald (2005) zu den typischen Elementen der Strandmorphologie im foreshore-Bereich. Die sog. *swash bars* zeigen im Allgemeinen eine durch Wellenenergie induzierte, auf die Küste gerichtete Migrationsrichtung (Hayes 1980; Jackson et al. 2007), die sich im Radargramm durch landwärts einfallende Reflexionen abbildet (Pedersen & Clemmensen 2005). Stratigraphisch kommen diese überwiegend als Vollformen ausgebildeten Sedimentkörper im Verbund mit parallel zur Küstenlinie verlaufenden linearen rinnen- oder wannenförmigen Geländedepressionen vor und gehören zu den temporären Sequenzen innerhalb des Strandprofils (FitzGerald 2005; Greenwood 2005).

Aus dem deutschsprachigen Raum sind diese intertidalen Vollformen mit den in Schäfer (2005: 228 ff.) angesprochenen „Strandriffen" vergleichbar, die als mehrfach aufeinander folgende, strandparallele Sandbänke in der Brecherzone von der senkrecht zur Küste auflaufenden Brandung aufgeworfen werden. Die Seeseite der Strandriffe ist flach.
Auf der Landseite bilden die steil einfallenden (18°–30°) Riffstirnschichten mit landwärts orientierten Anlagerungsflächen eine parallele Schrägschichtung aus (Schäfer 2005).

Oft sind diese vorwiegend aus Sand aufgebauten intertidalen Sedimentkörper stratigraphisch in das Strandprofil eingebaut und aufgrund des geringen morphologischen und sedimentologischen Unterschiedes zum Strand (Jackson et al. 2007) nur schwer anhand von Bohrungen zu identifizieren. Die Entstehung und Anlagerung von *swash bars* an den Strand ist vor allem auf ruhige Phasen zwischen oder nach Sturmfluten zurückzuführen (Jackson et al. 2007; Tanner 1995). Während den Sturmfluten werden die intertidalen Sedimentkörper zum Teil ausgeräumt, aufgearbeitet oder in ihrem oberen Bereich gekappt, sodass ein durch Wellen- und Brandungserosion bedingtes ebenes Strandprofil entsteht (FitzGerald 2005; Jackson et al. 2007).

Vollformen und Geländedepressionen wechseln sich innerhalb der Radarfazies Rf-AL-A2 ab und sind mit der in Greenwood (2005) beschriebenen typischen *ridge-and-runnel*-Topographie einiger Strände vergleichbar. Die konvexen Vollformen der *intertidal bars* oder *swash bars* repräsentieren dabei die Sedimentrücken (ridges). Rinneförmige Reflexionen entsprechen den sog. *runnels*, die von Schäfer (2005) auch als Strandpriele bezeichnet werden. Die *ridge-and-runnel*-Strukturen kommen in Verbindung mit den annähernd horizontalen Reflektoren von Rf-AL-B3 vor, die als nahezu söhlig lagernde, leicht in Richtung Meer einfallende Strandsandschichten gedeutet werden. Diese zeigen die von Schäfer (2005: 228) als „Hochenergie-Parallelschichtung" bezeichnete interne Sedimentstruktur. Die Ablagerung intertidaler Sedimentkörper erfolgt vorzugsweise in den Ruhephasen zwischen einzelnen Sturmfluten. Wiederkehrende Sturmfluten sorgen teilweise für die Erosion der intertidalen Vollformen und für die anschließende Ausbildung eines zeitweilig ebenen Strandprofils (Jackson et al. 2007).

Rf-AL-A3 Progradations-Fazies
Radarfazies
Die Radarfazies Rf-AL-A3 gehört zu den einfallenden Reflexionen und setzt sich aus sigmoidal bis schräg tangential geformten Reflexionen zusammen, die in einzelne Radarschichtpakete zusammengefasst sind. Rf-AL-A3 ist ausschließlich unterhalb des Grundwasserspiegels (Rf-AL-B1) nachzuweisen. Die Reflektoren von Rf-AL-A3 verlaufen kontinuierlich bis mäßig kontinuierlich und sind von mittlerer bis starker Amplitude. Die gebündelten Reflektoren enden in der Regel mit einem *downlap* und zeigen ein nach Westen gerichtetes Einfallen.

Sedimentfazies
Die Radarfazies Rf-AL-A3 wurde an keiner Stelle direkt durch Bohrungen durchteuft. Die Reflektoreigenschaften und Reflexionsgeometrien sowie der Vergleich ähnlicher Reflexionsmuster (Tillmann & Wunderlich 2011a, 2011b, 2013) lassen jedoch eine sandige Sedimentfazies vermuten.

Interpretation
Die sigmoidale Form der Reflexionen sowie die schräg tangentiale Beziehung der Reflektoren zueinander deuten auf eine progradierende Schichtung der Sedimente von Rf-AL-A3 hin. Die in *radar packages* gebündelten Reflexionen lassen auf eine strömungsbedingte Anlagerung einzelner sandiger Sedimentpaketen schließen. Das Vorkommen von Rf-AL-A3 unterhalb des Grundwasserspiegels lässt zudem rein marine Sedimente vermuten.

E&G / Vol. 62 / No. 2 / 2013 / 98–119 / DOI 10.3285/eg.62.2.02 / © Authors / Creative Commons Attribution License

Rf-AL-B1 Grundwasserspiegel

Radarfazies und Interpretation

Rf-AL-B1 markiert einen horizontalen, durchgehenden Hauptreflektor, der der Position des Grundwasserspiegels entspricht und folglich als solcher interpretiert wird. In den gezeigten Radargrammen befindet sich der Grundwasserspiegel Rf-AL-B1 im Liegenden oder innerhalb der Dünen-Fazies (Rf-AL-A1) und teilt die Radargramme hinsichtlich ihrer elektromagnetischen Eigenschaften in einen wassergesättigten unteren und einen wasserungesättigten oberen Teil. Bedingt durch die hohe Leitfähigkeit und den starken dielektrischen Kontrast von wassergesättigten und wasserungesättigten Sedimenten zeigt der Reflektor des Grundwasserspiegels eine starke Amplitude. Im Bereich des heutigen Kniepsandes geht der Grundwasserspiegel mit Annäherung an die MThw-Linie im Westen in salzhaltiges Brack- und Meerwasser über. Der Kontaktbereich zwischen Meer- und Grundwasser zeigt sich in den Georadardaten durch eine allgemeine Abschwächung der Reflexionen im Untergrund sowie eine nach Westen verringerte Erkundungstiefe.

Rf-AL-B2 Watt-Fazies

Radarfazies

Die Radarfazies Rf-AL-B2 umfasst horizontal planare Reflektoren, die zueinander annähernd parallel orientiert sind. Die einzelnen Reflektoren verlaufen kontinuierlich bis mäßig kontinuierlich und zeigen eine mittlere bis schwache Amplitude. Rf-SS-B2a ist ausschließlich unterhalb des Grundwasserspiegels im Tiefenbereich zwischen -3,5 m NN bis -7 m NN zu finden.

Sedimentfazies

Sedimente der Radarfazies Rf-AL-B2 wurden durch die Bohrung AL6 abgeteuft und durch diese komplett durchdrungen. Rf-AL-B2 besteht aus einer sehr feinschichtigen Wechsellagerung von Feinsand und Silt mit eingeschalteten Tonlagen. Damit umfasst die Radarfazies Rf-AL-B2 die feinkörnigsten Sedimente des Untersuchungsgebietes. Das Korngrößenspektrum der gemessenen Sedimentproben variiert zwischen feinem Mittelsand (1,89 φ) und feinem Silt (7,07 φ). Der Anteil an reinem Ton beträgt zwischen 4,2 %–40,7 %.

Die Sortierung der feinkörnigen Sedimente aus der Feinsand- und Silt-Fraktion ist mäßig gut (0,59 φ) bis sehr schlecht (3,17 φ). Eingeschaltete Mittelsand-Lagen sind mit Werten von 0,60 φ–0,62 φ insgesamt besser sortiert. Die Korngrößenverteilung ist zumeist bimodal und zeigt neben dem Maximum im Feinsandbereich auch einen deutlichen Anteil an Ton. Die Sedimentfarbe ist grau bis schwarz. Innerhalb der Sedimentfazies von Rf-AL-B2 lassen sich zahlreiche gut erhaltene ca. 2–4 mm große Gehäuse der Wattschnecke (*Hydrobia ulvae*) sowie vereinzelte Mangan-Konkretionen nachweisen.

Interpretation

Im Radargramm ist Rf-AL-B2 durch horizontale Reflektoren gekennzeichnet, die auf eine ungestörte Sedimentation in horizontalen Schichten hindeuten. Im Bohrkern wird diese durch eine feinschichtige Lamination von Feinsand, Silt und Ton bestätigt.

Die dunkle Sedimentfarbe, der Gehalt an organischer Substanz und Mangan lassen auf eine Sedimentation unter reduzierenden Bedingungen schließen. Die überwiegend feinen Korngrößen von Feinsand und Silt sowie der insgesamt hohe Tongehalt zwischen 4,2 %–40,7 % sprechen für ein geringes energetisches Strömungsregime zur Zeit der Sedimentation. Gemäß der gebräuchlichen Klassifizierung nach Sindowski (1973, 1979) werden die Sedimente von Rf-AL-B2 als feinsandiges Mischwatt bis Schlickwatt interpretiert. Zahlreiche Gehäuse der Wattschnecke (*Hydrobia ulvae*) bestätigen diesen Lebens- und Sedimentationsraum.

Rf-AL-B3 Strand-Fazies

Radarfazies

Die Radarfazies Rf-AL-B3 ist im Radargramm in direktem Verbund mit Reflexionen der Radarfazies Rf-AL-A2 zu finden. Im Gegensatz Rf-AL-A2 verlaufen die einzelnen Reflektoren von Rf-AL-B3 horizontal, verhalten sich zueinander parallel bis subparallel und sind von mittlerer bis schwacher Amplitude. Wie schon die Radarfazies Rf-AL-A2 umfasst auch Rf-AL-B3 den Tiefenbereich zwischen 0 m und -4 m NN und kommt damit ausschließlich unterhalb des Grundwasserspiegels vor.

Sedimentfazies

Sedimente der Radarfazies Rf-AL-B3 umfassen schillführende Sande aus der Kornfraktion Feinsand und Mittelsand. Die durchschnittliche Korngröße bewegt sich zwischen 1,00 φ und 2,13 φ. Mit Werten zwischen 0,60 φ und 0,97 φ sind die Sande von Rf-AL-B3 von einer mäßigen bis mäßig guten Sortierung. Die Kornverteilung ist unimodal und bimodal und zeigt nur geringe Abweichungen von der beinahe symmetrischen Schiefe. Eingeschaltete Schillhorizonte innerhalb der Strand-Fazies sind dagegen von schlechter Sortierung (1,35 φ) und weisen eine polymodale Kornverteilung auf. In den Bohrungen ließen sich Oxidations- und Reduktionszonen innerhalb der Sedimentfazies von Rf-AL-B3 belegen. Die Oxidationszonen sind durch Rostflecken sowie die eisenhaltige Umkrustung von Sandkörnern und -konkretionen gekennzeichnet.

Interpretation

Zusammen mit der Radarfazies Rf-AL-A2 umfasst die Radarfazies Rf-AL-B3 den Sedimentationsraum Strand. Rf-AL-A2 bildet im Radargramm die in das Strandprofil eingeschalteten intertidalen Sedimentkörper (*swash bars*) ab. Diese sind für die im Untersuchungsgebiet typische unruhige Strandmorphologie bestehend aus einer Kombination aus Vollformen und Geländedepressionen (*ridge-and-runnel*-Strukturen) verantwortlich. Dagegen besteht Rf-AL-B3 aus vorwiegend parallelen, horizontalen Reflektoren, die als annähernd söhlig lagernde, leicht in Richtung Meer einfallende Strandsandschichten gedeutet werden.

Diese lassen sich mit der von Schäfer (2005: 228) als „Hochenergie-Parallelschichtung“ bezeichneten, internen Sedimentstruktur vieler Strände vergleichen.

Rf-AL-C1 Geschiebenester im Geestkern

Radarfazies und Interpretation

Kennzeichnend für die Radarfazies von Rf-AL-C1 sind zahlreiche, sich zum Teil überlagernde Diffraktionshyperbeln, die in den Georadardaten ein chaotisches, wellenförmiges Reflexionsmuster hinterlassen. Rf-AL-C1 ist ausschließlich unterhalb des Grundwasserspiegels sowie unterhalb

der Radarschichtfläche von Rf-AL-D1 nachzuweisen und kommt häufig in unmittelbarer Nachbarschaft zu den Reflexionen von Rf-AL-C2 vor.

Das Vorkommen von Rf-AL-C1 unterhalb der Radarschichtfläche von Rf-AL-D1 deutet auf Sedimentstrukturen innerhalb des pleistozänen Geestkerns hin. Chaotische, wellenförmige Reflexionsmuster in Kombination mit zahlreichen Diffraktionshyperbeln wurden auch in Jakobsen & Overgaard (2002) und Van Overmeeren (1998) mit glazialen Sedimenten in Verbindung gebracht.

Auf Amrum bestehen die Sedimente der Saale-Eiszeit vorwiegend aus fluvioglazialen Schmelzwassersanden (vgl. Meier 1987; Voigt 1969) und stark sandigem Geschiebelehm (Jessen 1932). Kalkhaltiger, toniger Geschiebemergel, wie er am Roten Kliff im Westen Sylts oder am Goting Kliff auf Föhr ansteht, ist auf Amrum nicht nachzuweisen (Müller & Fischer 1937).

Nach Krause (1913) sind die Ablagerungen der Geest auf Amrum ursprünglich durch „Ausschlämmung“ aus einer aufbereiteten Grundmoräne hervorgegangen und bestehen heute aus partiell geschichteten, geröllreichen Sanden. Der Blockreichtum Amrums im Vergleich zu den Geestkernen der Nachbarinseln spricht ebenfalls für das Hervorgehen aus einer Grundmoräne (Krause 1913).

Der Geestkern der Insel Amrum zeichnet sich demnach besonders durch einen überdurchschnittlichen Geschiebereichtum aus. Jessen (1932) weist seinerseits auf das Vorkommen sog. „Geschiebenester“ im Geestkern Amrums hin. Diese bilden eine Konzentration von Geschieben die sich im Radargramm deutlich in Form von Diffraktionshyperbeln abbilden. Unter Rf-AL-C1 werden diese Geschiebeansammlungen innerhalb des Inselgeestkerns zusammengefasst.

Rf-AL-C2 Geestkern-Fazies

Radarfazies

Die Radarfazies Rf-AL-C2 zeigt schwache, diskontinuierliche Reflexionen, die insgesamt ein chaotisches Reflexionsmuster bilden. Diffraktionshyperbeln innerhalb der Radarfazies von Rf-AL-C2 sind häufig und in der Regel chaotisch innerhalb der Radarfazies verteilt. Eine untere Grenze von Rf-AL-C2 ist in den Radargrammen aufgrund verstärkter Dämpfung mit zunehmender Untergrundtiefe nicht auszumachen. Auch Rf-AL-C2 ist ausschließlich unterhalb des Grundwasserspiegels (Rf-AL-B1) und unterhalb der Radarschichtfläche (Rf-AL-D1) nachzuweisen.

Sedimentfazies

Das Amrumer Pleistozän, sofern es anhand der freiliegenden Geestoberfläche, der aufgeschlossenen Kliffabbrüche und durch die durchgeführten Bohrungen bestimmt werden konnte, besteht aus Sand- und Kiesschichten mit eingelagerten Geschieben.

Die Geestkern-Fazies Rf-AL-C2 wurde durch die Bohrungen AL1, AL2 und AL6 in unterschiedlichen Tiefen abgeteuft und setzt sich aus stark glimmerhaltigen (Muskovit) Fein- und Mittelsanden zusammen. Die durchschnittli-

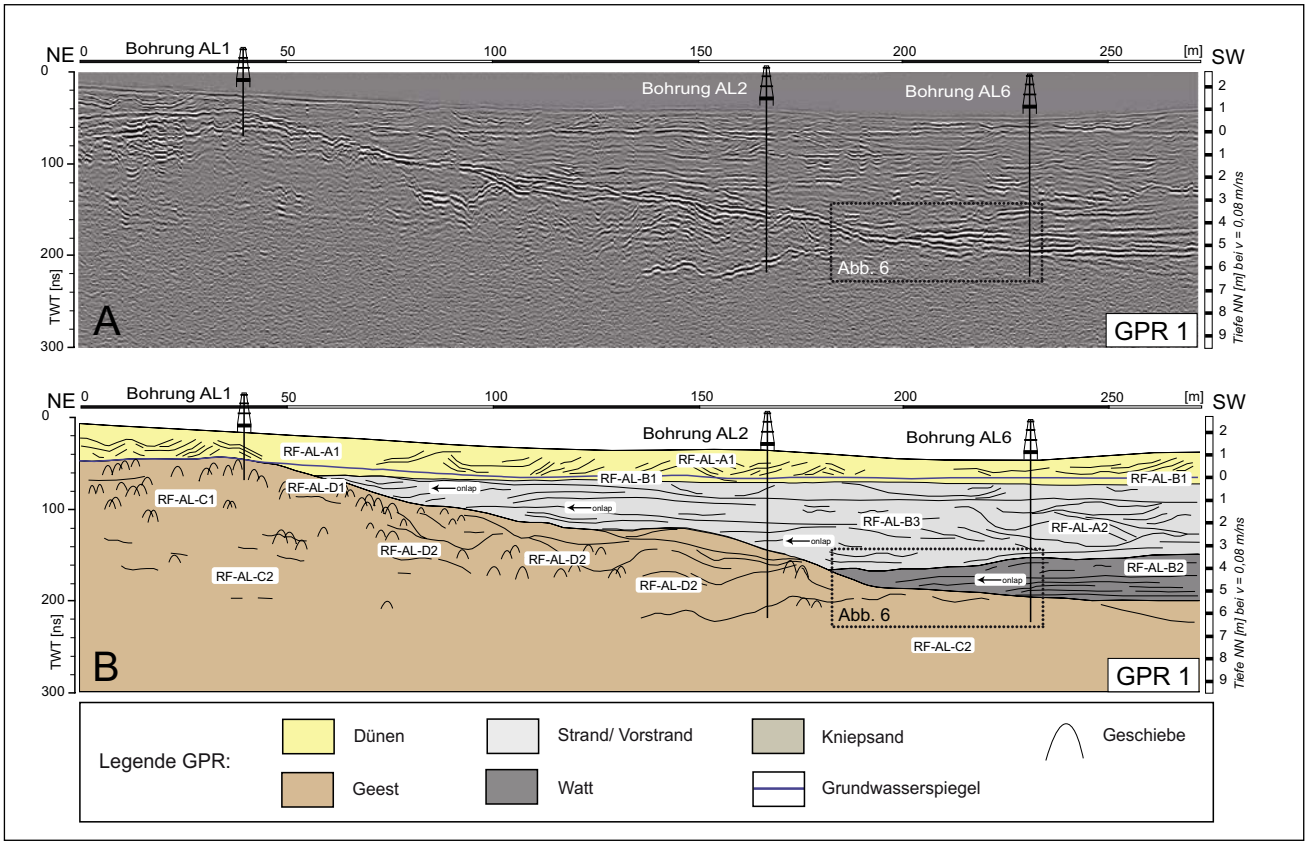

Abb. 5: GPR-Profil 1 und Position der Bohrungen AL1, AL2 und Al6. A: Für die GPR-Daten wurde ein Basis-Processing aus (static correction, subtract-mean dewow, Bandpassfilter, background removal, gain und Migration) angewandt und die Topographie mit Hilfe von dGPS Koordinaten ausgeglichen. B: Radarfazies und Interpretation von GPR-Profil 1. Die Legende gilt auch für alle weiteren GPR-Profile dieser Studie.

Fig. 5: GPR-profile 1 and position of core AL1, AL2 and Al6. A: Processing (static correction, subtract-mean dewow, bandpassfilter, background removal, gain and migration) and topographic correction of the radargramm were already applied. B: Radarfacies and interpretation of GPR-profile 1. Legend is valid for all GPR-profiles shown in this study.

E&G / Vol. 62 / No. 2 / 2013 / 98–119 / DOI 10.3285/eg.62.2.02 / © Authors / Creative Commons Attribution License

che Korngröße der Geest-Sande beträgt 1,34 φ und 2,77 φ. Die Sortierung ist mit Werten zwischen 0,95 φ und 0,52 φ mäßig bis mäßig gut und ist an der Oberfläche der Geest zunehmend schlechter. Es dominieren unimodale und bimodale Korngrößenverteilungen. Vereinzelt ließen sich im Bohrkern moderat gerundete Kiese nachweisen. Muscheln oder Schillanteile konnten dagegen nicht bestätigt werden.

Interpretation

Die Radarfazies Rf-AL-C2 entspricht der internen Struktur und Schichtung im Geestkern, die sich bedingt durch geringe Materialunterschiede in Form von Reflexionen im Radargramm abzeichnet. Ursache der internen Struktur im Geestkern können sowohl primäre fluvioglaziale Sedimentationsprozesse als auch die periglaziale Umformung des oberflächennah anstehenden Geestkerns sein.

Im Gegensatz zum zentralen Sylter Geestkern bei Kampen ist der Geestkern der Insel Amrum weniger tonhaltig und setzt sich vorwiegend aus fluvioglazialen Schmelzwassersanden und stark sandigem Geschiebelehm zusammen (vgl. Jessen 1932; Meier 1987; Müller & Fischer 1937; Voigt 1969). Durch die geringen Tonanteile wurden innerhalb der Geestkern-Fazies von Amrum beachtliche Erkundungstiefen von bis zu 350 ns TWT bzw. 13,5 m Tiefe erreicht (Tillmann & Wunderlich 2012).

Rf-AL-D1 Geestkernoberfläche

Radarfazies

Die nach Westen einfallende Radarschichtfläche Rf-AL-D1 zeichnet sich durch einen kontinuierlichen Hauptreflektor mit starker Amplitude aus, der ausschließlich unterhalb des Grundwasserspiegels verläuft. An der Basis des Hauptreflektors sind zahlreiche Diffraktionshyperbeln konzentriert. Unterhalb der Radarschichtfläche kommen Reflexionen von Rf-AL-C1, Rf-AL-C2 und Rf-AL-D2 vor.

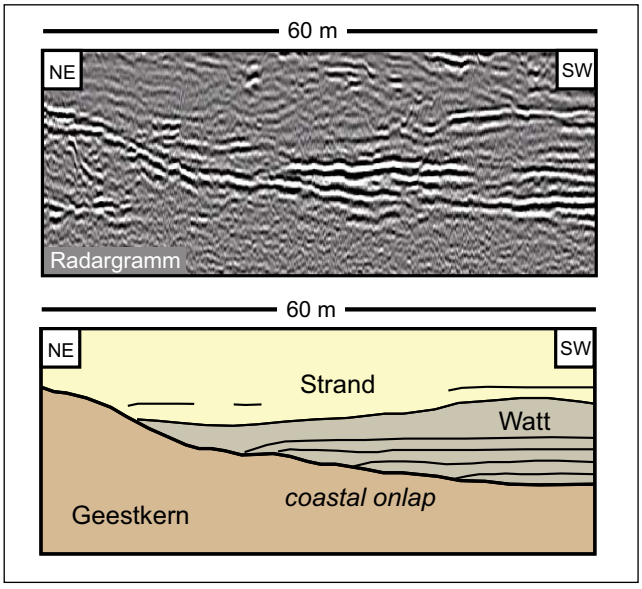

Abb. 6: Der vergrößerte Ausschnitt aus GPR-Profil 1 zeigt die coastal-onlap-Konfiguration der Reflexionen im Detail. Die Position des Ausschnitts ist im Radargramm in Abbildung 5 dargestellt.

Fig. 6: The close up of GPR-profile 1 shows the coastal-onlap configuration in detail. For position of the section see figure 5.

Sedimentfazies

Die Radarschichtfläche von Rf-AL-D1 wurde durch die Bohrungen AL1, AL2 und AL6 durchteuft und besteht im Bohrkern aus Mittelsanden mit einer durchschnittlichen Korngröße von 1,34 φ–1,81 φ, die in Kombination mit größeren, moderat gerundeten Kiesen vorkommen. In Bohrung AL6 ließen sich im Bereich der Radarschichtfläche Wurzeln und Vegetationsreste nachweisen, die auf einen terrestrischen Sedimentationsraum bzw. eine ehemalige Landoberfläche hindeuten. Die Sedimente dieser Geestkernoberfläche sind mit Werten zwischen 1,45 φ–1,53 φ in der Regel etwas schlechter sortiert als die Sedimente, die mittels Bohrungen aus dem Inneren des Geestkerns abgeteuft wurden.

Interpretation

Die Radarschichtfläche von Rf-SS-D3 markiert die Oberfläche des nach Westen abtauchenden Inselgeestkerns und stellt zugleich die Grenze zwischen dem Holozän im Hangenden und dem Pleistozän im Liegenden dar. Die im Radargramm an der Basis der Radarschichtfläche konzentrierten Diffraktionshyperbeln entsprechen Geschieben, die sich an der Geestkernoberfläche deflationsbedingt angereichert und dort eine Steinsohle ausgebildet haben.

Rf-AL-D2 fossile Kliffs

Radarfazies

Rf-AL-D2 zeigt im Radargramm eine steil einfallende Radarschichtflächenkonfiguration mit starker Amplitude und kontinuierlichem Verlauf. Diffraktionshyperbeln lassen sich sowohl an der Basis sowie im Hangenden der Radarschichtfläche nachweisen.

Sedimentfazies

Die Radarschichtfläche Rf-AL-D2 wurde durch die Bohrung AL2 durchdrungen. Charakteristisch für Rf-AL-D2 ist eine starke Anreicherung von moderat bis gut gerundeten Kiesen. Hinsichtlich der Korngröße besteht die Radarschichtfläche aus Grobsand (0,73 φ), der eine schlechte Sortierung (1,26 φ) aufweist.

Interpretation

Unter Rf-AL-D2 werden Strukturen zusammengefasst, die an der Oberfläche des Geestkerns entstanden sind und sich in diesem an einigen Stellen lateral eingeschnitten haben. Die konkaven Erosionsstrukturen werden als fossile Kliffabbrüche im Bereich des Geestkerns interpretiert. Diese fossilen Kliffs entstanden infolge sturmflutbedingter Erosion am nach Westen abtauchenden Inselgeestkern. Brandungserosion führte am Geestkern zur Ausbildung von Brandungshohlkehlen und damit zur Kliffbildung.

Diffraktionshyperbeln zeugen sowohl an der Basis sowie im Hangenden der Radarschichtfläche von Rf-AL-D2 von Geschieben. Die an der Basis konzentrierten Hyperbeln entsprechen Geschiebeansammlungen am Fuße des Kliffs.

Schwerkraftbedingte Denudation von lockeren Geschieben und Kliffmaterial an den durch Sturmfluterosion versteilten Kliffhängen ist wahrscheinlich. Daher sind Geschiebe in Form von Diffraktionshyperbeln auch in der Hangrutschmasse enthalten. Hinsichtlich der Radarfazies und Sedimentfazies besteht kein bedeutender Unterschied

zwischen dem anstehenden Geestkern und dem in der Hangrutschmasse enthaltenen Abbruchmaterial.

4.2 Georadar-Profile

Eine Besonderheit der GPR-Profile im Untersuchungsgebiet sind materialbedingte Geschwindigkeitsänderungen sowohl in vertikaler als auch in lateraler Richtung. Die Ausbreitungsgeschwindigkeit innerhalb trockener Dünensande beträgt 0,14 m/ns–0,11 m/ns. In wassergesättigten Dünen- und Strandsanden unterhalb des Grundwasserspiegels verringert sich die Ausbreitungsgeschwindigkeit auf 0,09–0,07 m/ns. Innerhalb der saaleeiszeitlichen Geschiebeablagerungen wurden lediglich Ausbreitungsgeschwindigkeiten von 0,05–0,08 m/ns erreicht. Auch die Wattsedimente zeichnen sich durch geringe Laufzeiten von 0,06–0,04 m/ns aus. Für die Berechnung eines einheitlichen Maßstabes wurde eine durchschnittliche Ausbreitungsgeschwindigkeit von 0,08 m/ns zugrunde gelegt. In den GPR-Profilen wurde eine maximale Erkundungstiefe von 300–400 ns TWT erreicht. Dies entspricht im Gelände einer tatsächlichen Tiefe von 8–9 m unter NN.

GPR-Profil 1

Der obere Profilbereich wird ausschließlich von Reflexionen der Radarfazies Rf-AL-A1 eingenommen (Abb. 5). Innerhalb der Radarfazies Rf-AL-A1 verläuft der annähernd horizontale Hauptreflektor von Rf-AL-B1. Im südwestlichen Profilbereich von GPR-Profil 1, ab einer Entfernung von 60 m vom Startpunkt, finden sich im Liegenden von Rf-AL-A1 Reflexionen der Radarfazies Rf-AL-B3 und Rf-AL-A2. Während Rf-AL-B3 vorwiegend horizontale, nahezu parallele Reflektoren umfasst, beinhaltet Rf-AL-A2 zum Teil auch wellenförmige bis leicht geneigte Reflexionen. Die benachbarten Reflexionen von Rf-AL-B3 und Rf-AL-A2 kommen in einem Tiefenbereich von bis zu -3,5 m NN vor.

Die horizontalen, annähernd parallelen Reflektoren von Rf-A-B2 und Rf-A-B3 enden im Nordosten von Profil 1 mit einer deutlich ausgeprägten *onlap*-Konfiguration auf der Radarschichtfläche Rf-AL-D1. Besonders deutlich ist dies in Abbildung 6 ersichtlich, die einen vergrößerten Ausschnitt aus GPR-Profil 1 (Abb. 5) darstellt.

Der *onlap* von Rf-A-B3 vollzieht sich in einem Tiefenbereich zwischen -0,15 m und -4 m NN (60 ns–160 ns TWT). Im Liegenden von Rf-A-B3 in einer Tiefe von -4 m bis -7 m NN (160 ns–220 ns TWT) enden die Reflektoren von Rf-A-B2 ebenfalls durch eine *onlap*-Konfiguration auf der nach Westen abtauchenden Radarschichtfläche von Rf-AL-D1.

Besondere Strukturen stellen die unter Rf-AL-D2 zusammengefassten Reflexionen dar. Diese steil einfallenden Radarschichtflächen treten im Radargramm durch ihre starke Amplitude hervor und schneiden sich in die Reflexionen von Rf-AL-C2 ein. Diffraktionshyperbeln sind sowohl an der Basis als auch im Hangenden von Rf-AL-D2 konzentriert.

GPR-Profil 3

Das GPR-Profil 3 (Abb. 7) stellt das südwestliche Profilende der GPR-Profile dar und umfasst den Profilbereich zwischen 460 m und 810 m Länge, der über den Kamm der Vordüne bis auf den Kniepsand reicht (vgl. Abb. 1).

Auch in GPR-Profil 3 wird der oberste Abschnitt von Reflexionen der Radarfazies Rf-AL-A1 eingenommen. Im südwestlichen Profilbereich ist eine verstärkte Signaldämpfung und die damit einhergehende Verringerung der Erkundungstiefe zu beobachten. Im Südosten der Düne werden im Profilbereich zwischen 725 m–745 m Länge Erkundungstiefen von -4 m NN erreicht. Ab dem Profilmeter 745 kommt es zu einer abrupten Signaldämpfung im Untergrund, die bis zum Ende des Profils deutlich zu verfolgen ist. Grund dafür ist das von Südwesten, aus dem Strand- und Überflutungsbereich des heutigen Kniepsandes, eindringende salzhaltige Meerwasser.

Der nordöstliche Profilbereich setzt sich in einer Tiefe zwischen 225 ns–165 ns TWT (0 m bis -2 m NN) aus Reflexionen der Radarfazies Rf-AL-A2 und Rf-AL-B3 zusammen. Ab einer Tiefe von 225 ns TWT dominieren Reflexionen der Radarfazies Rf-AL-A3. Diese sigmoidal bis schräg tangentialen Reflexionen sind in einzelne, wohl definierte Radarschichtpakete gebündelt, die ein Einfallen in nordöstliche Richtung aufweisen. Zwischen 540 m–610 m Profillänge enden die Reflexionsbündel von Rf-AL-A3 in einer Tiefe von 320–350 ns TWT (ca. -5 bis -6 m NN) durch eine downlap-Konfiguration (Abb. 8).

4.3 Sedimentologische Daten

Bohrungen AL1, AL2 und AL6

In das Georadar-Transekt 1 wurden an drei Stellen die Bohrungen AL1, AL2 und AL6 eingebracht. AL1 befindet sich in 40 m Entfernung vom nordöstlich gelegenen Startpunkt des Profils und erreicht eine Bohrtiefe von 2 m unter der Geländeoberfläche (0 m NN). AL2 und AL6 wurden in 168 m und 231 m Entfernung vom Startpunkt eingebracht und wurden bis zu einer Tiefe von 8 m unter der Geländeoberfläche abgeteuft. Bohrung AL2 erreicht eine Geländetiefe von -6,25 m NN, während die maximale Geländetiefe in Bohrung AL6 -6,40 m NN entspricht. Die Ergebnisse und Korngrößenverteilung der Bohrungen AL2 und AL6 sind in den Abbildungen 9 und 10 dargestellt.

Der obere Bereich der Bohrungen AL1, AL2 und AL6 wird von holozänen Dünensanden der Fein- bis Mittelsandfraktion eingenommen. Die äolischen Fein- und Mittelsande (2,11 φ–1,73 φ) sind mäßig (0,81 φ) bis mäßig gut (0,60 φ) sortiert und zeigen insgesamt nur geringe Abweichung innerhalb des Korngrößenspektrums. Makroskopisch erkennbare Muscheln oder Schillanteile sind nicht vorhanden. Die Kornverteilung ist unimodal bis bimodal mit dem größten Anteil an der Korngröße Mittelsand. Die Schiefe variiert zwischen -0,172 φ und 0,148 φ.

Wurzeln des Strandhafers (*Ammophila arenaria*) sind in den Bohrungen AL1, AL2 und AL6 häufig und durchziehen den oberen Meter der Bohrungen AL2 und AL6. In Bohrung AL2 wurde überdies in einer Tiefe von 0,75 m ein ca. 20 cm mächtiger organisch angereicherter Boden- bzw. Wurzelhorizont nachgewiesen (Abb. 9 Bild 1), der sich bereits aufgrund des Farbunterschiedes innerhalb der hellen Dünensanden abzeichnet.

In den dargestellten Bohrungen AL2 und AL6 gehen die äolischen Dünensande im Hangenden ab einer Bohrtiefe von 1,30–1,40 m in die marinen Strandsande des Liegenden über (Abb. 9 und 10). Die Dünenbasis befindet sich damit

E&G / Vol. 62 / No. 2 / 2013 / 98–119 / DOI 10.3285/eg.62.2.02 / © Authors / Creative Commons Attribution License

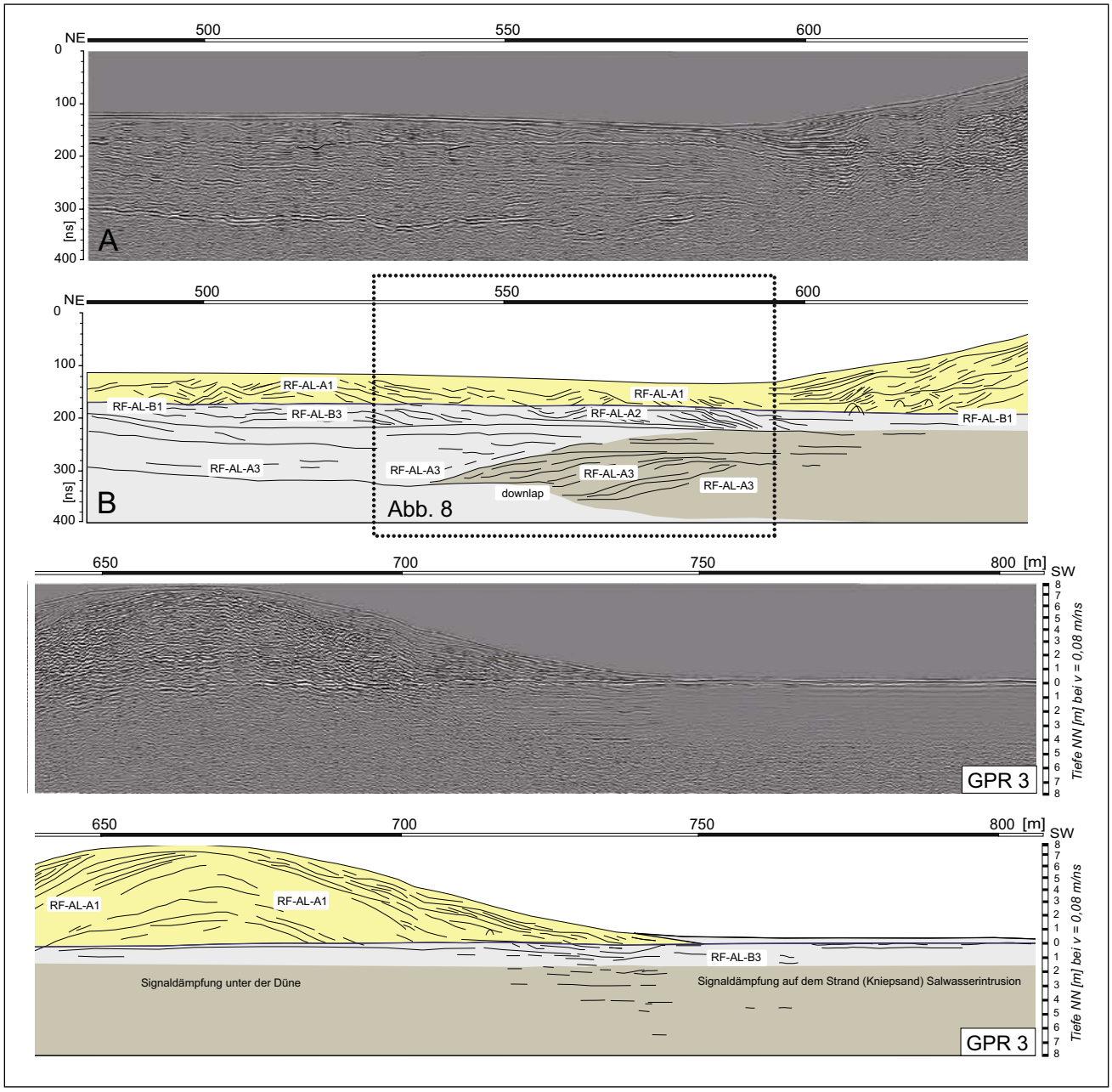

Abb. 7: GPR-Profil 3. A: Für die GPR-Daten wurde ein Basis-Processing aus (static correction, subtract-mean dewow, Bandpassfilter, background removal, gain und Migration) angewandt und die Topographie mit Hilfe von dGPS Koordinaten ausgeglichen. B: Radarfazies und Interpretation von GPR-Profil 3. Legende siehe Abbildung 5.

Fig. 7: GPR-profile 3. Processing (static correction, subtract-mean dewow, bandpassfilter, background removal, gain and migration) and topographic correction of the radargramm were already applied. B: Radarfacies and interpretation of GPR-profile 1. For legend see figure 5.

zwischen 1 m NN und -0,5 m NN und liegt damit im Bereich des heutigen Grundwasserspiegels.

Die Strand-Fazies in Bohrung AL2 zeigt im Vergleich zu Bohrung AL6 insgesamt eine stärkere Variation hinsichtlich der Korngröße und Sortierung. Im Bohrkern von AL6 lässt sich anhand der Korngröße und Sortierung kaum ein Unterschied zwischen Dünen- und Strandfazies feststellen. Es dominieren Fein- und Mittelsande (1,899 φ–2,003 φ). Alle Proben weisen eine mäßig gute Sortierung (0,602 φ–0,612 φ) auf und besitzen eine symmetrische bis leicht positive Schiefe. Hinweise auf ein marines Ablagerungsmilieu geben im Bohrkern AL6 lediglich die ab einer Tiefe von 2 m unter der Geländeoberfläche (ca. -0,8 m NN) vermehrt vorkommenden Muschelschalen.

In einer Bohrtiefe zwischen 3 m–5 m wechseln sich Oxidations- und Reduktionshorizonte ab. Der Wechsel von Oxidation und Reduktion spricht für die zeitweilige Überflutung des Sedimentationsraums und kann daher ebenso als Indiz für ein marines Milieu gedeutet werden.

Der Strand aus Bohrung AL2 besteht aus schillführenden Fein- und Mittelsanden (1,00 φ–2,13 φ), die eine mäßige bis mäßig gute (0,60 φ–0,97 φ) Sortierung und eine unimodale bis bimodale Kornverteilung aufweisen (Abb. 9). Eingeschaltete Schillhorizonte innerhalb der Strand-Fazies sind von schlechter Sortierung (1,35 φ) und weisen eine polymodale Kornverteilung auf. Wie auch in Bohrung AL6 sind die Sedimente des Strandbereichs von AL2 durch zahlreiche Oxidations- und Reduktionsspuren gekennzeichnet. Rost-

flecken sind detailliert in Abbildung 9 (Bild 2) hervorgehoben. Überdies sind innerhalb der Strand-Fazies aus Bohrung AL2 immer wieder schwach ausgebildete Wurzelreste nachzuweisen. Im unteren Strandbereich von Bohrung AL2 lassen sich ab einer Bohrtiefe von 3 m zunehmend gröbere Korngrößen wie mäßig bis gut gerundete Kiese dokumentieren. Auch die Sortierung ist im unteren Strandbereich von AL2 generell schlechter als in Bohrung AL6.

Die Unterschiede der Strandsedimente von AL2 und AL6 lassen sich mit der Nähe bzw. Entfernung zu dem sich im Nordosten anschließenden Geestkliff erklären. So stellt Bohrung AL2 den kliffnahen Strandbereich dar. Dies wird vor allem durch die Anreicherung von Kiesen und Geröllen im unteren Strandbereich des Bohrkerns deutlich. Dieser Bereich entspricht morphologisch dem fossilen Klifffuß des Geestkliffs und ist so im weitesten Sinne als Teil einer Abrasionsplattform anzusehen. Die Kiese stammen ursprünglich aus dem pleistozänen Kliff und wurden durch die Brandung zu gut gerundeten Brandungsgeröllen aufgearbeitet.

Die Wurzelreste aus Bohrung AL2 deuten auf Vegetation hin, die im Vergleich zum Standort von Bohrung AL6 durch ihre Nähe zum Inselgeestkern bzw. ihrer größeren Entfernung zum Meer und der damit einhergehenden geminderten Überflutungshäufigkeit die besseren Lebensbedingungen vorgefunden hat. Es handelt sich dementsprechend um den trockenen Strand im *backshore*-Niveau.

Der sedimentologische Übergang zwischen Strand-Fazies im Hangenden und Watt-Fazies im Liegenden vollzieht sich im Bohrkern nur allmählich und kann durch einen Übergangsbereich beschrieben werden. Der Übergangsbereich setzt sich aus Fein- und Mittelsanden zusammen, die eine ähnliche Sortierung wie die überlagernden Strandsedimente zeigen. Eine eindeutige, allein auf sedimentologischen Kriterien basierende Unterscheidung von Strand-Fazies und Sandwatt-Fazies ist in diesem Abschnitt von Bohrung AL6 nicht möglich. Aufgrund der typischen Reflexionsgeometrien in den GPR-Daten wurde dieser Abschnitt durch die Radarstratigraphie dennoch eher zum Strandbereich gezählt.

Erst ab einer Bohrtiefe von 6,60 m (-3,75 m NN) wird ein deutlicher Wechsel hin zum feinkörnigen Misch- und Schlickwatt deutlich, das sich durch eine sehr fein laminierte Wechsellagerung von Feinsand, Silt und Ton auszeichnet. Das Korngrößenspektrum der Watt-Fazies variiert zwischen feinem Mittelsand (1,89 φ) und feinem Silt (7,07 φ). Der Anteil an reinem Ton beträgt zwischen 4,2 %–40,7 %.

Die in AL6 erbohrte Watt-Fazies vor der Westküste Amrums lässt sich in ein Schlick- und Mischwatt unterteilen. In Bohrtiefen von 6,60 m–7,35 m wurde ein Schlickwatt mit einem reinen Tonanteil von 13,5 %–40,7 % nachgewiesen. Zahlreiche Gehäuse der Wattschnecke (*Hydrobia ulvae*) sprechen ebenfalls für ein Schlickwatt, das für die zum Makrobenthos zählende und sich als Weidegänger ernährende Schnecke einen bevorzugten Lebensraum darstellt (Ott 1996; Sommer 2005). Die Gehäuse der Schnecken sind intakt und gut erhalten. Die graue bis schwarze Sedimentfarbe und das Vorkommen von Mangan-Konkretionen geben Hinweise auf reduzierende Bedingungen (Sommer 2005) bzw. sind als Beleg für die Reduktionszone im Watt anzuführen (vgl. Köster 1998; Ott 1996; Pott 2003; Sindowski 1973).

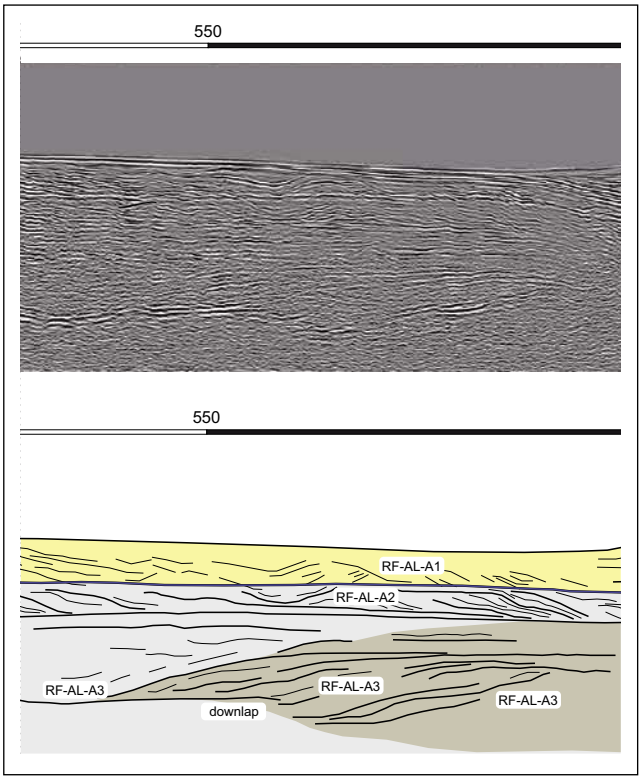

Abb. 8: Vergrößerter Ausschnitt aus GPR-Profil 3. Zur Position des Ausschnitts innerhalb des Profils siehe Abbildung 7. Der Ausschnitt zeigt die ostwärts gerichtete Wanderung des Kniepsandes.

Fig. 8: The close up of GPR-profile 3. For position of the close up see figure 7. The section shows the eastward migration of the Kniepsand.

In Bohrung AL6 wird das Schlickwatt zum Hangenden hin zunehmend grobkörniger und geht ab einer Bohrtiefe von 6,60 m in ein feinsandiges Mischwatt mit einem Tonanteil von unter 5,6 % und einer durchschnittlichen Korngröße von 2,45 φ–1,89 φ über. Die Sedimentfarbe wird zum Hangenden hin insgesamt heller (Abb. 10) und deutet auf weniger stark reduzierende Bedingungen bzw. eine bessere Durchlüftung der Sedimente mit Sauerstoff hin.

Die feinen Korngrößen von Feinsand und Silt sowie der insgesamt hohe Tongehalt sprechen für ein geringes energetisches Strömungsregime zur Zeit der Sedimentation. Infolgedessen wird angenommen, dass die Wattsedimente aus Bohrung AL6 aus einer Stillwassersedimentation an einer „Niederenergieküste“ (Schäfer 2005: 243) hervorgegangen sind. Solche ruhigen Sedimentationsbedingungen sind heute hauptsächlich im Bereich der Rückseitenwatten und im strömungsberuhigten Lee einer Insel oder Küstenbarriere zu finden.

Heute herrschen an der Westküste Amrums jedoch hochenergetische Strömungsbedingungen. Die erbohrten Wattsedimente müssen demzufolge unter abweichenden, ruhigeren Sedimentationsbedingungen dort zur Ablagerung gelangt sein. Es ist davon auszugehen, dass dies im Lee einer der Westküste vorgelagerten Barriere oder Sandbank geschah. Es wird daher angenommen, dass der damals noch weit vor der Küste Amrums liegende Kniepsand diese Barriere bildete und so an der Westküste für strömungsberuhigte Sedimentationsbedingungen sorgte.

Die Geest-Fazies wurde durch die Bohrungen AL1, AL2 und AL6 direkt erreicht (Abb. 9 und 10). Dabei fällt die Ober-

E&G / Vol. 62 / No. 2 / 2013 / 98–119 / DOI 10.3285/eg.62.2.02 / © Authors / Creative Commons Attribution License

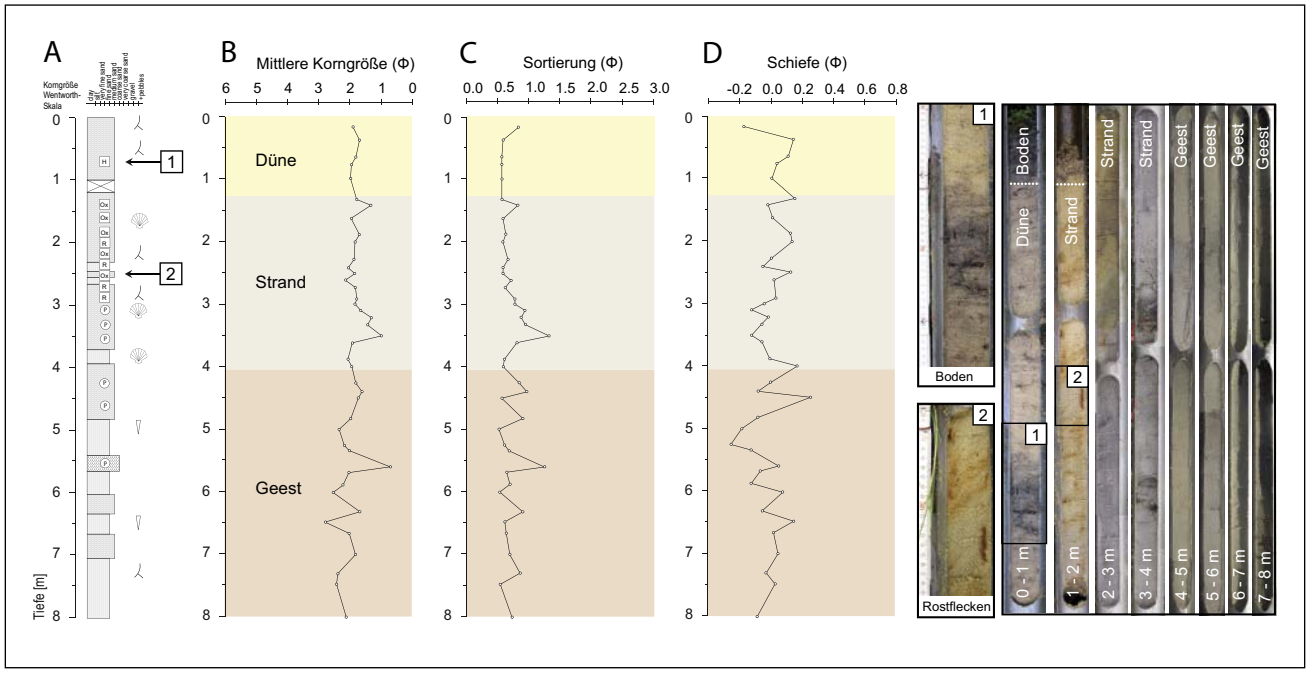

Abb. 9: Bohrkern (A) und Korngrößenstatistik (B – D) von Bohrung AL2. Legende siehe auch Abbildung 10. Bild 1 markiert einen Paläoboden innerhalb der Dünenfazies. Bild 2 zeigt eine Oxidation der Strandsedimente.

Fig. 9: Core log (A) and grain size statistic (B – D) of core AL2. Legend is provided in figure 10. Picture 1 shows a palaeosoil within the dune facies. Picture 2 shows oxidation of beach deposits.

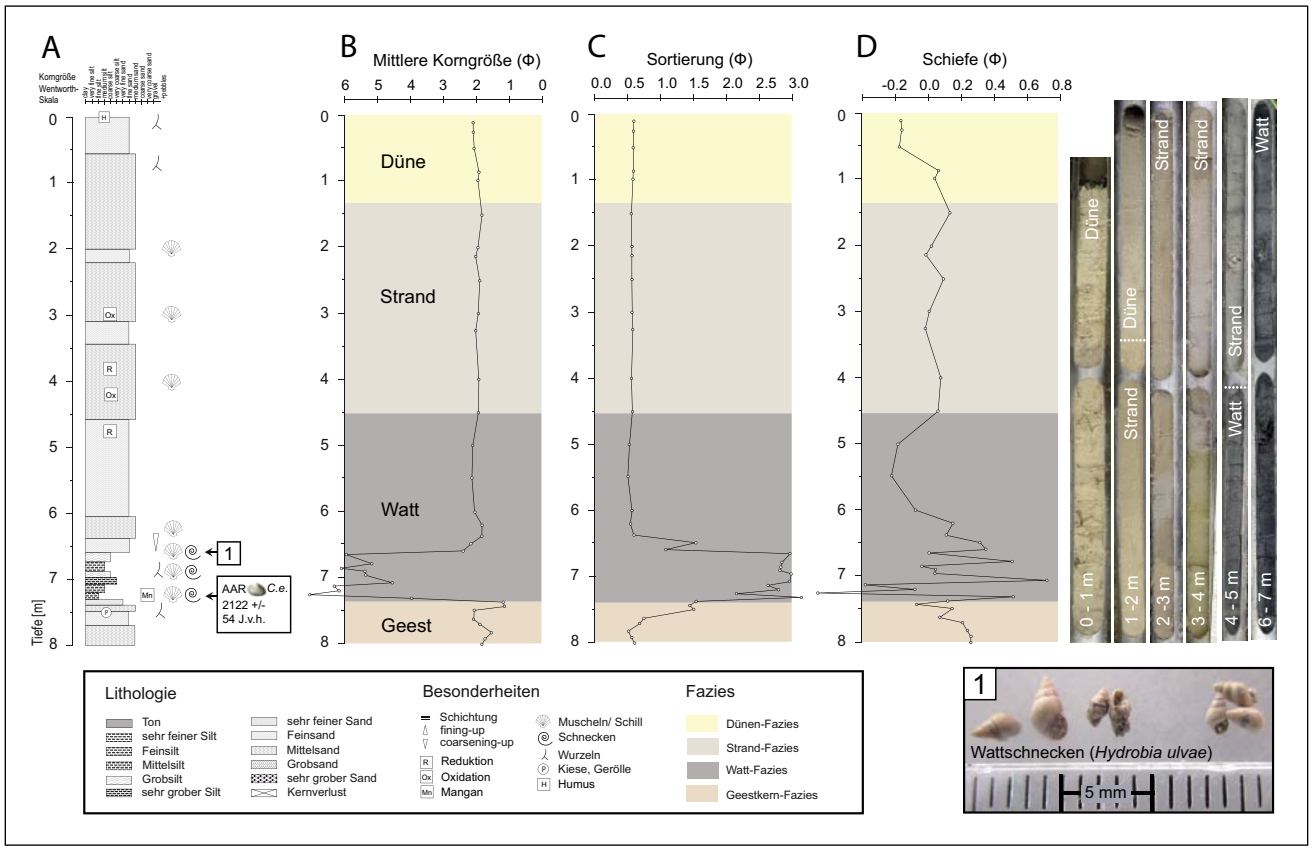

Abb. 10: Bohrkern (A), Korngrößenstatistik (B–D) und Legende von Bohrung AL6. Bild 1: Hydrobia ulvae.

Fig. 10: Core log (A), grain size statistic (B–D) and legend of core AL6. Picture 1: Hydrobia ulvae.

fläche der Geest in den Bohrungen AL1, AL2 und AL6 von Nordosten nach Südwesten ab. Während die Geest in Bohrung AL1 direkt unterhalb der Dünenfazies ansteht und in einer Bohrtiefe von 1,20 m (0,8 m NN) erreicht wurde, fällt die Oberfläche in den Bohrungen AL2 und AL6 auf 4 m und 7,45 m Tiefe ab. Damit steht die Geest in Bohrung AL2 bei -3,15 m NN und in Bohrung AL6 bei -5,25 m NN an.

Die Geestkern-Fazies setzt sich in den Bohrungen AL1, AL2 und AL6 aus stark glimmerhaltigen Fein- und Mittelsanden zusammen. Es dominiert der helle Glimmer (Muskovit). Die durchschnittliche Korngröße der Geest-Sande beträgt 1,34 φ und 2,77 φ. Die Sortierung ist mit Werten zwischen 0,95 φ und 0,52 φ mäßig bis mäßig gut und ist an der Oberfläche der Geest meist etwas schlechter. Der Übergang von der Geest-Fazies im Liegenden zur Watt-Fazies im Hangenden wird durch eine Anreicherung von groben Kornkomponenten und Kiesen begleitet, die sedimentologisch auf eine gut ausgebildete Steinsohle hinweisen.

Überdies konnten in Bohrung AL6 in einer Tiefe von 7,45 m (-5,25 m NN) Wurzeln nachgewiesen werden. Wurzeln an dieser stratigraphischen Position sprechen für den Bewuchs der Geestoberfläche und damit für ehemals terrestrische Bedingungen an dieser einstigen Landoberfläche. Die Annahme eines terrestrischen Ablagerungsraumes wird durch das Fehlen von Muscheln und Schill unterstützt.

5 Diskussion

5.1 Coastal onlap Modell

Auf der Grundlage der gemessenen GPR-Profile und durchgeführten sedimentologischen Analysen aus den Bohrungen AL1, AL2 und AL6 wurde ein stratigraphisches Modell entwickelt. Das Modell beschreibt die Landschaftsentwicklung an der Westküste Amrums in einer Zeit, bevor sich der von Westen heranwandernde Kniepsand an die Insel angelagert hat.

Die geologische Ausgangssituation ist ein leicht nach Westen abfallender Geestkern bestehend aus Endmoränenrelikten der Saale-Eiszeit. Von Westen aus folgt die Anlagerung rein mariner Sedimente, die als „*coastal onlap*“ (Catuneanu 2002; Emery & Myers 1996) beschrieben werden kann. *Coastal onlap* Konfigurationen sind vor allem aus seismischen Daten vom Kontinentalhang bekannt (vgl. Emery & Myers 1996). In Georadardaten konnte ein *coastal onlap*-Prozess hingegen bislang noch nicht nachgewiesen bzw. unmittelbar durch Radargramme abgebildet werden.

Sedimentologisch besteht der Geestkern im Untersuchungsgebiet aus muskovithaltigen Fein- und Mittelsanden mit vereinzelt eingeschalteten Geschieben, die auf fluvioglaziale Schmelzwassersande zurückzuführen sind (vgl. auch Jessen 1932; Krause 1913; Meier 1987; Voigt 1969).

Der Übergang zwischen Geestkern im Liegenden und Watt im Hangenden wird durch eine Steinsohle gebildet, die der ehemaligen Landoberfläche entspricht und zugleich die Grenze zwischen Pleistozän und Holozän darstellt. Wurzeln zeugen von terrestrischen Bedingungen und dem einstigen Bewuchs dieser Landoberfläche, die durch einsetzende Transgression allmählich von Westen her überflutet wurde.

Mit der Transgression folgten Ablagerungen eines Watts. Die Wattsedimentation im Vorfeld des nach Westen abtauchenden Geestkerns stellt damit die zeitlich erste aus den o. g. Daten ersichtliche Phase dar (Abb. 11 Bild 1). Die Ablagerungen dieses Westküstenwatts konnten in den Daten bis zu einer Tiefe von -7 m NN verfolgt werden. Im Liegenden wurden zunächst horizontal geschichtete Wattsedimente eines Misch- bis Schlickwatts abgelagert, die zum Hangenden hin grobkörniger werden und in ein Sandwatt übergehen. Der Sedimentationsraum wird durch Funde von Wattschneckengehäuse in der Bohrung AL6 bestätigt.

Eine grobe zeitliche Einordnung des Westküstenwatts aus Bohrung AL6 erfolgte lediglich mittels AAR-Datierung an einer intakten Muschelschale der Herzmuschel (*Cerastoderma edule*), die aus einer Bohrtiefe von 728 cm gewonnen wurde. Auf diese Weise konnte für die Wattsedimente in einer Tiefe von -5 m NN ein Mindestalter von 2122 +/-54 Jahren definiert werden. Die datierten Wattsedimente zählen zu den ersten, die auf dem „ertrinkenden“ Geestkern abgelagert wurden und entsprechen damit der Position des Transgressionskontaktes. Es ist demzufolge davon auszugehen, dass die Überflutung dieses Bereiches der Westküste Amrums bereits vor 2122 +/-54 Jahren einsetzte.

Bereits Falk (2001) geht vor der Westküste Amrums von wattähnlichen Bedingungen aus. Im Vorfeld der Bohrungen AL2 und AL6 wurden nach Falk (2001) im Subboreal ausschließlich marine klastische Sedimente abgelagert, die allerdings bisher nicht näher hinsichtlich ihrer Genese identifiziert, unterteilt sowie räumlich und zeitlich abgegrenzt wurden.

So wurde nach Übereinstimmung mit Falk (2001) das Gebiet der Westküste Amrums zunehmend an der Grenze zwischen Subboreal und einsetzendem Subatlantikum von der Transgression erreicht, sodass mit steigender Überflutung Wattsedimente dort abgelagert wurden. Da eine Torfbildung an der Basis der holozänen Wattsedimente fehlt wird von einem raschen Vordringen der See ausgegangen. Die transgredierende Nordsee erreicht im Subboreal zuerst über das Tief der Norderaue das Untersuchungsgebiet von Südosten her (Falk 2001). Die Bohrungen AL2 und AL6 lagen im Subboreal noch außerhalb des Überflutungsbereichs.

Aus Chroniken ist zu entnehmen, dass es noch Anfang des 19. Jahrhunderts „grüne Marschwiesen“ weit westlich von Amrum gegeben haben soll, auf denen „Schafe“ weiden konnten (Meyn 1876; Müller & Fischer 1937; Jessen 1914). Eine genaue Lagebestimmung und Position dieser „Marschwiesen“ vor der Küste Amrums wurden jedoch nie überliefert. Festgehalten werden kann dennoch, dass im Vergleich zu heute ruhigere Sedimentationsbedingungen im Vorfeld der Westküste Amrums geherrscht haben müssen.

Aus historischen Land- und Seekarten (vgl. Abb. 2) ist hingegen ersichtlich, dass sich der Kniepsand auf der Höhe des Leuchtturms bereits vor 1841 an die Insel angelagert haben muss, sodass zu und nach dieser Zeit und an dieser Stelle vor der Westküste Amrums keine „Schafe“ auf „Marschwiesen“ weiden konnten.

Glaubt man der Landkarte von Johannes Mejer aus dem Jahr 1648 (Danckwerth 1652), so lag der Kniepsand 1648 als solitäre Sandbank oder Untiefe noch weit vor der

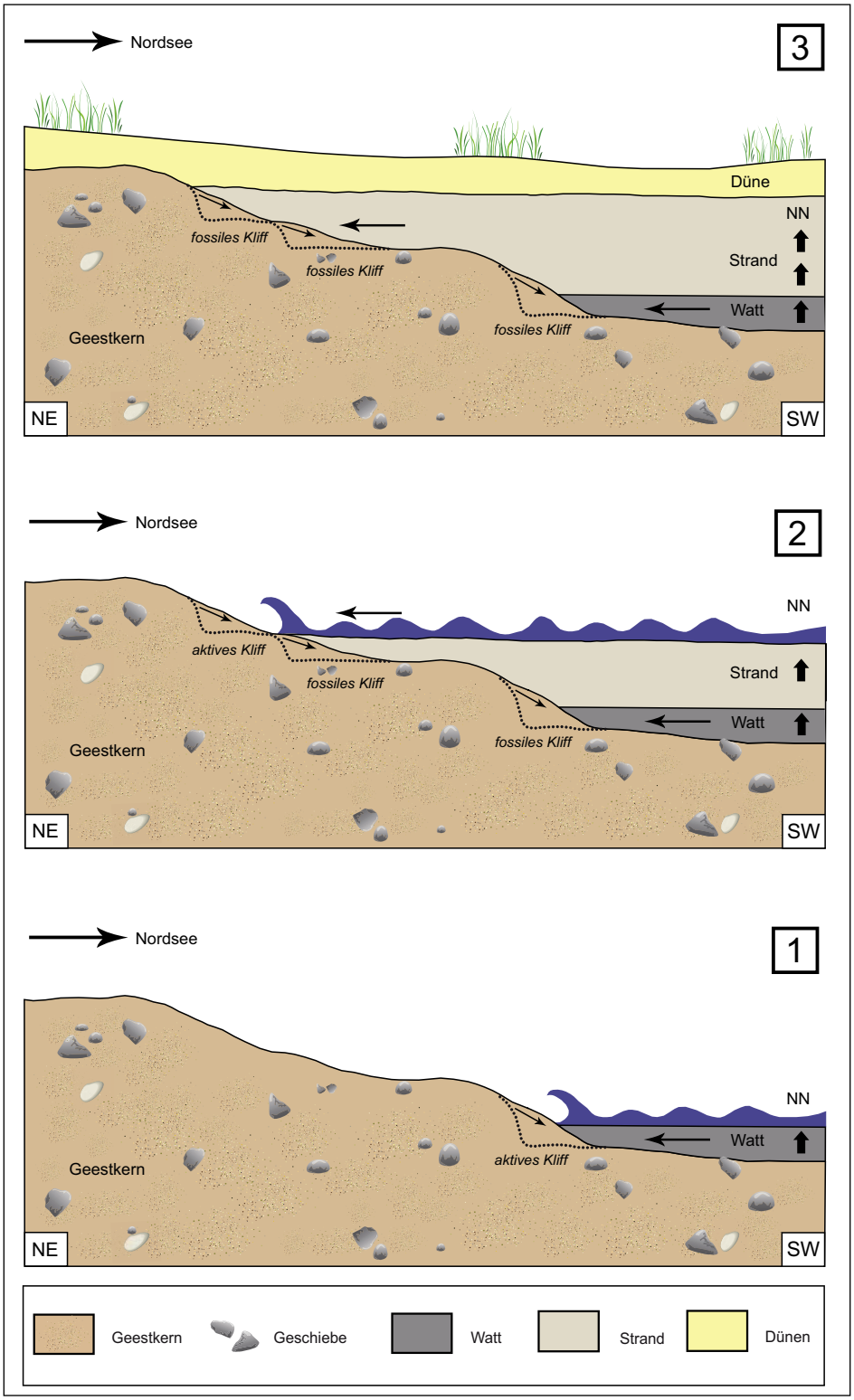

Abb. 11: Das Coastal-onlap Modell zeigt die Landschaftsentwicklung vor der Westküste der Insel Amrum. Bild 1: Im Küstenvorfeld der Insel Amrum wurden zunächst feinkörnige Wattsedimente abgelagert. Bild 2: Durch einen Anstieg des Meeresspiegels und die ostwärts gerichtete Migration des Kniepsandes folgten gröbere Strandsedimente. Sturmfluten führten gleichzeitig zur Erosion am Geestkern und schufen aktive Kliffs, die mit ansteigendem Meeres- und Sturmflutspiegel in fossile Kliffs übergingen. Bild 3: Durch die endgültige Anlagerung des Kniepsandes an die Insel wurde der nötige Sedimentinput für großflächige Dünenbildung geliefert.

Fig. 11: The coastal-onlap Model shows the landscape development in front of the westcoast of Amrum. Picture 1: Before the barrier sandbar was connected to the island, tidal flat deposits had been accumulated in a low energy environment. Picture 2: Tidal flat deposits show a general coarsening upward trend and turn into overlying coarser grained beach deposits under a rising sea level. Old cliffs formed through several storm surges are also preserved in GPR data. Picture 3: Fine to medium grained beach sand was reworked and blown out to build up some primary foredune ridges which enhance to shape the present dune area.

Westküste Amrums. Demnach können in der Zeit von 1648 bis zur Anlagerung des Kniepsandes an die Insel durchaus strömungsberuhigte Sedimentationsbedingungen geherrscht haben, die im Westküstenvorfeld zu Ausbildung von Watt- und Marschflächen führten. Denkbar ist, dass der solitäre Kniepsand seinerseits eine Barriere darstellte und so im Lee die ruhigen Sedimentationsbedingungen an der Westküste Amrums zum Teil förderte.
Eine Anlagerung des Kniepsandes an die Insel wird daher für die Zeitspanne zwischen 1648 und 1841 angenommen.

Im weiteren Verlauf der Transgression wurden die Ablagerungen zunehmend gröber. Im Hangenden des Westküstenwatts folgten Strandablagerungen (Abb. 11 Bild 2), die im Vergleich zum Watt eine unruhige Strandmorphologie zeigen. Die Morphologie wird durch vereinzelte in das Strandprofil eingeschaltete intertidale Sedimentkörper (*intertidal bars, swash bars*) und parallel zur Küste verlaufende Rinnen bedingt, die eine *ridge-and-runnel*-Topographie des Strandes hervorrufen.

Die verhältnismäßig große Breite sowie die flache nur leicht in Richtung Meer einfallende Topographie des Strandes und die Anlagerung von intertidalen Sedimentkörpern

lassen auf einen dissipativen Strand schließen. Sturmfluten führten neben Klifferosion am Geestkern ebenso zur Erosion und morphologischen Umgestaltung im Strandbereich. Dabei wurden die intertidalen Sedimentkörper zum Teil ausgeräumt, aufgearbeitet oder in ihrem oberen Bereich gekappt (FitzGerald 2005; Jackson et al. 2007), sodass zeitweilig ein ebenes Strandprofil aus horizontalen Strandsandschichten mit ausgeprägter Hochenergie-Parallelschichtung (Schäfer 2005) entstand.

Die fossilen Geestkernkliffs zeigen im Radargramm (Abb. 5) deutliche, durch wiederholte Abrasion infolge von Sturmfluten geschaffene Brandungshohlkehlen im unteren Kliffbereich. Gravitative Hangabtragung des oberen Kliffbereichs bzw. ein denudatives Nachrutschen von Kliffmaterial aus dem Hangenden ist anhand von Schutthalden am Klifffuß erkennbar. Diese Kliffhalden sind in den GPR-Daten durch eine Anreicherung von Diffraktionshyperbeln ersichtlich. Auch sedimentologisch lassen sich dem Bereich insgesamt gröbere Korngrößen sowie vereinzelt Brandungsgerölle nachweisen. Damit entspricht dieser dem Kliff vorgelagerte Strandbereich geomorphologisch einer Abrasions- oder Strandplattform.

Bereits Müller & Fischer (1937: 10) entdeckten westlich des Leuchtturms ein „[…] Steinplaster aus groben, teils faustgroßen Geröllen […]“, das sie als „[…] Brandungsterrasse, die aus den bei der Unterspülung nachgestürzten Geschieben […]“ im damaligen Kliffbereich gebildet wurde deuteten.

Die Abfolge aus Geestkern, Kliff, Brandungshohlkehle, Kliffhalde und Abrasionsplattform mit Brandungsgeröllen kann als „littorale Serie“ zusammengefasst werden, die allerdings weniger stark ausgeprägt ist. Begründet ist dies auf der Tatsache, dass sich der Geestkern von Amrum an dieser Stelle nur durch gering verfestigte pleistozäne Sande mit Geschiebeeinlagerungen darstellt, der nur bedingt ein Kliff von geringer Höhe ausbildet. Dementsprechend unscheinbar ist auch die dem Kliff vorgelagerte Abrasionsplattform, die sich ebenso aus Lockersedimenten zusammensetzt.

Fossile Kliffs in unterschiedlichen Höhenpositionen im Bereich des Geestkerns lassen auf unterschiedliche Meeresspiegelniveaus schließen. Ein Anstieg des Meeres- und Sturmflutspiegels führte zur Erosion und Kliffbildung am Geestkern. So entspricht die Höhe des jeweiligen Klifffußes dem Sturmflutspiegelniveau der entsprechenden Bildungszeit (Abb. 5 und 11). Das obere fossile Kliff kann als Vorstufe des Littorina Kliffs gesehen werden. Remde (1972) geht davon aus, dass sich das Nord- und Südende des Littorina Kliffs noch vor etwa 150 Jahren im Abbruch befand und sich erst danach zum fossilen Kliff entwickelte.

Die jüngste stratigraphische Einheit im Untersuchungsgebiet stellen die heutigen Dünen dar, die sich nach Ende der Transgression und mit Anlagerung des Kniepsandes an die Westküste der Insel großflächig bildeten und damit die Geest allmählich bedeckten (Abb. 11 Bild 3).

5.2 Andockmodell des Kniepsandes an die Insel Amrum

Auf der Grundlage von GPR-Profil 3 konnte ein zweites Modell entwickelt werden, das die Migration und letztendlich das „Andocken“ des Kniepsandes an den zentralen Inselgeestkern an der Westküste Amrums beschreibt (Abb. 12).

Generell zeigt der ehemalige Weststrand der Insel Amrum noch vor Anlagerung des heutigen Kniepsandes eine leicht nach Südwesten einfallende Schichtung im Unterwasserbereich (Abb. 12 Bild 1). Auf westlicher Seite erfolgten das Heranwandern und die Annäherung des ehemals als solitäre Sandbank vor der Westküste lagernden Kniepsandes (Abb. 12 Bild 2). Die nach Nordosten gerichtete Wanderungstendenz des Kniepsandes zeigt sich in GPR-Profil 3 besonders deutlich zwischen den Profilmetern 540–610 (Abb. 7 und 8). Die sigmoidale Form der Reflexionen sowie die tangentiale Beziehung der Reflektoren deuten dort auf eine progradierende Schichtung der Sedimente hin. Die in Radarschichtpakete gebündelten Reflexionen lassen auf eine strömungsbedingte Anlagerung einzelner sandiger Sedimentpakete schließen. Die Anlagerung von Sedimenten an die „Stirn“ des Kniepsandes erforderte einen strömungsbedingten Sedimenttransport in östliche Richtung.

Zeitlich erfolgte die Bildung des ursprünglichen Strandes an der Westküste von Amrum vor der Anlagerung des Kniepsandes an die Insel. Stratigraphisch ist der Kniepsandkörper in die ursprünglichen Sedimente des Strandes vor der Westküste Amrums eingearbeitet (Abb. 12 Bild 2).

Die deutlich erkennbare *downlap*-Konfiguration aus den GPR-Daten zeigt, dass sich der Kniepsandkörper an seiner „Stirn“ auf die Strand- und Vorstrandsedimente heraufgeschoben hat. Der Bereich zwischen den Profilmetern 540 - 610 wird infolgedessen als „Andockzone“ interpretiert und stellt damit geologisch die Grenzen zwischen der Insel und dem Kniepsand dar. Die Zone zwischen dem ursprünglichen Strand und dem heranwandernden Kniepsand zeigt im Radargramm nur wenige Reflexionen. Gründe dafür können ein homogener Sedimentkörper bzw. eine nur undeutlich bis wenig ausgeprägte Schichtung innerhalb der Mischzone der Andockstelle sein. Die Vermischung der beiden Sedimentkörper wurde in der Folgezeit durch strömungsbedingte marine Vorgänge im Unterwasserbereich sowie durch äolische Vorgänge im trockenen Bereich des Strandes gefördert (Abb. 12 Bild 3).

Nach Ende der Transgression bzw. mit dem Trockenfallen der entstandenen Sandflächen wurden die Bedingungen für die anschließende großflächige Dünenbildung geschaffen. Höchstwahrscheinlich führte die Anlagerung des Kniepsandes im Westen zum Sedimentinput und stellte den Sand zur vermehrten Dünenbildung zur Verfügung (Abb. 12 Bild 4).

Die Dünen generierten sich aus dem Kniepsand, wanderten über den Strand hinweg, begruben das Geestkliff und schoben sich den flachen Geestkern hinauf. Auf diese Weise wurde das Geestkliff vor der Brandung und vor fortschreitender Abrasion geschützt und entwickelte sich allmählich zum toten Kliff.

Morphologisch ist das Geestkliff im Untersuchungsgebiet als verdeckter Teil des weiter nördlich bei „A Hörn“ oberflächennah aufgeschlossenen Littorina Kliffs zu sehen und steht mit diesem in unmittelbarer Verbindung. Bei „A Hörn“ („die Ecke“) erreicht das Littorina Kliff mit 13 m NN heute seine größte Höhe und taucht in Richtung Leuchtturm relativ kontinuierlich ab (Remde 1972).

Auch die Dünen auf dem Geestkern Amrums wurden daher vermutlich erst nach Anlagerung des Kniepsandes

E&G / Vol. 62 / No. 2 / 2013 / 98–119 / DOI 10.3285/eg.62.2.02 / © Authors / Creative Commons Attribution License

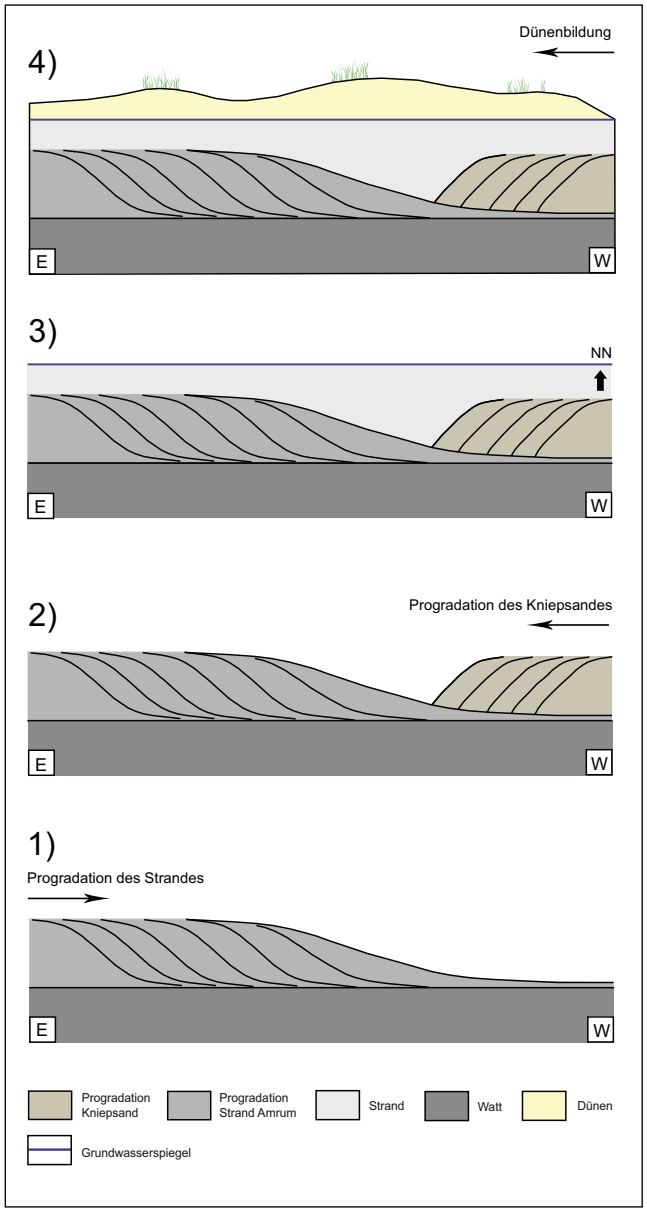

Abb. 12: Andockmodell des Kniepsandes an die Insel Amrum. Bild 1 zeigt den ursprünglichen Strand an der Westküste der Insel Amrum. Bilder 2–3 zeigen das Heranwandern des Kniepsandes an die Insel unter steigendem Meeresspiegel. Bild 4: Anschließend setzte durch vermehrten Sedimentinput großflächig Dünenbildung ein.

Fig. 12: Picture 1 shows the early beach in front of the west coast of Amrum. Pictures 2–3 show how the Kniepsand migrates to the island under a rising sea level. Picture 4: The input of sediment leads to dune building.

an die Insel gebildet. Zeitliche Anhaltspunkte für die Dünenbildung liefern die „mittelalterlichen Ackerbeete" die als Kulturspuren unter den Dünen der Geest hervortreten (Gripp 1968). Unweit des Amrumer Leuchtturms wurden zudem Pflugfurchen, Viehspuren und Ackerbeete entdeckt, deren Kultivierung gemäß der darin enthaltenen Scherben auf das 14. Jahrhundert zurückgeht (Kersten 1969; Remde 1972). Weiter zeitlich eingrenzen lässt sich die Anlagerung des Kniepsandes an die Insel Amrum unter Beachtung historischer Land- und Seekarten. So wird ein Andocken des Kniepsandes an die Insel auf der Höhe des Untersuchungsgebietes für die Zeitspanne zwischen 1648 und 1841 angenommen.

In seiner „Chronik der friesischen Uthlande" vermerkte C. P. Hansen (zitiert nach Müller & Fischer 1937: 65) für das 16. Jahrhundert jedoch: „[…] Amrum war damals wie jetzt ein mehrenteils dürres Land von Heide und Dünen, klein an Fläche, aber mit großen, weit hinausreichenden, für die Seefahrer gefahrvollen Sandbänken umgeben […]" und schilderte auf diese Weise morphologisch die Situation sowohl des noch unweit vor der Küste liegenden Kniepsandes als auch der einsetzenden Dünenbildung. Auch Hanssen (1835: 484) teilte in einem Bericht über die Pastoratsländereien von 1629 mit: „[…] schon damals war Wiesenland durch Dünen verloren gegangen […]" und beschrieb damit die Auswirkungen der Dünenbildung.

Der Kniepsand stellt heute aus geomorphologischer Sicht den Strand an der Westküste der Insel Amrum dar. Dieser erstreckt sich heute südwestlich des ersten Dünengürtels. Die ursprüngliche aus den Georadar-Daten ersichtliche „Andockstelle" des Kniepsandes an die Insel befindet sich jedoch 50 m nordöstlich der Vordüne und liegt damit heute bereits im rückwärtigen Dünengelände. Damit befindet sich die Andockstelle bzw. die Nahtstelle zwischen Kniepsand und eigentlicher Insel etwa 200 m weiter nordöstlich als dies heute der Fall ist.

6 Zusammenfassung und Schlussfolgerung

Georadarmessungen, Bohrungen und sedimentologischen Analysen haben sich als geeignete Methodenkombination zur Rekonstruktion der Landschaftsentwicklung an der Westküste der Insel Amrum erwiesen. Auf Grundlage der gewonnenen Daten wurden zwei stratigraphische Modelle entwickelt, welche die geologisch-geomorphologischen Prozesse und Sedimentationsbedingungen im Westküstenvorfeld erklären.

Das erste Modell zeigt die Landschaftsentwicklung an der Westküste Amrums und beschreibt die Sedimentationsbedingungen, die im Vorfeld der Westküste herrschten, bevor der Kniepsand an die Insel heranwanderte. Die geologische Ausgangssituation stellt der leicht nach Westen abfallende Inselgeestkern bestehend aus Endmoränenrelikten der Saale-Eiszeit dar. Von Westen aus folgte eine Anlagerung rein mariner Sedimente (*coastal onlap*).

Auf der Landoberfläche des ertrinkenden Geestkern wurden zu Beginn der Transgression feinkörnige Sedimente eines Misch- bis Schlickwatts abgelagert.

Diese zeugen von Stillwassersedimentation und ruhigeren Strömungsbedingungen als diese heute an der hochenergetischen Westküste Amrums herrschen. Es ist davon auszugehen, dass der damals noch weit vor der Küste Amrums liegende Kniepsand eine Barriere bildete und so an der Westküste für strömungsberuhigte Sedimentationsbedingungen sorgte. Der Transgressionskontakt konnte mit Hilfe einer mittels der AAR-Methode auf 2122 +/-54 Jahren datierten Muschelschale der Gattung *Cerastoderma edule* bestimmt werden. In Übereinstimmung mit Falk (2001) wurde das Gebiet der Westküste Amrums zunehmend an der Grenze zwischen Subboreal und einsetzendem Subatlantikum von der Transgression erreicht.

Im Hangenden des Westküstenwatts folgten Ablagerungen eines Strandes, der eine ausgeprägte *ridge-and-runnel*-Topographie aufgrund von zahlreichen in das Strandpro-

fil eingeschalteten intertidalen Sedimentkörpern aufweist. Durch Sturmfluterosion am Geestkern konnten sich Brandungshohlkehlen ausbilden, die zur Kliffbildung führten. Fossile Kliffs in unterschiedlichen Höhenpositionen lassen auf unterschiedliche Meeresspiegelniveaus schließen.

Das zweite Modell beschreibt die Migration und den Andockmechanismus des der Insel im Westen vorgelagerten Kniepsandes an Amrum. Es erfolgte eine strömungsbedingte Anlagerung von Sedimenten an die „Stirn" des Kniepsandkörpers. Dies führte allmählich zur Progradation und zum Heranwandern des Kniepsandes an die Insel. Dabei schob sich der Kniepsand zum Teil auf die zuvor an der Westküste Amrums abgelagerten, stratigraphisch älteren Strand- und Vorstrandsedimente hinauf. Die einstige Andockstelle befindet im Vergleich zu heute etwa 200 m weiter im Nordosten. Eine Anlagerung des Kniepsandes an die Insel wird für die Zeitspanne zwischen 1648 und 1841 angenommen.

Mit dem Trockenfallen der entstandenen Sandflächen nach Ende der Transgression wurden die Bedingungen für die anschließende großflächige Dünenbildung geschaffen, die durch den Sedimentinput aus dem Kniepsand zunehmend generiert werden konnten. Mit fortschreitender Dünenbildung wurde das Geestkliff vor der Brandung und vor fortschreitender Abrasion geschützt und entwickelte sich allmählich zum toten Kliff.

Danksagung

Ein besonderer Dank geht an die Deutsche Bundesstiftung Umwelt (DBU) für die finanzielle Unterstützung durch ein Promotionsstipendium. Ferner danken wir den Freunden und Förderern der Goethe-Universität, der FAZIT-Stiftung, der Hermann Willkomm Stiftung, der GEOPRAX Projektförderung, dem AK Geomorphologie sowie dem DAAD für die Bereitstellung von Sach- und Reisekosten. Für die Genehmigungen für unsere Arbeiten im Gelände bedanken wir uns beim Amt für Kreisentwicklung, Bau und Umwelt/ Untere Naturschutzbehörde in Husum. Dem GEORADAR-FORUM sowie Herrn Prof. Dr. Andreas Junge (Goethe-Universität Frankfurt/ Institut für Angewandte Geophysik) sei herzlich für die Bereitstellung des benötigten GPR-Equipments gedankt. Ferner danken wir zwei anonymen Gutachtern für das Verfassen der Reviews, die uns halfen das Manuskript zu verbessern.

Literatur

Allen, J. R. L. (1982): Sedimentary structures: their character and physical basis. Vol. 1, Developments in sedimentology, Vol. 30 A. – 593 p.; Amsterdam (Elsevier).

Annan, A. P. (2001): Ground Penetrating Radar – Workshop Notes. Sensors and Software Inc., Ontario, Kanada.

Annan, A. P. (2009): Electromagnetic Principles of Ground Penetrating Radar. – In: Jol, H. M. (ed.): Ground Penetrating Radar: Theory and Applications: 3–40; Amsterdam (Elsevier).

Blindow, N., Richter, T. & Petzold, H. (2005): Bodenradar. – In: Knödel, K., Krümmel, H. & Lange, G. (eds.): Handbuch zur Erkundung des Untergrundes von Deponien und Altlasten Band 3: Geophysik: 389–424; Berlin (Springer).

Blott, S. J. & Pye, K. (2001): Gradistat: A grain size distribution and statistics package for the analyses of unconsolidated sediments. – Earth Surface Processes and Landforms, 26: 1237–1248.

Botha, G. A., Bristow, C. S., Porat, N., Duller, G., Armitage, S. J., Roberts, H. M., Clarke, B. M., Kota, M. W. & Schoeman, P. (2003): Evidence for dune reactivation from GPR profiles on the Maputaland coastal plain, South Africa. – In: Bristow, C. S. & Jol, H. M. (eds.): Ground penetrating radar in sediments. – Geological Society, London, Special Publications, 211. Brassmill Lane: 29–46.

Bristow, C. S. (2009): Ground penetrating radar in aeolian dune sands. – In: Jol, H. M. (ed.): Ground Penetrating Radar: Theory and Applications: 273–297; Oxford (Elsevier).

Bristow, C. S., Augustinus, P. C., Wallis, I. C., Jol, H. M. & Rhodes, E. J. (2010a): Investigation of the age and migration of reversing dunes in Antarctica using GPR and OSL, with implications for GPR on Mars. – Earth and Planetary Science Letters, 289: 30–42.

Bristow, C. S., Bailey, S. D. & Lancaster, N. (2000a): The sedimentary structure of linear sand dunes. – Nature, 406: 56–59.

Bristow, C. S., Chroston, P. N. & Bailey, S. D. (2000b): The structure and development of foredunes on a locally prograding coast: insights from ground-penetrating radar surveys, Norfolk, UK. – Sedimentology, 47 (5): 923–944.

Bristow, C. S., Jol, H. M., Augustinus, P. & Wallis, I. (2010b): Slipface whaleback dunes in a polar desert, Victoria Valley, Antarctica: Insights from ground penetrating radar. – Geomorphology, 114: 361–372.

Bristow, C. S. & Pucillo, K. (2006): Quantifying rates of coastal progradation from sediment volume using GPR and OSL: the Holocene fill of Guichen Bay, south-east South Australia. – Sedimentology, 53 (4): 769–788.

Bristow, C. S., Pugh, J. & Goodall, T. (1996): Internal structure of aeolian dunes in Abu Dhabi determined using ground-penetrating radar. – Sedimentology, 43 (6): 995–1003.

Campbell, C. V. (1967): Lamina, laminaset, bed and bedset. – Sedimentology, 8: 7–26.

Catuneanu, O. (2002): Sequence stratigraphy of clastic systems: concepts, merits, and pitfalls. – Journal of African Earth Sciences, 35: 1–43.

Danckwerth, C. D. (1652): Die Landkarten des Johann Mejer, Husum, aus der neuen Landschaftsbeschreibung der zwei Herzogtümer Schleswig und Holstein von Casper David Danckwerth 1652, Hamburg-Bergedorf 1963 (Reprint).

Davis, R. A. (1992): Depositional Systems: an introduction to Sedimentology and Stratigraphie. – Prentice Hall, Englewood Cliffs, New Jersey: 591 p.

Demarchi, B., Williams, M. G., Milner, N., Russell, N., Bailey, G. & Penkman, K. (2011): Amino acid racemization dating of marine shells: a mound of possibilities. – Quaternary International, 239: 114–124.

Emery, D. & Myers, K. (1996): Sequence Stratigraphy. – 297 p.; Oxford (Blackwell Science Ltd).

Falk, G. C. (2001): Die Paläogeomorphologie ausgewählter Standorte der schleswig-holsteinischen Nordseeküste im Früh- und Mittelholozän. – Dissertation, Universität Berlin: 171 S.

Fisher, S. C., Steward, R. R. & Jol, H. M. (1996): Ground-penetrating radar (GPR) data enhancement using seismic techniques. – Journal of Environmental Engineering & Geophysics, 1: 89–96.

FitzGerald, D. M. (2005): Tidal Inlets. – In: Schwartz, M. L. (ed.): Encyclopedia of Coastal Science: 958–965; (Springer).

Folk, R. L. & Ward, W. C. (1957): Brazos River bar (Texas): a study in the significance of grain size parameters. – Journal of Sedimentary Petrology, 27: 3–26.

Girardi, J. D. & Davis, D. M. (2010): Parabolic dune reactivation and migration at Napeague, NY, USA: Insights from aerial and GPR imagery. – Geomorphology, 114: 530–541.

Goodfriend, G. A. (1987): Chronostratigraphic studies of sediments in the Negev Desert, using amino acid epimerization analysis of land snail shells. – Quaternary Research, 28: 374–392.

Gray, J. S. & Elliott, M. (2009): Ecology of marine sediments: from science to management. – 225 p.; Oxford, New York (Oxford University Press).

Greenwood, B. (2005): Bars. – In: Schwartz, M. L. (ed.): Encyclopedia of Coastal Science: 120–129 ; (Springer).

Gripp, K. (1968): Zur jüngsten Erdgeschichte von Hörnum / Sylt und Amrum mit einer Übersicht über die Entstehung der Dünen in Nordfriesland. – Die Küste, 16: 76–117.

Hansen, C. P. (1845): Die Insel Sylt in geschichtlicher und statistischer Hinsicht. – Langhoffsche Buchdruckerei, 203 S.

Hanssen, G. (1835): Statistische Mitteilungen über nordfriesische Distrikte. – Neues Staatsbürgerliches Magazin, Bd. 3, Schleswig.

Harari, Z. (1996): Ground-penetrating radar (GPR) for imaging stratigraphic features and groundwater in sand dunes. – Journal of Applied Geophysics, 36: 43–52.

Hassenpflug, W. (1985): Die Vielfalt der Küstenfomen im Überblick. – In: Hassenpflug, W., Kortum, G., Newig, J., Pollex, W., & Schmidtke,

K. (eds.): An Nord- und Ostsee. Schleswig-Holsteins Küsten: 7–47; Husum (Husum Druck- und Verlagsgesellschaft).

Hayes, M. O. (1980): General morphology and sediment patterns in tidal inlets. – Sedimentary Geology, 26: 139–156.

Jackson, D. W. T., Anfuso, G. & Lynch, K. (2007): Swash bar dynamics on a high-energy mesotidal beach. – Journal of Coastal Research, 50: 738–745.

Jakobsen, P. & Overgaard, T. (2002): Georadar facies and glaciotectonic structures in ice marginal deposits, northwest Zealand, Denmark. – Quaternary Science Reviews, 21: 917–927.

Johannsen, C. (1861): Die Insel Amrum. – In: Jahrbuch für die Landeskunde Schleswig-Holstein, Bd. 4, Schleswig.

Johannsen, C. (1867): Das Westschleswigsche Küstenland im 13. und 14. Jahrhundert und die Johann Meyer'schen Karten des alten Nordfrieslands vom Jahre 1240. – Schleswig.

Jol, H. M. & Bristow, C. S. (2003): GPR in sediments: advice on data collection, basic processing and interpretation, a good practice guide. – In: Bristow, C.S. & Jol, H. M. (eds.): Ground penetrating radar in sediments. Geological Society, London, Special Publications, 211, pp. 9–27.

Jol, H. M. & Smith, D. G. (1991): Ground-penetrating radar of northern lacustrine deltas. – Canadian Journal of Earth Sciences, 28: 1939–1947.

Jessen, O. (1914): Morphologische Beobachtungen an den Dünen von Amrum, Sylt und Röm. – Landeskundliche Forschungen 21.

Jessen, O. (1932): Die postdiluviale Entwicklung Amrums und seine subfossilen und rezenten Muschelpflaster. – In: Jahrbuch der Preuß. Geolog. Landesanstalt zu Berlin, 53: 1–69.

Kersten, K. (1969): Die Vorzeit der Insel Amrum. – In: Hansen, M. & Hansen, N. (eds.): Amrum: Geschichte und Gestalt einer Insel: 7–11; Itzehoe-Münsterdorf (Hansen & Hansen).

Köster, R. (1998):Wattsedimente. – In: Umweltatlas Wattenmeer, Band 1: Nordfriesisches und Dithmarscher Wattenmeer. – 270 S.; Stuttgart (Eugen Ulmer).

Krause, A. (1913): Die Insel Amrum: Eine Landeskunde. – In: Ule, W. (eds.): Geographische Arbeiten. – 88 S.; Stuttgart (Strecker & Schröder).

Lang, A. W. (1973): Historisches Seekartenwerk der Deutschen Bucht. – Neumünster (Wachholtz).

McKee, E. D. & Weir, G. W. (1953): Terminology for stratification and cross-stratification in sedimentary rocks. – Bull. Geol. Soc. Am., 64: 381–390.

Meier, O. G. (1987): Die Naturschutzgebiete auf Sylt und Amrum. – 147 S.; Heide, Holstein (Boyens & Co).

Meyn, L. (1876): Geognostische Beschreibung der Insel Sylt und ihrer Umgebung. – Abhandlungen zur geologischen Spezialkarte von Preußen I (4), Berlin, 74 S.

Miall, A. D. (1991): Hierarchies of architectural units in terrigenous clastic rocks, and their relationship to sedimentation rate. In: Miall, A. D. and Tayler, N., (eds.): The tree-dimensional facies architecture of terrigenous clastic sediments and its implications for hydrocarbon discovery and recovery. Concepts in Sedimentology and Palaeontology, Vol. 3. Tulsa, OK., SEPM: pp. 6–12.

Mitchum, R. M., Vail, P. R. & Sangree, J. B. (1977): Stratigraphic interpretation of seismic reflection patterns in depositional sequences. – In: Payton, C. E. (ed.): Seismic stratigraphy: applications to Hydrocarbon Exploration. AAPG Mem. 16: 117–123.

Müller & Fischer (1937): Amrum. Das Wasserwesen an der schleswig-holsteinischen Nordseeküste. – Teil II: Die Inseln, Band 5. – 237 S.; Berlin (Dietrich Reimer).

Murray-Wallace, C. V. & Belperio, A. P. (1994): Identification of remanié fossils using amino acid racemisation. – Alcheringa, 18: 219–227.

Neal, A. (2004): Ground-penetrating radar and its use in sedimentology: principles, problems and progress. – Earth-Science Reviews, 66: 261–330.

Ott, J. (1996): Meereskunde: Einführung in die Geographie und Biologie der Ozeane. – 2. Aufl. 424 S.; Stuttgart (UTB).

Payton, C. E. (1977): Seismic Stratigraphy – Applications of Hydrocarbon Exploration, American Association of Petroleum Geologists, Tulsa, Oklahoma, Memories. 16.

Pedersen, K. & Clemmensen, L. B. (2005): Unveiling past aeolian landscapes: A ground penetrating radar survey of a Holocene coastal dunefield system, Thy, Denmark. – Sedimentary Geology, 177: 57 –86.

Pott, R. (2003): Die Nordsee: Eine Natur- und Kulturgeschichte. –339 S.; München (C. H. Beck).

Quedens, G. (2008): Amrum. 23. Aufl. – 144 S. (Breklumer Verlag)

Remde, F. (1972): Amrum. Ein Beitrag zur Genese und Struktur einer Inselsiedlung. Dissertation, Wilhelms-Universität, Münster: 181 S.

Schäfer, A. (2005): Klastische Sedimente. Fazies und Sequenzstratigraphie. 1. Aufl. 414 S.; München (Elsevier/ Spektrum).

Schwartz, M. L. (2005): Encyclopedia of Coastal Science. – 1211 p.; Dordrecht (Springer).

Sindowski, K.-H. (1973): Das ostfriesische Küstengebiet: Inseln, Watten und Marschen.– Sammlung Geologischer Führer 57. – 162 S.; Berlin, Stuttgart (Borntraeger).

Sindowski, K.-H. (1979): Zwischen Jadebusen und Unterelbe. – Sammlung Geologischer Führer 66. – 145 S.; Berlin, Stuttgart (Borntraeger).

Sommer, U. (2005): Biologische Meereskunde. – 2. Aufl. – 412 S.; Berlin, Heidelberg (Springer).

Stolt, R. H. (1978): Migration by Fourier transform. – Geophysics, 43: 23–48.

Tanner, W. F. (1995): Origin of beach ridges and swales. – Marine Geology, 129: 149–161.

Tillmann, T. & Wunderlich, J. (2011a): Facies and Development of a Holocene Barrier Spit (Southern Sylt/ German North Sea). Proceedings of the 6th International Workshop on Advanced Ground Penetrating Radar (IWAGPR 2011 June 22–24, 2011, Aachen, Germany): pp. 188–194.

Tillmann, T. & Wunderlich, J. (2011b): Genese eines Strandhakens am Beispiel der Hörnum-Odde (Süd-Sylt): Untersuchungen des oberflächennahen Untergrundes durch die Kombination von geophysikalischen und sedimentologischen Methoden. In: Karius, V., Hadler, H., Deicke, M., von Eynatten, H., Brückner, H. & Vött, A. (eds.): Dynamische Küsten: Grundlagen, Zusammenhänge und Auswirkungen im Spiegel angewandter Küstenforschung. – Coastline Reports, 17: 177–190.

Tillmann, T. & Wunderlich, J. (2012): Ground-penetrating radar in coastal environments: Examples from the islands Sylt and Amrum. – Bremer Beiträge zur Geographie und Raumplanung, 44: 60–76.

Tillmann, T. & Wunderlich, J. (2013): Barrier rollover and spit accretion due to the combined action of storm surge induced washover events and progradation: Insights from ground-penetrating radar surveys and sedimentological data. – Journal of Coastal Research, Special Issue No 65 (1): 600–605.

Tucker, M. E: (1985): Einführung in die Sedimentpetrologie. – 265 S.; Stuttgart (Enke).

van Dam, R. L. (2012): Landform characterization using geophysics – recent advances, applications, and emerging tools. – Geomorphology, 137 (1): 57–73.

van Overmeeren, R. A. (1998): Radar facies of unconsolidated sediments in The Netherlands: a radar stratigraphy interpretation method for hydrogeology. – Journal of Applied Geophysics, 40: 1–18.

Voigt, H. (1969): Die Insel Amrum: Landschaft und Entwicklung. – In: Hansen, M. & Hansen N. (eds.): Sylt: Geschichte und Gestalt einer Insel: 11–34; Itzehoe (Hansen & Hansen).

Zausig, F. (1939): Veränderungen der Küsten, Sände, Tiefs und Watten der Gewässer um Sylt (Nordsee) nach alten Seekarten, Seehandbüchern und Landkarten seit 1585. – Geologie der Meere und Binnengewässer, 3 (4): 401–505.

Ziehe, D. (2009): Aminosäure-D/L-Verhältnisse in biogenem Carbonaten als Schlüssel zur Datierung holozäner Sedimentationsvorgänge im norddeutschen Küstenraum. – Dissertation, Carl von Ossietzky Universität Oldenburg: 219 S.

E&G Quaternary Science Journal
Volume 62 / Number 2 / 2013 / 120–126 / DOI 10.3285/eg.62.1.03
www.quaternary-science.net

GEOZON SCIENCE MEDIA
ISSN 0424-7116

The inventories of archaeological horizons 4 and 3 and the loess section of Grub/Kranawetberg, a Gravettian site in Lower Austria

Walpurga Antl

How to cite: Antl, W. (2013): The inventories of archaeoligical horizons 4 and 3 and the loess section of Grub/Kranawetberg, a Gravettian site in Lower Austria. – E&G Quaternary Science Journal, 62 (2): 120–126. DOI: 10.3285/eg.62.2.02

Abstract: Excavations at the Gravettian site Grub/Kranawetberg from 1993 to 2011 exposed four archaeological horizons (AH) separated by sterile loess deposits. The lowest AH 4 contains a number of features, consisting of two hearths which both are surrounded by small pits. The overlying AH3 is separated from AH4 by 8 to 10 cm of loess. In AH3 there are no features. Above AH3 there are two more AHs (AH2 and AH1) with significantly lower find densities.
Chronologically both AH4 and 3 are very close (Antl-Weiser et al., 2010) but there are big differences in the assemblages and the presence/absence of features. According to the present state of research the assemblages of the two AHs seem to reflect the presence of different groups using this territory possibly under changing environmental conditions. In 2010 and 2011 a series of samples for an IRSL- and OSL-dating program (Zöller et al., this volume) has been collected from two deep trenches in the east of the excavated area. Results suggest an occupation of AH4 to AH1 between 30ka BP and 27ka BP. The site gives an insight not only into an important part of the cultural development before the Last Glacial Maximum but possibly also into climatic changes during a longer time span of the Upper Pleniglacial period in this part of Austria.

Das Inventar der archäologischen Horizonte 4 und 3 und das Lössprofil von Grub/Kranawetberg, einem Lagerplatz des Gravettien in Niederösterreich

Kurzfassung: Die Ausgrabungen an der Gravettienfundstelle Grub/Kranawetberg bei Stillfried erbrachten vier archäologische Horizonte. Der unterste (AH4) enthält zwei Herdstellen, die beide von einer Reihe von Grübchen umgeben sind. Der darauf folgende Horizont (AH3) ist durch eine 8–10 cm mächtige Lössschicht von AH4 getrennt. In AH3 gibt es keine evidenten Strukturen. Über AH3 liegen zwei weitere archäologische Horizonte mit lediglich einigen verstreuten Funden. Chronologisch sind beide Horizonte zwar nahe beisammen, sie sind aber sehr unterschiedlich, was die Strukturen und das Inventar angeht. Zum gegenwärtigen Zeitpunkt scheinen die beiden Horizonte die Anwesenheit von zwei Gruppen widerzuspiegeln, die dieses Gebiet möglicherweise unter sich ändernden Umweltbedingen nutzten.
In den Jahren 2010 und 2011 wurde eine Reihe von Proben für IRSL und OSL Datierungen an zwei langen Profilen im Osten der ausgegrabenen Fläche genommen. So gesehen gibt der Platz nicht nur Einblick in einen bedeutenden Abschnitt der kulturellen Entwicklung vor dem Kältemaximum der letzten Eiszeit, sondern auch in die klimatischen Veränderungen des Hochglazial in diesem Teil von Österreich.

Keywords: *Gravettian, cultural changes, raw material, settlement structures, personal adornments*

Address of author: **Dr. Walpurga Antl**, Prähistorische Abteilung, Naturhistorisches Museum Wien, Burgring 7, A-1010 Wien, walpurga.antl@nhm-wien.ac.at

1 Introduction

After surface collections of Palaeolithic artefacts on the fields of the Kranawetberg, a hill west of the village Grub near Stillfried in the March valley in the northeast of Lower Austria (Fig.1), the Prehistoric Department of the Natural History Museum Vienna started archaeological investigations in 1993 (Antl et al. 1997). From 1993 to 2011 excavations at the site Grub/Kranawetberg exposed two different areas of activity (Antl & Fladerer 2004). First, from 1993 to 1995, a bone accumulation with remains of mammoth, rhino, giant deer, wild horse and reindeer was excavated (Antl et al. 1997; Bosch et al. 2012). Then, approximately 20 metres to the east an area with hearths and high find density was exposed (Antl et al. 1997; Antl & Fladerer 2004). The focus of this paper shall be put on this second area.

2 Methods

Fieldwork methods: First, we removed the recent top soil (30 to 40cm) and 120 to 180 cm of sterile loess covering the deposits containing the AHs 1 to 4. Then, AHs were excavated following the lithostratigraphic boundaries. All objects larger than 0.5cm were recorded three-dimensionally, i.e. piece-plotted. Until 2001, this was done manually by drawing maps in scales of 1:10 and 1:5 to record the location, inclination and position (dorsal or ventral down) of all find

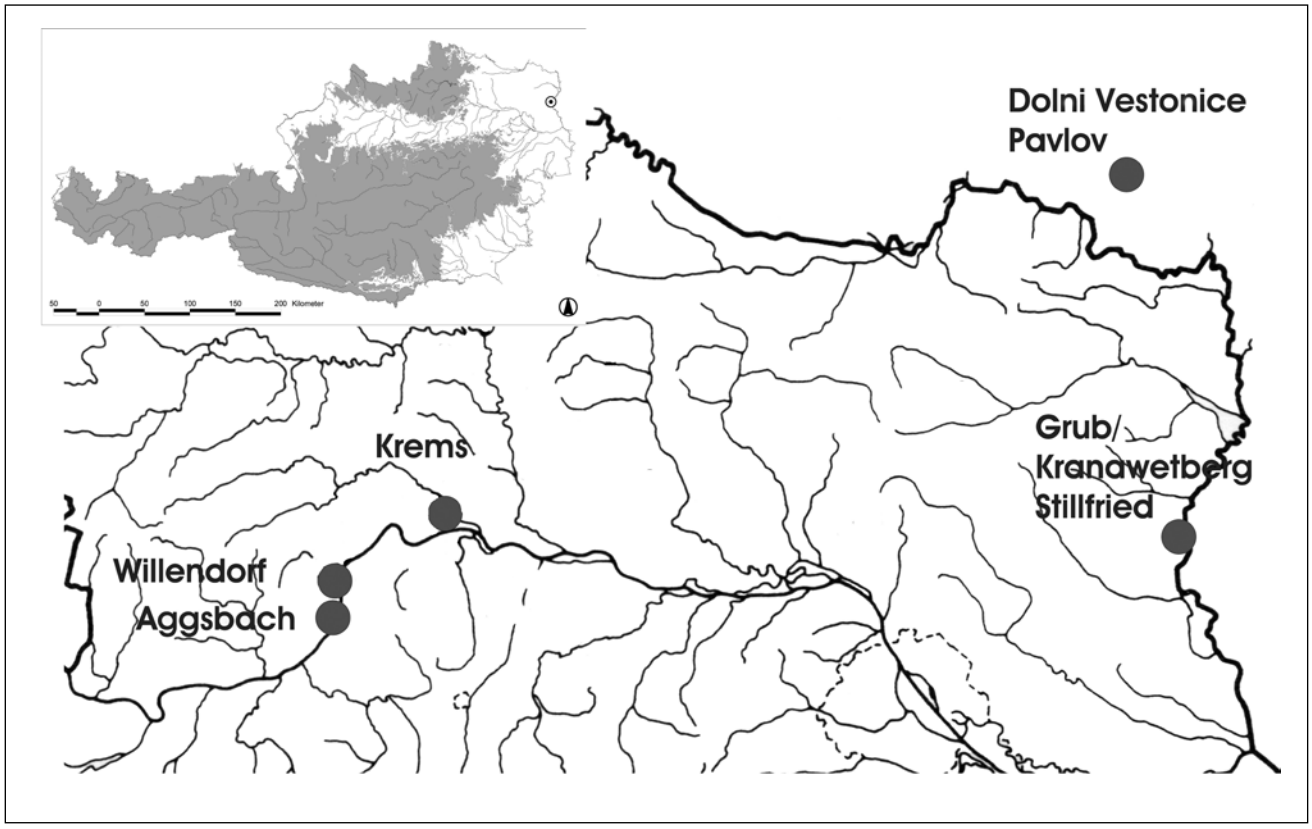

Fig. 1: Map of Austria with the geographical position of Grub/Kranawetberg (small inset) and a more detailed view to the north of Lower Austria and Southern Moravia with the geographical position of Grub/Kranawetberg and other sites mentioned in the text.

Abb. 1: Österreichkarte mit der geographischen Lage von Grub/Kranawetberg (kleines Rechteck) und eine Detailansicht des nördlichen Niederösterreich und Südmähren mit der Lage von Grub/Kranawetberg und anderen im Text erwähnten Fundstellen.

categories. Starting in 2002, we implemented a digital documentation system using totalstations, a field database, and rectified photos (Nigst et al. 2004; 2010). The final product is an interactive database and GIS of the site. Additionally to the digital excavation documentation system, we kept a separate diary (by the archaeologist in charge of the excavation) containing various sorts of further remarks, drawings with the position of measured points, finds in special context and instant remarks concerning structure of the sediment and discussion of the situation as a whole. Parallel to the measurements minutes are kept containing the reference points and the degree of possible deviations. All sediment removed is collected per quarter-square meter and wet-sieved with a grid size of 1 mm.

Laboratory methods: As to the lithic raw material microscopic analysis of a reference sample of one thousand pieces was carried out by Alexander Binsteiner. As a first step to a detailed technological analysis a preliminary type list of the lithic material has been established. As far as the fauna is concerned a detailed analysis of the faunal remains of the bone accumulation was made by F. Fladerer and M. Bosch (Antl-Weiser, Fladerer, Nigst & Verpoorte 2010; Bosch, Nigst , Fladerer & Antl-Weiser 2012). The malacological analysis was based on sediment samples from series at the western periphery of the settlement structures. Different types of molluscs and their preferred habitat were described and the number of each species was listed by F. Stadler (Antl-Weiser, Fladerer, Peticzka, Stadler & Verginis 1997).

In the East of O16 and O19 series of sediment samples from 1.5 to 4m below surface were taken (Fig. 2). The samples for IRSL and OSL dating were taken parallel to the sediment samples in O16 and O19.

3 Results

Within the area with hearths four AHs can be distinguished. Most of the archaeological material is concentrated within AH 4 and 3. Both AHs are clearly separated by 8 to 10 cm of loess; only in the area of hearth II (Fig.3) AH 4 and 3 are extremely close.

All features like hearths and pits belong to AH4. Hearth I and hearth II show repeated use and seem to be covered by AH4 (Fig. 4). As the distribution of finds in AH4 corresponds to the distribution of features (Nigst, 2003; 2004; Nigst & Antl-Weiser 2012) it is clear that the features and AH4 constitute a unit but it will be a matter of further discussions in which way post-depositional processes possibly contributed to this impression. Above the shallow depression of hearth II there are several rather big bones on the top of AH4, which were not completely covered by loess and therefore must have been visible during the initial occupation of AH3.

Both hearths are surrounded by a series of small pits. On the bottom of these pits there are often rather big stone tools or stones with traces of grinding. The areas with pits are approximately 5 to 6 m in diameter and about 7.5 to 8 m apart from each other (Fig. 3). Between the two concentra-

Fig. 2: Grub/Kranawetberg: Sequence of AHs and loess in O19 with sample locations for pollen analysis on the left and sedimentological analysis on the right.

Abb. 2: Ostprofil in O19 mit Spuren der Probennahme für Pollenanalyse links und für Sedimentanalyse rechts.

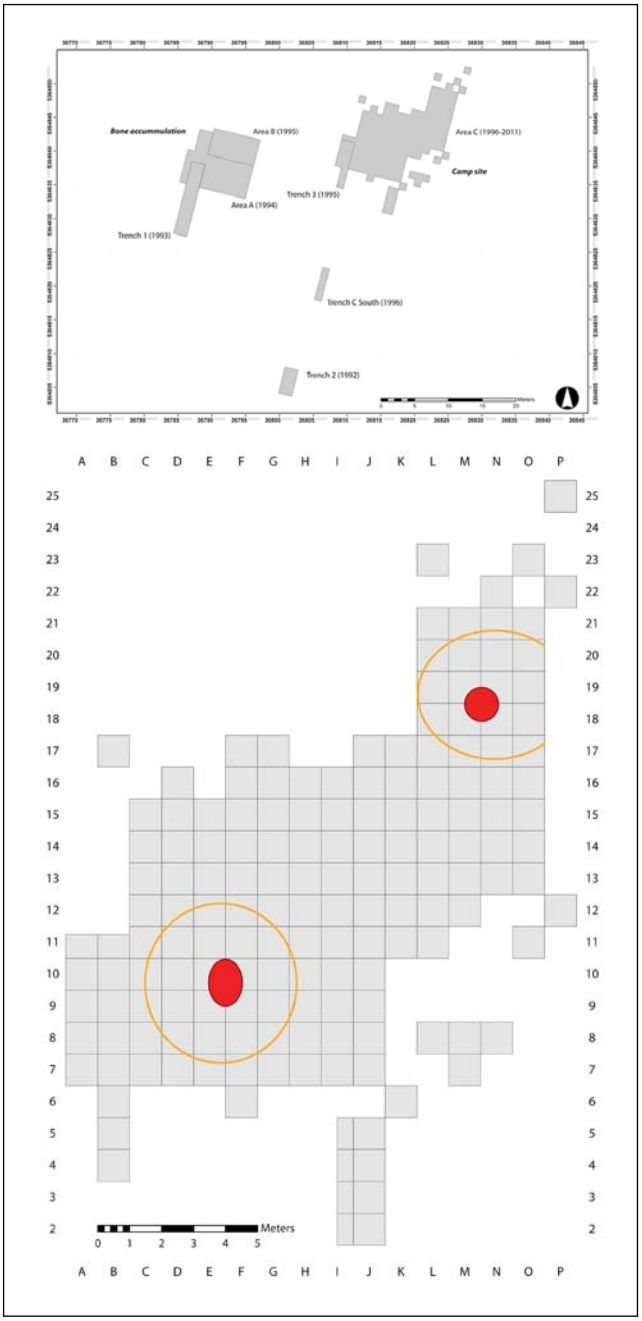

Fig. 3: Grub/Kranawetberg: General map of the excavated area (small inset) with a more detailed view of the area with settlement structures after Ph. R. Nigst, showing the two hearths (in red) and the area with pits around the hearths (in orange).

Abb. 3: Übersichtsplan des ausgegrabenen Bereiches (kleines Rechteck) mit einer Detailansicht des Bereiches mit den Siedlungsstrukturen nach Ph. R. Nigst, die die beiden Feuerstellen (Rot) und den Bereich der Grübchen um die Feuerstellen (Orange) zeigt.

tions of pits there is a continuous high density of finds. The base of AH4 is slightly folded in this area as a consequence of periglacial processes. Apart from the hearths different traces of fire as burned sediment and big pieces of charcoal burned *in situ* could be detected, especially in the north and northwest of the eastern concentration.

Around hearth I in the west of the excavated area a sudden decrease of find density has been observed 0.5 to 1 m outside the pits to the north, west and south, whereas the find density around hearth II is only decreasing to the north. South of the pits of hearth II there is an area with a lower find density than in the concentration itself. The eastern and western border of this concentration has not been fully excavated. In some places AH4 is separated by thin lenses of loess into two small layers which indicates that AH4 consists at least of two occupations, the hearths even show up to four periods of use, which is clearly visible by the superposition of four different phases of firing.

The centre of overlying AH3 is only 2 m to the NW of AH4's hearth II. In AH3 there are no evident structures. Below the centre of AH3 there are traces of fire like burnt bones, large (4–5 cm) pieces of charcoal and patches of

E&G / Vol. 62 / No. 2 / 2013 / 120–126 / DOI 10.3285/eg.62.2.03 / © Authors / Creative Commons Attribution License

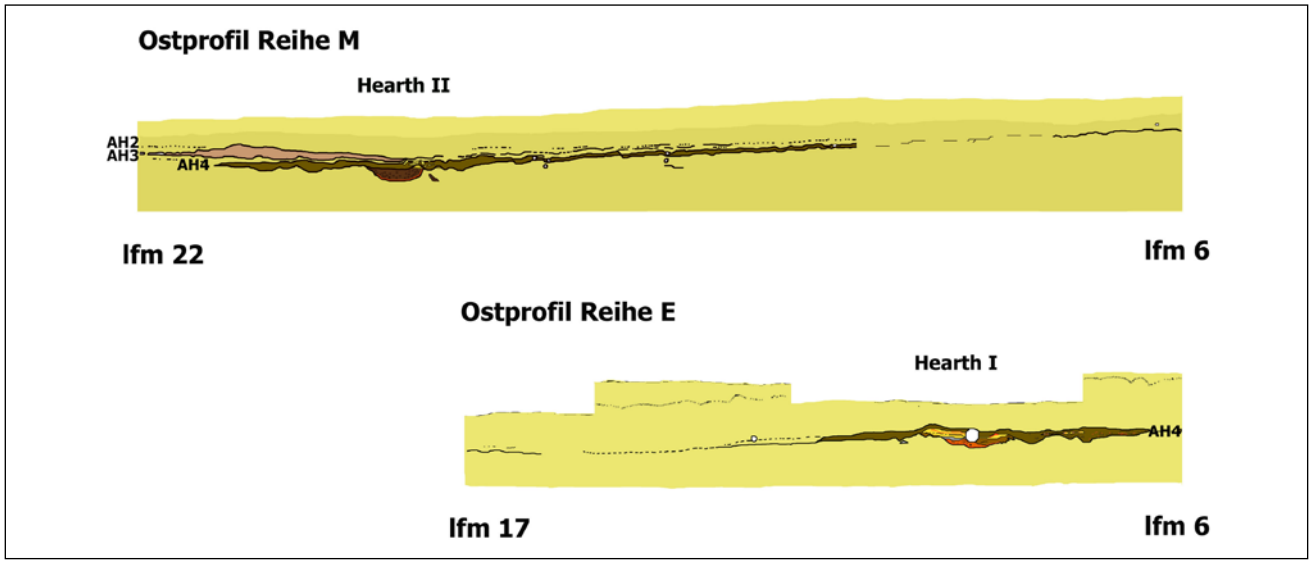

Fig. 4: Grub/Kranawetberg: Section through hearth I in the east of row E from south to north and through hearth II in the east of row M from south to north.

Abb. 4: Schnitt durch Feuerstelle I, Ostprofil Reihe E von Süd nach Nord und Schnitt durch Feuerstelle II, Ostprofil Reihe M von Süd nach Nord.

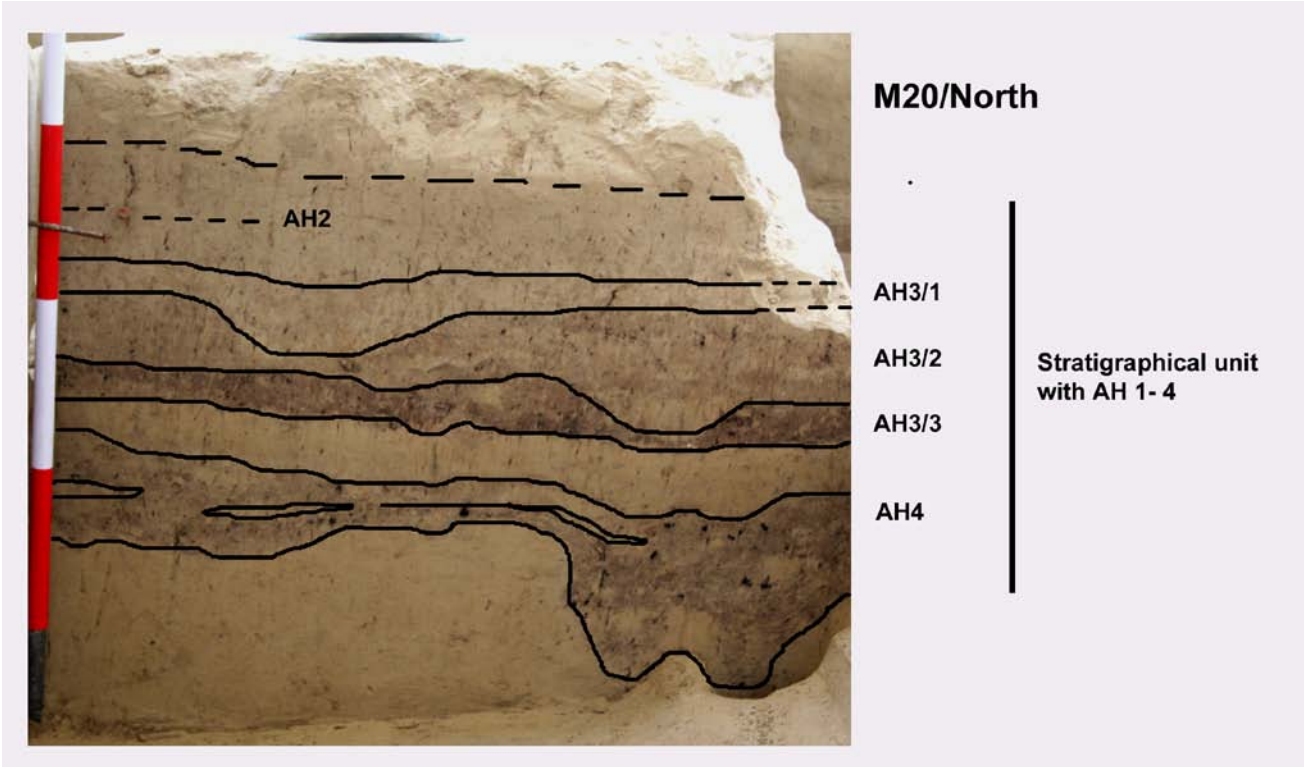

Fig. 5: Grub/Kranawetberg: North-section of square M20 showing the stratigraphic positions of AH1 to AH4.

Abb. 5: Nordprofil von M20 mit der stratigraphischen Lage von AH 1–4.

burnt sediment, but there no structured hearths comparable to those of AH4 have been found. The occupation of AH3 covers the whole excavated area. In the west (row A to G) (Fig. 3) AH3 is a horizon with only some scattered bones and artefacts. From row I (Fig. 3) to the east and especially to the northeast find density in AH3 increases. AH3 is associated with a clearly visible light brown horizon, which can be distinguished from the loess, from row J to the east and row 10 to the north (Fig.3). Within square M21 (Fig. 3), AH3 is about 16 cm thick and decreases dramatically in thickness in M22 to approx. 5 cm. In M21 AH3 can be divided into three different events of occupation (Fig. 5).

Above AH3 there are two more archaeological horizons (AH2 and AH1) with only some scattered finds. These horizons yielded individual finds in the western part of the excavated area, e.g. a fragmented mammoth tusk in square G11. In the east (squares L-O/19-21) especially AH2 yielded a more regular scatter of finds. Above AH1, the sediment structure changes considerably. Whereas the layer containing the archaeological horizons with a maximum thickness of 0.8 m shows many traces of organic activity the loess above is characterized by a brighter colour and higher density of the sediment.

Tab. I: Grub/Kranawetberg: radiocarbon dates for AH 4 and 3. Abbreviations: AH: Archaeological Horizon, lab.nr.: radiocarbon dating laboratory number.

Tab. I: Grub/Kranawetberg: Radiokohlenstoff-Alter für AH4 und 3. Abkürzungen: AH: Archäologischer Horizont, lab.nr.: Labornummer des Radiokohlenstoff-Datierungslabors.

AH	material	pre-treatment	lab.nr.	^{14}C date	1 sigma	reference
AH3	charcoal	ABA	GrA-28183	24,780	+/-140 BP	Antl-Weiser et al., 2010
AH3	charcoal	ABA	GrA-28184	25,640	+/-160 BP	Antl-Weiser et al., 2010
AH3	charcoal	ABA	GrA-28185	25,010	+/-150 BP	Antl-Weiser et al., 2010
AH4/hearth I	charcoal	ABA	GrA-9066	24,830	+/-230 BP	Antl-Weiser et al., 2010
AH4/post hole	charcoal	ABA	GrA-9065	24,930	+/-240 BP	Antl-Weiser et al., 2010
AH4	charcoal	ABA	GrA-9063	24,620	+/-230 BP	Antl-Weiser et al., 2010
AH4	charcoal	ABA	VERA-364	25,300	+/- 90 BP	Antl-Weiser et al., 2010

The radiocarbon dates suggest that AH4 and AH3 had been deposited within a relatively short interval (Table I). The above mentioned list shows that the dates of AH4 and AH3 overlap clearly. Statistically the dates of AH3 appear even older than those of AH4. This is partly due to one rather old date from AH3, which is the oldest one of all. One reason for this discrepancy might be found in the relatively small number of items dated so far. Also the use of collected wood of different ages cannot be excluded and has a strong effect on a small series. Nevertheless on the base of given data we have to expect a rather short time span between the two horizons. In spite of the rapid succession of AH4 and AH3 there are big differences concerning the archaeological material of the two AHs. Apart from differences concerning the presence/absence of features, the raw material used for lithic artifacts is completely different. From AH4 we have mainly flints and cherts whereas from AH3 radiolarites are the most abundant raw material type. AH4 and AH3 of Grub Kranawetberg yielded more than 1000 formal lithic tool types, between 4000 and 5000 blades and bladelets and thousands of flakes. At the present state of analysis it is not yet possible to give a detailed list of formal tools of each AH. This is due to the fact that between 1995 and 2001 artefacts had been drawn manually on plans which are not yet fully digitalized. Nevertheless an estimate of the distribution of formal tools from AH1 to AH4 might already give an impression of the high density of finds in AH4 (Fig. 6). Among the formal tool types of AH4, microgravettes are dominant; in AH3 there are mainly backed bladelets and small bladelets with fine retouching. Two complete and one fragmented notched backed point have been excavated in AH4.

Until now we found 245 beads and pendants of ivory, which are restricted to AH4. The number of ivory objects is still incomplete because the majority of the tiny beads (most of them 6–8 mm) was found within the remains of the sediment after wet sieving. As there are still a lot of samples yet to be sieved and a big amount of remains to be separated into the different find categories (silex, stone, bones, grains of coloured material, charcoal etc. which are smaller than 0.5 cm) a detailed list of bead types at the present state of analysis would be premature. Personal adornments made of mollusc shells (174 pieces) as well as remains of colour are abundant in both AH3 and AH4. Also tools of antler and bone are present in AH4 as well as in AH3. Worked pieces of ivory are more typical for AH4. Although the analysis of the faunal remains has yet to come, it seems that there is a great abundance of mammoth in AH4 and of reindeer and horse in AH3.

4 Discussion

Chronologically both AH4 and AH3 are very close (Antl-Weiser et al. 2010), but there are big differences concerning structure and contents. Compared to the settlement structures in AH4 we have only a concentration of finds with a clear centre in AH3. There are evident differences in raw material procurement and in personal adornments. Remains of mammoth seem more abundant in AH4 but detailed zooarchaeological analyses concerning preferred game have yet to be conducted.

First analyses of spatial organization around hearth I (Nigst 2004; Nigst & Antl 2012a; 2012b) showed different zones of artefact distribution. One zone with a high density of artefacts was interpreted as the place of a dwelling while the other zones were interpreted as the periphery of it. This interpretation was also supported by the distribution of pits around hearth I. As to hearth II there are similar structures, which have yet to be analyzed. Comparable structures with central hearths and pits have been excavated in Dolní Věstonice II, occupation unit 3 (Southern Moravia) (Svoboda 2003; Nigst & Antl 2012) and during recent excavations at Krems Wachtberg around the big central hearth (Lower Austria) (Einwögerer, et al. 2006; Einwögerer 2010; Nigst & Antl 2012).

A very interesting aspect is that there is evidence for AH4 to be contemporaneous with the bone accumulation (Bosch 2009; Bosch et al. 2012). This is based on the fact that an upper left first molar of mammoth, found in the AH4, belongs to the same maxilla as a right upper first molar found at the bone accumulation. This observation fits very well with the intense use of ivory in AH4.

E&G / Vol. 62 / No. 2 / 2013 / 120–126 / DOI 10.3285/eg.62.2.03 / © Authors / Creative Commons Attribution License

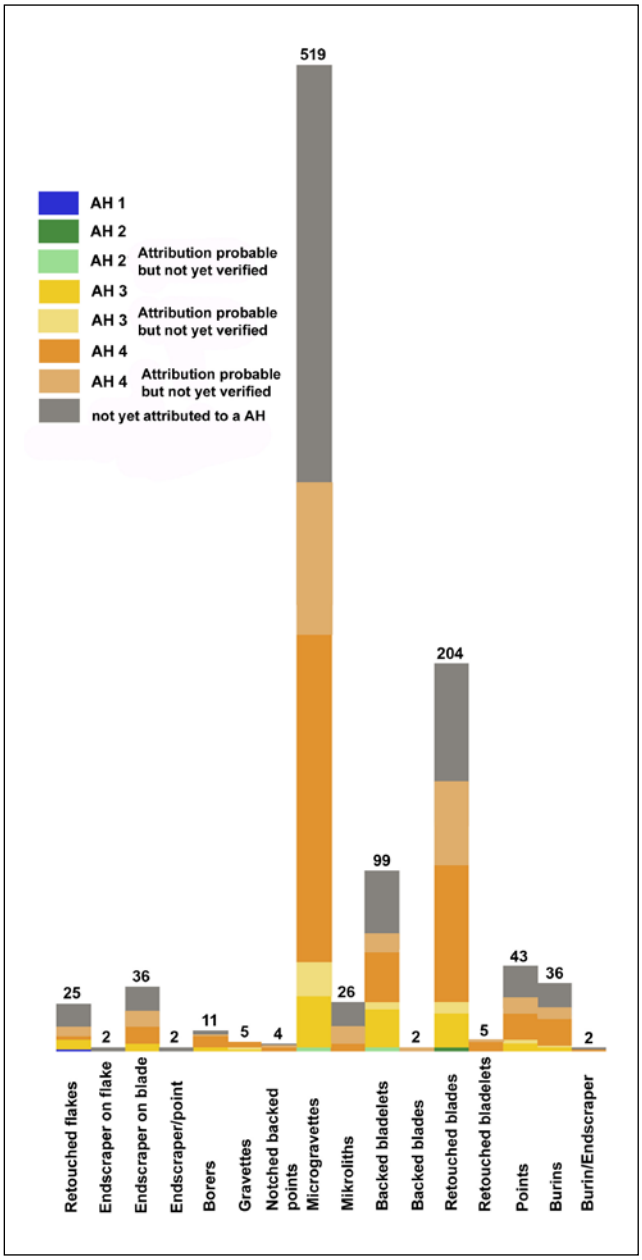

Fig. 6: Grub/Kranawetberg: Distribution of formal lithic tool types from AH1 to AH4.

Abb. 6: Verteilung der retuschierten Geräte auf die archäologischen Horizonte 1–4.

The radiocarbon dates as well as the material culture of AH4 suggest a position of the occupation at the end of the Pavlovian. Apart from the lithic raw material there are also some varieties of personal adornments which support the assumption of closer connections to the north in the course of AH4's occupation, but it must be mentioned that the role of the gravels of the river March as a source of Moravian chert used by the humans occupying Grub/Kranawetberg has yet to be analyzed.

As to the lithic material of AH3, the Carpathian Mountains in the east are a possible source for the radiolarites. The nearly exclusive use of radiolarites, resembling material from the Carpathian Mountains, may indicate increased relations to the East. Having a look at the personal adornments used in AH4 and AH3, we can observe a significant change, which supports the idea that different groups of people are behind the formation of AH3 and AH4. Further analyses shall clarify the role of the site in a bigger regional context. It will be necessary to discuss to which extent the change in raw material procurement from AH4 to AH3 might correspond to a shift of population to the east at the end of the Pavlovian as has been suggested (Otte, 1993; Otte, 2004; Escutenaire et al., 1999). This shift of population as a consequence of the expansion of the Fennoscandinavian glacier and the climatic deterioration in central Europe is also being discussed by J. Svoboda (Svoboda, 2000; Svoboda, 2007) for the time after 25 ka BP.

Within the excavated area the occupations of AH2 and AH1 consist only of some scattered finds. There are some individual finds at this level in the western part of the site and a slight increase of find density in the eastern part. As we dispose of sufficient charcoal from these horizons we will be able to date these occupations in the near future. The analyses will show how near to the Last Glacial Maximum the cultural sequence from the Kranawetberg ended. The calibrated dates for the youngest sample in the profile of Zöller (Zöller et al. in this volume) from O19 (Fig. 2) support this presumption.

First malacological analyses suggest a cold climate in an environment of some bushes and trees (Antl-Weiser et al. 1997). According to F. Stadler there are indications for warmer climatic conditions shortly before the deposition of the AHs or the beginning of warmer conditions (Antl-Weiser et al. 1997; Antl et al. 2010). As warmer phases are observed at Pavlov and Willendorf II/8 (Haesarts et al. 1996; Haesaerts et al. 2004) around 25.5ka BP we can expect that warmer conditions prevailed mainly before the deposition of the AHs at Grub/Kranawetberg.

In order to examine the role of climate change during the occupations after AH4 a series of samples for sediment, pollen and mollusc analyses have been collected. Apart from samples within the geological unit containing the archaeological horizons sampling comprised a length from 150 to 37 cm below surface. In 2010 and 2011 a series of samples for IRSL- and OSL-dates have been collected there. The upper parts from surface to -150 cm were sampled in various sequences in the west of the dwelling area as well as at the bone accumulation (Antl et al. 1997, 1999). A drilling program executed by S. Verginis in 1996 in the west of the dwelling structures proved that there is at least a sequence of 7 m of loess at this place (Antl et al. 1997, 1999).

5 Conclusion

Comparing AH4 and AH3 of Grub/Kranawetberg we could observe a clear change in settlement structures, raw material procurement and personal adornments as well as some differences concerning the frequency of certain tool types. According to the present state of research the assemblages of the two AHs seem to reflect the presence of different groups using this territory possibly under changing environmental conditions, one of them showing closer contacts to the north and the other to the east. The strongest argument for the preference of the existence of different groups seems to be the clear change in personal adornments within a short period of time. Chronologically the sequence of Grub/Kranawetberg overlaps with the sequence of Willen-

dorf II starting with AH4 and AH3 with radiocarbon dates between those of AHs 8 and 9 of Willendorf II (Haesaerts et al. 1996). AH2 and AH1 of Grub/Kranawetberg are younger than Willendorf II/AH9 and thus extend the cultural sequence of the Gravettian in Lower Austria.

Combined with a thick loess deposit below the AHs Grub/Kranawetberg gives an insight not only into an important part of the cultural development before the Last Glacial Maximum but also into climate changes during a longer time span of the Upper Pleniglacial period in this part of Austria.

Acknowledgements

I would like to thank the Department of Prehistory (Natural History Museum, Vienna), the Austrian Federal Ministry of Education, Art and Cultural Affairs, the Fonds zur Förderung der Wissenschaftlichen Forschung (FWF, Austrian Science Foundation, Vienna; project n° P11.140GEO), and the Freunde des Naturhistorischen Museums Wien for funding the research excavation. Further, thanks to the municipality of Angern as well as to numerous honorary collaborators for multiple support.

I would also like to thank my reviewers for their helping comments.

References

Antl-Weiser, W., Fladerer, F. A., Peticzka, R., Stadler, F. C. & Verginis, S. (1997): Ein Lagerplatz eiszeitlicher Jäger in Grub bei Stillfried. – Archäologie Österreichs 8/1: 4–20.

Antl-Weiser, W. & Verginis, S. (u. Mitarbeit v. H. Hoffert, A. Schierhuber, T. Nichterl) (1999): Geoelektrische Untersuchungen an einem Lagerplatz des Gravettien in Grub bei Stillfried (Niederösterreich). – Préhistoire Européenne 12: 59–71.

Antl, W. & Fladerer, F. (2004): Outlook to the East. The 25 KY BP Gravettian Grub/Kranawetberg campsite (Lower Austria) – In: The Gravettian along the Danube. – Proceedings of the Mikulov Conference, 20.–21. November 2002, Institute of Archeology, AS ČR, Brno, The Dolní Věstonice Studies, Vol. 11: 116–130.

Antl-Weiser, W., Fladerer, F. A., Nigst, Ph. R., Verpoorte A. (2010): Grub/Kranawetberg (Lower Austria) – Insights into a Gravettian micro-region in Eastern Austria. – In: Neugebauer-Maresch Ch.; Linda Owen (Eds.): New aspects of the Central and Eastern European Upper palaeolithic – methods, chronology, technology and subsistence. – MPK 72: 231–245.

Bosch, M. D. (2009): Age-at-death profiles of mammoth molars in the Mid-Upper Palaeolithic in the Middle Danube region. – MA Thesis, University of Leiden, the Netherlands.

Bosch, M. D., Nigst, Ph. R., Fladerer, F. A., Antl-Weiser, W. (2012): Humans, bones and fire: Zooarchaeological, taphonomic, and spatial analyses of a Gravettian mammoth bone accumulation at Grub-Kranawetberg (Austria). – Quaternary International 252: 109–121.

Einwögerer, T., Friesinger, H., Händel, M., Neugebauer-Maresch, CH., Simon, U., Teschler-Nicola, M. (2006): Upper Palaeolithic Infant Burials. – Nature 444: 285.

Einwögerer T. (2010): Excavations at the Krems-Wachtberg Site and the Discovery of the Infant Burials. – In: Neugebauer-Maresch Ch.; Owen, L. (Eds.): New aspects of the Central and Eastern European Upper palaeolithic – methods, chronology, technology and subsistence. – MPK 72: 273–285.

Escutenaire, C., Kozlowski, J., Sitlivy, V., Sobczyk, K. (1999): Les Chasseurs de Mammouths de la Vallée de la Vistule. Krakow-Spadzista B, un Site Gravettien à amass d´ Ossements de Mammouths. – Brüssel.

Haesaerts, P., Borziak, I., Chririca, V., Damblon, F., Koulakovska, L. (2004): Cadre stratigraphique et chronologique du Gravettien en Europe Centrale. – In: The Gravettian along the Danube. – Proceedings of the Mikulov Conference, 20.–21. November 2002, Institute of Archeology, AS CR, Brno, The Dolni Vestonice Studies, Vol. 11, 2004: 33–56.

Haesarts, P., Damblon, F., Bachner, M., Trnka, G. (1996): Revised stratigraphy and chronology of the Willendorf II sequence. – Archäologia Austriaca 80, 25–42.

Nigst, Ph. R. (2003): Fundverteilungen um Feuerstellen, die *Ring and Sector method* und Grub/Kranawetberg: eine Studie zur Analyse latenter Strukturen altsteinzeitlicher WildbeuterInnenlager. – Ungedr. Diplomarbeit Wien.

Nigst, Ph. R. (2004): Some preliminary observations on intrasite spatial patterning of Grub/Kranawetberg (1995 and 1996 area). – In: The Gravettian along the Danube. – Proceedings of the Mikulov Conference, 20.–21. November 2002, Institute of Archeology. AS ČR, Brno, The Dolní Věstonice Studies, Vol. 11, 2004: 131–141.

Nigst, Ph. R., Viola, T. B., Doneus, M., Antl-Weiser, W. (2004): Digitale Dokumentation paläolithischer Grabungen. – Archäologie Österreichs, 15/1: 36–48.

Nigst, Ph. R., Viola, B. T., Antl-Weiser, W. (2010.): Digital Documentation of Palaeolithic Excavations: A Case Study. – In: Neugebauer-Maresch, C. & Owen, L. R. (Eds.), New Aspects of the Central and Eastern European Upper Palaeolithic – methods, chronology, technology and subsistence. – Vlg. der Österreichischen Akademie der Wissenschaften, Vienna, 311–317.

Nigst, Ph. R. & Antl-Weiser, W. (2012a): Intrasite spatial organization of Grub/Kranawetberg: Methodology and interpretations – Insights into the spatial organization of Gravettian sites in Eastern Central Europe. – In: Gaudzinski-Windheuser, S., Jöris, O., Sensburg, M., Street, M., Turner, E. (Eds.), Site internal spatial organization of hunter-gatherer societies: Case studies from the European Palaeolithic and Mesolithic. – RGZM-Tagungen, Vlg. des RGZM, Mainz, 11–29.

Nigst, Ph. R. & Antl-Weiser, W. (2012b): Les structures d'occupation gravettiennes en Europe centrale: le cas de Grub/Kranawetberg, Autriche. – L'Anthropologie, 116 (5): 639–664.

Peticzka, R. & Riegler, D. (2004): Sedimentologisch-bodenkundliche Untersuchungen im Bereich Stillfried-Grub. – Beiträge zur Quartärforschung und Landschaftsökologie, Gedenkschrift zum 60. Geburtstag von Spyridon Verginis, Wien, 47–55.

Otte, M. & Noiret, P. (2004): Evolution du Gravettien au moyen Danube. – In: Svoboda, J. A. & Sedlackova, L. (Eds.): The Gravettian along the Danube. – Proceedings of the Mikulov conference, 20–21 November 2002, Dolni Vestonice Studies 11, Brno, 8–33.

Otte, M. (1993): Upper Palaeolithic Relations between Central and Eastern Europe. – In: Chapman, J. & Dolukhanov, P. (Hrsg.): Cultural Transformations and Interactions in Eastern Europe. – Worldwide Archaeology Series 6: 56–64.

Svoboda, J. (2000): The Gravettian in Moravia. – In: Roebroeks, W., Mussi, M., Svoboda, J. et al. (Hrsg.): Hunters of the Golden Age. The Mid Upper Palaeolithic of Eurasia 30.000–20.000 BP. – Leiden, 198–211.

Svoboda, J. (2003): The Gravettian in Moravia.: landscape, settlement and dwellings. – In: Vasil'ev, S. A., Soffer O., Kozlowski J. (Eds.), Perceived Landscapes and Built Environments. The cultural geography of Late Paleolithic Eurasia. – Actes du XIVme Congrès UISPP, Univerité de Liège, 2–8. Septembre 2001, Archaeopress, Oxford, BAR International Series 1122: 121–129.

Svoboda, J. (2007): The Gravettian on the middle Danube. Spécial table ronde (1er partie): Le Gravettien: entités régionales d´une paléoculture européenne, Les Eyzies, Juillet 2004. – Paléo 19: 203–220.

Svoboda, J., Bochenski, Z. M., Culikova, V., Hladilova, S., Hlozek, M., Horácek, I., Ivanov, M., Kralik, M., Novák, M., Pryor, A. E. J., Sázelová, S., Stevens, R. E., Wilczynski, J., Wojtal, P. (2011): Palaeolithic Hunting in a Southern Moravian Landscape: The Case of Milovice IV, Czech Republik. – Geoarchaeology 26, 6: 838–866.

Zöller, L., Richter, D., Masuth, St., Wunner, L., Fischer, M., Antl-Weiser, W. (2013): Luminescence chronology at the Grub-Kranawetberg site, Austria. – E&G Quaternary Science Journal (this volume).

E&G Quaternary Science Journal
Volume 62 / Number 2 / 2013 / 127–135 / DOI 10.3285/eg.62.2.04
www.quaternary-science.net

GEOZON SCIENCE MEDIA
ISSN 0424-7116

Luminescence chronology of the Grub-Kranawetberg site, Austria

Ludwig Zöller, Daniel Richter, Stefanie Masuth, Lisa Wunner, Manfred Fischer, Walpurga Antl-Weiser

How to cite: Zöller, L., Richter, D., Masuth, S., Wunner, L., Fischer, M., Antl-Weiser, W. (2013): Luminescence chronology of the Grub-Kranawetberg site, Austria. – E&G Quaternary Science Journal, 62 (2): 127–135. DOI: 10.3235/eg.62.2.04

Abstract: Eight samples from a loess profile at the open air site of Grub-Kranawetberg (Lower Austria) were dated by Infrared Stimulated Luminescence (IRSL) of the polymineral fine-grain (4–11 µm) fraction and Optically Stimulated Luminescence (OSL) of quartz grains in the size range of 38–63 µm. Calibrated radiocarbon ages of ca. 30 ka BP on charcoal from the main archaeological layer AH4 agree with the IRSL and OSL age estimates within error limits. Anomalous fading of the feldspar-dominated IRSL from fine grain fraction could not be detected in the laboratory and the MAAD-IRSL ages were therefore not corrected. Most IRSL and OSL ages agreed within error limits, however, some IRSL ages were significantly underestimated as compared to the OSL ages, and in general the mean of the OSL ages was higher compared to the mean of individual IRSL ages. The OSL ages place the deposition of the exposed loess including an interstadial pedocomplex ("Stillfried B") to between ca. 47 ka and ca. 30 ka. Potential pedostratigraphic correlations with some European loess areas as well as palaeoecological implications on Upper Palaeolithic human occupation patterns are discussed.

Lumineszenz-Chronologie der Fundstelle Grub-Granawetberg, Österreich

Kurzfassung: Das Alter von acht Proben aus einem Lössprofil der Freilandfundstelle Grub-Kranawetberg (Niederösterreich) wurde mittels der Lumineszenzmethoden der IRSL-Datierungen an der polymineralischen Feinkornfraktion und der OSL-Datierungen an der Mittelkornfraktion von Quarzen bestimmt. Kalibrierte Radiokohlenstoffalter von ca. 30 ka für den archäologischen Hauptfundhorizont AH4 werden innerhalb der Fehlergrenzen durch IRSL- und OSL-Alter bestätigt. Anomales Ausheilen der feldspat-dominierten Feinkornfraktion konnte im Labor nicht nachgewiesen werden, weshalb die MAAD-IRSL Alter nicht korrigiert wurden. Während die meisten IRSL- und OSL-Alter innerhalb ihrer Fehlergrenzen übereinstimmen, unterschätzen einige IRSL-Alter die OSL-Alter aus bisher unbekannten Gründen signifikant, wobei die Mittelwerte der OSL-Resultate tendenziell älter als die IRSL-Datierungen sind. Nach den OSL-Altern wurde der aufgeschlossene Löss einschließlich eines interstadialen Bodenkomplexes („Stillfried B") im Zeitraum zwischen ca. 47 ka und ca. 30 ka gebildet. Mögliche pedostratigraphische Korrelationen mit einigen europäischen Lössgebieten sowie paläoökologische Überlegungen zur menschlichen Besiedlung im Jungpaläolithikum werden diskutiert.

Keywords: *Luminescence dating, Grub-Kranawetberg, loess, palaeoecology, Stillfried B, correlations*

Addresses of authors: **L. Zöller***, **D. Richter**, **S. Masuth**, **L. Wunner**, **M. Fischer**, Geomorphology Chair, University of Bayreuth, Germany. **W. Antl-Weiser**, Naturhistorisches Museum Wien, Prähistorische Abteilung, Vienna, Austria. **D. Richter**, Department of Human Evolution, Max Planck Institute for Evolutionary Anthropology, Leipzig, Germany.
corresponding author: ludwig.zoeller@uni-bayreuth.de

1 Introduction

The Lower Gravettian open air site of Grub-Kranawetberg (Lower Austria) has been studied since the mid-1990. The site is described and discussed in detail in Antl-Weiser (this volume). The age of the archaeological horizons, in particular of the main horizon AH4 attributed to the Gravettian period, is constrained by several radiocarbon ages. Further minor archaeological assemblages located a few cm above AH4 and labelled as "first upper AH" are followed by the "second upper AH" (Antl-Weiser 2008). Another human occupation was detected 20 cm below AH 4 (Lower layer in Table 4). A section of ca. 210 cm thick brownish loess loam was observed from ca. 30 cm below AH4 and is interpreted as a pedocomplex, probably related to Stillfried-B. A more detailed pedological analysis is however pending. The timing of the deposition of the under- and overlying loess, the occurrence of potential sedimentation hiatuses, and relative sedimentation rates were unknown so far. A contribution to these questions is attempted here by luminescence dating within the framework of an interdisciplinary team using a diachronic landscape reconstruction approach (Waters 1996), which examined the entire profile of the 2010 and 2011 excavations. The present contribution tries to unravel the chronostratigraphy and geochronology of the site within the Danube loess sequence of Austria and relates these to palaeoecological interpretations.

2 Sampling

The Kranawetberg-site is situated west of the village Grub on the western side of the March River at N 48°25'08" and E 16°50'02", altitude 185 m a.s.l. Samples for optical dating (IRSL, OSL) were extracted from the excavation site (for lo-

cation see Antl-Weiser 2008) by one of us (W.A.-W.) during the summer of 2010. Coordinates of the sampled profile O16 relative to the reference point of the excavation are x=15.07 and y=15.86 m. Steel cylinders of 100 cm^3 volume were hammered horizontally into the loess wall and sealed by light-tight lids. One of the main research focus was the verification of the radiocarbon dating of the main archaeological horizon (AH 4). Luminescence dating of such a horizon, that would have been mixed by the prehistoric anthropogenic activities, is considered as difficult. Thus, the sampling was performed at positions in 'clean' loess directly above and below this horizon. These were with the aim to provide bracketing ages. Further to understand the sedimentation history, additional samples were taken wherever feasible, in the entire available profile.

3 Sample preparation and IRSL/OSL measurements

Sample preparation for luminescence measurements were carried out in the dark laboratory under subdued red diode light (640±20 nm). Approximately 1 cm of material from each end of the cylinders was scraped off and used for dosimetry measurements using thick source alpha counting to determine U and Th contents (Zöller & Pernicka 1989) and ICP-MS (for K contents). Samples were then pretreated with 1N HCl and 30% H_2O_2, followed by wet sieving and extraction of the 4–11 µm polymineral fine-grain fraction in Atterberg cylinders using Stoke's law. IRSL dating was carried out using the MAAD (Multiple Aliquot Additive Dose) protocol following Mauz et al. (2002), with further experimental details given in Fuchs et al. (2008). IRSL measurements were carried out on a Risø TL/OSL-DA15 reader equipped with a Chroma D410 detection filter (transmission over 425±15 nm band). The use of a MAAD protocol ensured that sensitivity changes were not an issue. All aliquots, including the ones for the fading experiment, were preheated at 220°C for 300 s before IRSL measurement. No normalization was required due to good reproducibility of the luminescence signals of the 5–6 aliquots for each of the additive dose points of 70, 140, 280 and 560 Gy. For data processing and calculation of equivalent doses by exponential fitting and extrapolation we used the Analyst (3.07b) software supplied with the Risø reader and followed Mauz et al. (2002). All aliquots used for the construction of the MAAD growth curve (Figure 5) were stored at 70°C for one week between laboratory irradiation and IRSL measurements, to allow for the decay of short lived IRSL signals and also permit for the occurrence of any potential short term anomalous fading. Such a procedure in general equals storage of 4 weeks at room temperature (Berger 1988, p. 26). A fading test was carried out by measuring the IRSL of 5 additional aliquots which had received the largest additive laboratory dose (ca. 560 Gy) immediately after irradiation and comparing this IRSL signal intensity with the signal from stored aliquots of the same dose group, which were used for the construction of the MAAD growth curve. The percentage of fading was calculated as the ratio of the intensities (N+ß+delay)/(N+ß) of the IRSL-signal for each sample except BT 1009, which failed due to machine error.

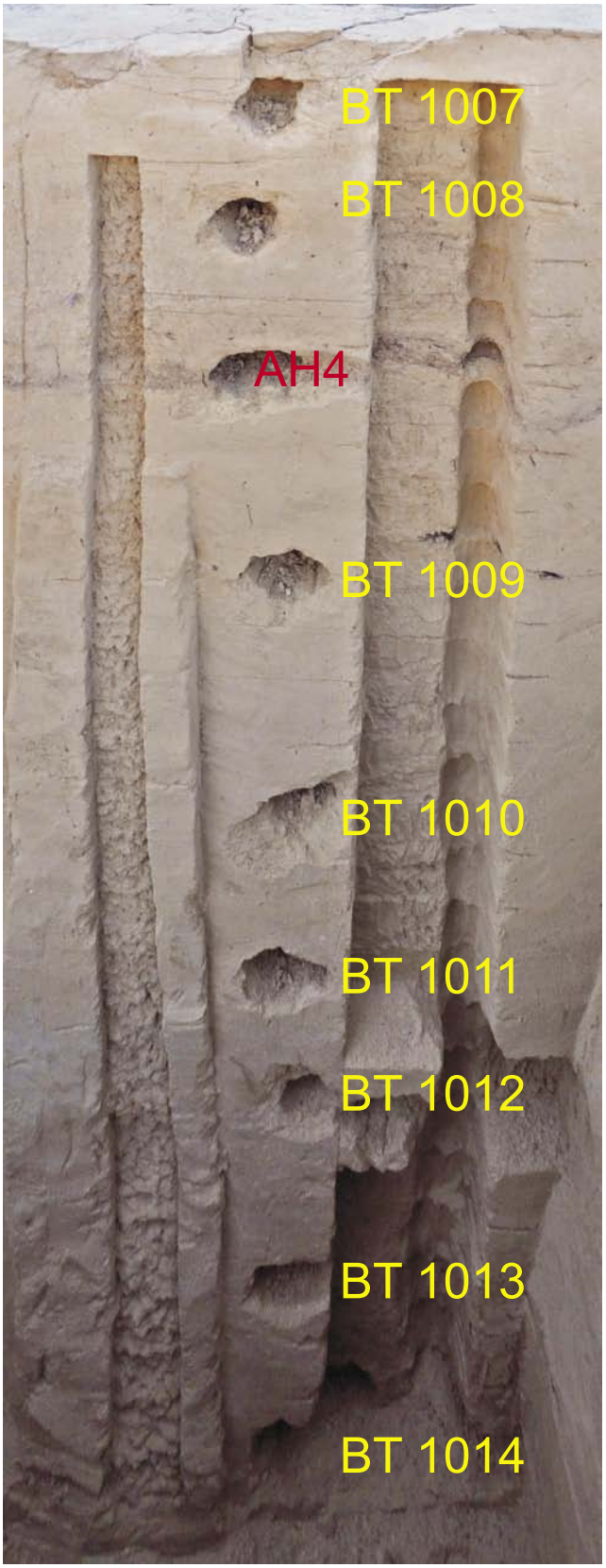

Fig. 1: Loess section of the Grub-Kranawetberg excavation 2010 and sample numbers. Note the reddish-yellow hue below and partly also above the main Archaeological Layer AH 4 and the increasing reddish-brown hue below sample BT 1012 indicating weak interstadial soil formation.

Abb. 1: Lössprofil von der Grabung Grub-Kranawetberg 2010 und Probennummern. Man beachte den rötlich-gelblichen Farbton unterhalb und teilweise auch oberhalb des Archäologischen Fundhorizontes AH 4 sowie den zunehmend rötlich-braunen Farbton unterhalb der Probe BT 2012 als Hinweise auf schwache interstadiale Bodenbildung. (Foto: W. Antl-Weiser)

E&G / Vol. 62 / No. 2 / 2013 / 127–135 / DOI 10.3285/eg.62.2.04

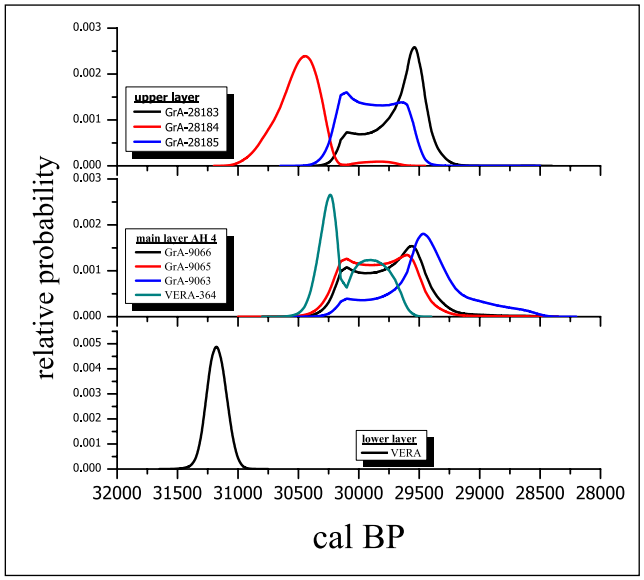

Fig. 2: Cumulative (black line, not normalized) and single (coloured) probability distributions of calibrated ^{14}C ages from the Grub-Kranawetberg site (Calib 6.11 with IntCal09).

Abb. 2: Kumulative Wahrscheinlichkeitsverteilungen (schwarz, unnormiert) und einzelne Wahrscheinlichkeitsverteilungen (farbig) der kalibrierten ^{14}C-Alter von der Fundstelle Grub-Kranawetberg (Calib 6.11 mit IntCal09).

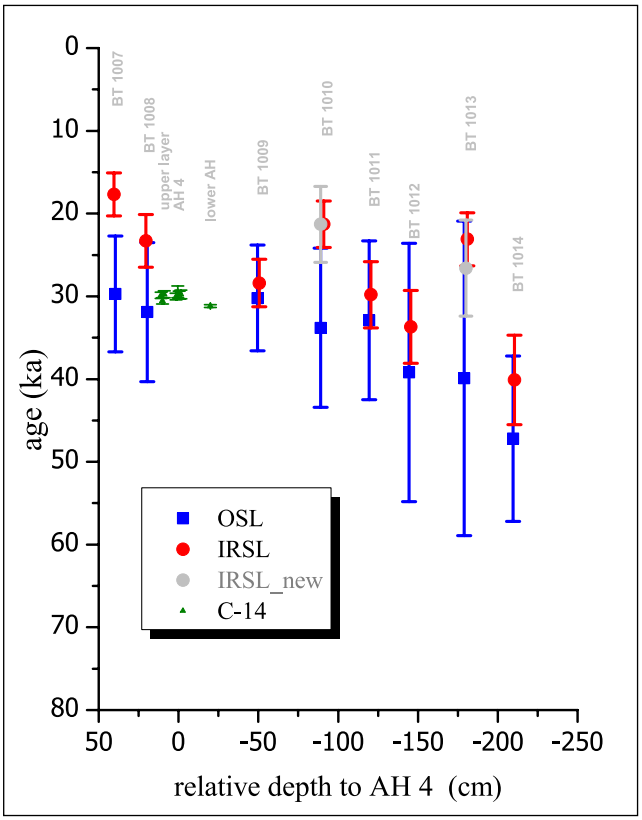

Fig. 3: Age-depth plot of ^{14}C (calibrated), OSL and IRSL ages (2-σ). Sample depth positions were slightly shifted for clarity.

Abb. 3: Alters-Tiefenplot von ^{14}C (kalibriert) -, OSL- und IRSL-Altern (2-σ). Probenpositionen wurden zur besseren Sichtbarkeit leicht versetzt dargestellt.

The quartz extracts from the middle grain size fraction (38–63 µm) were obtained by wet sieving and etching in hydrofluoric acid (H_2SiF_6) following Fuchs et al. (2005) for OSL measurement by blue light stimulation. Feldspar contamination was ruled out by IRSL measurements yielding intensities at background level. OSL measurements followed the SAR protocol (Murray & Wintle 2000) and experimental details as described in Fuchs et al (2012), including analytical details like acceptance criteria etc. A preheat of 200°C for 10 s was applied. Due to the scarcity of quartz middle grains size, the study was hampered by the low number of aliquots available for D_E-determination. Results from only 10–22 aliquots (excluding 0–10% rejection) could be obtained, and these resulted in relatively larger uncertainties and precluded elaborate statistical analysis of the D_E data.

4 Results

4.1 Dosimetry Results

Dose-rates were calculated assuming secular equilibrium of U decay series and using conversion factors given by Guerin et al. (2011). The cosmic ray contribution was calculated after Prescott & Hutton (1994), using appropriate positional coordinates and approximate estimate of average sediment thickness. A moisture content of δ=1.15±0.05 (see Zimmerman 1971, Lang et al. 2003, Zöller et al. 2013) was assumed for all samples with respect to hydromorphic features. This was despite the fact that the measured actual moisture content was lower with values between 1.09 and 1.11. An alpha efficiency factor (a-value) of 0.08±0.02, derived as an average from numerous data from loess (see e.g. Lang et al. 2003; Lomax et al. 2013, take 0.07±0.02) was assumed for all polymineral fine-grain samples. An a-value of 0.035±0.05 was employed in dose-rate calculations for the quartz middle grain fraction (cf. Lai et al. 2008).

Analytical results for concentrations of radio-elements are given in Table 1 and the calculated dose-rate (in Gy/ka) for moist samples and the cosmic ray dose contributions are provided in Table 2 (data in all tables with 1σ uncertainty).

4.2 IRSL dating results

All IRSL samples yielded shine-down plateaus suggesting sufficient bleaching of the IRSL signal during and prior to deposition of the loess. The fading tests resulted in ratios between 1.04±0.08 and 0.98±0.06. Therefore, no correction for athermal fading was applied.

Equivalent doses together with effective dose-rates and the resulting IRSL ages are presented in Table 3 together with their 1σ uncertainty. While IRSL results generally provide increasing ages with depth, the IRSL ages of samples BT 1010 and 1013 do not conform with this trend and were significantly younger than their respective overlying samples (Figure 3). The location on a plateau and the sample being buried under several meters of loess, rules out major sedimentological disturbances as a cause. According to the fading tests, short-term athermal fading can be precluded

as a possible reason.[1] The dosimetry is not different from the other samples and radioelement concentrations (Table 1) and thus do not indicate different sediment source areas, which could have resulted in the vastly different alpha sensitivity necessary for such age discrepancies. No explanation can be presently put forward, and therefore these age estimates were considered as outliers, and excluded from further interpretation, pending further research. Given such an ambiguity, OSL dating using pure quartz separates from the identical sample material was carried out in order to verify the reliability of IRSL dating.

4.3 OSL dating results

Effective dose-rates for middle grain quartz are lower than for feldspar-dominated fine-grains due to significantly lower a-values. The equivalent doses together with effective dose-rates and resulting OSL ages are presented in Table 5 with 1σ uncertainties. It is noteworthy that samples BT 1010 and 1013, which provided suspicious IRSL dating results, yielded OSL ages which are consistent with OSL ages for samples stratigraphically located above and below, respectively. Furthermore, no significant age inversion of OSL ages with respect to stratigraphy was observed, and from this point of view none of the OSL ages is therefore suspected to be underestimated.

5 Comparison of OSL and IRSL dating results

Radiocarbon ages for the main archaeological layer (Antl-Weiser et al. 2010, Nigst & Antl-Weiser 2012) were calibrated with the "Calib Rev 6.1.1" program (Stuiver & Reimer 1993), employing the IntCal09 calibration curve (Reimer et al. 2009). Calibration results are given in Table 4 and probability distributions are plotted in Figure 2. For the main archaeological layer AH4 we calculated a summed probability ^{14}C age of 30405 to 29162 cal BP 2σ (see Table 4).

An age-depth plot of IRSL, OSL and calibrated ^{14}C ages is shown in Figure 3. Two IRSL ages from samples above AH4 of 23.3±1.6 ka (BT 1008) and 17.7±1.3 ka (BT 1007) are younger than the calibrated ^{14}C ages, while IRSL results down to 150 cm below AH4 are still in accordance within uncertainties. The OSL ages are all in agreement with radiocarbon data, except for the lowermost sample (BT 1014), which is significantly older. The OSL ages are all consistent with the stratigraphy and samples BT 1008 and 1009, which are bracketing AH4, agree with the radiocarbon ages. In general, uncertainties for OSL ages (middle grains) are remarkably larger than for IRSL dating due to relatively large scatter of equivalent doses obtained from single aliquots.This is in accordance with previous observations (e.g., Fuchs et al 2012). In Figure 4, the OSL and the accepted IRSL dating results with their 1-σ errors are plotted together with the stratigraphy of the sampled profile. Whereas OSL and the accepted IRSL ages agree within the error limits for all samples below AH4, this is not the case for sample BT 1007 located stratigraphically above AH4.

As mentioned above, significant anomalous fading as a reason for the age underestimates of this IRSL age with respect to the OSL age is precluded. The fading experiment would have revealed at least short term fading as it equals

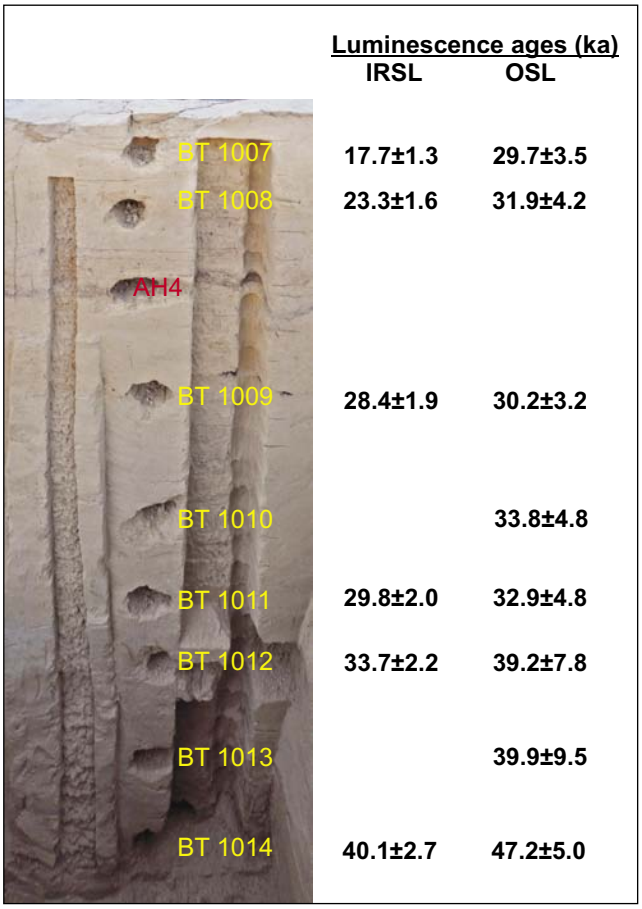

Fig. 4: Sample positions along the profile and comparison of OSL and IRSL dating results.

Abb. 4: Positionen der Proben im Profil und Vergleich von OSL- und IRSL-Datierungsergebnissen.

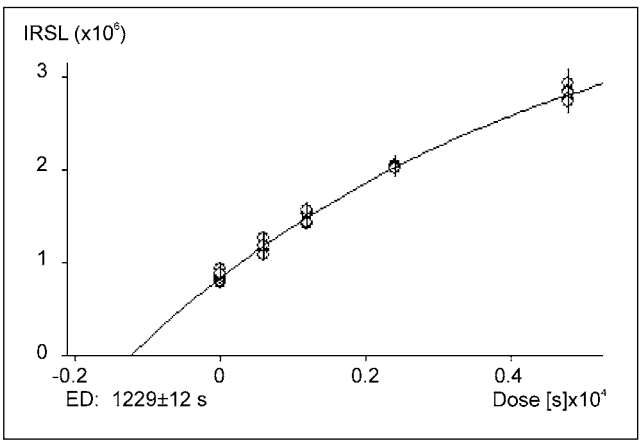

Fig. 5: Additive IRSL dose-response curve (MAAD) for sample BT 1012.

Abb. 4: Additive IRSL-Wachstumskurve (MAAD) für Probe BT 1012.

1) The measurements for these two samples were repeated in order to confirm the results. An identical equivalent dose (ED) was obtained for BT 1010_new (76.8±3.6 Gy) and, thus, the identical apparent age. In case of BT 1013 the ED changed significantly from 91.9±1.3 Gy to 105.7±2.3 Gy for reasons unknown so far (BT 1013_new), whereas the apparent ages of 23.1±1.6 and 26.6±2.9 ka, respectively, agree within uncertainties. Nevertheless, the apparent IRSL age of BT 1010_new remains a significantly underestimated outlier in an internal consistency check, where the identical systematic uncertainties are excluded.

E&G / Vol. 62 / No. 2 / 2013 / 127–135 / DOI 10.3285/eg.62.2.04 / © Authors / Creative Commons Attribution License

Tab. 1: Radioelement concentrations.

Tab. 1: Konzentrationen der Radioelemente.

Sample no.	Th	δTh	U	δU	K	δK
	[ppm]	[ppm]	[ppm]	[ppm]	[%]	[%]
BT 1007	11.49	1.44	3.73	0.44	1.54	0.15
BT 1008	9.12	1.31	4.10	0.40	1.59	0.16
BT 1009	10.22	1.11	4.19	0.34	1.58	0.16
BT 1010	7.63	0.97	4.15	0.30	1.65	0.17
BT 1011	9.27	0.95	3.67	0.29	1.76	0.18
BT 1012	11.11	1.06	4.12	0.32	1.82	0.18
BT 1013	11.01	1.14	3.49	0.35	1.75	0.18
BT 1014	9.35	1.14	3.32	0.35	1.78	0.18

Tab. 2: Dose-rates for moist samples assuming δ=1.15

Tab. 2: Dosisleistungen für feuchte Proben bei δ=1.15

Sample no.	$D_{\alpha\ moist}$	$\delta[D_{\alpha\ moist}]$	$D_{\beta\ moist}$	$\delta[D_{\beta\ moist}]$	$D_{\gamma\ moist}$	$\delta[D_{\gamma\ moist}]$	Depth	D_{cosm}	$\delta[D_{cosm}]$
	[Gy/ka]	[Gy/ka]	[Gy/ka]	[Gy/ka]	[Gy/ka]	[Gy/ka]	[m]	[Gy/ka]	[Gy/ka]
BT 1007	9.96	0.66	1.78	0.15	1.15	0.10	1.5	0.195	0.02
BT 1008	8.09	0.55	1.81	0.15	1.10	0.09	1.7	0.193	0.02
BT 1009	9.00	0.61	1.84	0.15	1.15	0.09	2.4	0.186	0.02
BT 1010	6.88	0.48	1.82	0.15	1.06	0.08	2.8	0.182	0.02
BT 1011	8.15	0.55	1.88	0.16	1.10	0.08	3.1	0.179	0.02
BT 1012	9.71	0.65	2.02	0.17	1.23	0.09	3.4	0.176	0.02
BT 1013	9.54	0.63	1.89	0.16	1.16	0.09	3.7	0.173	0.02
BT 1014	8.16	0.55	1.85	0.16	1.08	0.09	4.0	0.170	0.02

Tab. 3: Equivalent doses (ED), effective dose-rates (Gy/ka) and IRSL ages (ka). Ages in italics are considered as outliers and discarded from further discussion.

Tab. 3: Äquivalenzdosen (ED), effektive Dosisleistungen und IRSL-Alter (ka). Alter in Kursivschrift werden als Ausreißer betrachtet und in der weiteren Diskussion nicht berücksichtigt.

Sample no.	ED	δED	D_{eff}	$\delta[D_{eff}]$	**Age**	**δAge**
	[Gy]	[Gy]	[Gy/ka]	[Gy/ka]	**[ka]**	**[ka]**
BT 1007	69.4	2.1	3.93	0.28	**17.7**	**1.3**
BT 1008	87.5	2.2	3.75	0.25	**23.3**	**1.6**
BT 1009	110.7	1.5	3.90	0.26	**28.4**	**1.9**
BT 1010 _new	*76.8* *76.8*	*1.5* *3.6*	*3.61*	*0.22*	*21.3* *21.3*	*1.4* *2.3*
BT 1011	113.5	1.7	3.81	0.25	**29.8**	**2.0**
BT 1012	141.6	1.4	4.20	0.28	**33.7**	**2.2**
BT 1013 _new	*91.9*	*1.3*	*3.98*	*0.27*	*23.1* *26.6*	*1.6* *2.9*
BT 1014	150.4	1.7	3.75	0.25	**40.1**	**2.7**

4 weeks of room temperature storage. We cannot preclude, however, mid- or long-term fading (Xie & Aitken 1991) which cannot be detected in the laboratory within the available time. Inspection of the shapes of luminescence decay and growth curves (Figure 5) did not reveal any clues, where especially the latter are well below the onset of saturation and therefore do not appear to be critical. The same applies to possible discrepancies in alpha sensitivity. Provided the uniformity of the source material, which is indicated by the lack of variability in radioelement concentration, a significant discrepancy in the alpha sensitivity is considered most unlikely as reason. We like to mention, however, that during sampling in the field we observed crotovinas extending downwards almost to the upper archaeological layer and causing some problems during sampling. Furthermore, the area was used as a vineyard in previous times and remnants of deep roots of grapevines were detected in the uppermost loess. Even if sampling tried to steer clear of crotovinas and tracks of former grapevines we cannot be totally certain to have entirely avoided sampling material affected by bioturbation. Thus, the obtained age, possibly including the other sample located above AH4 (BT 1008) may be a mixed age and thus underestimating the original deposition age of the loess. It would be a surprise, however, if only fine grains contaminated the loess due to bioturbation and not coarse silt grains used for OSL dating. This question will be studied further using soil micromorphology during ongoing research by other members of the working group.

The IRSL ages from above AH4 may suggest erosional hiatuses or strongly reduced sedimentation rate. Although traces of solifluction were detected in this part of the section, other possible reasons for these rather young apparent ages need to be identified. As far as AH4 and deeper horizons are concerned, we can state that within uncertainties IRSL and OSL ages are consistent with calibrated radiocarbon ages on charcoal which yielded congruent results from different laboratories (Antl-Weiser et al. 2010, Nigst & Antl-Weiser 2012) and an age of ca. 30 ka for AH4 is confirmed by luminescence dating results. The chronostratigraphic position of the loess above the upper archaeological layer so far remains a matter of debate.

6 Discussion

The luminescence dating results for the Grub-Kranawetberg site have implications for the regional loess stratigraphy and the supposed relation of human occupation patterns to specific palaeoecologies. If the uppermost OSL ages correctly reflect the deposition ages of the loess above AH4 the entire exposed loess sequence presumably accumulated during a time period corresponding to a late phase of Marine Isotopic Stage MIS 3. The two uppermost IRSL ages, however, argue for deposition of the loess above the upper archaeological layer during MIS 2.

Constraints for palaeoecology

The archaeological layer AH4 overlies a brownish interstadial palaeosol which appears to be coeval with the nearby "Stillfried B" palaeosol at its type locality. The loess in which AH4 is embedded exhibits, however, features of hydromorphic soils and of solifluction (as so far no indication of harsh permafrost conditions was observed in this layer we were cautious in using the term gelifluction). These observations as well as preliminary malacological results (Antl-Weiser et al. 1997) indicate a climatic deterioration (cooling) after the thermal optimum of the interstadial for the time of occupation. The presence of humans in such palaeoecological conditions is usually neglected, based on an oversimplifying geodeterministic view that in general Upper Palaeolithic humans inhabited Central Europe at the onset or during thermal optimum of interstadials and withdrew at the onset of climatic cooling. Instead, moister and cooler climate at the onset of a stadial could have triggered higher bioproductivity of the landscape with respect to a summer-dry loess steppe and, thus, better conditions for game (e.g., Zech & Hintermaier-Erhard 2002, p. 12; Schultz 2002). Möller & Thannheiser (2011) point out that tundra soils of moist habitat can produce a high amount of below-ground phytomass "which is important for plant growth and for building up soil organic matter" (p. 255).

In many classical loess-palaeosol sequences of Central Europe the time span between ca. 30 and ca. 26 ka is poorly resolved due to erosion (e.g., Zöller & Semmel 2001, Zöller et al. 2004). Convincing evidence for rapid loess sedimentation starting around 30 ka ago (i.e., late MIS 3) with intercalation of up to 4 or 5 tundra gley soils was reported from the Nussloch site, Germany (Antoine et al. 2009) and from the Dolní Věstonice (with less thickness) in, Czech Republic (Fuchs et al. 2012), as also from the Krems-Wachtberg site, Austria (Lomax et al. 2013, Zöller et al. 2013). In the upper part of the relevant section at Nussloch, Antoine et al. (2009) observed "cryo-dessication micro cracks" (layer 24, see legend to their Figure 2). Even if Nussloch is situated ca. 630 km WNW of Grub the drastic climatic cooling starting around 30 ka ago must have affected the surroundings of Grub and Stillfried as well. Lüthgens & Böse (2011) suggest that the ice advance of the "Brandenburg phase" (local glacial maximum) of the last glaciation (Weichselian) occurred during the time interval under question. This dramatic palaeoecological event in northern Central Europe may be reflected some Central European loess areas.

Constraints for Austrian and European loess stratigraphy

The chronostratigraphic position of the "Stillfried B" palaeosol has been a matter of debate (Terhorst et al. 2011). At the "classical" site in the north-western corner of the former Stillfried brickyard (N 48° 24' 32,4'', E 16° 50' 31,6'') the substratum of the weakly developed "Stillfried B" soil was dated 29.8±3.7 ka by TL (Zöller et al. 1994). It directly overlies Rissian loess (Hambach & Zöller, unpublished results) from which it is separated by an erosional hiatus. For this reason, the "Stillfried B" pedocomplex is supposed to have developed only with its youngest part at this site. Peticzka et al. (2010) described a "revised profile" from the western part of the abandoned brickyard which appears stratigraphically more complete and resembles the stratigraphy of the Grub-Kranawetberg excavation. Using field methods mentioned by Petitzka et al. (2010) the authors distinguish 3 fossil BC horizons at their "Stillfried B 2005" site which corresponds to 3 buried interstadial soils at Grub-Kranawetberg. Unfor-

Tab. 4: Uncalibrated and calibrated (2-σ) radiocarbon ages (Calib Rev 6.1.1 & IntCal09).
** no laboratory number available*

Tab. 4: Unkalibrierte und kalibrierte (2-σ) Radiokohlenstoff-Alter (Calib Rev 6.1.1 & IntCal09).
** keine Labornummer verfügbar*

Archaeological	relative	Laboratory	uncalibrated	error	calibrated
layer	depth	code	age [aBP]	[a]	age range [a calBP]
Upper layer	10	GrA-28183	24780	140	30172 - 29346
	10	GrA-28184	25640	160	30939 - 30191
	10	GrA-28185	25010	150	30254 - 29501
Main layer AH4	0	GrA-9066	24830	230	30284 - 29257
	0	GrA-9065	24930	240	30321 - 29359
	0	GrA-9063	24620	230	30189 - 28748
	0	VERA-364	25300	90	30409 - 29645
Lower layer	-20	VERA*	26700	120	31336 - 31013

Tab. 5: Equivalent doses (ED), effective dose-rates (Gy/ka) and quartz OSL ages (ka)

Tab. 5: Äquivalenzdosen (ED), effektive Dosisleistungen und Quarz-OSL-Alter (ka)

Sample no.	ED	δ_{ED}	D_{eff}	**Age**	δ_{Age}
	[Gy]	[Gy]	[Gy/ka]	**[ka]**	**[ka]**
BT 1007	101	9	3.40	**29.7**	**3.5**
BT 1008	106	11	3.31	**31.9**	**4.2**
BT 1009	103	7	3.41	**30.2**	**3.2**
BT 1010	108	13	3.23	**33.8**	**4.8**
BT 1011	111	14	3.37	**32.9**	**4.8**
BT 1012	144	28	3.68	**39.2**	**7.8**
BT 1013	138	27	3.47	**39.9**	**9.5**
BT 1014	156	16	3.31	**47.2**	**5.0**

tunately, no dating results have been published so far from the "Stillfried B 2005" site. The time of this pedocomplex at the Grub-Kranawetberg excavation is bracketed by our IRSL ages between 28.4±1.9 ka and 40.1±2.7 ka and by our OSL ages between 30.2±3.2 ka and 47.2±6.0 ka. Thus, the Grub-Kranawetberg site and the "Stillfried B 2005" site both appear well-suited to complete the Austrian loess stratigraphy in the period between ca. 40 and ca. 30 ka (MIS 3, upper part) by increasing the number of observed soils from one (Stillfried B) to a complex of three paleosols. Furthermore, our new dating results can inform the discussion on the correlation of the Stillfried B palaeosol with loess stratigraphies from other European areas, such as Southern Moravia (Fuchs et al. 2012), Serbia (Fuchs et al. 2008), Hungary (Zöller et al. 1994, Thiel et al. 2013), Austria (Thiel et al. 2011), Ukraine (Rousseau et al. 2011), and Germany (Antoine et al. 2009, Kadereit et al. 2013). The pedo-complex at Grub-Kranawetberg below AH4 and the revised "Stillfried B 2005" section appear to be coeval with interstadial soils or pedocomplexes in the mentioned areas. But with respect to palaeo-moisture conditions, palaeo-temperatures and sedimentation rates in the different regions the palaeosols manifest different soil typologies ranging from tundra-gleys or (sub-) arctic cambisols to chernozems. It may prove of particular interest that the range of apparent OSL ages bracketing the lowermost soil of the Grub-Kranawetberg pedocomplex (samples BT 1013 and 1014) includes the TL age of 43±4 ka for the substratum of the "MF1" palaeosol (chernozem) in Hungary (Zöller et al. 1994, cf Thiel et al. 2013). On the other hand, high sedimentation rates and locally dry climate impeded well-distinguishable interstadial palaeosols at the Krems-Wachtberg site. Therefore, an equivalent of the Stillfried B pedocomplex cannot be clearly identified so far at Krems-Wachtberg, although the same age range is covered (Terhorst et al. 2013).

7 Conclusions

The application of an IRSL-MAAD protocol for polymineral fine grain loess has once more (as in e.g. Lang et al. 2003; Fuchs et al. 2008) yielded age estimates congruent in their majority with OSL and radiocarbon dating. While this in itself indicates the absence of anomalous fading of

the feldspar luminescence component used, a fading test neither did show any loss of signal, and it appears that the occurrence of feldspar fading might be related to detection (here: blue band wavelength) and protocol (here: MAAD) used. OSL ages from quartz middle grains are, however, stratigraphically consistent without exception and also agree with radiocarbon dating results.

Luminescence dating confirms an age of ca. 30 ka for the main archaeological horizon AH4. According to proxy data, the main human occupation documented in level AH4 occurred after the thermal optimum of an interstadial at the onset of colder and moister conditions. A threefold complex of interstadial soils underlies the archaeological layers of Lower Gravettian age. This pedocomplex developed in a time span ranging from ≥40 ka to ca. 30 ka and includes the palaeosol known as "Stillfried B" soil. The pedocomplex at the Grub-Kranawetberg site appears, however, coeval with a nearby pedocomplex introduced as "Stillfried B 2005" (Peticzka et al. 2010) and with interstadial palaeosols or pedocomplexes of different typologies in various European loess regions. The Grub-Kranawetberg site is, thus, well-suited to complete the Austrian loess stratigraphy for the upper part of MIS 3 and to refine correlation with neighbouring European loess areas. For the loess overlying the archaeological layers at the Grub-Kranawetberg site a significant difference between IRSL and OSL ages still exists which calls for further investigations, e.g. the application of the NCF protocol for quartz OSL (Singhvi et al. 2011).

References

Antl-Weiser, W. (2013): The inventory of archaeological Horizon 4 and 3 and the loess section of Grub-Kranawetberg, a Gravettian camp site in Lower Austria. – E&G Quaternary Science Journal (this volume).

Antl-Weiser, W. (2008): Grub/Kranawetberg and Ollersdorf/Heidenberg (Lower Austria) – two Gravettian camp Sites in Eastern Austria. – Wiss. Mitt. Niederösterr. Landesmuseum, 19: 59–78.

Antl-Weiser, W., Fladerer, F. A., Nigst, P.R. & Verpoorte, A. (2010): Grub/Kranawetberg (Lower Austria) – Insights into a Gravettian Micro-Region in Eastern Austria. – Mitteilungen der Prähistorischen Kommission, 72: 231–243.

Antl-Weiser, W., Fladerer, F.A., Peticzka, R., Stadler, F. C. & Verginis, S. (1997): Ein Lagerplatz eiszeitlicher Jäger in Grub bei Stillfried. – Archäologie Österreichs 8/1, 1997: 4–20.

Antoine, P., Rousseau, D.-D., Moine, O., Kunesch, S., Hatté, C., Lang, A., Tissoux, H. & Zöller, L. (2009): Rapid and cyclic aeolian deposition during the Last Glacial in European loess: a high-resolution record from Nussloch, Germany. – Quaternary Science Reviews, 28: 2955–2973.

Berger, G. (1988): Dating Quaternary events by luminescence. – In: D.J. Easterbrook (ed), Datingh Quaternary Sediments. – Geological Society of America, Special Paper 227: 13–50.

Fuchs, M., Straub, J. & Zöller, L. (2005): Residual luminescence signals of recent river flood sediments: A comparison between quartz and feldspar of fine- and grain-sized sediments. – Ancient TL, 23: 25–20.

Fuchs, M., Rousseau, D.-D., Antoine, P., Hatté, C., Gauthier, C., Marković, S. & Zöller, L. (2008): Chronology of the Last Climatic Cycle (Upper Pleistocene) of the Surduk loess sequence, Vojvodina, Serbia. – Boreas, 37: 66–73.

Fuchs, M., Kreutzer, S., Rousseau, D. D., Antoine, P., Hatté, C., Lagroix, F., Moine, O., Gauthier, C., Svoboda,J. & Lisá, L. (2012): The loess sequence of Dolní Věstonice, Czech Republic: A new OSL-based chronology of the Last Climatic Cycle. – Boreas, DOI: 10.1111/j.1502-3885.2012.00299.x. ISSN 0300-9483.

Guerin, G., Mercier, N. & Adamiec, G. (2011): Dose-rate conversion factors: update. – Ancient TL, 29: 5–8.

Kadereit, A., Kind, C.-J. & Wagner, G.A. (2013): The chronological position of the Lohne Soil in the Nussloch loess section – re-evaluation for a European loess-marker horizon. – Quaternary Science Reviews, 59: 67–86.

Lai, Z. P., Zöller, L., Fuchs, M. & H. Brückner, H. (2008): Alpha efficiency determination for OSL of quartz extracted from Chinese loess. – Radiation Measurements, 43: 767–70.

Lang, A., Hatte, C., Rousseau, D.-D., Antoine, P., Fontugne, M., Zöller, L. & Hambach, U. (2003): High-resolution chronologies for loess: comparing AMS ^{14}C and optical dating results. – Quaternary Science Reviews 22: 953–959.

Lomax, J., Fuchs. M., Preusser, F. & Fiebig, M (2013): Luminescence based loess chronostratigraphy of the Upper Palaeolithic site Krems-Wachtberg, Austria. – Quaternary International, DOI: 10.1016/j.quaint.2012.10.037

Lüthgens, C. & Böse. M. (2011): Chronology of Weichselian main ice marginal positions in north-eastern Germany. – E&G Quaternary Science Journal, 60: 236–247.

Mauz, B., Bode, T., Mainz, E., Blanchard, H., Hilger, W., Dikau, R. & Zöller, L. (2002): The luminescence dating laboratory at the University of Bonn: Equipment and procedures. – Ancient TL, 20: 53–61.

Möller, I. & Thannheiser, D. (2011): Ecosystem Dynamiocs of Subpolar and Polar Regions. – In: Millingten, A.C:, Blumler, M.A. & Schickhoff, U. (eds.) – Biogeography. 598 p., SAGE.

Murray, A.S. & Wintle A.G. (2000): Luminescence dating of quartz using an improved singlealiquot regenerative-dose protocol. – Radiation Measurements, 33: 57–73.

Nigst, P.R. & Antl-Weiser, W. (2012): Les structures d'occcupation gravettiennes en Europe centrale: le cas de Grub/Kranawetberg, Autriche. – L'anthropologie, 116: 639–664.

Peticzka, R., Holawe, F. & Riegler, D. (2010): Structural analyses on the modified paleosol-sequence of "Stillfried B" with high resolution measurements of selected laboratory parameters. – Quaternary International, 222: 168–177.

Prescott, J.R. & Hutton, J.T. (1994): Cosmic ray contributions to dose rates for luminescence and ESR dating: large depths and long term variations. – Radiation Measurements, 23: 497–500.

Reimer, P., Baillie, M., Bard, E., Bayliss, A., Beck, J., Blackwell, P., Bronk Ramsey, C., Buck, C., Burr, G., Edwards, R., Friedrich, M., Grootes, P., Guilderson, T., Hajdas, I., Heaton, T., Hogg, A., Hughen, K., Kaiser, K., Kromer, B., McCormac, F., Manning, S., Reimer, R., Richards, D., Southon, J., Talamo, S., Turney, C., van der Plicht, J. & Weyhenmeyer, C. (2009): IntCal09 and Marine09 Radiocarbon Age Calibration Curves, 0–50,000 Years cal BP. – Radiocarbon, 51: 1111–1150.

Rousseau, D.-D., Antoine, P., Gerasimenko, N., Sima, A., Fuchs, M., Hatté, C., Moine, O. & Zöller, L. (2011): North Atlantic abrupt climate events of the last glacial period recorded in Ukrainian loess deposits. – Climate of the Past, 7: 221–234.

Schultz, J. (2002^3): Die Ökozonen der Erde. – Stuttgart (Ulmer UTB).

Singhvi, A., Stokes, S., Chauhan, N., Nagar, Y. & Jaiswal, M. (2011): Changes in natural OSL sensitivity during single aliquot regeneration procedure and their implications for equivalent dose determination. – Geochronometria 38: 231–241.

Stuiver, M. & Reimer, P. J. (1993): Extended ^{14}C data base and revised CALIB 3.0 ^{14}C age calibration program. – Radiocarbon, 35: 215–230.

Terhorst, B., Thiel, C., Peticzka, R., Sprafke, T., Frechen, M., Fladerer, F.A., Roetzel, R. & Neugebauer-Maresch, C. (2011): Casting new light on the chronology of the loess/palaeosol sequences in Lower Austria. – E&G Quaternary Science Journal, 60: 270–277.

Terhorst, B., Kühn, P., Damm, B., Hambach, U., Meyer-Heintze, S. & Sedov, S. (2013): Paleoenvironmental fluctuations as recorded in the loess-paleosol sequence of the Upper Paleolithic site Krems-Wachtberg. – Quaternary International (2013), DOI: 10.1016/j.quaint.2013.03.045

Thiel, E., Terhorst, B., Jaburová, I., Buylaert, J.-P., Murray, A.S., Fladerer, F.A., Damm, B., Frechen, F. & Ottner, F. (2011): Sedimentation and erosion processes in Middle to Late Pleistocene sequences exposed in the brickyard of Langenlois/Lower Austria. – Geomorphology,135: 295–307.

Thiel, C., Horváth, E. & Frechen, M. (2013): Revisiting the loess/palaeosol sequence in Paks, Hungary: A post-IR IRSL based chronology for the 'Younger Loess Series'. – Quaternary International (2013), DOI: 10.1016/j.quaint.2013.05.045

Waters, M.R. (1996): Principles of Geoarchaeology. – 398 p.; Tucson (The University of Arizona Press).

Xie, J., & Aitken, M.J. (1991): The hypothesis of mid-term fading and its trial on Chinese loess. – Ancient TL, 9: 21–25.

Zech, W. & Hintermaier-Erhard, G. (2002): Böden der Welt. – 120 p. Heidelberg, Berlin (Spektrum).
Zimmerman, D.W. (1971): Thermoluminescent dating using fine grains from pottery. – Archaeometry, 13, 29–52.
Zöller, L. & Pernicka, E. (1989): A note on overcounting in alpha-counters and its elimination. – Ancient TL, 7: 11–14.
Zöller, L. & Semmel, A. (2001): 175 years of loess research in Germany – long records and "unconformities". – Earth Science Reviews, 54: 19–28.
Zöller, L., Oches, E. A. & McCoy, W. D. (1994): Towards a revised chronostratigraphy of loess in Austria with respect to key sections in the Czech Republic and in Hungary. – Quaternary Geochronology (Quaternary Science Reviews), 13: 465–472.
Zöller, L., Rousseau, D.-D., Jäger, K.-D. & Kukla, G. (2004): Last interglacial, Lower and Middle Weichselian – a comparative study from the Upper Rhine and Thuringian loess areas. – Z. Geomorph. N.F., 48: 1–24.
Zöller, L., Richter, D., Blanchard, H., Einwögerer, T., Händel, M. & Neugebauer-Maresch, C. (2013): Our oldest children – age constraints for the Krems-Wachtberg site obtained from various thermoluminescence dating approaches. – Quaternary International, DOI: 10.1016/j.quaint.2013.05.003

E&G Quaternary Science Journal
Volume 62 / Number 2 / 2013 / 136–149 / DOI 10.3285/eg.62.2.05
www.quaternary-science.net

GEOZON SCIENCE MEDIA
ISSN 0424-7116

Impact of atmospheric warming on permafrost degradation and debris flow initiation – a case study from the eastern European Alps

Bodo Damm, Astrid Felderer

How to cite: Damm, B., Felderer, A. (2013): Impact of atmospheric warming on permafrost degradation and debris flow initiation – a case study from the eastern European Alps. – E&G Quaternary Science Journal, 62 (2): 136–149. DOI: 10.3285/eg.62.2.05

Abstract: The present study demonstrates the importance of recent atmospheric warming for the spatial distribution of debris flow initiation in a central alpine area of the Eastern Alps. In particular, permafrost degradation due to increasing mean annual air temperature (MAAT) since the end of the Little Ice Age (LIA) caused mechanical instabilities of sediments and slopes. In the study area, the Rieserferner-Ahrn Nature Park, it can be shown that almost half of the debris flow initiation zones originate in areas with loose rock that were still stabilized by glacier ice and/or permafrost about 150 years ago.
At present, the permafrost area covers 109 km² in the study area, while it covered ~211 km² during thermal conditions at the end of the LIA. Since then glacier recession and permafrost degradation exposed extended areas of unconsolidated debris that are uniformly distributed in the Rieserferner-Ahrn Nature Park. In general, present-day debris flows mainly originate from corresponding sediments, where permafrost degraded since the end of the LIA. These sediments are now susceptible to debris flow hazards.
Compared to present conditions the permafrost area would decrease by approximately 72 % by the middle of the 21st century with regard to an increased air temperature of +1 to +2 K. Moreover, glaciers widely disappear in this scenario. Ongoing glacier recession and permafrost degradation increase the amount of instable debris as well as the potential of debris flow detachment zones in the future.

Der Einfluss der atmosphärischen Erwärmung auf Permafrostdegradation und das Anreißen von Muren – eine Fallstudie aus den Ostalpen

Kurzfassung: In der vorliegenden Arbeit wird die Bedeutung der Erwärmung der Kryosphäre seit dem Ende der Kleinen Eiszeit (LIA) für die räumliche Verbreitung von Muranrissen in einem zentralalpinen Gebiet der Ostalpen untersucht. Vor dem Hintergrund der atmosphärischen Erwärmung verursachte hier insbesondere die Degradation von Permafrost bodenmechanische Instabilitäten. Im Untersuchungsgebiet, dem Naturpark Rieserferner-Ahrn in Südtirol lässt sich zeigen, dass mehr als die Hälfte der Muranrisse in Lockergesteinen auftreten, unter anderem in Moränen- und Hangschuttablagerungen, die vor rund 150 Jahren noch durch Gletschereis und Permafrost stabilisiert waren.
Derzeit sind rund 109 km² des Untersuchungsgebietes von Permafrost unterlagert, während unter den thermischen Bedingungen der Kleinen Eiszeit diese Fläche noch rund 211 km² umfasste. Die seither von Gletscherschwund und/oder Permafrostdegradation betroffenen Areale mit schlecht oder nicht konsolidierten Ablagerungen sind über das untersuchte Gebiet weitgehend gleichmäßig verteilt. Ein Großteil der erfassten Muranrisse tritt in entsprechenden und nun für gefährliche Prozesse disponierten Sedimenten auf.
Unter Berücksichtigung aktueller Klimaszenarien mit einem Anstieg der Lufttemperaturen um +1 bis +2 K bis zur Mitte des 21. Jahrhunderts würde sich das von Permafrost unterlagerte Areal im Untersuchungsgebiet um annähernd 72% gegenüber aktuellen Bedingungen verringern. Gleichzeitig würden die Gletscherflächen weitgehend verschwinden. In Zukunft ist durch anhaltenden Gletscherschwund und Permafrostdegradation daher mit einer Zunahme instabiler Schuttvorkommen und einer räumlichen Zunahme von Muranrissen und Murprozessen zu rechnen.

Keywords: *atmospheric warming, climate change, glacier recession, permafrost degradation, natural hazards, debris flow initiation, Little Ice Age, European Alps*

Addresses of authors: **B. Damm**, University of Vechta, ISPA, Universitätsstraße 5, D-49377 Vechta, Germany. E-Mail: bdamm@ispa.uni-vechta.de;
A. Felderer, Umweltbundesamt Wien, Umweltfolgenabschätzung & Klimawandel, Spittelauer Lände 5, A-1090 Wien, Austria.

1 Introduction

Glacier ice and permafrost ice react sensitive to climate variability in the European Alps (cf. Beniston et al. 1997, Davies et al. 2001, Arenson 2003, Damm & Langer 2006, Harris et al. 2009). Since the end of the "Little Ice Age" (LIA), about 150 years ago, the temperature increase especially affected the mountain cryosphere (e.g. Lewin & Warburton 1994, Harris et al. 2003, Stötter et al. 2003, Haeberli & Gruber 2009). High-mountain environments are presumed to response to atmospheric warming with glacier recession, increased permafrost temperatures and increased slope instabilities (Stoffel & Huggel 2012). In turn, these changes affect present and future natural hazards (cf. Haeberli et

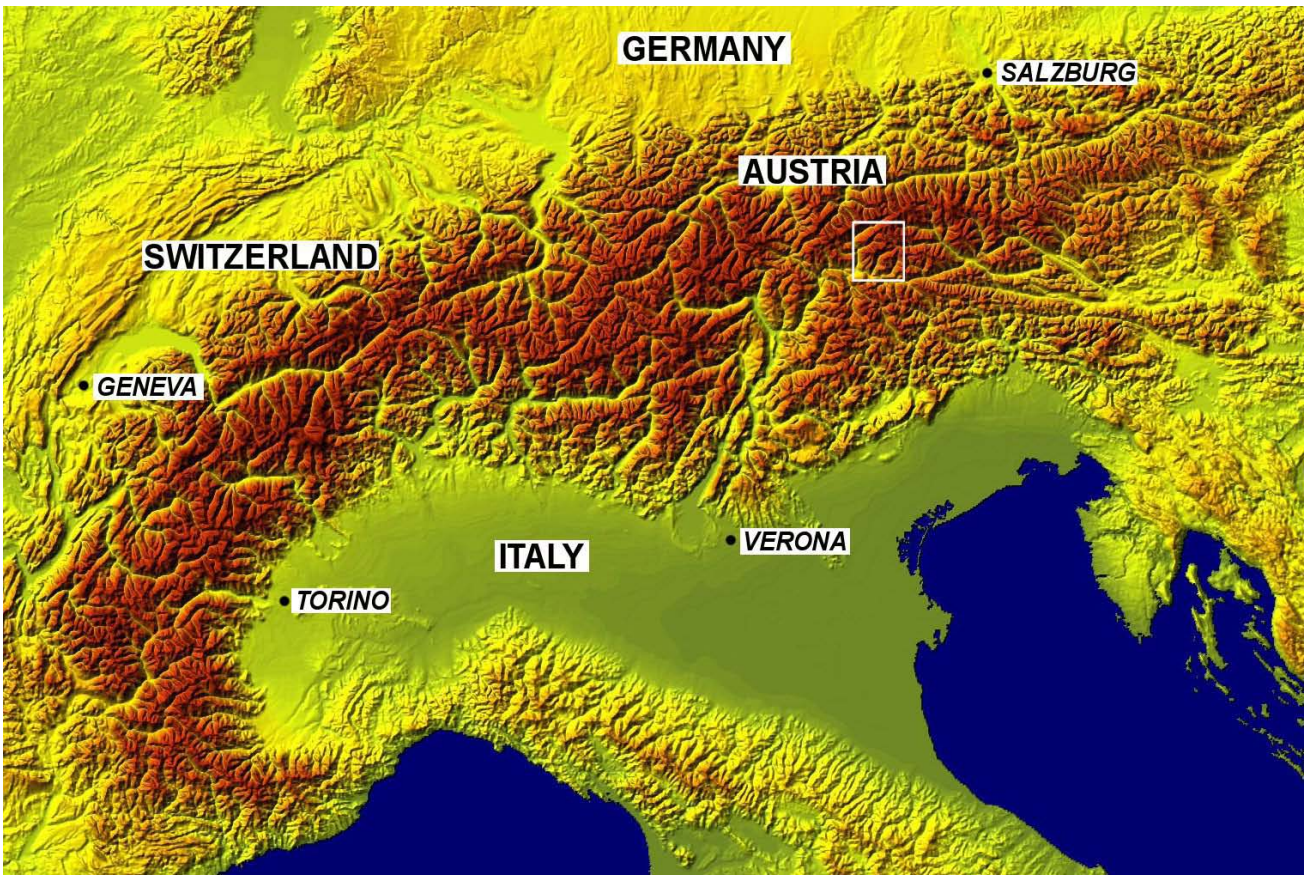

Fig. 1: European Alps with the location of the study area Rieserferner-Ahrn Nature Park (box) and the adjacent areas in South Tyrol (Italy).

Abb. 1: Der Alpenraum mit der Lage des Untersuchungsgebietes Naturpark Rieserferner-Ahrn (Kasten) und angrenzenden Gebieten in Südtirol (Italien).

al. 1999, Davies et al. 2001, Harris et al., 2001, Gruber et al. 2004, Harris 2005, Fischer et al. 2006, Damm & Felderer 2008, Pröbstl & Damm 2009, Keiler et al. 2010).

The glacier retreat since the end of the LIA is well documented in the European Alps (e.g. Damm 1998, Lambrecht & Kuhn 2007, Zemp et al. 2007, Winkler 2009, Winkler et al. 2010). In contrast, knowledge on the occurrence and distribution of permafrost and its spatiotemporal change during the last 150 years is comparatively scarce (cf. Vonder Muehll et al. 2007, Mair et al. 2008). Early investigations estimated an increase of the mean annual air temperature (MAAT) of about +1 to +2 K since the end of the LIA in permafrost areas of the European Alps (cf. Kuhn 1990, Patzelt & Aellen 1990, Haeberli 1992). Thus, based on a thermal gradient of 0.5–0.6 K/100 m, the lower limit of permafrost increased by 150–300 m during the last 150 years (e.g. Damm & Langer 2006, see also Haeberli 1999). Similarly, the prognosticated increase of air temperature of +1 to +2 K in the Eastern Alps by the middle of the 21st century (cf. Matulla et al. 2002, Matulla 2005) may lead to an additional rise of equilibrium line altitudes (ELA) of alpine glaciers of approximately 150–350 m and a further increase of the lower limits of permafrost of 200–400 m. According to this scenario, numerous glaciers within the eastern Alps would disappear and permafrost diminish to the highest summits. Both processes would affect the stability of mountain slopes and walls (e.g. Davies et al. 2001, Zemp et al. 2006, 2007).

The thawing of mountain permafrost is expected to significantly affect geotechnical properties of perennially frozen and unconsolidated debris and may result in a regional increase of debris flow frequency and magnitude (cf. Zimmermann et al. 1997, Harris 2005, Stoffel & Huggel 2012). Both, the complete melting of the permafrost body and the lowering of the thaw front within permafrost may reduce the shear strength of debris. Instabilities appear most likely to occur in areas near the lower limit of contemporary permafrost distribution, where permafrost bodies are thin and have temperatures close to 0°C (Haeberli 1992). Successive failure of the unconsolidated debris destabilized in such a manner can be triggered by the oversaturation of the active layer or debris above water-impermeable rock (e.g. Damm et al. 2012, Sandmeier et al. 2012) or by the release of fine grained material formerly fixed in the ice matrix (Sattler et al. 2011). However, the mechanisms of permafrost degradation and related slope stability are rather complex and many aspects and links remain uncertain to date (Stoffel & Huggel 2012).

The theoretical relation between permafrost degradation in non-creeping slope material and the initiation or increase of debris flow activity has hardly been verified. Field studies of debris flow-triggering mechanisms on thawing slopes remain a challenge given the difficulties to predict where and when slope instabilities occurs (cf. Harris 2005). Still, there are some observations of large numbers of debris flows originating in areas presumed to be at the margin of contemporary permafrost distribution supporting the hypothesis mentioned above (e.g. Zimmermann & Haeberli 1992, Stötter et al. 2003, Sattler et al. 2011). However, these studies are based on comparatively small study areas and/or short time-frames.

The present study aims to identify and to prove the rela-

tion among atmospheric warming, the spatial variability of glaciers and permafrost and the spatial distribution of debris flows in the study area during the last 150 years. Furthermore, the study aims to predict future spatial development of glacier and permafrost distribution in relation to debris flows as hazardous geomorphic processes using a GIS-based modelling approach. Climatic basis of the scenario is an expected increase of air temperature by +1.5 K until the middle of the 21st century (cf. Matulla et al. 2002, Matulla 2005, IPCC 2007b). Thus, for the first time this study provides data of the development of hazard potential from debris flow processes in the eastern Alps that exceed the spatial dimension of a catchment area (cf. Stötter et al. 2003, Kneisel et al. 2007, Damm & Felderer 2008).

2 Regional setting

The study area (fig. 1) extends to 450 km² and covers the Rieserferner-Ahrn Nature Park in South Tyrol (Italy) and adjacent areas of the Hohe Tauern National Park (Austria). It comprises the Rieserferner and Durreck Mountains, parts of the Zillertaler Alps south flank, and the outer west parts of the Venediger Mountains. Highest peaks in the study area reach up to 3,500 m a.s.l.

The central parts of the study area are dominated by granodiorite and tonalite bedrock. Additionally, pegmatite, paragneiss, mica schist, and orthogneiss are present. Large areas in the upper valleys are covered by poorly consolidated or unconsolidated sediments, particularly debris cones, talus, till and slide masses (Sandmeier et al. 2012). These sediments of Late Glacial and Holocene age can reach thickness of several decametres (Damm 1996). In general, most of the material is not or only sparsely vegetated. Erosion and debris flow processes can be frequently observed.

In general, the study area is characterized by comparably continental climate. Mean annual precipitation varies throughout the study area and is highest in the northern part of the Rieserferner-Ahrn Nature Park with up to 1030 mm (meteorological station of Prettau, period of 1981–2000), as this region is close to the central Alpine divide. Main precipitation period is the summer with frequent convective rainfall.

The thermal gradient shows significant seasonal variations and ranges from 0.7° C/100 m (summer) to 0.35° C/100 m (winter) based on data of nine meteorological stations between 821 m a.s.l. and 3105 m a.s.l. for the period 1994–2004 (tab. 1, cf. Damm & Langer 2006). Using a mean thermal gradient of 0.57 K/100 m (tab. 2), the calculated 0°C-isotherm is at 2323 m a.s.l.

Since the end of the Little Ice Age about AD 1860 the glacier area decreased by 50 to 65% in the Rieserferner-Ahrn Nature Park. The loss of glacier surface was marginally above-average compared to surrounding mountain groups of the Eastern Alps (cf. Damm 1998, Rösen 2005). Strong glacier recession was recorded during the last three decades when the ELA partially rose up to 3100 m a.s.l. within the study area. Significant mass losses occurred during this period, which were related to the decrease of the Accumulation Area Ratios (AAR), for example at the Western Rieser glacier (cf. Secchieri & Valentini 1985, Autonome Provinz Bozen 2010, 2011).

Meteorological station	Coordinate	Altitude [m a.s.l.]
Bruneck	11° 55′ 53″ E / 46° 48′ 16″ N	821
Mühlen	11° 56′ 25″ E / 46° 54′ 06″ N	870
Steinhaus	11° 58′ 34″ E / 46° 59′ 46″ N	1080
Antholz - Mittertal	12° 06′ 55″ E / 46° 51′ 30″ N	1236
Antholz - Obertal	12° 06′ 55″ E / 46° 52′ 14″ N	1320
Prettau	12° 05′ 51″ E / 47° 02′ 13″ N	1449
Rein in Taufers	12° 04′ 34″ E / 46° 56′ 46″ N	1600
Prettau - Merbalm	12° 07′ 21″ E / 47° 02′ 11″ N	2002
Prettau - Lengspitze	12° 07′ 52″ E / 47° 00′ 57″ N	3105

Tab. 1: Position and altitude of meteorological stations used for the calculation of thermal gradients of monthly and annual air temperature in the Rieserferner-Ahrn Nature Park and adjacent areas (source: Autonomous Province of Bozen-South Tyrol – Hydrographic Office).

Tab. 1: Lage und Höhe von Wetterstationen zur Berechnung thermischer Gradienten der monatlichen und jährlichen Lufttemperaturen im Naturpark Rieserferner-Ahrn und angrenzenden Gebieten (Quelle: Autonome Provinz Bozen-Südtirol – Hydrographisches Amt).

Tab. 2: Thermal gradients of monthly and annual air temperature and 0°C-isotherm based on data of nine meteorological stations in the Rieserferner-Ahrn Nature Park and adjacent areas for the period 1994–2004 according to Damm & Langer (2006).

Tab. 2: Thermische Gradienten der monatlichen und jährlichen Lufttemperatur sowie 0°C-Isotherme auf der Grundlage von neun Wetterstationen im Naturpark Rieserferner-Ahrn und angrenzenden Gebieten für den Zeitraum 1994–2004 nach Damm & Langer (2006).

Month	Jan	Feb	Mar	Apr	May	Jun	Jul	Aug	Sep	Oct	Nov	Dec	Year
Thermal gradient [K/100 m]	0,36	0,51	0,64	0,70	0,70	0,68	0,70	0,62	0,59	0,53	0,48	0,35	0,57
0°C – Isotherm [m a.s.l.]	-34	917	1633	2009	2801	3356	3473	3857	3072	2536	1439	280	2323

E&G / Vol. 62 / No. 2 / 2013 / 136–149 / DOI 10.3285/eg.62.2.05 / © Authors / Creative Commons Attribution License

3 Methods and data sets

Ground survey

Field work comprises the identification, mapping and assessment of geomorphological, hydrological and physical permafrost indicators, such as active and intact rock glaciers, frozen talus, frozen till and perennial snow patches, as well as measurements of basal temperature of snow cover (BTS) and temperature of meltwater from permafrost springs (Damm & Langer 2006).

Rock glaciers (fig. 2) and frozen talus are characterized by flow structures and were mapped, similar as snow patches, by use of aerial photographs in combination with ground-truth data. In contrast, frozen till and ice saturated talus (fig. 3) were identified by field survey. A total of 30 rock glaciers that still containing ice were recorded (cf. Damm 1996, 1999), indicating a mean lower limit at 2600 m a.s.l. In addition, ice saturated talus and till was mapped at 69 locations in altitudes between 2240 m a.s.l. and 3160 m a.s.l.

Ground surface temperatures (GST) were logged over a 5-years period from 2003 to 2008 using temperature loggers with a resolution of ±0.2 K. The ONSET HOBO loggers were positioned at 32 measuring points in altitudes of 2434 to 3340 m a.s.l. on different locations of rock glaciers, frozen talus, frozen till as well as in the surroundings of perennial snow patches. The recorded temperatures of -2.9°C to -9.5°C on south oriented slopes (2760 to 3040 m a.s.l.) and -2.9°C to -7.9°C on north oriented slopes (2560 to 2680 m a.s.l.) both characterize the long-term thermal conditions in permafrost areas during winter period and below snow cover. The basal temperature of snow cover (e.g. Haeberli 1973, Ishikawa & Hirakawa 2000) was detected with a transportable BTS sensor in February 2006 in the proglacial area of the Rieserferner glacier and on the glacier tongue. On the basis of ground surface temperatures and BTS the lower limit of discontinuous permafrost is expected to be at 2530 m a.s.l. in north orientation and at 2730 m a.s.l. in south orientation, indicating for this limit mean annual air temperatures (MAAT) of -1.5°C and -2.6°C respectively (fig. 4).

Use of analogues and digital spatial data

Ground survey and mapping were carried out using aerial photographs of 1997 and 1999 with a resolution of 4 m, digital

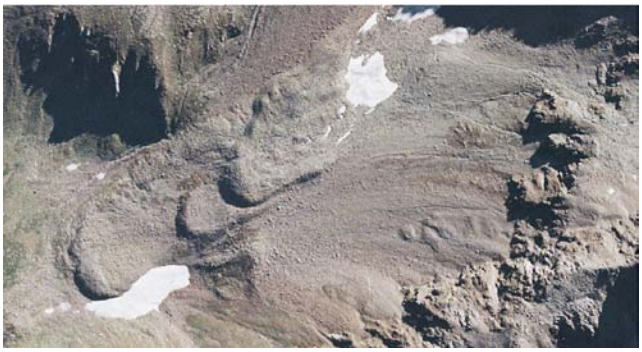

Fig. 2: Rock glaciers at 2500–2650 m a.s.l. in the Rieserferner-Ahrn Nature Park. These geomorphologic phenomena are characterized by flow structures and were mapped by use of aerial photographs and field survey (source: orthophoto of the Autonomous Province of Bozen).

Abb. 2: Durch Fließstrukturen charakterisierter Blockgletscher in 2500–2650 m ü.M. im Naturpark Rieserferner-Ahrn. Blockgletscher wurden für die vorliegende Arbeit auf der Grundlage von Orthophotos und Feldarbeiten kartiert (Quelle: Orthophoto der Autonomen Provinz Bozen-Südtirol).

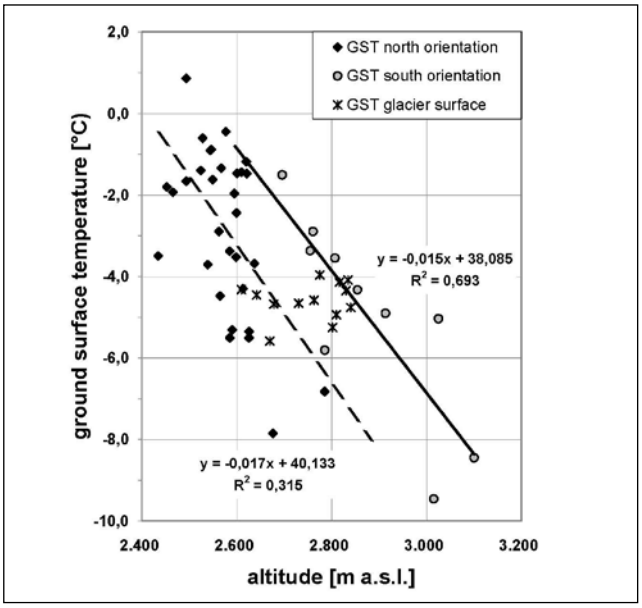

Fig. 4: Relationship between ground surface temperature and altitude derived from temperature logging and BTS measurements in the Rieserferner-Ahrn Nature Park (modified from Damm & Langer 2006).

Abb. 4: Beziehung zwischen BTS-Werten aus Temperaturlogger- und Sondenmessungen sowie der Geländehöhe der Messpunkte in unterschiedlichen Expositionen im Naturpark Rieserferner-Ahrn (verändert aus Damm & Langer 2006).

Fig. 3: Permafrost degradation in frozen till of a LIA terminal moraine at 2700 m a.s.l. (left hand) and ice saturated talus at 2600 m a.s.l. in the Rieserferner-Ahrn Nature Park (right hand) (photographs: B. Damm).

Abb. 3: Degradation von Permafrost in einer Stirnmoräne des neuzeitlichen Gletscherhochstandes um 1850 in rund 2700 m Höhe (links) und eisgesättigter Hangschutt in 2600 m Höhe im Naturpark Rieserferner-Ahrn (rechts) (Aufnahmen: B. Damm).

orthophotos with a resolution of 1 m, land cover maps and a digital elevation model (DEM 20x20 m grid) allocated by the government of the Autonomous Province of South Tyrol. Land cover maps are based on aerial photo interpretation and were available in a scale of 1:10,000 (Zanvettor et al. 2006).

Mapping of debris flow initiation areas

Debris flow initiation areas were identified using digital orthofotographs of the summer/autumn 1999 with a resolution of one meter and mapped as point data within ArcGIS 9.1 using the DEM of the Autonomous Province of South Tyrol. In general, initiation areas were defined as areas on which material is released due to erosion or land slide and from which the material is subsequently transported by flow processes in channelized and open-slope debris flows. The mapped debris flow source areas were classified based on spatial distribution, elevation and slope and intersected with the grid information of the DEM.

Assessment and simulation of permafrost distribution and glacier recession

The calculation of the present mountain permafrost distribution is based on the spatial distribution of perennial snow patches, which can be detected easily with remote sensing techniques. Widespread remnants of snow cover at the end of the late summer suggest low or negative ground temperatures underneath. Hence, the frequent occurrence of perennial snow patches may imply the existence of permafrost in the immediate vicinity (cf. Furrer & Fitze 1970, Rolshoven 1982).

The spatial distribution of 3000 perennial snow patches (total area: ca. 390 ha) between 2100 m a.s.l. and 3450 m a.s.l. was proved and mapped using aerial photographs of 1985, 1997, and 1999. Taking topography, terrain orientation and altitude into account, the assessment and simulation of permafrost distribution was operated by CRYOSNOW (cf. Damm & Langer 2006, Langer & Damm 2008). CRYOSNOW represents a statistical approach for the simulation of mountain permafrost and identifies to what extend the spatial frequency of perennial snow patches correspond to the spatial distribution of permafrost. In addition to the analysis of snow patches, the simulation also tested the measured and recorded characteristics of hydrological, physical and geomorphologic permafrost indicators (see above). Measured and approximated permafrost areas are significantly correlated. Thus, these parameters allow the determination of the lower limit of discontinuous permafrost areas in the study area (cf. Damm & Langer 2006).

Data about the recession of the glaciers in the Rieserferner-Ahrn Nature Park were derived from studies of Damm (1998), Rösen (2005) and supplementary analysis of aerial photographs and orthofoto images. Assuming a future increase of air temperature (Matulla et al. 2002, Matulla 2005, see below), the ELA of glaciers rises, based on a thermal gradient of 0.66° C per 100 m related to summer temperatures.

Analysis and prediction of hazard susceptibility in relation to a variable cryosphere

The distribution of permafrost areas and glacier extent for colder and warmer climatic conditions in the past and future was calculated to analyse and predict hazard susceptibility in relation to a variable cryosphere (cf. Damm & Langer 2006). Referring to this, the end of the LIA is supposed to represent an environmental status of increased geomorphologic stability with more extended permafrost and glacier areas compared to the present situation. In contrast, the future environmental status with an expected increase of air temperature by 1.5 K until the middle of the 21st century (cf. Matulla et al. 2002, Matulla 2005, IPCC 2007a, 2007b) is presumed to change to more unstable geomorphologic conditions with reduced permafrost area and shrunken glaciers compared to the current state. Thermally controlled permafrost extent is linked to the variability of the lower permafrost limit and was calculated using a thermal gradient of 0.57 K per 100 m in the study area (for general discussion see Ishikawa & Hirakawa 2000, Lewkowicz & Ednie 2004).

Erosion surfaces and detachment zones of debris flows predominantly occur in unconsolidated debris bare of vegetation in the study area. Hence, current areas with related sediments and absent vegetation cover were located from land cover maps and intersected with areas of permafrost degradation derived from permafrost and glacier modelling (cf. Damm & Langer 2006) to identify areas that would be exposed to debris flow processes under warmer climate conditions.

Fig. 5: 10 m thick section of a debris flow gully in the Klammbach catchment area. Extended surface area is covered by talus, debris cones and till deposits of Late Glacial and Holocene glaciations (photograph: B. Damm).

Abb. 5: Aufschluss in einem rund 10 Meter hohen Anriss einer Mure im Klammbach-Einzugsgebiet. Ausgedehnte Flächen im Umfeld sind von Hangschutt, Schuttkegeln und Moränen spät- und postglazialer Gletscher bedeckt (Aufnahme: B. Damm).

4 Results

4.1 Cryosphere-hazard-interactions: The Klammbach example

The Klammbach is a tributary stream of the Antholz creek and located in the south-eastern part of the Rieserferner Mountains (see fig. 8). The south facing drainage basin comprises an area of 6.5 km². Altitudes reach from 1,310 m to 3,270 m a.s.l. along a horizontal distance of 3,000 m. The catchment area of the Klammbach is composed of plutonic rock of the Rieserferner-Tonalite. Extended surface area is

E&G / Vol. 62 / No. 2 / 2013 / 136–149 / DOI 10.3285/eg.62.2.05

Fig. 6: Klammbach catchment area and main debris flow channel (left-hand photo) and extent of the August 2005-debris flow deposits in Antholz-Mittertal village (right-hand photo) (source: Autonomous Province of Bozen, flood protection office).

Abb. 6: Einzugsgebiet des Klammbachs mit dem zentralen Murgraben (links) und Ausdehnung der Murablagerungen vom August 2005 in Antholz-Mittertal (rechts) (Quelle: Autonome Provinz Bozen-Südtirol, Amt für Wasserschutzbauten).

covered by talus, debris cones and till deposits of Late Glacial and Holocene age (fig. 5). In general, in the upper parts of the Klammbach basin, in particular above the timberline, this material is poorly consolidated and sparsely covered by vegetation.

Several debris flows in the past were supplied from the above-mentioned debris sources. In order to evaluate the sediment characteristics in the Klammbach catchment, different sediment bodies were sampled and analysed concerning their particle size distribution. Grain size distribution was analysed from till of moraine bodies, talus of debris cones and frost debris of an ancient rock glacier (cf. tab. 3). Five samples were taken from debris flow initiation areas and another three samples from fluvial reworked sediments (cf. Sandmeier et al. 2012). In general, sampling was undertaken at natural cuts in the proximity of debris flow gullies and deposits. Particle size of the sediment was established according to DIN 18123 by wet-sieving using the required mesh width (DIN 18123).

Analyses result in contents of 37% to 76% of coarse grain fraction. Fine grain fraction contents high percentage of Sand (70–95%) and partly of silt (4–27%), the percentage of clay (0.3–2%), in contrast, is low (cf. tab. 3). The different sediments show substantial similarity in their composition and the grain size distribution of samples from debris flow initiation areas is highly similar to samples from debris cones or the rock glacier. According to grain size distribution (Bonnet-Staub 1999), existing proportion of fine and coarse grain (Iverson 2005) and weak consolidation these sediments are potential sources for debris flows and have to be considered to be controlling factors of these processes (cf. Znamensky & Gramani 2000, Remaître et al. 2005).

In summer 2005 a series of three debris flows occurred in the Klammbach gully. In total, about 140,000 m³ of debris was deposited on the alluvial cone in Antholz-Mittertal village (fig. 6). Agricultural area was inundated and the Antholz creek was dammed and displaced (Damm 2005). Run-off events and the successive two debris flows in July 2005 were triggered by comparatively low rainfall intensities of 0.5 to 3 mm per minute, which were measured in the upper part of the drainage basin. In contrast, torrential rainfall of 30 mm during 60 minutes on August 1st 2005 triggered the third debris flow with a total volume of about 100,000 m³ (cf. Sandmeier et al. 2012). This major event originated from a steep debris cone, sparsely covered by vegetation and located below rock flanks and, on the base of ground survey, debris-covered dead ice. The latter are relics of a glacier that melted continuously during the last 80 years. Overland flow from bedrock and dead ice was rapidly conducted into the sediment. Due to several former but smaller events (e.g.

*Tab. 3: Grain size distribution of different sediments in the Klammbach basin (modified from Sandmeier et al. 2012). *: sample originates from debris flow initiation area. +: sample originates from fluvial reworked sediment.*

*Tab. 3: Korngrößenverteilung unterschiedlicher Sedimente im Einzugsgebiet des Klammbachs (verändert nach Sandmeier et al. 2012). *: Probe aus Muranrissbereich. +: Probe aus fluvial umgelagertem Sediment.*

Source / Grain size class [mm]	Glacial sediment */+	Glacial sediment *	Glacial sediment	Glacial sediment +	Glacial sediment	Debris cone, talus *	Debris cone, talus *	Debris cone, talus *	Debris cone, talus	Debris cone, talus	Debris cone, talus +	Rock glacier, protalus
Coarse grain [> 2]	47.35	72.28	52.62	36.71	62.55	67.10	55.79	53.72	53.45	75.79	56.75	55.26
Fine grain [< 2]	52.65	27.72	47.38	63.26	37.45	32.90	44.21	46.28	46.55	24.21	43.25	44.74
Sand [0,02-1]	79.59	71.61	84.14	82.84	87.08	74.23	83.55	83.92	85.57	95.30	69.87	77.70
Silt [0,002-0,02]	18.54	26.55	15.10	15.83	12.00	23.74	14.99	13.07	13.73	4.41	27.20	20.32
Clay [<0,002]	1.88	1.84	0.76	1.33	0.92	2.03	1.46	3.01	0.70	0.29	2.93	1.98

1882, 1947, 1979) the Klammbach drainage system was already known to be an active debris-flow system (Amt für Wasserschutzbauten 2005). Hence, a storage basin with total retention capacity of 100,000 m³ was constructed on the alluvial cone as a response to the 2005-events.

The following parameters favoured and/or triggered runoff and debris flow processes in particular (Amt für Wasserschutzbauten 2005, Damm, 2005, 2008):

- On the base of ground survey, extended areas of low or not consolidated talus and till deposits occur in the sparse or not vegetated areas above 2,200 m a.s.l. They enclose an area of about 25% of the total drainage basin (6.5 km²).
- The source area of the August-2005-debris-flow was located in a more than 10 m thick talus cone in contact to bedrock. As result of the GIS-based simulations, this area was most likely underlain with permafrost and stable related to soil-mechanics until the middle of the 19th century. Ground survey indicates that meanwhile permafrost has completely melted.
- Since 1940 mean annual air temperature rose by 1 K in the Antholz valley (meteorological station of Antholz-Mittertal). The increase of MAAT caused a rise of the lower permafrost limit of most likely 100–180 m in the Klammbach drainage basin, using a mean thermal gradient of 0.57 K/100 m.
- Terrain surface properties controlled overland flow. The existence of extended debris covered dead ice without water retention capacity and steeply sloping rock flanks (approx. 60°) may have intensified runoff quantity and velocity in the rainfall area. Field study subsequent to the event indicates that runoff infiltrated into the talus cone and increased the soil water pressure.

On the base of ground survey and permafrost modelling, the debris flow processes in the Klammbach basin supposed to be substantially controlled by permafrost degradation in the study area. The detachment area of the main debris flow mentioned above is south exposed and located at an altitude of 2,600 m a.s.l. Until a few decades ago mountain permafrost still occurred in altitudes and expositions like these throughout the Rieserferner-Ahrn Nature Park (e.g. Damm & Langer 2006).

The degradation of permafrost due to the increase of MAAT caused soil mechanical instabilities of sediments and slopes. Similar to the Klammbach example, our study during the last two decades could frequently verify cryosphere-hazard-interactions in other areas of the Rieserferner-Ahrn Natural Park and the surroundings. This information is recorded in the natural hazard database for the study area and partly in the ED-30 hazard database of the South Tyrol state (Zischg et al. 2007).

4.2 Thermally-controlled development of the cryosphere in the Rieserferner-Ahrn Nature Park

Development of glaciation

The glacier retreat since the end of the LIA is comparably well documented in the Rieserferner-Ahrn Nature Park. The glacier surface decreased by 50% in the Rieserferner Mountains and by 65% in the upper Ahrntal Mountains over the past 150 years (Damm 1998, Rösen 2005). In general a reduction of glacier area is observed for all glaciers of the eastern European Alps since the end of the LIA (Zemp et al. 2007) however it was slightly above-average in the study area compared to other mountain ranges. Glacier volume in total decreased by 70% in the Rieserferner-Ahrn Nature Park, even though changes of individual glaciers show a wide variability, depending on their size, physiographic setting and altitude (cf. Lambrecht & Kuhn 2007). For this reason, maximum losses generally occurred in ablation zones, but numerous small glaciers completely disappeared.

At present glaciers of the Rieserferner-Ahrn Nature Park are retreating with increasing equilibrium line altitudes up to 3,000 to 3,100 m a.s.l. since the latest advance during

E&G / Vol. 62 / No. 2 / 2013 / 136–149 / DOI 10.3285/eg.62.2.05 / © Authors / Creative Commons Attribution License

Tab. 4: Equilibrium line altitudes (ELA) of glaciers in the Rieserferner-Ahrn Nature Park related to climatic conditions at the end of LIA (ca. "1850"), the present day situation (basis "2000") and compared with the scenario +1.5 K. Assuming that alpine summer temperature increases by +1.5 K, the ELA of glaciers rises by 230 m in the study area, based on a thermal gradient of 0.66° C per 100 m related.

Tab. 4: Mittlere Gleichgewichtslinie (ELA) auf Gletschern im Naturpark Rieserferner-Ahrn für Temperaturbedingungen zum Ende der „Kleinen Eiszeit" (um „1850"), für aktuelle Bedingungen (um „2000") und für ein Temperaturszenario +1.5 K. Auf der Grundlage eines thermischen Gradienten von 0.66° C /100m ist bei Zunahme der Sommertemperatur um 1.5 K mit einem Anstieg der Gleichgewichtslinie um rund 230 m zu rechnen.

Glacier area	ELA „1850" [m]	ELA, rise [m]	ELA „2000" [m]	ELA +1.5 K [m]
Rieserferner Mountains	2747	99	2846	3077
Ahrntal Mountains	2586	107	2693	2920
Study area, mean	2667	105	2772	2999

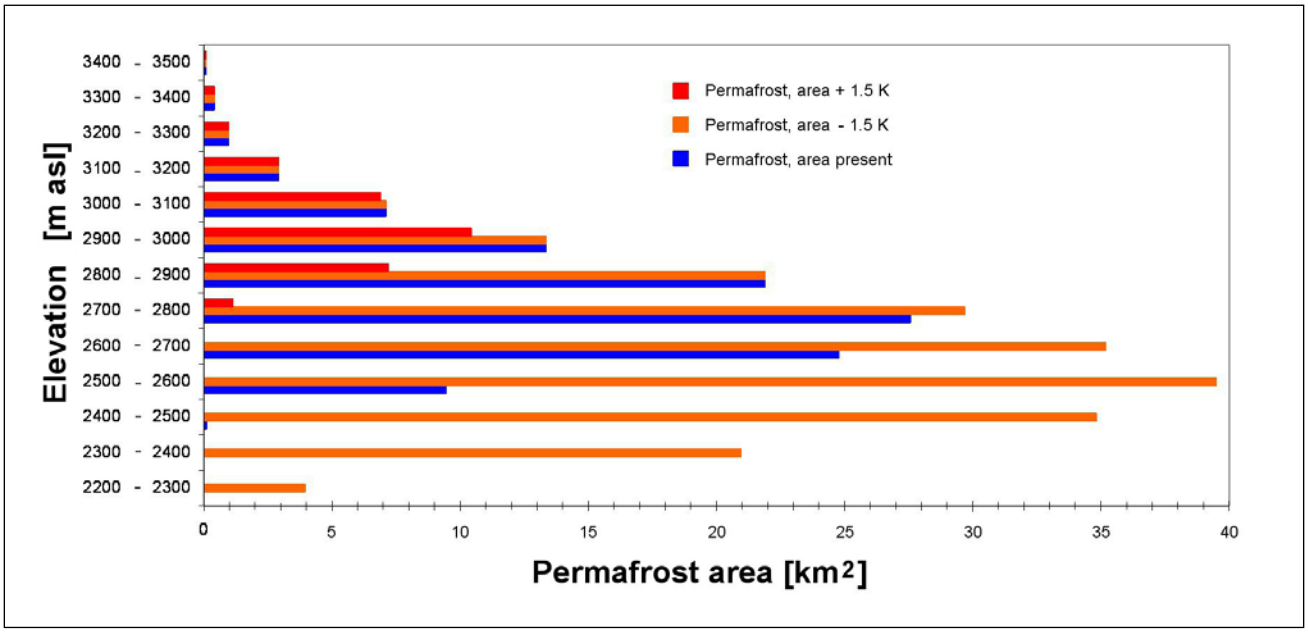

Fig. 7: Present-day extent of permafrost area in the Rieserferner-Ahrn Nature Park related to altitude and different thermal scenarios with lower (-1.5 K) and higher (+1.5 K) mean annual air temperature.

Abb. 7: Von Permafrost unterlagerte Flächen im Naturpark Rieserferner-Ahrn unter aktuellen Klimabedingungen sowie bei um 1.5 K höheren bzw. tieferen Temperaturen, differenziert nach Höhenstufen.

the 1970ies and 1980ies. Air temperature of the ablation period showed a rise of 0.3 to 0.5 K since 1981 and precipitation increased by 14%, as data of the meteorological station Antholz-Mittertal (1236 m a.s.l.) indicate. Based on reports of glaciological survey (Comitato Glaciologico Italiano 1977–2011), the development of the ablation area from about <50% of the glacier surface at the end of the 1970s to about 20% in 2010 (cf. Secchieri & Valentini 1985, Autonome Provinz Bozen 2010, 2011) is connected with the rise of ELA of 150–300 m, which seems to be the principle reason of the latest glacier recession in the study area (cf. Escher-Vetter & Siebers 2007).

Assuming the scenario of Matulla et al. (2002) and Matulla (2005) that forecast the increase of alpine summer temperature by +1.5 K during the next 40 years, the ELA of glaciers can rise by 230 m in the study area (cf. chapter 3, tab. 4). Hence, numerous glaciers continue to retreat and can be affected by significant loss of volume and extent. The total glacier area decreases to 1.1 km² in the Rieserferner Mountains and to 0.7 km² in the upper Ahrntal Mountains.

Development of permafrost distribution

Different scenarios of the spatial variation of mountain permafrost in the Rieserferner-Ahrn Nature Park (Damm & Langer 2006, Damm 2008) are interrelated with lower (-1.5 K) and higher (+1.5 K) MAAT compared to the present situation. The lower temperature represents the environmental situation before significant warming at the end of LIA, while the simulation with the higher temperature may describe possible future developments according to predicted climatic scenarios. The variability of the lower permafrost limit was calculated using a thermal gradient of 0.57 K per 100 m in the study area.

On the basis of field evidence and permafrost modelling, the present permafrost area in the Rieserferner-Ahrn Nature Park and that related to the thermal conditions at the end of LIA is calculated to be 109 km² and 211 km², respectively. Similarly, permafrost area would decrease by approximately 72% compared to present conditions with increasing MAAT of +1 to +2 K (fig. 7). The permafrost areas calculated for the present conditions and different sce-

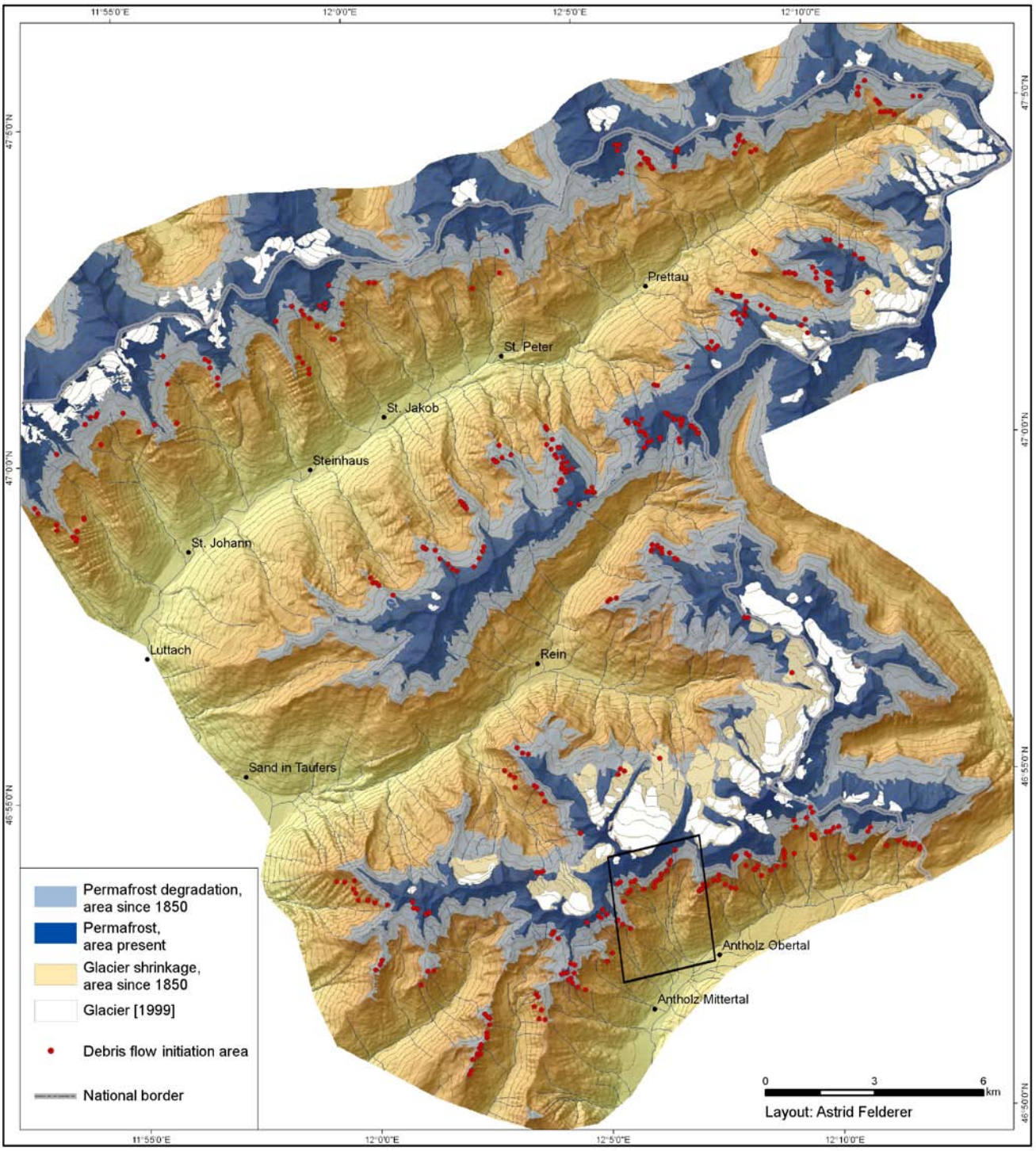

Fig. 8: General map of glacier extent, permafrost distribution and debris flow initiation areas in the Rieserferner-Ahrn Nature Park. In total, 408 debris flow initiation zones were mapped. The Klammbach drainage area is located in the south-eastern part of the study area (box).

Abb. 8: Gletscherflächen, Verbreitung von Permafrost und Lage von Muranrissen im Naturpark Rieserferner-Ahrn. Insgesamt konnten 408 Muranrisse kartiert werden. Das Einzugsgebiet des Klammbachs liegt im südöstlichen Teil des Untersuchungsgebiets (Kasten).

narios include all types of permafrost landforms and materials, such as loose rock, talus, rock glaciers and bedrock. Based on these assumptions present and future debris flow hazard potential is estimated as follows.

4.3 Debris flow initiation zones and debris flow hazards

Characterization and distribution of debris flow initiation zones

In total, 408 debris flow initiation zones were identified and mapped in the study area (fig. 8). In general, these zones occur throughout the study area and are concentrated in drainage basins of torrents and in various debris accumulations. Debris flow initiation zones are located to almost 50% in areas, where discontinuous permafrost degraded since the end of the LIA and to approximate 20% within the present area of probable permafrost. In contrast, only few detachment areas were identified in positions, where discontinuous permafrost is supposed to outlast the increase of temperature by +1.5 K.

E&G / Vol. 62 / No. 2 / 2013 / 136–149 / DOI 10.3285/eg.62.2.05 / © Authors / Creative Commons Attribution License

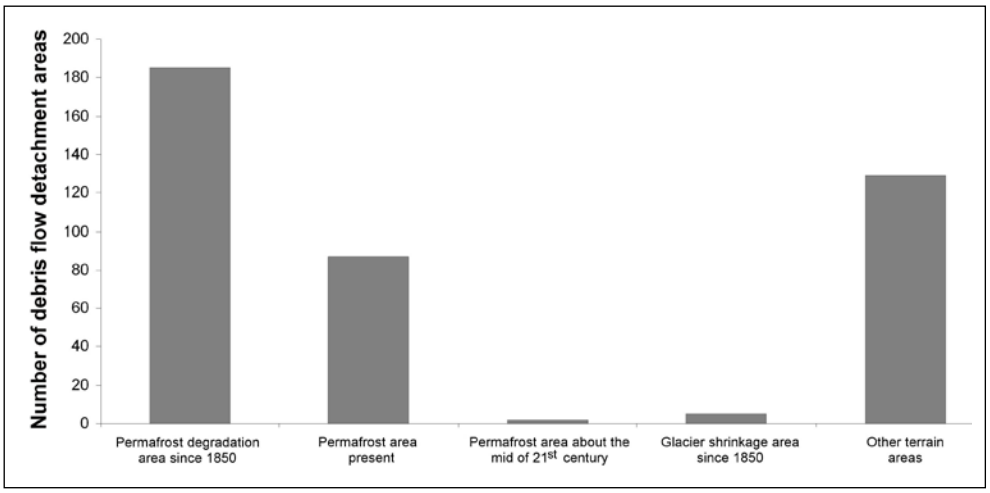

Fig. 9: Debris flow detachment areas in the Rieserferner-Ahrn Nature Park related to temporal variability of permafrost distribution and glacier extent.

Abb. 9: Häufigkeit von Muranrissen im Naturpark Rieserferner-Ahrn differenziert nach zeitlicher Variabilität von Permafrostverbreitung und Gletscherausdehnung.

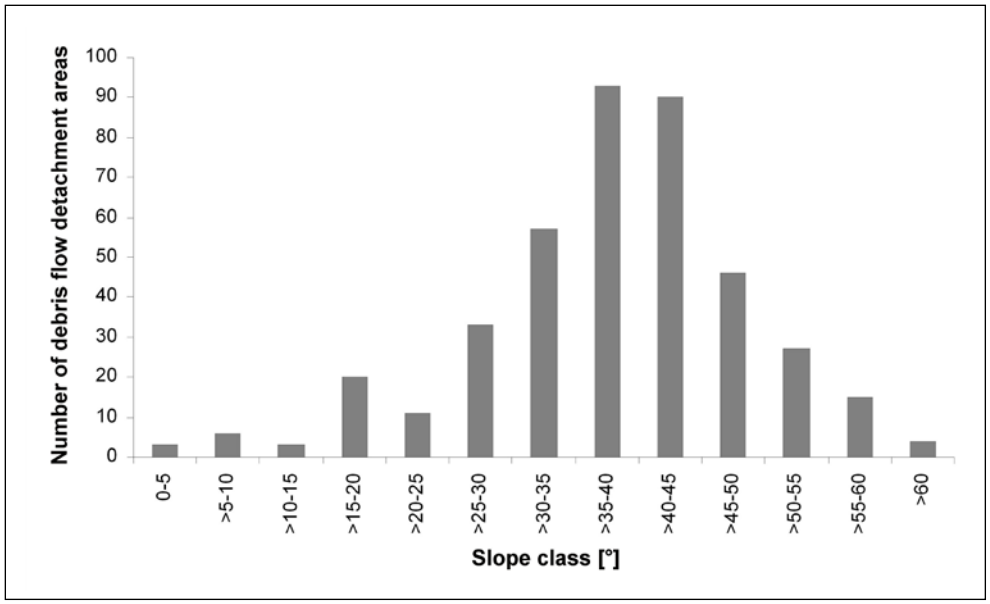

Fig. 10: Debris flow initiation areas in the Rieserferner-Ahrn Nature Park related to slope gradient. Two thirds occur at slopes of more than 35°.

Abb. 10: Verteilung von Muranrissen im Naturpark Rieserferner-Ahrn differenziert nach der Geländeneigung. Zwei Drittel der Prozesse ereignen sich oberhalb von 35°.

Debris flow source areas in reference to altitude, surface characteristics and slope

Debris flow detachment areas occur between 1,800 and 3,000 m a.s.l. in the Rieserferner-Ahrn Nature Park. The major part of initiation areas is located in altitudes between 2,100 and 2,800 m a.s.l. with a maximum between 2,300 and 2,700 m a.s.l., which coincide with the distribution of present discontinuous permafrost calculated by Damm & Langer (2006). Below 1,800 m a.s.l. close vegetation cover consisting of krummholz and forest as well as relief properties reduce the potential of debris flow sources.

Almost 47% of the mapped debris flows originated in loose rock, such as thick talus and till deposits, 37% in areas of alpine meadows and another 13% in shallow detritus covering bedrock (fig. 9). In general, source areas appear at slopes up to 66° with a maximum occurrence between 35–40° in the study area (fig. 10). Two thirds of these zones occurred at a slope steeper than 35°.

Permafrost degradation and stability of loose rock deposits

The distribution of debris flow initiation zones coincides significantly with the spatial occurrence of unconsolidated debris in the study area. Thus, areas are susceptible to debris flow processes, where permafrost ice is degrading and talus or till deposits exist in (steep) slopes, where soil mechanical stability is just near the limit.

In general, present-day debris flows mainly originate from areas covered with loose rock, where vegetation cover is absent and where permafrost degraded since the end of the LIA. Corresponding sediments cover about 38 km² and are uniformly distributed in the Rieserferner-Ahrn Nature Park. Furthermore, approximately 15 km² (39%) of the permafrost degradation area has a critical slope of 25–45° (fig. 10) and is therefore susceptible to debris flow processes with increasing MAAT.

According to field evidence and GIS-based permafrost modelling, the total area of loose rock underlain by permafrost amounts to 21.7 km² in the Rieserferner-Ahrn Nature Park (cf. Damm & Langer 2006). Increasing permafrost degradation enhances instability of talus and till deposits and generates possible debris flow initiation areas in the future. According to topographic and environmental conditions of the study area the complete degradation of permafrost in areas of loose rock is expected due to a long-term increase of MAAT by +1.5 K. In such a scenario, permafrost in rock faces solely remains above 3,000 m a.s.l. and cover 1.8 km². Overall, the area of debris sources and possible debris flow initiation zones increases to 20.1 km² in the study area.

5 Discussion

Climate variability mainly controls the cryosphere by changing air temperature and influences the mass balance of glaciers and the thickness and spatial extent of permafrost. As a consequence, glacier recession and permafrost degradation affect slope stability and enhance the susceptibility to mass movement and debris flow processes, as it is demonstrated in several studies (e.g. Haeberli 1999, Haeberli et al. 1999, Gruber et al. 2004, Damm & Felderer 2008).

In the context of debris flow processes, it is fundamental that permafrost degradation influences debris supply to talus and torrential systems, for instance by rock fall from destabilized rock walls and/or by permafrost creep processes (Davies et al. 2001, Gruber et al. 2004, Damm 2007). In addition, the lowering of the permafrost table may increase the susceptibility of slopes for instabilities and consequently the initiation of debris flows. In this case, the thickening of the active layer can increase sediment availability in potential debris flow initiation zones and may also reduce the shear strength of debris (for this discussion see Sattler et al. 2012).

The permafrost table acts as aquiclude and as potential failure plane during periods of elevated pore pressure, such as thaw periods or after strong summer rainfall (cf. Larsson 1982). Laboratory experiments of Rist (2007) showed that the active-layer instability was much stronger affected by the release of fine-grained material formerly fixed in the ice matrix than by the oversaturation of material at the base of the active layer. But for all, the most important factor seems to be the loss of internal ice in loose rock by permafrost melting, a process that was frequently observed in the study area (fig. 11, Damm & Langer 2006, Damm 2008, Sandmeier et al. 2012). The melting of interstitial ice leads to the loss of cohesion of previously frozen debris, which becomes available for mobilization by surface processes. The development of enhanced and irregular pore space and incomplete consolidation following permafrost thaw influences the hydraulic conductivity and reduces the overall mechanical slope stability (cf. Zimmermann & Haeberli 1992).

The hypothesized connection between permafrost degradation in non-creeping slope material and enhanced debris flow activity has not been proven yet, but observations of debris flows originating in areas presumed to be at the margin of contemporary permafrost distribution support this hypothesis (e.g. Zimmermann and Haeberli 1992; Stötter 1994; Damm and Felderer 2008, Sattler et al. 2012). Furthermore, it is supposed that slopes currently underlain by degrading permafrost become less stable with ongoing climate change, even with increasing altitude (Harris et al. 2001, 2009, Stoffel & Huggel 2012).

The cryosphere development in mountain regions has particular importance for issues of future research on climate impact (IPCC 2007a, 2007b). According to the „Special Report" of the IPCC from 2011 the number of cold days and nights will decrease, while the number of warm days and nights will increase in Europe (IPCC 2012). Corresponding changes are supposed to affect the alpine cryosphere directly by intensifying the continuous deglaciation and permafrost degradation.

In the present study the assessment of future natural hazard potential in the Rieserferner-Ahrn Nature Park is based on a scenario that forecasts an increase of air temperature by 1.5 K until the middle of the 21st century. Even though the world climate report (IPCC 2007b) forecasts a global rise of mean air temperature by 1.1 to 6.4 K by the end of the 21st century, in our study a more detailed differentiation seemed to be necessary for assessing climate impact. The climate change scenario assumes that the MAAT increases by +2 K within the next 30 to 40 years in the Eastern Alps showing a pronounced warming during summer time with +2.5 K (cf. Matulla 2005, OcCC 2007, Formayer et al. 2008). In this scenario, the mean annual precipitation hardly varies, while precipitation exhibits a significant seasonal variability. Overall, an increase of summer temperature (summer-JJA-season) by +1.5 to +2.5 K and winter temperature (winter-DJF-season) by +2 to +3 K is assumed for the study area and the surroundings. Hence, this study is based on a restrained assessment for the degradation of cryosphere and the resulting natural hazard potential by using a moderate climatic scenario of +1.5 K.

Fig. 11: Internal ice of talus and till deposits uncovered by sliding at the Hochgall peak north face in July 2011. Thickening of the seasonally unfrozen active layer and the loss of internal ice by permafrost degradation destabilize loose rock and favour the detachment of debris (photograph: B. Damm).

Abb. 11: Durch Rutschung freigelegtes Eis in Hangschutt- und Moränenablagerungen in der Nordflanke des Hochgalls im Juli 2011. Zunehmende Mächtigkeit der saisonalen Auftauschicht und tiefgreifende Permafrostdegradation destabilisieren Lockergesteine und begünstigen deren Abgleiten (Aufnahme: B. Damm).

The warming of the cryosphere in the study area exposed extended sources of destabilized debris in till deposits, creeping permafrost and talus during the past 150 years. Such sediments are susceptible to debris flow processes now. About 68% of the mapped debris flows originated in areas of destabilized debris. Furthermore, 74% of the detachment zones are located between 2,300 and 2,700 m a.s.l. Taking into account the climatic conditions of differing exposure this altitude range coincides with the present lower limit of permafrost in the Rieserferner-Ahrn Nature Park, which rose due to increased air temperature since the end of the LIA. In this perspective, the observable evidence of the recent past suggests a spatial expansion of the debris flow initiation area under warming conditions. In the Rieserferner-Ahrn Nature Park, the potential debris flow detachment area is calculated to increase by 52%, if long-term MAAT rises by +1.5 K.

E&G / Vol. 62 / No. 2 / 2013 / 136–149 / DOI 10.3285/eg.62.2.05 / © Authors / Creative Commons Attribution License

Similarly to the results of our study, significant correlation between debris flow source areas and permafrost degradation areas were found amongst others by Zimmermann & Haeberli (1992) in the Swiss Alps and by Stötter et al. (2003, 2012) in the Suldental in northern Italy. In contrast, the case study of Sattler et al. (2012) documents that distinct changes in the spatial position of debris flow initiation zones mainly occur at elevations above the current permafrost degrading areas in the Schnals valley (Ötztal Alps / Italy). The study was based on comparing debris flow activity since 1983 with modelled contemporary permafrost distribution. The authors conclude that the changes detected in debris flow activity were probably not influenced by atmospheric warming-induced permafrost degradation, but were connected with the thickening of the active layer. In accordance to the study of Sattler et al. (2012), about 20% of debris flow detachment area in the Rieserferner-Ahrn Nature Park occurred above the simulated lower limit of permafrost. On the one hand, this may be due to uncertainties of the modelling of permafrost distribution. On the other hand, it seems to be probable that numerousness debris flows are related to the thickening of the seasonally unfrozen active layer and were triggered by increased ground-water circulation and pressure.

About 40% of debris flow detachment areas are located at slopes between 26–45° in the Rieserferner-Ahrn Nature Park. Depending on lithologic characteristics slope inclinations like that are principally assumed to be susceptible to debris flow processes (e.g. Johnson & Rahn 1970, Lewin & Warburton 1994). Thus, relevant terrain needs to be especially considered when assessing potential debris flow hazards, when permafrost continues to thaw with warming conditions.

The present study has tried to shed light on the effects of climate change on the high mountain cryosphere and the response of morphodynamics. With focus on the identification of present causalities and the prediction of potential future processes, the investigation has addressed the impacts of glacier recession and permafrost degradation on the spatial occurrence and distribution of debris flow initiation areas. Despite of the recent progress in climate impact research, the study illustrated that some questions have to be treated in greater detail, so as to bridge the gaps in knowledge, which still exist.

6 Conclusions

Atmospheric warming in high mountain environments causes a range of impacts, including glacier recession, reduction of permafrost extent and distribution as well as changes in thermal permafrost properties. Furthermore, it is likely that climate change affects the occurrence of natural hazards, like shallow landslides and debris flows, as their initiation is related to the degradation of the cryosphere. However, changes in mass movement activity can hardly be detected so far.

The present study indicates the importance of atmospheric warming for the occurrence and susceptibility of debris flow processes in the eastern Alps. There is first evidence that it is possible to quantify the regional debris flow hazard potential on the basis of field survey, in-situ measurements, climate data analyses, and GIS-based simulations for different climate scenarios and variable geomorphic stability.

The presented scenarios of the future distribution of instable areas susceptible to debris flow hazards are based on the assumption that MAAT increases by 1.5 K by the middle of the 21st century. This may presumed to be a moderate increase of temperature in relation to the predicted climate development of the IPCC. The quantitative results of the present study can provide a basis for spatial planning and risk assessment.

Acknowledgements

The Autonomous Province of Bozen-South Tyrol supported the present study. The authors thank the Nature Parks Office for funding this research (Prot. Nr. 28.3.14.05/5399 /5270 /6408) and the Hydrographic Office – Meteorological Service for providing climate data.

References

Amt für Wasserschutzbauten (2005): ED-30 Datenbank Hochwasser- und Murereignisse. Autonome Provinz Bozen Südtirol.

Autonome Provinz Bozen (2010): Glacier Report – Westlicher Rieserferner, Haushaltsjahr 2008/2009. – Hydrographisches Amt Bozen, Sonderdruck zum Climareport Nr. 179, Bozen.

Autonome Provinz Bozen (2011): Glacier Report – Westlicher Rieserferner, Haushaltsjahr 2009/2010. – Hydrographisches Amt Bozen, Sonderdruck zum Climareport Nr. 192, Bozen.

Arenson, L.U. (2003): Unstable Alpine Permafrost: a Potentially Important Natural Hazard – Variations of Geotechnical Behaviour with Time and Temperature. – Publications of the Institute for Geotechnical Engineering (IGT), 218: 4/03. Vdf Hochschul-Verlag der ETH, Zürich.

Beniston, M., Diaz, H.F. & Bradley, R.S. (1997): Climate change at high elevation sites. An overview. – Climatic Change, 36(2): 233–251.

Böhm, R., Schöner, W., Auer, I., Hynek, B., Kroisleitner, C. & Weyss, G. (2007): Gletscher im Klimawandel. Vom Eis der Polargebiete zum Goldbergkees in den Hohen Tauern. – Zentralanstalt für Meteorologie und Geodynamik (ZAMG), Wien.

Bonnet-Staub, J. (1999): Définition d'une typologie des dépôts de laves torentielles et identification de critères granulométriques et géotechniques concernant les zones sources. – Bulletin of Engineering Geology and the Environment, 57: 359–367.

Comitato Glaciologico Italiano (1977–2011): Relazioni della campagna glaciologica. – Geografia Fisica e Dinamica Quaternaria, 1–35.

Damm, B. (1996): Gletscher-, Landschafts- und Klimaentwicklung in der Rieserfernergruppe (Tirol) seit dem Spätglazial. – Göttinger Geographische Abhandlungen, 104: 1–186.

Damm, B. (1998): Der Ablauf des Gletscherrückzuges in der Rieserfernergruppe (Tirol) im Anschluss an den Hochstand um 1850. – Zeitschrift für Gletscherkunde und Glazialgeologie, 34: 141–159.

Damm, B. (1999): L' evolutione dei ghiacciai, del paesaggio e del clima nei Monti di Tures (Alto Adige) dal Tardiglaciale. – Geografia Fisica e Dinamica Quaternaria, 22: 49–55.

Damm, B. (2005): Murereignisse am Klammbach im Antholzertal im Juli/August 2005 – Ergebnisse der Feldbegehungen. Universität Göttingen, unveröffentlichter Bericht.

Damm, B. (2007): Temporal Variations of Mountain Permafrost Creep in the Eastern European Alps derived from Rockglacier Monitoring. – Quaternary International 167–168 (Supplement): 88–89.

Damm, B (2008): Auswirkungen von Permafrostdegradation und Gletscherschwund im Naturpark Rieserferner-Ahrn. – Abschlussbericht, Autonome Provinz Bozen (unpublished).

Damm, B. & Langer, M. (2006): Kartierung und Regionalisierung von Permafrostindikatoren im Rieserfernergebiet (Südtirol/Osttirol). – Mitteilungen der Österreichischen Geographischen Gesellschaft, 148: 295–314.

Damm, B. & Felderer, A. (2008): Identifikation und Abschätzung von Murprozessen als Folge von Gletscherrückgang und Permafrostdegradation im Naturpark Rieserferner-Ahrn (Südtirol). – Abhandlungen der Geologischen Bundesanstalt, 62: 29–32.

Damm, B., Pröbstl, U. & Felderer, A. (2012): Perception and Impact of Natural Hazards as Consequence of Warming of the Cryosphere in Tourism Destinations. A Case Study in the Tux Valley, Zillertaler Alps, Austria. – Interpraevent, 12: 90–91.

Davies, M.C.R., Hamza, O. & Harris, C. (2001): The Effect of Rise in Mean Annual Temperature on the Stability of Rock Slopes Containing Ice-Filled Discontinuities. – Permafrost and Periglacial Processes, 12: 137–144.

DIN 18123 (1996): Baugrund, Untersuchung von Bodenproben. Bestimmung der Korngrößenverteilung, Normenausschuß Bauwesen im DIN Deutsches Institut für Normung e.V., Berlin.

Escher-Vetter, H. & Siebers, M. (2007): Sensitivity of glacier runoff to summer snowfall events. – Annals of Glaciology, 46: 309–315.

Fischer, L., Kääb, A., Huggel, C. & Noetzli, J. (2006): Geology, glacier retreat and permafrost degradation as controlling factors of slope instabilities in a high-mountain rock wall: the Monte Rosa east face. – Natural Hazards and Earth System Sciences, 6: 761–772.

Formayer, H., Clementschitsch, L., Kromp-Kolb, H. (2008): Regionale Klimaänderung in Österreich. Global2000 Umweltforschungsinstitut (http://www.global2000.at./files/klimawandel_oesterreich.pdf).

Furrer, G. & Fitze, P. (1970): Beitrag zum Permafrostproblem in den Alpen. – Vierteljahrsschrift der Naturforschenden Gesellschaft Zürich, 115: 353–368.

Gruber, S., Hoelzle, M. & Haeberli, W. (2004): Permafrost thaw and destabilization of Alpine rock walls in the hot summer of 2003. – Geophysical Research Letters, 31: L13504.

Haeberli, W. (1973): Die Basis-Temperatur der winterlichen Schneedecke als möglicher Indikator für die Verbreitung von Permafrost in den Alpen. – Zeitschrift für Gletscherkunde und Glazialgeologie, 9: 221–227.

Haeberli, W. (1990): Permafrost. Internationale Fachtagung über Schnee, Eis und Wasser der Alpen in einer wärmeren Atmosphäre. – Mitteilungen der Versuchsanstalt für Wasserbau, Hydrologie und Glaziologie, ETH Zürich, 108: 71–88.

Haeberli, W. (1992): Possible effects of climate change on the evolution of Alpine Permafrost. – Catena Supplement, 22: 23–35.

Haeberli, W. (1999): Hangstabilitätsprobleme im Zusammenhang mit Gletscherschwund und Permafrostdegradation im Hochgebirge. – Relief, Boden, Paläoklima, 14: 11–30.

Haeberli, W., Kääb, A., Hölzle, M., Bösch, H., Funk, M., Vonder Mühll, D. & Keller, F. (1999): Eisschwund und Naturkatastrophen im Hochgebirge. – Vdf Hochschul-Verlag ETH Zürich.

Haeberli, W. & Gruber, S. (2009): Global warming and mountain permafrost. In: Margesin, R. (Ed): Permafrost Soils. – Soil Biology, 16: 205–218.

Harris, C. (2005): Climate change, mountain permafrost degradation and geotechnical hazard. – In: Huber, U., Bugmann, H. & Reasoner M. (Eds): Global Change and Mountain Regions. – Advances in Global Change Research V. 23, Dordrecht (Springer), 215–224.

Harris, C., Davies, M. & Etzelmüller, B. (2001): The assessment of potential geotechnical hazards associated with mountain permafrost in a warming global climate. – Permafrost and Periglacial Processes, 12: 145–156.

Harris, C., Vonder Mühll, D., Isaksen, K., Haeberli, W., Sollid, J.L., King, L., Holmlund, P., Dramis, F., Guglielmin, M. & Palacios, D. (2003): Warming Permafrost in European Mountains. – Global and Planetary Change, 39: 215–225.

Harris, C., Arenson, L.U., Christiansen, H.H., Etzelmüller, B., Frauenfelder, R., Gruber, S., Haeberli, W., Hauck, C., Hölzle, M., Humlum, O., Isaksen, K., Kääb, A., Kern-Lutschg, M.A., Lehning, M., Matsuoka, N., Murton, J.B., Noetzli, J., Phillips, M., Ross, N., Seppala, M., Springman, S.M. & Vonder Muehll, D.V. (2009): Permafrost and climate in Europe: Monitoring and modelling thermal, geomorphological and geotechnical responses. – Earth-Science Reviews, 92: 117–171.

IPCC (2007a): Climate Change 2007: The Scientific Basis. Summary for Policymakers, Cambridge. www.ipcc.ch (12.12.07).

IPCC (2007b): Climate Change 2007: Synthesis Report. http://www.ipcc.ch/publications/.

IPCC (2012): Managing the risks of extreme events and disasters to advance climate change adaption. http://ipcc-wg2.gov/SREX/.

Ishikawa, M. & Hirakawa, K. (2000): Mountain Permafrost Distribution Based on BTS Measurements and DC Resistivity Soundings in the Daisetsu Mountains, Hokkaido, Japan. – Permafrost and Periglacial Processes, 11: 109–123.

Iverson, R.M. (2005): Debris-flow mechanics. In: Jakob, M. & Hungr, O. (Eds.): Debris-flow Hazards and Related Phenomena. Springer, Berlin, 105–134.

Johnson, A.M. & Rahn, P.H. (1970): Mobilization of debris flows. – Zeitschrift für Geomorphologie N.F, Suppl.-Bd., 9:168–186.

Keiler, M., Knight, J. & Harrison, S. (2010): Climate change and geomorphological hazards in the eastern European Alps. – Philosophical Transactions of the Royal Society – Mathematical Physical and Engineering Sciences, 368(1919): 2461–2479.

Kneisel, C., Rothenbühler, C., Keller, F. & Haeberli, W. (2007): Hazard assessment of potential periglacial debris flows based on GIS-based spatial modelling and geophysical field surveys: a case study in the Swiss Alps. – Permafrost and Periglacial Processes, 18: 259–268.

Kuhn, M. (1990): Energieaustausch Atmosphäre – Schnee und Eis. – Int. Facht. Schnee, Eis u. Wasser der Alpen in einer wärmeren Atmosphäre. – Mitteilungen VAW, ETH Zürich, 108: 21–32.

Lambrecht, A. & Kuhn, M. (2007): Glacier changes in the Austrian Alps during the last three decades, derived from the new glacier inventory. – Annals of Glaciology, 46: 177–184.

Langer, M. & Damm, B. (2008): CRYOSNOW – An approach for mapping and simulation of mountain permafrost distribution based on the spatial analyses of perennial snow patches. – Geophysical Research Abstracts 10 (http://meetings.copernicus.org/www.cosis.net/abstracts/EGU2008/11263/EGU2008-A-11263.pdf.)

Larsson, S. (1982): Geomorphological effects on the slopes of Longyear Valley, Spitsbergen, after a heavy rainstorm in July 1972. – Geografiska Annaler, Series A Physical Geography, 64: 105–125.

Lewin, J. & Warburton, J. (1994): Debris flow in an alpine environment. – Geog. J. Geog. Assoc. 343, 79(2): 98–107.

Lewkowicz, A. & Ednie, M. (2004): Probability Mapping of Mountain Permafrost Using the BTS Method, Wolf Creek, Yukon Territory, Canada. – Permafrost and Periglacial Processes, 15: 67–80.

Mair, V., Lang, K., Tagnin, S., Zischg, A., Krainer, K., Stötter, J., Zilger, J., Belitz, K., Schenk, A., Damm, B., Kleindienst, H., Bucher, K. & Munari, M (2008): PROALP – Rilevamento e Monitoraggio dei Fenomeni Permafrost. – Neve e Valanghe, 64: 50–59.

Matulla, C. (2005): Regional, seasonal and predictor-optimized downscaling to provide groups of local scale scenarios in the complex structured terrain of Austria. – Meteorologische Zeitschrift, 14/1: 31–47.

Matulla, C., Groll, N., Kromp-Kolb, H., Scheifinger, H., Lexer, M.J. & Widmann, M. (2002): Climate change scenarios at Austrian National Forest Inventory sites. – Climate Research, 22: 161–173.

OcCC (2007): Climate Change and Switzerland 2050 – Expected Impacts on Environment, Society and Economy. – OcCC – Organe consultatif sur les changements climatiques (Swiss Academy of Sciences), http://proclimweb.scnat.ch/portal/ressources/794.pdf.

Patzelt, G. & Aellen, M. (1990): Gletscher. – Int. Facht. Schnee, Eis u. Wasser der Alpen in einer wärmeren Atmosphäre. – Mitteilungen VAW, ETH Zürich, 108: 49–70.

Pröbstl, U. & Damm, B. (2009): Perception and evaluation of natural hazards as a consequence of glacier retreat and permafrost degradation in tourism destinations – a case study in the Tux Valley (Zillertaler Alps, Austria). In: Kromp-Kolb, H. & Schwarzl, I. (Eds.) StartClim 2008 „Adaption to Climate Change in Austria", BOKU, Vienna, 23–24 and 38–41.

Remaître, A., Malet, J.P. & Maquaire, O. (2005): Morphology and sedimentology of a complex debris flow in a clay-shale basin. – Earth Surface Processes and Landforms 30: 339–348.

Rist, A. (2007); Hydrothermal processes within the active layer above alpine permafrost in steep scree slopes and their influence on slope stability. – Universität Zürich, Schriftenreihe Physische Geographie, Volume 57.

Rösen, P. (2005): Die rezente Gletscherentwicklung im oberen Ahrntal (Prettau/Südtirol). – Diploma thesis, University of Göttingen.

Rolshoven, M. (1982): Alpines Permafrostmilieu in der Lasörlinggruppe/Nördliche Deferegger Alpen (Osttirol). – Polarforschung, 52: 55–64.

Sandmeier, C., Damm, B. & Terhorst, B. (2012): Murgangpotential eines alpinen Einzugsgebietes im Antholzer Tal (Südtirol). – Interpraevent 12/1: 339–350.

Sattler, K., Keiler, M., Zischg, A. & Schrott, L. (2011): On the Connection between Debris Flow Activity and Permafrost Degradation: A Case Study from the Schnalstal, South Tyrolean Alps, Italy. – Permafrost and Periglacial Processes, 22: 254–265.

Secchieri, F. & Valentini, P. (1985): Indagine glaciologica sulla Vedretta Alta e sulla Vedretta Occidentale di Ries (Alto Adige). – Geografia Fisica e Dinamica Quaternaria, 8: 137–143.

Stötter, J., Fuchs, S., Keiler, M. & Zischg, A. (2003): Oberes Suldental. Eine Hochgebirgsregion im Zeichen des Klimawandels. – Innsbrucker Geographische Studien, 33/3: 239–281.

Stötter, J., Zischg, A. & Sailer, R. (2012): Entwicklung des Permafrostes in Südtirol. – Innsbrucker Geographische Studien, 39: 45–66.

Stoffel, M. & Huggel, C. (2012): Effects of climate change on mass movements in mountain environments. – Progress in Physical Geography, 36: 421–439.

Vonder Muehll, D., Noetzli, J., Roer, I., Makowski, K. & Delaloye, R. (2007): Permafrost in Switzerland 2002/2003 and 2003/2004. – Glaciological Report (Permafrost) No. 4/5 of the Cryospheric Commission (CC) of the Swiss Academy of Sciences (SCNAT) and Department of Geography, University of Zurich.

Winkler, S. (2009): Gletscher und ihre Landschaften – eine illustrierte Einführung. – WBG Darmstadt.

Winkler, S., Chinn, T., Gärtner-Roer, I., Nussbaumer, S.U., Zemp, M. & Zumbühl, H.J. (2010): An introduction to mountain glaciers as climate indicators with spatial and temporal diversity. – Erdkunde 64: 97–118.

Zanvettor, G., Colmano, D. & Iellici, M. (2006): Landeskartographie und Geographisches Informationssystem – Beschreibung der Kartographischen Daten. – Autonome Provinz Bozen-Südtirol, Amt für überörtliche Raumordnung.

Zemp, M., Haeberli, W., Hoelzle, M., & Paul, F. (2006): Alpine glaciers to disappear within decades? – Geophysical Research Letters, 33: L13504.

Zemp, M., Paul, F., Hoelzle, M. & Haeberli, W. (2007): Glacier fluctuations in the European Alps 1850–2000: an overview and spatio-temporal analysis of available data. – In: Orlove, B., Wiegandt, E. & Luckman, B. (Eds.): The darkening peaks: Glacial retreat in scientific and social context: 152–167, University of California Press.

Zimmermann, M. & Haeberli, W. (1992): Climatic change and debris flow activity in high mountain areas; a case study in the Swiss Alps. – Catena Supplement, 22: 59–72.

Zimmermann, M., Mani, P., Gamma, P., Gsteiger, P., Heiniger, O. & Hunziker, G. (1997): Murganggefahr und Klimaänderung – ein GIS-basierter Ansatz. – Schlussbericht NFP31, Vdf Hochschulverlag an der ETH Zürich, 161 pp.

Zischg, A., Macconi, P., Pollinger, R., Sperling, M., Mazzorana, B., Marangoni, N., Berger, E. & Staffler, H. (2007): Historische Überschwemmungs- und Murgangereignisse in Südtirol. Erhebung und Dokumentation. – Der Schlern, 81/3: 3–16.

Zischg, A., Mair, V., Tonidandel, D. & Lang, K. (2012): Berücksichtigung von Permafrost in der Gefahrenzonenplanung in Südtirol. – Innsbrucker Geographische Studien, 39: 173–187.

Znamensky, D. & Gramani, M. (2000): Debris-flow grain-size analysis. In: Wieczorek, G. & Naeser, N. (Eds.): Debris-Flow Hazards Mitigation: Mechanics, Prediction, and Assessment. Balkema, Rotterdam, 537–545.

E&G Quaternary Science Journal
Volume 62 / Number 2 / 2013 / 150–161 / DOI 10.3285/eg.62.2.06
www.quaternary-science.net

GEOZON SCIENCE MEDIA
ISSN 0424-7116

Geomorphological and geophysical analyses in a landslide area near Ebermannstadt, Northern Bavaria

Daniel Jäger, Christine Sandmeier, Daniel Schwindt, Birgit Terhorst

How to cite: Jäger, D., Sandmeier, C., Schwindt, D., Terhorst, B. (2013): Geomorphological and geophysical analyses in a landslide area near Ebermannstadt, Northern Bavaria. – E&G Quaternary Science Journal, 62 (2): 150–161. DOI: 10.3285/eg.62.2.06

Abstract: The region close to Ebermannstadt is highly prone to landslide activity. Geomorphological mapping, geophysical surveys (electric resistivity and seismic refraction) and substrate analyses were applied to investigate a landslide which was triggered in 1957. The study aims to reconstruct observations of the 1957 event and to compare the earlier situation with the recent surface and subsurface conditions.
It was possible to trace the former observations in the relevant slope area and furthermore, to classify different slide masses and processes. The study also shows area-wide occurrence of ancient slide masses, which were incorporated during the landslide event of 1957. A remobilization of these accumulations cannot be excluded.

Geomorphologische und geophysikalische Untersuchungen auf einer Rutschung bei Ebermannstadt, Nordbayern

Kurzfassung: Die Region um Ebermannstadt ist stark anfällig für Massenbewegungen. Eine Rutschung aus dem Jahr 1957 wurde geomorphologisch kartiert und mit geophysikalischen Messungen (Gleichstromgeoelektrik sowie Refraktionsseismik) untersucht. Die Ziele der Untersuchungen waren eine Rekonstruktion der Beobachtungen von 1957 sowie deren Vergleich mit der heutigen Oberfläche und dem oberflächennahen Untergrund.
Die Ergebnisse zeigen, dass die früheren Beobachtungen auch heute noch Gültigkeit besitzen. Darüber hinaus ist es möglich, einzelne Rutschungselemente und Prozesse zu differenzieren. Die Studie zeigt zudem die Verbreitung von alten Rutschmassen, welche in die Rutschung von 1957 eingebunden waren. Eine erneute Remobilisierung dieser Ablagerungen kann nicht ausgeschlossen werden.

Keywords: *Cuesta landscape, Franconian Alb, landslide, earth flow, geomorphological mapping, Electric resistivity tomography, Seismic refraction tomography*

Addresses of authors: **D. Jaeger***, **C. Sandmeier**, **D. Schwindt**, **B. Terhorst**, University of Wuerzburg, Institute for Geography and Geology, Am Hubland, 97074 Würzburg, Germany. E-mail: Daniel.Jaeger@uni-wuerzburg.de; **corresponding author*

1 Introduction

Cuesta scarp slopes are highly prone to slide activity due to susceptible geological and geomorphological conditions. The development of cuesta landscapes like the Franconian Alb is controlled by slightly inclined permeable and non-permeable bedrock. The geological setting results in the characteristic cuesta landforms of almost flat backslopes and steeper front slopes (Schmidt & Beyer 2001). The latter usually consist of steep, sometimes cliff-like upper slopes, formed in the resistant, permeable bedrock and a less inclined lower slope in non-resistant, impermeable layers. This bipartite structure leads to a strong disposition for mass movements. Water can be easily drained through fissures in the upper bedrock – in particular in karstic structures of limestones. In the middle and lower slope areas, impermeable clay- and marlstones lead to an accumulation of water, decreased consolidation and the formation of slip surfaces.

Although mass movements are a common hazard in low mountain areas like the Franconian Alb, only devastating events, endangering buildings, roads or infrastructure are noticed in public (Hütteroth 1994). Various scientific landslide studies at the Franconian Alb investigate the distribution of landslides for selected regions. In general, the focus is set on internal (lithological, structural and internal morphometric) controlling factors (von der Heyden et al. 1993, Hütteroth 1994, von der Heyden 2004), comparable to studies from other German low mountain areas (e.g. Wenzel 1994, Terhorst 2001, Beyer 2002, Schmidt & Beyer 2001). Geological studies (e.g. Zürl 1980, Hammer 1984) primarily comprise soil and rock mechanisms or deal with hydraulic patterns within slide masses.

One of the first works on landslide distribution in the Wiesent River valley was published by Dorn (1920). After the respective movements Freyberg (1957, 1961), Müller (1957) and Hegenberger (1961) described visible processes, triggers and morphological landslide elements of the major slides close to Ebermannstadt and provided first information on the slide events. The present study is based on the observations of Müller (1957) at the Hasenberg landslide area.

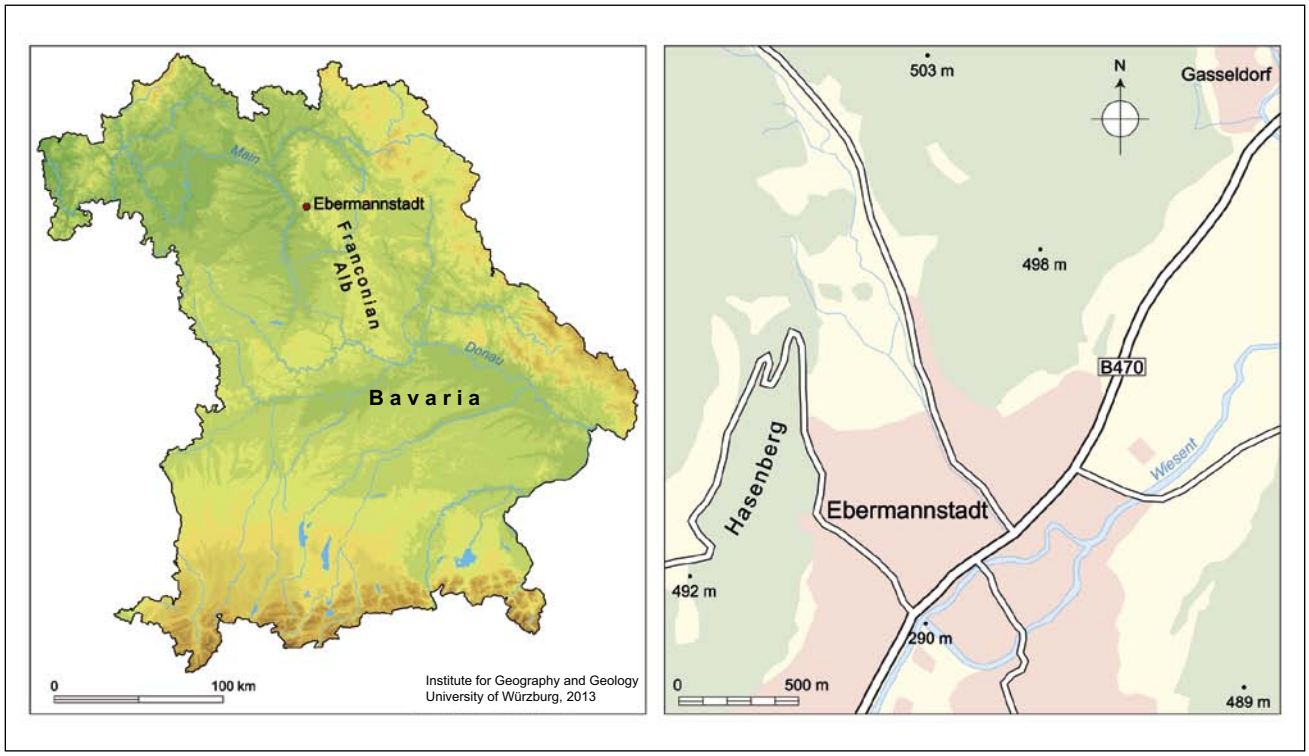

Fig. 1: Location map of the study area.

Abb. 1: Übersichtskarte des Arbeitsgebiets.

In order to analyze controlling factors as well as past processes in the landslide mass, an accurate inventory of the slope is necessary (McKean & Roering 2004). High resolution Digital Terrain Models (DTM) derived from airborne laser altimetry (LiDAR) provide detailed information of the earths' surface (van Westen et al. 2002) and therefore enable more detailed mapping of relief units, which include landsystem, landform and elementary form (Minar & Evans 2008). As surface morphology provides indications for determining the type of a landslide (Hutchinson 1995), high resolution datasets are commonly used for field mappings on any scale (e.g. Montgomery et al. 2000, Lee 2001, Crosta & Agliardi 2002). The combination of these geo-information tools with additional deterministic input data, such as shallow geophysics, provides a profound method for analyzing landslide hazard and vulnerability as well as risk assessment (Bruno & Martillier 2000, van Westen et al. 2002).

Within the last decades geophysical methods have developed as standard methods for the minimal-invasive investigation of the shallow subsurface in the fields of environmental research (e.g. Telford et al. 1990; Schrott et al. 2003; Reynolds 2011), and likewise in the studies of landslides (i.e. McCann & Forster 1990; Hack 2000; Bichler et al. 2004; Friedel et al. 2006; Jongmans & Garambois 2007; Schrott & Sass 2008; Socco et al. 2010). Recently, the development of 2D and 3D techniques can be regarded as a major advance for imaging the often complex and heterogeneous subsurface. A comprehensive review on the geophysical investigation of landslides is given by Jongmans & Garambois (2007). So far, no geophysical studies were applied on landslides in the region of Ebermannstadt.

As Müller (1957) described slide processes by the use of geomorphological observations, this study obtains slide processes using surface and subsurface data: A Digital Terrain Model (DTM) was primarily employed for geomorphological mapping, focusing on reconstructing formerly described processes on the surface. Based on these data designated geophysical surveys aimed at obtaining new insights into the subsurface. Besides, the focus was set on defining the type of movement by applying the concepts of Varnes (1978), Hutchinson (1988) and Cruden & Varnes (1996). A further aim is to assess the susceptibility of the slopes for future movements.

With the towns' expansion already reaching the foot of the landslide, detailed studies of the slide mass are essential for the Hasenberg area.

2 Regional characteristics and study area

The study area is situated in the Franconian Alb, approximately 40 km north of Nuremberg (Fig. 1). The Franconian Alb is part of the south German cuesta landscape, formed by Mesozoic rocks from the upper Triassic, Jurassic and Cretaceous. Related to the occurrence of mass movements, the cuesta scarps of the Rhaethian/Hettangian (Upper Triassic/Lower Jurassic), the Aalenium (Middle Jurassic) and the Oxfordian (Upper Jurassic) are of major interest.

In general, the slopes of the cuesta scarps are affected by different types of mass movements, such as topples, slides, lateral spreads and flows, either in single or in combined occurrence. Falls can be observed on vertical cliffs and fronts of slide blocks. Unconsolidated material and/or old slide masses often cause secondary (translational) landslides.

Due to its extension from north to south, the northern Franconian Alb acts as a barrier for weather-effective air

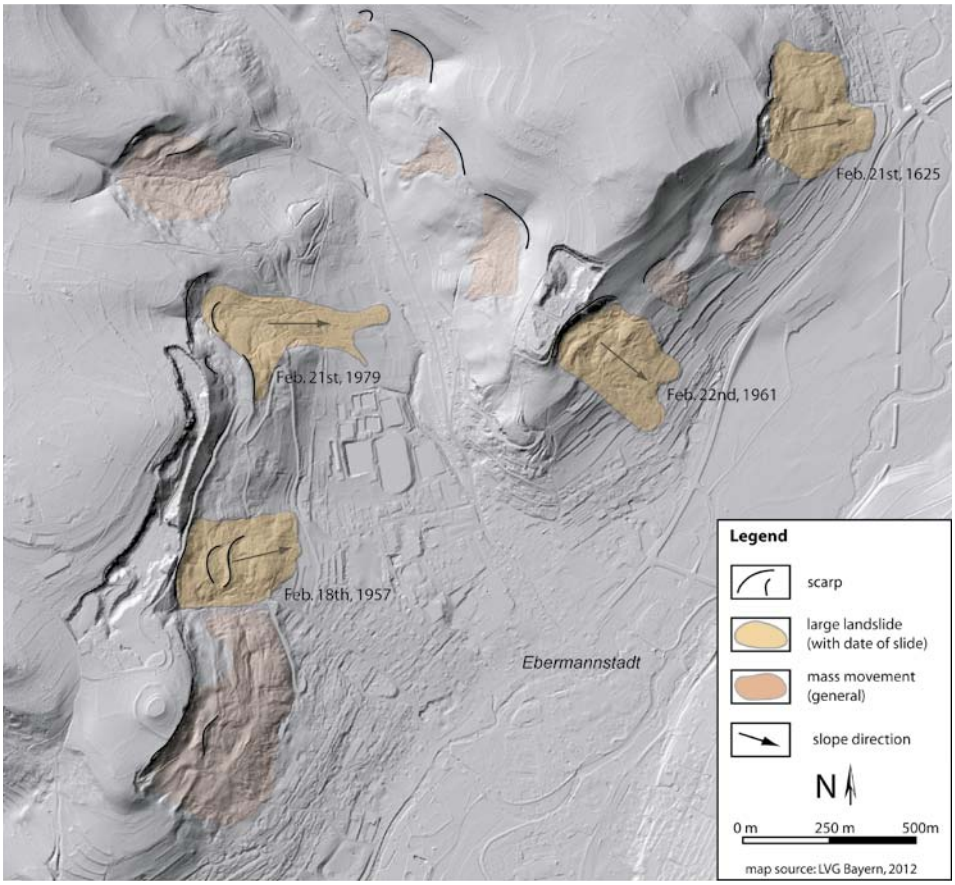

Fig. 2: Mass movements around Ebermannstadt.

Abb. 2: Massenbewegungen im Raum Ebermannstadt.

masses coming in from the north Atlantic. As a result, the wind-facing west side of the mountain ridge, where the study area is situated, receives higher precipitation than the western lowlands (Forchheim 684 mm, Ebermannstadt 898mm) (purchased data from DWD (German Meteorological Service)).

Ebermannstadt is located in the broad valley of the Wiesent River at an altitude of 292 m a.s.l. The adjacent mountains rise up to over 500 m a.s.l. (Wachknock: 517 m a.s.l.) and therefore receive a significant amount of precipitation as snowfall during winter.

The geology in the region of Ebermannstadt can be seen as exemplarily for the structure of the Franconian Alb with permeable and impermeable layers. The flat valley floors of the Wiesent river valley, as well as the lower slopes in the region consist of claystones from Lower Aalenian layers (Opalinuston). Above, Upper Aalenian sandstone (Doggersandstein) forms steeper slopes covered by layers of impervious Callovian Claystones (Ornatenton). Most parts of the area are covered by debris from the overlying Oxfordian Limestones (Malm α / β). This unit is built up by thick, marly limestones divided by thinner schistose layers. Uppermost parts of the slope are formed by Lower Kimmeridgian Marls and Limestones, the latter of which are mined in the municipal quarry, located above the study area. Measured over a distance of 500 m, all described layers show similar dipping of 8-10 m (= approximately 1°) towards the east (Müller 1957).

Due to dipping and aspect, several groundwater springs are found on the east-facing Hasenberg. The most important horizons in terms of groundwater springs are the transitions between Lower Aalenian layers and Upper Aalenian Sandstone, as well as between Callovian layers and Oxfordian Limestones. There are no karstic springs found in the vicinity of Ebermannstadt. The mainly concave slopes of the surrounding mountains are often covered by landslide masses, especially in the Eschlipp valley towards the north of Ebermannstadt and on the eastern slopes of the Wiesent valley (Fig. 2).

In 1625, 1957, 1961 and 1979, four major landslides took place around Ebermannstadt (Fig. 2). All of them occurred in the Callovian Clay layers, which underlie the Oxfordian limestones. These geological settings were already described by Hütteroth (1994), who investigated mass movements at the "Lange Meile" southwest of Ebermannstadt.

The study area is situated at the eastern flank of the Hasenberg, adjacent to the western town limits, which extend onto the foot of Hasenberg. Müller (1957) describes the region at Hasenberg as affected by numerous past landslides, proven by outcrops of landslide derived debris layers. According to Müller (1957), lacking soil formation between single debris layers indicate rather close successions of the different mass movements.

3 Methods

3.1 Geomorphological mapping

A detailed mapping of surface morphology and existing failures on a slope is fundamental for determining the landslide type (Hutchinson 1995), and for analyzing regional distribution of landslide patterns (Guzetti et al. 1999, 2000). Therefore, a detailed geomorphological map was cre-

E&G / Vol. 62 / No. 2 / 2013 / 150–161 / DOI 10.3285/eg.62.2.06

ated in order to capture this spatial reference of the slopes' structure as well as movement processes and to delineate potential instable areas through localization of active scars and accumulation forms of the 1957-event.

Geomorphological mapping of the present study was based on a 1-m DTM to precisely detect and locate landslide elements. Hence, a reconstruction of processes can be concluded as well as the influence of single geological layers. GIS-derivates, for example hillshades, contour lines, surface curvature, slope gradients and aspect were used during field work and data processing.

The geomorphological mapping was accomplished on a scale of 1:3000. The focus was set on the most important landforms and geomorphological units of the 1957-landslide.

With slight modifications, the symbols for steps, slope gradients, surface and valley forms are based on the mapping keys of Terhorst & Kirschhausen (2001), who developed a legend on mass movements. The mentioned mapping key is based on the geomorphological mapping instructions from Leser & Stäblein (1978).

3.2 Geophysics

Geophysical methods and sites were selected based on the results of the geomorphological mapping and in order to correlate detected landforms to subsurface structures.

Electric resistivity tomography (ERT) measurements were conducted using a 72-channel multi-electrode resistivity meter from IRIS instruments (Syscal Junior Switch) using 36 electrodes per array. With respect to the aimed penetration depth and resolution, a unit electrode spacing of 3 m has been applied. The array types Wenner (robust; high signal-to noise ratio) and dipole-dipole (more prone to errors, but high sensitivity to horizontal and vertical structures) were used (e.g. Telford et al. 1990; Burger et al. 2006; Reynolds 2011).

Three ERT-surveys were conducted, beginning below the debris deposits at 441 m a.s.l., and ending in the lower parts of the landslide mass at 381 m a.s.l. (see figure 4). To achieve best possible data coverage within the subsurface, ERT arrays were measured using a roll-along technique with an overlap distance of 15 m between arrays 1 and 2 and 18 m between arrays 2 and 3.

Datasets were concatenated (Loke 2010) and inverted within the software package RES2DINV (GEOTOMO) using the robust inversion scheme (L1-norm). To reduce side-block effects an extended model (additional model blocks at both sides and beneath the original data array) was used to calculate resistivity models (Loke 2010). Areas within the tomograms that are not covered with data points are shaded.

Seismic refraction tomography (SRT)-measurements were conducted using a 24 channel seismograph (Geode) from Geometrics with 24 geophones. A unit electrode spacing of 3 m has been applied, stating a trade-off between aimed penetration depth and resolution of the subsurface. A 5kg sledgehammer was used to generate the seismic signal. To achieve high data coverage, and in consideration of an expected distinct subsurface heterogeneity, shot locations were situated between each geophone pair, as well as in front of and behind the spreads (remote sources), resulting in 25 shot locations per array. As for ERT-measurements, a roll-along technique with an overlap distance of 3 m between spreads 1 and 2 and 6 m between spreads 2 and 3 has been applied. More details on the setups of ERT- and SRT-measurements are given in Table 1.

For data processing and inversion the software package SEISIMAGER/2D (GEOMETRICS) with the modules PICKWIN (picking of first arrivals) and PLOTREFA (concatenation of datasets; tomographic inversion) was used. Areas in the tomograms that are not covered by raytraces are shaded to prevent over-interpretations.

The topography of each ERT and SRT survey line has been recorded as the estimated relative vertical distance between two neighbouring electrodes/geophones, to enable an incorporation of relief data into the inversion process within RES2DINV and PLOTREFA, respectively.

3.3 Substrate analyses

Along geophysical surveys, additional analyses of substrates were realized to validate and improve the obtained data from geoelectrical and seismic measurements.

A total of 38 study sites in form of small pits of 20–40 cm in depth were dug over a distance of 380 m. Texture was determined by finger testing according to the Ger-

Tab. 1: Details of the ERT and SRT measurements on Hasenberg study site.
Tab. 1: Details der ERT und SRT Messungen im Arbeitsgebiet Hasenberg.

	ERT	SRT
# of concatenated spreads	3	3
electrode / geophone spacing [m]	3	3
# of electrodes / geophones per spread	36	24
spread length [m] [singe spreads]	105	69
overlap distance [m]	15 m / 18 m	3 m / 6 m
overall spread length [m]	282 m	246 m
altitude [m a.s.l.] [begin/end of spread]	381 m / 441 m a.s.l.	391 m / 427 m a.s.l.
# of stacks	Wenner, dipole-dipole	25 / 75
array type / # of shot points [per array/overall]		10
sample interval [ms]		0.25
record length [ms]		128

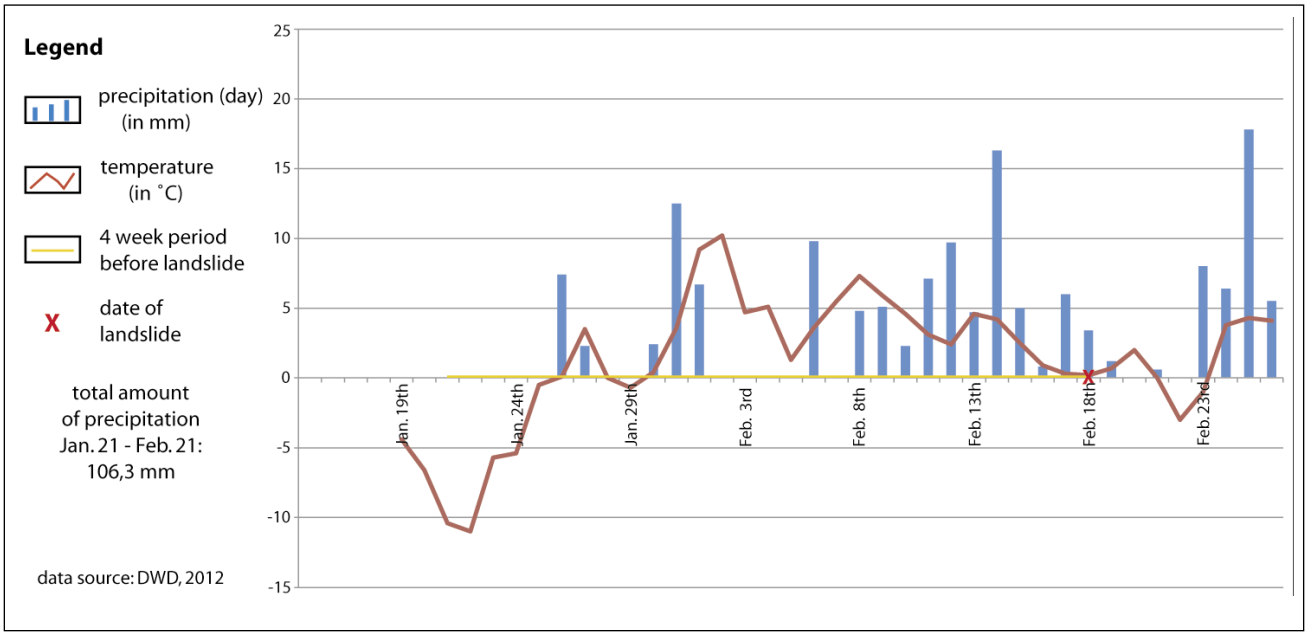

Fig. 3: Precipitation and temperature trend before the landslide of 1957.

Abb. 3: Niederschlags- und Temperaturverlauf vor der Rutschung 1957.

man Field Book for Soil Survey (Ad-Hoc-Arbeitsgruppe Boden 2005).

One focus was set on the occurrence of limestone debris skeleton, which may indicate a slide mass for the middle and lower slope areas. Furthermore, it was important to quantify the amount of fine grained, i.e. clayey material.

4 History of the landslide at Hasenberg 1957

The studied landslide at the slope of Hasenberg occurred in late winter of 1957. According to descriptions of Müller (1957), slope failure became apparent on February 17th, when several cracks opened in the mid slope area of the Callovian Clays covered by Oxfordian Limestone debris. These processes continued for at least twelve hours and initiated further slide movements uphill and flow processes in the lower slope areas. Overall, the landslide covered an area of 225 m (width) x 350 m (length) with an estimated volume of approximately 625.000 m^3. Average velocity during the major movements was approx. 10 cm per minute, with local maxima up to 1 m per minute (Müller 1957).

The landslide mass mainly comprises Oxfordian Limestone debris mixed with clay material from Callovian layers. Most parts of the slide mass did not contain fresh limestone fragments but remobilized debris from older slide masses. Furthermore, in the lower parts of the accumulation, upper Aalenian Sandstone fragments were intermingled into the slide mass (Müller 1957). The upper parts of the landslide area in the Callovian layers were dominated by cracks and slide surfaces, while tongues with an irregular, hummocky surface were formed in the lower areas, underlain by Aalenian layers. Vegetation remained intact on most parts of the landslide, except of the foot. Here, it was destroyed due to the more turbulent flow pattern and the steep front (Müller 1957).

According to Müller (1957), the landslide in 1957 was presumably triggered by an exceptionally high amount of water input. Meteorological data for late January and February 1957 (see Fig. 3), showed several days of (heavy) rainfalls, summing up to an amount of 107 mm for the period of 4 weeks before the landslide event. Compared to further datasets between 1931 and 2012, this sum is definitely above the long-term average (65.9 mm).

On the other hand, precipitations in January of 1957 (77.8 mm) and December, 1956 (55.4 mm) were below average. Furthermore, some years (e.g., 1946 and 1970) show even higher precipitations in February which did not cause landslides in the study area.

Temperature records of early 1957 display values increasing to degrees around zero and above, four weeks before the landslide event. This is supposed to having caused intensive snow melting processes in that time span which lead to a significant increase of the soil moisture (the presence of a snow cover was reported by contemporary witnesses [see Müller 1957]). Due to this additional water input, the actual water intake at the Hasenberg slope was much higher than precipitation data proposes. This example illustrates that soil moisture is influenced by different factors (e.g. type of precipitation, snow cover, snow melting, subsurface freezing and others) over a varying time span. Due to its complexity, this factor cannot be discussed in detail in this paper.

5 Results

5.1 Geomorphological Map

The first geomorphological map of the slide area after the event of 1957 was published by Müller (1957). The map is more of a rough sketch which records the observed processes (e.g., the formation of shear planes), basic geomorphological information (e.g. land surface forms, fissures, scarps) as well as geological layers. The linking of morphological forms to slide processes was limited to a minimal extent.

E&G / Vol. 62 / No. 2 / 2013 / 150–161 / DOI 10.3285/eg.62.2.06 / © Authors / Creative Commons Attribution License

Figure 4 shows a detailed geomorphological map of the landslide area based on high resolution DTM. Moreover, a colorized, GIS-processed hillshade combined with slope gradient information provides a precise visualization of the landforms in the study area. The hillshade accurately localizes the geomorphological forms without the problem of GPS-offsets.

The uppermost slope sections are dominated by thick debris deposits. Geologically, this area represents the transition from Oxfordian Limestones (above) to Callovian Clays (below). The area is completely covered by limestone debris and blocks with diameters from a few centimeters to approximately 1 m.

North of the footpath, a large limestone block has been detached from the wall. The rock formation of the block is still intact and can be directly linked to the adjacent rockwall behind. This indicates a relatively constant and slow drifting, without major destruction probably moving on underlying clay layers.

In the upper area of the Callovian Clay (approx. 425–435 m a.s.l.), slopes are characterized by lower inclinations. Although initial soil formation is present in form of thin litter layers, the area is still dominated by limestone debris. Numerous parallel fissures (orientated rectangular to the slope) are present primarily in the center of the slide area. Most fissures provide widths of approximately 2 m, depths of 1-2 m and lengths between 5 and 25 m. The proper depth could not be measured exactly as all fissures are partially filled with soil material, debris and/or vegetation. Apart from the widespread mixed forest, vegetation in these areas shows ferns and mosses, which is an indicator for increased moisture, probably due to the clayey conditions.

Slide blocks become apparent in lower parts of the Callovian Clay (approx. 405–425 m a.s.l.). They are characterized by converse uphill slopes, with heights of 1–3 m and oversteepened downhill slopes. Small areas with a hummocky surface are present in front of larger blocks, due to secondary movements in form of creeping.

The largest block is situated in the center of the landslide area (approx. 410 m a.s.l.). It forms a significant ridge with a height of 3 m (view from uphill). The front slope represents a main scarp of the 1957 landslide (total height 12 m), with a ruptured surface, indicating intensified movements here. While the upper sections of the front slope are covered by a comparably thin layer of debris, lower areas are buried under large sediment masses. Due to the curved shape of the scarp, a rotational slide can be assumed.

The region downslope (east) of the forest road (approx. at 400 m a.s.l.) represents the accumulation area of 1957. Most parts of this area are dominated by a wavy pattern, forming relatively smooth surfaces. In the central part a significant "V-shaped" valley, with a maximum depth of 3 m, cuts through the rather flat slide mass. At its lower extensions, remnants of an old pavement become visible, identifying the valley as a former defile (see Müller 1957). Remnants of the undisturbed trail allow the reconstruction of its uphill course. It also identifies stagnant and displaced landslide segments: Gaps between single trail segments reveal rates of deposition between 20 to 30 m.

Lower sections of the slide area (around and below the second forest trail in the east, approx. 390m a.s.l.) are again characterized by a wavy surface. At two minor rims, slope

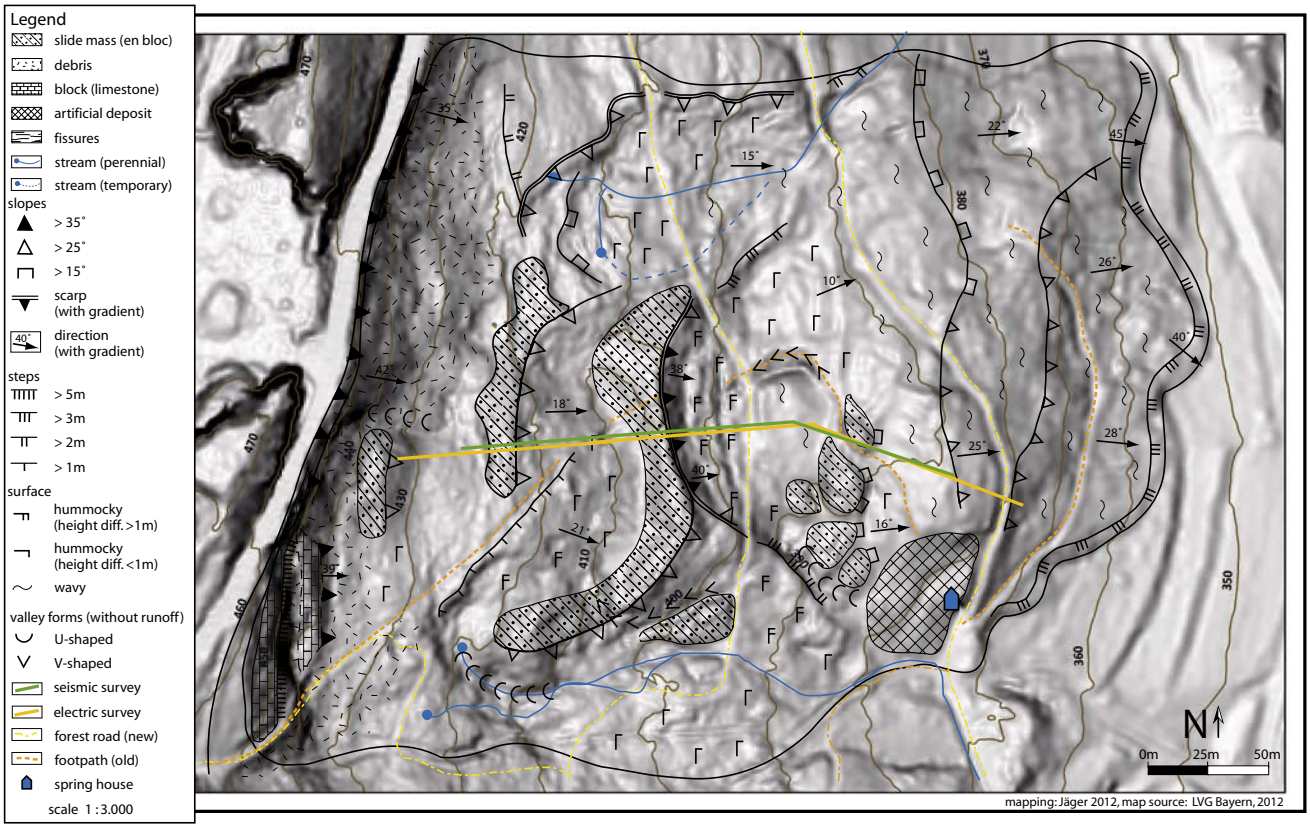

Fig. 4: Geomorphic map of the landslide at Hasenberg. The background map is showing slope gradients.

Abb. 4: Geomorphologische Karte der Rutschung am Hasenberg. Die Hintergrundkarte zeigt die Hangneigungen.

gradients increase about 5°–8°. The toe of the slide mass is formed by a steep step (max. slope gradients 45°) with a maximum height between 3–4 m. At this clear boundary the landslide mass can easily be differentiated against the undisturbed surroundings. In the northwestern part, the tip is only 5 meters west of a new road, which has been built after the landslide of 1957.

5.2 Substrate Analyses

Figure 5a outlines the changes of substrate at the surface. The profile is coherent with the geoelectric surveys but extends to the slide's boundaries. In total, substrates were analyzed over a length of 380 m.

Substrate in the steep uphill region is clearly dominated by limestone debris and blocks with maximum diameters of 80-100 cm and an average of around 20–50 cm. Deposition on the surface is loose due to slope parallel orientation of the fragments' x-axis, with fine-grained material only partially filling the interspaces. Below the depth of 20 cm, initial fillings tend to stabilize the deposit; however, several unfilled cavities are still left. The amount of large debris fragments and blocks decreases downslope in favor of finer material.

The section between the upper ridge and main scarp (horizontal length 100–160 m) offers varying amounts of fine grained material and debris/coarse grains. A composition of limestone fragments embedded in a dense/loamy fine grained matrix characterizes the ridges (such as the upper ridge or main scarp). In contrast, straight slope sections are dominated by clayey material with small amount of coarse grains. Mostly behind (upslope) the ridges, shallow organic horizons (5–10 cm) could accumulate.

Below the main scarp, a composition dominated by a fine grained, mostly clayey matrix was found. The amounts of limestone debris and coarse grains average approximately 50 %. In two small sectors, the amount of clay and fine grains increase to rates of approximately 70–80 %. In any case, clayey material is less dense and slightly less moist compared to the area above the main scarp.

In summary, three different substrate areas could be determined: The uppermost area is dominated by debris and coarse grains while clayey material dominates the midslope sections of the Callovian layers. In the lower parts of the study area, the slide mass contains a composition of both materials.

5.3 Geophysics

Figure 5 b & c presents the electrical resistivity- and seismic refraction tomograms in comparison to substrate anal-

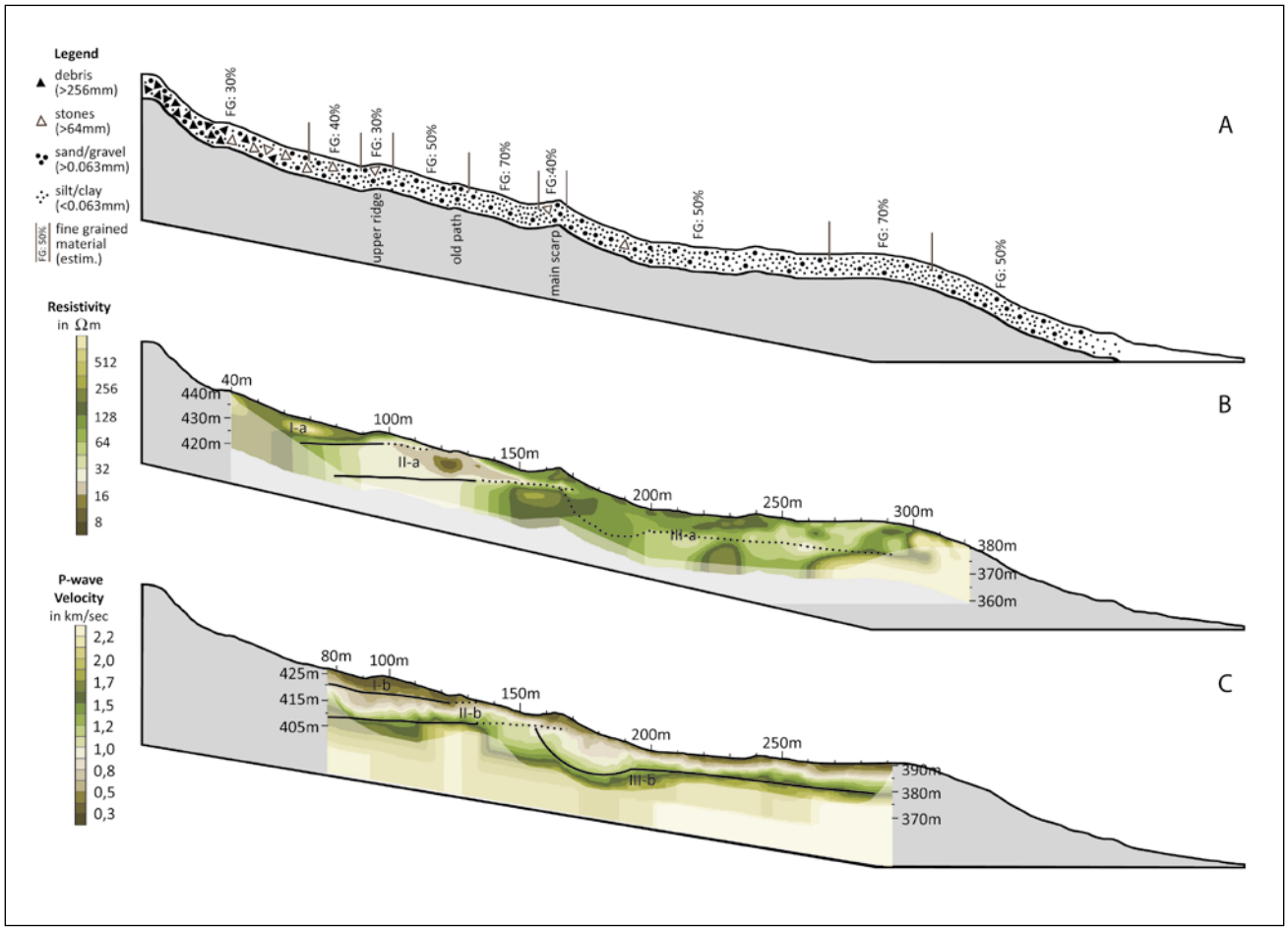

Fig. 5 a, b, c: Profiles showing results drawn from substrate analyses (a), geoelectric surveys (b) and seismic surveys (c). See Fig. 4 for location. The shaded areas could not be interpreted as they are not sufficiently covered by data.

Abb. 5 a, b, c: Profilschnitte mit den Ergebnissen aus Substratanalyse (a), geoelektrischen Sondierungen (b) und seismischen Sondierungen (c). Lagebeschreibung in Abbildung 4. Schattierte Flächen sind nicht ausreichend mit Daten aufgelöst und daher nicht interpretiert.

E&G / Vol. 62 / No. 2 / 2013 / 150–161 / DOI 10.3285/eg.62.2.06 / © Authors / Creative Commons Attribution License

yses. Results from ERT and SRT allow for defining three differentiated subsurface sections (see markings in the tomograms) that will be analyzed in the following section.

The subsurface resistivity distribution is recorded over a total profile length of 282 m. The presented tomogram exhibits three major units with varying resistivity characteristics. High resistivities (≥200 Ωm) were obtained in the uppermost region (I-a) and in single spots downslope. Adjacent to this area a unit of very low values (8 - 32 Ωm) was measured in the slope section above the main scarp (II-a). The lower half of the profile (III-a) is characterized by mostly intermediate values around 64–128 Ωm, with several lenses of higher or lower resistivities.

In the uppermost sections (I-a), a relatively homogeneous area with high resistivities (>200 Ωm) is detected, reaching from the surface as deep as 10 m (deeper layers cannot be taken into account due to survey geometry). Tapering out downslope, the body covers the top of the small ridge (at 225 m survey length), before it disappears completely. The transition between sections I-a and II-a is characterized by a sharp boundary and a strong contrast in resistivity values.

Resistivity values in unit II-a are mainly between 24–32 Ωm, primarily detected for rather homogeneous sections below a depth of 9 m. Within the shallow subsurface (0–9 m depth) an anomaly with distinct lower resistivity values is detected. Most probably this structure can be ascribed to higher moisture contents there rather than to differing substrate properties. This interpretation is confirmed by substrate analyses that show increased amounts of clayey material. In a depth of approx. 5 m, this unit extends close to the main scarp downslope (horizontal distances 130–160 m). At the surface (0–5 m depth) the unit is covered by a layer of higher resistivity values (max. 100 Ωm)

From the main scarp to the lower extensions of the survey a heterogeneous resistivity distribution is apparent. The section records an intensively disturbed composition as deep as 15 m. The unit (III-a) can be subdivided into the steep slope section below the main scarp (horizontal distances 165–200 m) with resistivity values between 64–128 Ωm and the gently inclined section between horizontal distances 200–300 m. The resistivity distribution in the latter section indicates a vertical differentiation of the subsurface into three layers, with a conductive layer (5–1.5m depth, 24–32 Ωm) embedded between two layers with higher resistivity values (>64 Ωm). The conductive layer is horizontally differentiated into three lenses, which are cropping out to the surface between horizontal distances 260–290 m. Upslope (horizontal distances 260–200 m) this layer is superimposed by a heterogeneous layer of up to 5 m in thickness with rather high resistivity values between 64–128 Ωm. The area below 15m depth is characterized by a homogeneous resistivity distribution. However, data coverage at this depth is rather poor. In general, the transitions between all parts are relatively smooth.

Seismic surveys cover a total profile length of 215 m. Corresponding to ERT data, three major units can be identified over the course of the profile: (I-b) very low velocities between 0.3–0.5 km/sec, found at the surface and as deep as 4 m in the upper regions, as well as at the ridge of the main scarp. This unit is underlain by a section with medium velocities (II-b) constantly increasing from 0.5 to 1.2 km/sec, which also tends to reach the surface in some areas. Unit III-b is characterized by rather fast velocities between 1.2 and 1.7 km/sec. Acceleration within this unit mostly occurs over short vertical distances.

In the uppermost section, the unit of low velocities (I-b) is dominant at the surface. Below the small upper ridge, velocity slowly increases to 1.1 km/sec. The only refractor is detected in a depth of 15 m, with velocities rapidly increasing from 1.2 to 1.6 km/sec on a vertical distance of approximately 5 m.

The step of the old footpath (horizontal distance 195 m) limits the downslope extent of the low velocities at the surface. Here, velocities > 0.9 km/sec were obtained at the surface (unit II-b), constantly increasing with depth. Below a depth of 10 m, values increase more rapidly from 1.2 to max. 2.2 km/sec.

This pattern significantly differs from the situation underneath the main scarp. Again, low velocities were found in the surface near layers, similar to the small upper ridge. With depth, they moderately increase forming a pocket of medium resistivities (0.5–0.9 km/sec) in the steep area downslope of the main scarp. The pocket is underlain by a refractor as deep as 20 m forcing velocities to rapidly increase from 1.2 km/sec to 1.8 km/sec.

The gently inclined section between horizontal profile lengths of 200–290 m presents all three units arranged in a uniform subsurface set-up. From the surface as deep as 3 m, low velocities (0.3 km/sec) are detected. Velocities constantly increase over a vertical distance of 15 m to max. 1.8 km/sec. A refractor can be presumed in a depth of 18 m due to further velocity acceleration (> 2.0 km/sec).

6 Interpretation and discussion

The region around Ebermannstadt provides three factors favoring landslides: (I) a bipartite geologic structure with permeable and impermeable layers, (II) increased precipitation resulting from conditions at the windward site of the Franconian Alb and (III) dipping towards the direction of the hillslope (in case of east-facing slopes). This leads to the occurrence of several mass movements in the area. As geophysical surveys show, all processes are linked closely to local geology, indicating an important influence of this slope internal factor. The major part of the slope movements occur on the boundary between (Callovian) Clay and debris cover. Obviously, slope parallel dipping of the geological layers additionally favors the development of slip surfaces. As a result, east facing slopes are affected by numerous landslides (Müller 1957) as described by DORN (1928).

6.1 Subsurface structure and formation

In order to create a generalized model of the 1957 landslide at Hasenberg, geophysical surveys and supporting substrate analyses are combined.

The uppermost slope sections are characterized by debris-rich deposits on the surface. As substrate analyses reveal, a loose accumulation is prevalent. Parts of the interspaces are filled with fine-grained (weathered) mate-

rial. High resistivity data (unit I-a) and low velocity values (unit I-b) indicate the presence of debris (Knödel et al. 2003, Reynolds 2011) not only at the surface, but at least as deep as 10 m. Fissures (see Fig. 4) cause reduced interspace-fillings between horizontal distances of 60 - 80 m, which is represented by a lens of increased resistivities in this segment.

From top of the survey downslope, the amount and size of limestone blocks and fragments by trend decreases. However, the upper ridge contains a higher amount of debris, as substrate analyses reveal. Again, this is supported by resistivity data and seismic velocities. Both surveys lead to the assumption of comparably solid, debris dominated cover (Telford 1990, Knödel et al. 2003, Reynolds 2011), approximately 3–5 m in thickness, building up the ridge. This layer is underlain by unit II-a and II-b values.

Below the ridge (horizontal length 95–125 m) in downslope direction, a denser (packed) and/or moister subsurface is present, due to reduced debris and increased amounts of fine grained material. Seismic velocities at the surface are still low (unit I-b: 0.3–0.6 km/sec) as deep as 4 m. Below, they constantly increase to unit II-b values. The ERT displays considerably lower resistivities, compared to the debris dominated areas upslope. Both, the SRT and ERT values, can be interpreted as a compound of fine grained (clayey) material with a large amount of limestone debris (> 50%) included (Knödel et al. 2003, Bichler 2004, Reynolds 2011). Moist conditions, indicated by mosses and ferns and also obtained in substrate analyses, cause an additional decrease of resistivities in this area.

Between the small forest trail and the main ridge (horizontal lengths of 130–150 m), substrate analyses revealed considerably higher amounts of clayey material close to the surface. From uphill directions, the course of the old footpath is interrupted in this area, as a gap of approximately 20 m in length was detected during geomorphological mapping (see Fig. 4 for details). The path can be rediscovered at the main ridge, indicating a displacement in this area. With this in mind, a clayey subsurface appropriate to the formation of slide surfaces is expected. The intermediate surface velocities (0.5–0.9 km/sec) exhibited in the SRT clearly support this assumption. Resistivity values between 64–128 Ωm (unit III-a) indicate comparably dry composition of clayey material (Telford 1990, Knödel et al. 2003, Reynolds 2011) and limestone fragments adjacent to the ridge.

To summarize, for the region between 95–165 m horizontal length, both ERT and SRT assume an extension of the in situ Callovian Clay to altitudes of approximately 422 m a.s.l. to 408 m a.s.l. This corresponds with the data of the geological map, which records a thickness of 16 m (Müller 1959) for this layer.

At the ridge of the main scarp, resistivity data (unit III-a) and velocity values (unit I-b) imply a composition of higher amounts of limestone fragments and less fine grains as deep as 5 m (Knödel et al. 2003, Reynolds 2011). The block (with the main scarp) is situated at the lower boundary of Callovian Clays covering Aalenian Sandstone. Both features are assumed to be exhibited in the ERT: A stripe of low resistivities (clay) covers a unit of high resistivities (sandstone) obtained in depths below 10 m. Due to hidden layer effects (see Reynolds 2011 for details), SRT is unable to detect the layer of soft clayey material. Constantly increasing velocities reveal no distinguishable refractor, which leads to the assumption of a heavily weathered and shattered structure of the Upper Aalenian Sandstone, assumed as deep as 15–20 m. These characteristics were also stated by Müller (1957).

Downslope of the main scarp, a composition of coarse and fine grained (50/50 %) material forms small ridges (e.g. at the steep slope areas below the scarp and at 110 m and 80 m survey length) at the surface. Higher amounts (>50%) of fine grained, mostly clayey material are found in the gently inclined sections of the accumulation area. As described above, the obtained resistivity data displays varying values in this unit III-a. In ERT, no in situ sandstone could be obtained as deep as 15 m. Poor data coverage prevents the detection of reliable data in greater depths (Telford 1990, Knödel et al. 2003, Reynolds 2011). The SRT shows very slow increasing velocities as deep as 12 m, assuming no significant changes in the fine grained slide mass substrate (Knödel et al. 2003, Glade et al. 2005). For depths of 12–19 m, curved layer structures are clearly visible in the SRT. This structure leads to the assumption of a rotational slip surface present in this area. Rapid increasing velocities in depths below 19 m mark the surface of rupture and the assumed transition to underlying sandstone.

In the gently inclined slope areas, the SRT exhibits increasing velocities over a vertical distance of 18 m. In combination with the varying resistivity data values, an unconsolidated slide mass, containing stones and debris, embedded in a matrix of fine grained material can be assumed (Knödel et al. 2003, Bichler et al. 2004, Glade et al. 2005). Below depths of 15 m, few high resistivity units suggest the presence of fragmented bedrock (Aalenian sandstone) (Knödel et al. 2003). In a corresponding location, the SRT displays no clear refractor, but constantly increasing values. Therefore, this again may be interpreted as an intensively fissured surface of the underlying bedrock (Aalenian sandstone).

6.2 Morphology, landslide processes and type

According to Müller (1957), the landslide was initiated by movement of water saturated debris in the lower areas of the slide area. Disappearance of the abutment led to further movement of limestone debris and blocks in the upslope regions. Müller (1957) defined the overall movement as an earth flow. This designation was used again by Hegenberger (1961), who described the landslide of 1961 at Ebermannstadt Einbühl, which was very similar to the 1957 event. Moser & Rentschler (1999) supported this assumption when they investigated types of movement in clay layers of the Franconian Alb. However, as our investigations show, the 1957 event contained heterogeneous material and displayed more processes than a single earth flow.

Detachment of a block from the bedrock took place on the uphill slopes in the southwestern part. A combination of topple (Varnes 1978, Dikau et al. 1996) and creeping (Schmidt & Beyer 2001) processes occur, as the detached

E&G / Vol. 62 / No. 2 / 2013 / 150–161 / DOI 10.3285/eg.62.2.06

block is slowly dipping forward while moving downslope on the underlying clay. Radbruch-Hall (1978) defines this movement as "creep of blocks over soft rocks". The soft bottom layer also enables rotation of the blocks (Beyer & Schmidt 1999).

Geophysical surveys revealed a shallow translational slab slide (Hutchinson 1988, Dikau et al. 1996) of debris in the clay dominated area uphill of the main scarp. Slab slides frequently occur in debris mixed with fine material (Hutchison 1988). According to Dikau et al. (1996), a shear zone close to the surface is characteristic, as well as movements in slightly weathered bedrock. Both characteristics were obtained at Hasenberg.

The undestroyed part of the footpath on the ridge of the main scarp proves an en bloc movement of this part as suggested by resistivity and seismic data, rather than involvement of buckling, wedging or heaving processes which may also occur at slab slides (Hutchison 1988). The ridge of the main scarp supposably contains a core of (relatively) solid rock. This may be a relic of limestone bedrock or sintered limestone debris, which were observed during field work. Besides, their occurrence on Hasenberg was reported by Müller (1957). Movement of the block was disrupted at the transition of the Callovian Clay to the underlying Aalenian Sandstones with a clayey slip surface tapering out.

Parts of the block presumably exceeded the step of the underlying Aalenian Sandstone.

At the step, the upper layers of the sandstone are shaped by intensive weathering (Müller 1957) and/or prior movements (Dorn 1928). Internal weaknesses lead to the formation of a curved slip surface (see SRT) and a small (debris) rotational slide (Varnes 1978, Dikau et al. 1996). The slide also affected the underlying sandstone, as substrate analyses obtained sandstone particles in the slide mass of the main body (see also Müller 1957).

Earth flow processes (Müller 1957) are characteristic for the lower parts of the slide area and have to be specified as they do not comply with the definitions of Varnes (1978), Hutchinson (1988) or Cruden & Varnes (1996). In terms of involved material ("*earth*"), resistivity data and substrate analyses at Hasenberg assume a significant amount of debris embedded in a matrix of fine material. According to the authors mentioned before, the limit of coarse material in an earth flow is 20 % (amounts exceeding 20 % = debris). On the other hand, a review of flow type processes by Hungr et al. (2001) determines clay contents of only 10–70 % for earth flows. Therefore, a distinct definition of the material properties is difficult to apply.

This is also the case in terms of movement mechanism ("flow"). Varnes (1978) classifies all slope movements with internal distortion involved as "flows". However, Hungr et al. (2001, p. 222) state, it is "often difficult to determine whether internal distortion or boundary sliding is dominant in a given case". Furthermore, investigations proved that several "flows" moved predominantly by sliding along a shear surface, rather than an irregular flow-pattern (Hutchinson 1970, Brunsden 1984). A coinciding characteristic for flows is a high content of involved water. According to a study of von der Heyden (2004) the accumulation of a landslide mass on permeable layers (like the Aalenian Sandstone) represents a rather stable condition, as water is able to percolate through debris and subsurface layers. Therefore, a saturation of debris, which may lead to a flow process, is rather unlikely. However, the recent classifications of flows by Hungr et al. (2001) reveal water contents near the plastic limit as sufficient for a slow moving earth flow.

In the case of Hasenberg, the old road may solve the problem of a designation. Although being displaced with different rates of movement, the old road mainly remained connected (Müller 1957). This indicates the existence of one or more relatively coherent masses/blocks with fine grained material involved (see also ERT).

According to the presented literature, movement in the lower parts of the landslide can basically be defined as "earth flow" sensu Hungr et al. (2001), with the constraint of a coherent mass instead of individually moving particles as mentioned by Dikau et al. (1996).

Concerning the entire landslide, the term "earth flow" is not wrong but rather misleading as it does not reflect the complexity and disparity neither of occurring processes nor of the involved materials.

An enhancement to "complex earth flow" is considered to be necessary. However, as involved material mainly comprises debris and the movements represents typical slide processes (see Dikau et al. 1996, Cruden & Varnes 1996) the classification of the studied landslide as "complex debris slide" or generalized as "complex landslide" (Cruden & Varnes 1996) seems to be most appropriate.

6.3 Future susceptibility

In order to stabilize the slope some adjustments were achieved after the 1957 landslide. The planting of cottonwood with its shallow roots was meant to stabilize layers close to the surface. However, movements in deeper stages, as detected by geophysical data, cannot be prevented by vegetation. A second regulation was the tapping of springs in order to prevent uncontrolled infiltration of water into the subsurface. This is one of the most important adjustments especially if impermeable layers, e.g. clay, are involved (Hammer 1984).

Until today, no further landslide has occurred. This is in favor of the interpretation of the Hasenberg as a stabilized landslide area. However, cracks and damages in the road indicate contemporary movements.

Additionally, recent climate change leads to modified precipitation patterns. Most notably, winter precipitation rises (Parry et al. 2007). Although reliable predictions for this most important trigger factor are not possible yet, a decreasing influence is not assumed. Ongoing investigations especially have to clarify the trend of precipitation along with effects concerning infiltration and consistency boundaries.

Considering all factors, processes and circumstances obtained in the study area are not restricted to the Hasenberg landslide – as illustrated by the event at Ebermannstadt Einbühl (1961) showing similar forms and processes. Also, slopes adjacent to the landslide area provide similar conditions. Assuming certain requirements (intensive snow melting, high precipitation rates), these facts indicate an endangered susceptible slope area.

7 Conclusions

The landslide on Hasenberg from 1957 combined a variation of movement processes like slab slide, rotational slide and earth flow. As a result, the whole movement should be defined as a "complex landslide" or, more detailed, as "complex debris slide".

Slide material is a composition containing varying amounts of limestone debris, clayey material and – in the downslope areas of the study site – fragments of Aalenian Sandstone. In 1957 only little amounts of fresh debris were produced, the majority corresponded to debris which resulted from weathering and/or older slope movements. With exception of the uppermost slope sections, debris contains all grain sizes between clay, silt to stones and debris. The thickness of debris accumulation differs from a few decimeters (covering the slip surface) to more than 10 m (downslope main scarp).

The obtained processes assume a very close relation to the internal factors of local geology (bipartite structure: permeable and impermeable layers) as well as dipping (analog to exposition). External triggers are (winter) precipitation combined with additional snow melting (and therefore temperature).

After the landslide, necessary adjustments for slope stabilization were achieved. Until today, no further landslide occurred in the study area. However, no guarantee can be given, especially since roadway damage indicates certain movements. Even if the 1957 slide area should be stabilized, similar movements may occur on adjacent slopes.

References

AD-HOC-Arbeitsgruppe Boden (2005): Bodenkundliche Kartieranleitung. – 438 S.; Hannover (Schweizerbart'sche Verlagsbuchhandlung).

Beyer, I. (2002): Massenverlagerungen an der Wellenkalk-Schichtstufe im Thüringer Becken und ihre Abhängigkeit von morphometrischen Steuerungsfaktoren. – Trierer Geographische Studien, **25**: 143–160.

Beyer, I. Schmidt, K.-H. (1999): Untersuchungen zur Verbreitung von Massenverlagerungen an der Wellenkalk-Schichtstufe im Raum nördlich von Rudolstadt (Thüringer Becken). – Hallesches Jahrbuch für Geowissenschaften, Reihe A 21: 67–82.

Bichler, A., Bobrowsky, P., Best, M., Douma, M., Hunter, J., Calvert, T. & Bums, R. (2004): Three-dimensional mapping of a landslide using a multi-geophysical approach: the Quesnel Forks landslide. – Landslides, 1(1): 29–40.

Bruno, F. & Martillier, F. (2000): Test of high resolution seismic reflection and other geophysical techniques on the Boup landslide in the Swiss Alps. – Surveys in Geophysics, 21(4): 335–350.

Brunsden, D. (1984): Mudslides. – In: Brunsden, D. & Prior, D.D. (ed.) (1984): Slope Instability, Chapter 9: 363–418; New York (Wiley and Sons).

Burger, H. R., Sheehan, A. F., Jones, C.H. (2006): Introduction to Applied Geophysics – Exploring the shallow subsurface. – 600S.; New York (W.W. Norton & Company).

Crosta, G.B. & Agliardi, F. (2002): How to obtain alert velocity thresholds for large rockslides. – Physics and Chemistry of the Earth, Parts A/B/C, 27 (36): 1557–1565.

Cruden, D.M. & Varnes, D.J. (1996): Landslide types and processes. – In: Turner, A.K. & Schuster, R.L. (ed.): Landslides Investigation and Mitigation. National Research Council: 36–75; Washington D.C. (Transportation Research Board, National Research Council).

Dikau, R., Brunsden, D., Schrott, L. & Ibsen, M.-L. (1996): Landslide Recognition. Identification, Movement and Causes – 251 S.; Chichester (Wiley & Sons).

Dorn, C. (1920): Bergstürze im Gebiet der Wiesentalb. – Die Fränkische Alb, 6: 18–20.

Dorn, P. (1928): Geologischer Exkursionsführer durch die Frankenalb und einige angrenzende Gebiete. – 183 S.; Nürnberg (Spindler).

Freyberg, B. v. (1957): Bilder vom Bergrutsch bei Ebermannstadt vom 18./19. Februar 1957. – Geologische Blätter NO-Bayern, 7: 125–132.

Freyberg, B. v. (1961): Das Bild des Bergrutsches 1961 vom Einbühl bei Ebermannstadt. – Geologische Blätter NO-Bayern, 11: 155–161.

Friedel, S., Thielen, A. & Springman, S.M. (2006): Investigation of a slope endangered by rainfall-induced landslides using 3D resistivity tomography and geotechnical testing. – Journal of Applied Geophysics, 60(2): 100–114.

Glade, T. & Dikau, R. (2001): Gravitative Massenbewegung. Vom Naturereignis zur Naturkatastrophe. – Petermanns Geographische Mitteilungen, 145(6): 42–55.

Guzzetti, F. (2000): Landslide fatalities and the evaluation of landslide risk in Italy. - Engineering Geology, 58(2): 89–107.

Guzzetti, F. Carrara, A., Cardinali, M., Reichenbach, P. (1999): Landslide hazard evaluation: A review of current techniques and their application in a multi-scale study, Central Italy. – Geomorphology, 31(1–4): 181–216.

Hack, R. (2000): Geophysics For Slope Stability. – Surveys in Geophysics, 21(4): 423–448.

Hammer, H. (1984): Systematische ingenieurgeologische Untersuchung von Hangrutschungen im Nordbayerischen Deckgebirge – 255 S.; Nürnberg (Veröffentlichungen Grundbauinstitut Landesgewerbeanstalt Bayern **42)**

Hegenberger, W. (1961): Der Bergsturz vom Einbühel bei Ebermannstadt. – Geologische Blätter NO-Bayern, 11: 145–155.

Hungr, O., Evans, S.G., Bovis, M.J., Hutchinson, J.N. (2001): A Review of the Classification of Landslides of the Flow Type. – Environmental & Engineering Geoscience, VII–3, 221–238.

Hutchinson, J.N. (1970): A coastal mudflow on the London Clay cliffs at Beltinge, North Kent. – Géotechnique, 20: 412–438.

Hutchinson, J.N. (1988): Morphological and geotechnical parameters of landslides in relation to geology and hydrogeology. – Landslides, Proceedings 5th International Symposium on Landslides, 1: 3–35.

Hutchinson, J.N. (1995): Landslide hazard assessment. – In: Bell, D.H. (ed.): Proceedings of the VI International Symposium on Landslides, Christchurch, New Zealand: 1805–1841.

Hütteroth, W. (1994): Bergrutsche an der nördlichen Fränkischen Alb. – Mitteilungen der Fränkischen Geographischen Gesellschaft, 41: 185–203.

Johnsen, G. & Schmidt, K.-H. (2000): Measurement of block displacement velocities on the Wellenkalk scarp in Thuringia. – Zeitschrift für Geomorphologie N.F., Suppl.-Bd. 123: 93–110.

Jongmans, D. & Garambois, S. (2007): Geophysical investigation of landslides: A review. – Bulletin Société Géologique de France, 178 (2): 11.

Kany, M. & Hammer, H. (1985): Statistische Untersuchungen von Rutschungen im Nordbayerischen Deckgebirge. – In: Heitfeld, K.-H. (ed.): Ingeniergeologische Probleme im Grenzbereich zwischen Locker- und Festgesteinen: 257–265; Berlin (Springer).

Knödel, K., Krummel, H. & Lange, G. (2003): Geophysik. – 1102 S.; Berlin (Springer).

Lee, E.M. (2001): Geomorpological mapping. – In: Griffiths, J.S. (ed.): Land Surface Evaluation for Engeneering Practice: 18, 53–56; London (Engeneering Geology Special Publications).

Leser, H. & Stäblein, G. (1978): Legende der Geomorphologischen Karte 1:25000 (GMK 25). – 3. Fassungen im GMK Schwerpunktprogramm. – Berliner Geographische Abhandlungen, 30: 79–90.

Loke, M. H. (2010): Tutorial: 2-D and 3-D electrical imaging surveys. 127 S.

McCann, D. M. & Forster, A. (1990). Reconnaissance geophysical methods in landslide investigations. – Engineering Geology 29(1): 59–78.

McKean, J. & Roering, J. (2004): Objective landslide detection and surface morphology mapping using high-resolution airborne laser altimetry. – Geomorphology, 57: 331–351.

Minar, J. & Evans, I.S. (2008): Elementary forms for land surface segmentation: The theoretical basis of terrain analysis and geomorphological mapping. – Geomorphology, 95: 236–259.

Montgomery, D.R., Schmidt, K.M., Greenberg, H.M., Dietrich, W.E. (2000): Forest clearing and regional landsliding. – Geology, 28(4): 311–314.

Moser, M & Rentschler, K. (1999): Geotechnik der Kriech- und Gleitprozesse im Bereich des Juras der Frankenalb. – In: Bibus, E. & Terhorst,

B. (ed.) (1999): Angewandte Studien zu Massenbewegungen: 193–212; Tübingen (Tübinger Geowissenschaftliche Arbeiten, D 5).

Müller, K.W. (1957): Der Bergrutsch von Ebermannstadt (Fränk. Alb) vom 18.–19. Februar 1957. – Geologische Blätter NO-Bayern, 7: 119–125.

Parry, M.L., Canziani, O.F., Palutikof, J.P., van der Linden, P.J., Hanson C.E. (eds.): Contribution of Working Group II to the Fourth Assessment Report of the Intergovernmental Panel on Climate Change, 2007. – 976 S.; New York (Cambridge University Press)

Radbruch-Hall, D.H. (1978): Gravitational creep of rock masses on slopes. – In: Voight, B. (ed.): Rockslides and avalanches: 607–675; Amsterdam.

Reynolds, J. M. (2011). An Introduction to Applied and Environmental Geophysics. – 785 S.; Chincester (John Wiley & Sons)

Schmidt, K.-H. & Beyer, I. (2001): Factors controlling mass movement susceptibility on the Wellenkalk-scarp in Hesse and Thuringia. – Zeitschrift für Geomorphologie N.F., Suppl,-Bd. 125: 43–63.

Schrott, L. & Sass, O. (2008): Application of field geophysics in geomorphology: Advances and limitations exemplified by case studies. – Geomorphology, 93(1-2): 55–73.

Schrott, L., Hördt, A., Dikau, R. (ed.) (2003). Geophysical applications in geomorphology. – Zeitschrift für Geomorphologie, N.F., Suppl.-Bd. 132: 190 S.

Socco, L. V., Jongmans, D. Boiero, D. Stocco, S., Maraschini, M., Tokeshi, K., Hantz, D. (2010): Geophysical investigations of the Sandalp rock avalanche deposits. – Journal of Applied Geophysics, 70, 4: 277–291.

Telford, W.M., Geldart, L.P., Sheriff, R.E. (1990): Applied Geophysics (2nd edition). – 751 S.; Cambridge (Cambridge University Press).

Terhorst, B. & Kirschhausen, D. (2001): Legends for mass movements in the MABIS Project. – Zeitschrift für Geomorphologie N.F., Suppl,-Bd. 125: 177–192.

Terhorst, B. (1997): Formenschatz, Alter und Ursachenkomplexe von Massenverlagerungen an der schwäbischen Juraschichtstufe unter besonderer Berücksichtigung von Boden- und Deckschichtenentwicklung – 212 S.; Tübingen (Tübinger geowissenschaftliche Arbeiten, Reihe D 2)

Terhorst, B. (2001): Mass movements of various ages on the Swabian Jurassic escarpment. Geomorphologic processes and their causes. – Zeitschrift für Geomorphologie N.F., Suppl.-Bd. 125: 65–87.

Van Westen, C.J., van Asch, T.W.J., Soeters, R. (2006): Landslide hazard and risk zonation - why is it still so difficult. - Bulletin Engeneering Geological Environment, 65: 167–184.

Varnes D. J. (1978): Slope movement types and processes. – In: Schuster R. L. & Krizek, R. J. (ed.): Landslides, analysis and control. Transportation Research Board Sp. Rep. No. 176: 11–33. Washington, D.C. (National Research Council).

Von der Heyden, D. (2004): Rutschungen an den Malmschichtstufen der nordwestlichen Frankenalb: Untersuchungen zu Formenschatz, Alter und Ursachen (Diss.) – 137 S.; Bamberg (WIKU-Verlag).

Von der Heyden, D., Garleff, K. & Buschwiewcke, P. (1993): Hangrutschungen um die Altenburg bei Bamberg. – Berichte der Naturforschenden Gesellschaft Bamberg 68: 33–43.

Wenzel, B. (1994): Zur Lithostratigraphie und Sedimentologie des Röt und zu den Massenverlagerungen an der Röt-/Muschelkalkgrenze in Nordosthessen – 379 S.; Gießen (Gießener Geologische Schriften 53).

Zürl, K. (1980): Rutschungen im Ornatenton. – LGA Rundschau 80–1: 14–19.

Purchased Data:

Deutscher Wetterdienst (DWD) (2012): Precipitation Data (per month) of measuring stations Forchheim and Gößweinstein (years: 1931–2012).

E&G Quaternary Science Journal
Volume 62 / Number 2 / 2013 / 162–174 / DOI 10.3285/eg.62.2.07
www.quaternary-science.net

GEOZON SCIENCE MEDIA
ISSN 0424-7116

Ice Age geomorphological Ahorn Valley and Ailsbach River terrace evolution – and its importance for the cave use possibilities by cave bears, top predators (hyenas, wolves and lions) and humans (Neanderthals, Late Palaeolithics) in the Frankonian Karst

Case studies in the Sophie's Cave near Kirchahorn, Bavaria

Cajus Diedrich

How to cite: Diedrich, C. (2013): Ice Age geomorphological Ahorn Valley and Ailsbach River terrace evolution – and its importance for the cave use possibilities by cave bears, top predators (hyenas, wolves and lions) and humans (Neanderthals, Late Palaeolithics) in the Frankonian Karst. Case studies in the Sophie's Cave near Kirchahorn, Bavaria. – E&G Quaternary Science Journal, 62 (2): 162–174. DOI: 10.3285/eg.62.2.07

Abstract: The Sophie's Cave in Upper Franconia, Bavaria (South Germany) eroded into Upper Jurassic reef dolomite and is a perfect model including all three stages of cave development ranging from a 1. ponor cave, to 2. intermediate periodically flooded cave to 3. dry cave. The key position of the cave along the Ahorn Valley, a side valley of the larger Wiesent River Valley, allow a cave genesis and evolution reconstruction which started in the Pliocene. The main refill took place in the Quaternary with Middle to Late Pleistocene river terrace sediments, present as relict sediments. Seven valley genesis stages between Pliocene to final Late Pleistocene can be separated in elevations of 440 to 375 meters a.s.l. The lowering of the Ailsbach River in the Ahorn Valley is important to understand the accessibility of caves for Pleistocene animals and Palaeolithic humans in different valley positions and elevations during different times in Upper Franconia, and the natural erosive opening/closing of cave entrances towards drainage valleys. The Sophie's Cave was used first in the Middle Pleistocene in elevations of 420 m. a.s.l. over small entrances only by small carnivores such as martens and later in the Late Pleistocene (412 m a.s.l.) by cave bears mainly, which denned over generations leaving hereby rich Late Pleistocene bonebeds. Hyenas also used the cave entrances as dens, similar as wolves, but over shorter periods only. The Ice Age top predators and cave bears seem to have been in competition within the fluent geomorphological change or collapse of cave entrances especially along river valleys during the late Middle (Neanderthals) to Late Paleolithic (Aurignacians-Gravettians), which humans did not occupy the present Sophie's Cave entrance. Late Palaeolithics (Gravettians, indirectly dated by reindeer antler: 25.750±130 BP and mammoth pelvic fragment: 24.150 ±130 BP) used in the final Late Pleistocene a deeper part of dry cave only as sanctuary in form of a shamanic deposition of selected mainly shed male reindeer antlers (and possibly two mammoth pelvic remains). This human caused antler accumulation was finally scattered at the end of the Ice Age (Dryas to Alleröd) and was damaged by large dropping ceiling blocks and by dropping waters under the last and main speleothem genesis period. After the disappearance of cave bears and predators within the last maximum glaciation (= LGM), and after glaciers (or larger snow fields) might have have been present in some of the Upper Franconian Valleys, such as the Ahorn Valley, there was no sign of cave use by large mammals or humans. After the LGM, during the Dryas to Alleröd periods, not far in the Ahorn Valley at the Rennerfels rock shelter a settlement of similar Late Magdalénian/Epipalaeolithic age is known on the Ailsbach River terrace in elevation about 380 m a.s.l.

Eiszeitliche geomorphologische Ahorntal- und Ailsbach-Flussterrassen Entwicklung – und ihre Bedeutung für die Höhlennutzungs-Möglichkeiten durch Höhlenbären, Top-Prädatoren (Hyänen, Wölfe und Löwen) sowie Menschen (Neandertaler, und Spät-Paläolithikum) im Fränkischen Karst – Fallstudien in der Sophienhöhle bei Kirchahorn, Bayern

Kurzfassung: Die Sophienhöhle in Oberfranken, Bayern (Süddeutschland) erodierte in die massiven Ober-Jura Riff-Dolomite und ist eine perfektes Modell inklusive aller drei Höhlengenese-Stadien von 1. Ponor-Höhle, 2. Intermediate zeitweilig geflutete Höhle, 3. Trocken-Höhle. Die Schlüsselposition entlang des Ahorn-Tales, einem Seitental des größeren Wiesent-Flusstales, erlaubt eine genaue Höhlengenese und Verfüllungsrekonstruktion, die bereits im Pliozän begann. Die Hauptverfüllung mit Flussterrassen-Relikt-Sedimentserien fand im Mittel- bis Spät-Pleistozän statt. Sieben Höhlen-Genese und Verfüllungs-Stadien zwischen dem Pliozän und ausgehenden Spät-Pleistozän können in den Höhlenlagen zwischen 440 to 375 ü. N.N. unterschieden werden. Die Eintiefungsschritte des Ailsbachs im Ahorn-Tal sind wichtig für das Verständnis der Zugangsmöglichkeit der talnahen Höhlen für Eiszeittiere und paläolithische Menschen in verschiedenen Tälern von Oberfranken zu unterschiedlichen Zeiten, sowie den generellen Höhleneingangs-Öffnungen und -Schließungen während der Entwässerungs-Phasen in den Tälern. Die Sophienhöhle wurde erstmals im Mittel-Pleistozän in der Höhenlage der Terrasse auf 420 m ü N.N. über einen kleineren Eingang durch Kleinraubtiere wie Marder genutzt. Später, als die Terrasse auf 412 m ü N.N. abgesunken war kamen kleine erste Höhlenbären-Arten über einen neuen Eingang die im Früh-/Mittel bis Spät-Pleistozän die Höhle als Horst nutzten. Diese hinterließen reichhaltige Knochenlagen. Hyänen nutzten nur gelegentlich und kurzfristig den damaligen Höhleneingang, wie auch Wölfe. Die Eiszeit-Top-Prädatoren (Hyänen, Wölfe) und Höhlenbären scheinen im steten Konflikt im Kampf um die wieder und wieder zusammenbrechenden und sich verändernden Höhleneingänge entlang der Täler gewesen zu sein, besonders im Mittel-Paläolithikum (Neandertaler) oder Spät-Paläolithikum (Aurignacien-Gravettian). Keine dieser Menschengruppen nutzte die Sophienhöhle oder deren heutigen Eingang. Spät-Paläolithiker (Aurignacias/Gravettians, indirect datiert an Rentiergeweihen: 25.750±130 BP und einem Mammut-Beckenrest: 24.150 ±130 BP) nutzten am Ende des mittle-

ren Spät-Pleistozän einen tieferen Bereich der trockenen Höhle nur als rituellen Ort in Form einer schamischen Anreicherung von überwiegend selektierten männlichen Abwurfstangen (und möglicherweise zwei Mammut-Pelvisresten). Diese durch Menschen verursachte Geweihanreicherung wurde letztendlich am Ende der eiszeit (Dryas bis Alleröd) von herab fallenden Deckenblöcken und Tropfwasser der letzten Speleogenese-Periode auseinander gerissen und verfrachtet. Nachdem Höhlenbären und Top-Prädatoren (Hyänen, Löwen) im Hochglazial-Maximum (= LGM) in der Region verschwanden, als tentative Gletscher in einigen Tälern Oberfrankens vorhanden waren, wie im Ahorntal, erschienen Spät-Magdalénian/Epipaläolithikum-Rentierjägergruppen. Ein Jagdlager wurde aus diesern Epochen am Rennerfels-Abri unweit der Sophienhöhle in einer Höhenlage um 380 Metern auf der Ailsbach-Terrasse gefunden.

Keywords: *Bavaria, Ice Age, cave, Ahorn Valley, Alsbach River, terrace evolution, bears, humans, Neanderthals, Late Palaeolithics*

Address of the author: C. Diedrich, PaleoLogic Research Institute, Petra Bezruce, 96, CZ-26751 Zdice, Czech Republic, www.paleologiceu, cdiedri@gmx.net

1 Introduction

The Ahorn Valley in Upper Frankonia (Bavaria) connects to the Wiesent Valley (Fig. 1) and has the most dense cave amount in the Frankonian Alb karst whereas most of them are only small clefts or cavities (Schabdach 1998). The caves are eroded into the massif Upper Jurassic reef and lagoonal inter-reef dolomites and limestones (Meyer & Schmidt-Kaler 1992, Fig. 2). The large caves of the region are the König Ludwigs Cave with its large portal including a single large chamber (entrance 385 m a.s.l.). The 1833 discovered higher elevated and herein studied (entrance 411 m a.s.l., Fig. 1) Sophie's Cave (Holle 1833, Wagner 1833) is situated opposite. Other larger caves in higher elevations between 550 to 430 m a.s.l. have also Late Pleistocene Ice Age vertebrate content such as the Große Teufels Cave, Moggaster Cave, Zoolithen Cave; or Geisloch Cave.–Smaller and fewer cave bear remains containing caves are the Zahnloch Cave, Neideck Cave, Wunders Cave and Esper Cave (Diedrich 2012a, 2013a, Fig. 1).

Already Neischl (1904) remarked first, that sediments in caves along Upper Frankonian river valleys are important for the landscape and glacial dewatering system reconstruction. First identifications of river terraces and their possible elevations discussed Spöcker (1952) for the Frankonian Pegnitz Valley, but with a coarse model only, whereas "problems of the valley genesis and dating" were reviewed by Habbe (1989).–Again, only karst evolution models were presented, especially for the earlier Cretaceous to Tertiary periods (Groiss et al. 1998). A new discussion about river terraces in the valleys of Upper Frankonia appeared with the new sedimentological research of the Zoolithen Cave along the Wiesent Valley, where 140 meters above today's river elevation the entrance must have been flooded postglacially, dated by cave bear tooth morphology and stratigraphy (Diedrich 2011, 2013a).

In this study, the Sophie's Cave in the Ahorn Valley is presented, which allows a detailed picture of the valley and cave genesis starting in the Early Pleistocene as a model for the Upper Frankonian geomorphological change, especially with details of river terraces and elevations for the late Middle Pleistocene to final late Pleistocene.

The Upper Frankonian Karst, which formed mainly into the massif Upper Jurassic dolomites and partly also in limestones, can be reconstructed in its geomorphological change between the Plio- and Pleistocene (latter in high resolution). The only data available are cave relict river terrace sequences, which were found on entrance areas of valley-cut caves. Here it is presented for a case study area of the Ahorn Valley between south of the village Kirchahorn and the Rabenstein Castle, especially in the larger Sophie's Cave of Upper Frankonia (Fig. 4).

Their three main sedimentary series are correlated and dated partly with megafauna remains, whereas repeating floods of the cave and resedimentation destroyed parts of older layers (Figs. 3–4). The Sophie's Cave with autochthonous cave genesis and allochthonous river terrace infills allows the reconstruction of the lowering of one of the Frankonian rivers in the Ahorn Valley starting 5 Mio years ago. The Sophie's Cave is furthermore a perfect model for Frankonian caves in dolomites with three main development stages from a 1. ponor, to 2. transitional and finally 3. dry cave, which much more details can be found in Diedrich (2012a-b).

2 Material and methods

From January to July of 2011 a first interdisciplinary cave survey of the Sophie's Cave allowed the genesis, refill (see sections Fig. 3) and use by animals and humans to be reconstructed (Fig. 4). The methodologies followed general cave genesis and morphology analyses (Bretz 1942, Jennings 1985), cave sedimentology (Dogwiler & Wicks 2004, Sasowsky & Mylroie 2007, White 2007) but also river terrace analyses (Kaiser 1961). Finally the recent chronostratigraphy for the Plio-Pleistocene of Gibbard & Cohen (2009) was used. Sections all over the Sophie's Cave in different positions and elevations were analysed in grain sizes, sediment structures and fossil contents (including reworked Jurassic fossils). Palaeomagnetic studies are still in progress. First and only relative dating was possible following "fluvial river terrace sequence stratigraphy" (Bridgland et al. 2004), and the "evolution of cave bear and especially tooth morphology" (Rabeder 1999, Stiller et al. 2010), but also the "cave megafauna bone assemblages" and "taphonomy" in Late Pleistocene mountainous regions in general (e.g. Diedrich 2011, 2012b, 2012a) and its change, which support the climatic interpretations.

The cave was explored geologically, palaeontologically, and archaeologically in January-August 2011. The historically opened sections at different parts of the cave system were prepared and studied being now accessible and protected for further studies and popular scientific presentations within the show cave. New Middle Pleistocene marten tracks were left in-situ, such as a new excavated large bonebed field in the Reindeer Hall, and a small bonebed field in the Bear's Passage. The Late Pleistocene megafauna remains, mainly cave

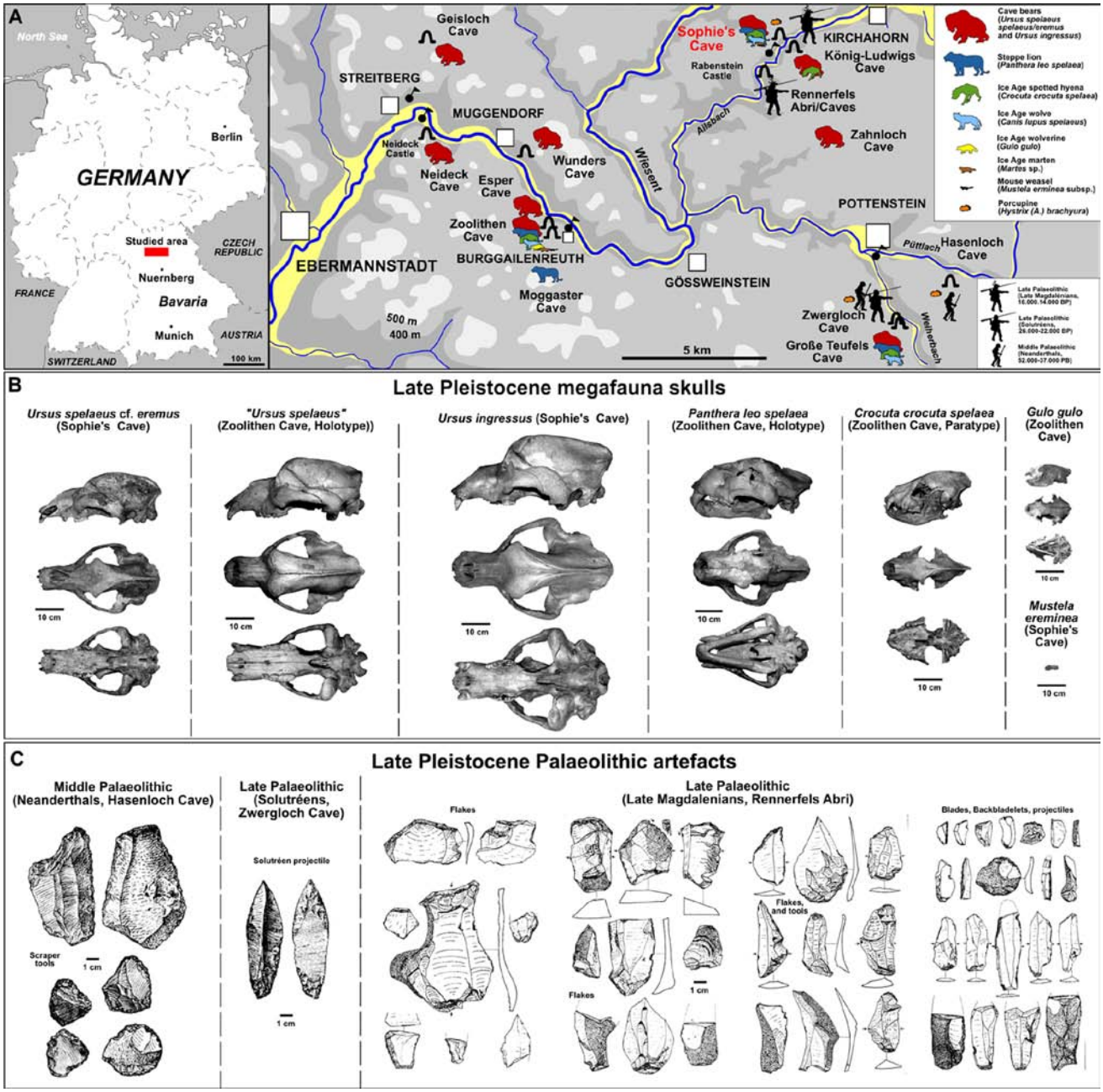

Fig. 1: A. Late Pleistocene cave bear, hyena, wolf, marten and weasel den cave sites and caves/valleys used by humans in the Middle (Neanderthals) and final Late Palaeolithic (Late Magdalénians/Epipalaeolithics). B. Selected Late Pleistocene Ice Age animal skulls (composed from Diedrich 2011, 2012a). C. Composed stone artifacts from the Hasenloch Cave (Middle Palaeolithic) and Rennerfels rock shelter (Late Magdalenian/ Epipalaeolithic) sites (selected from Gumpert 1981).

Abb. 1: A. Spätpleistozäne Höhlenbären-, Hyänen-, Wolf-, Marder- und Mauswiesel-Höhlen-Horste und Nutzung der Höhlen/Täler durch Mittel-Paläolithiker (Neandertaler) und spätem Spät-Paläolithikum (Spät-Magdalénian/Epipalaeolithikum). B. Ausgewählte spätpleistozäne Eiszeittier-Schädel (zusammengestellt aus Diedrich 2011, 2012a). C. Zussammengestellte Steinartefakte von der Hasenloch-Höhle (Mittel-Paläolithikum) und Rennerfels-Abri (Spät-Magdalénian/Epipaläolithikum) (zusammengestellt aus Gumpert 1981).

bear bones (about 98%), which were dumped historically in two areas of the Bear's Passage and the Bear's Catacombs (more then 1,600), were cleaned, inventoried and studied during this project and are housed now in the museum of the Rabenstein Castle which belongs to the cave (www.burg-rabenstein.de). Additionally the so far incorrectly composed "cave bear skeleton" was demounted and analysed. A new small cave bear species skeleton was compiled including all small bones which is presented since 2011 in a show case in the cave lying with the isolated bones in "hibernation bed position".

Finally two C14 datings were made on a reindeer antler and mammoth pelvic (both found both below last speleothem layer in the centre of the Reindeer Hall) by the Beta Analytic Laboratory, Florida, USA (www.radiocarbon.com).

3 Results and discussion

A. Pliocene-Early Pleistocene: Below a Pliocene plateau phreatic waters caused the main cave genesis in underground water level period (ponor cave stage, Fig. 5A). The first sediments were deposited fluvial by the underground

E&G / Vol. 62 / No. 2 / 2013 / 162–174 / DOI 10.3285/eg.61.2.07 / © Authors / Creative Commons Attribution License

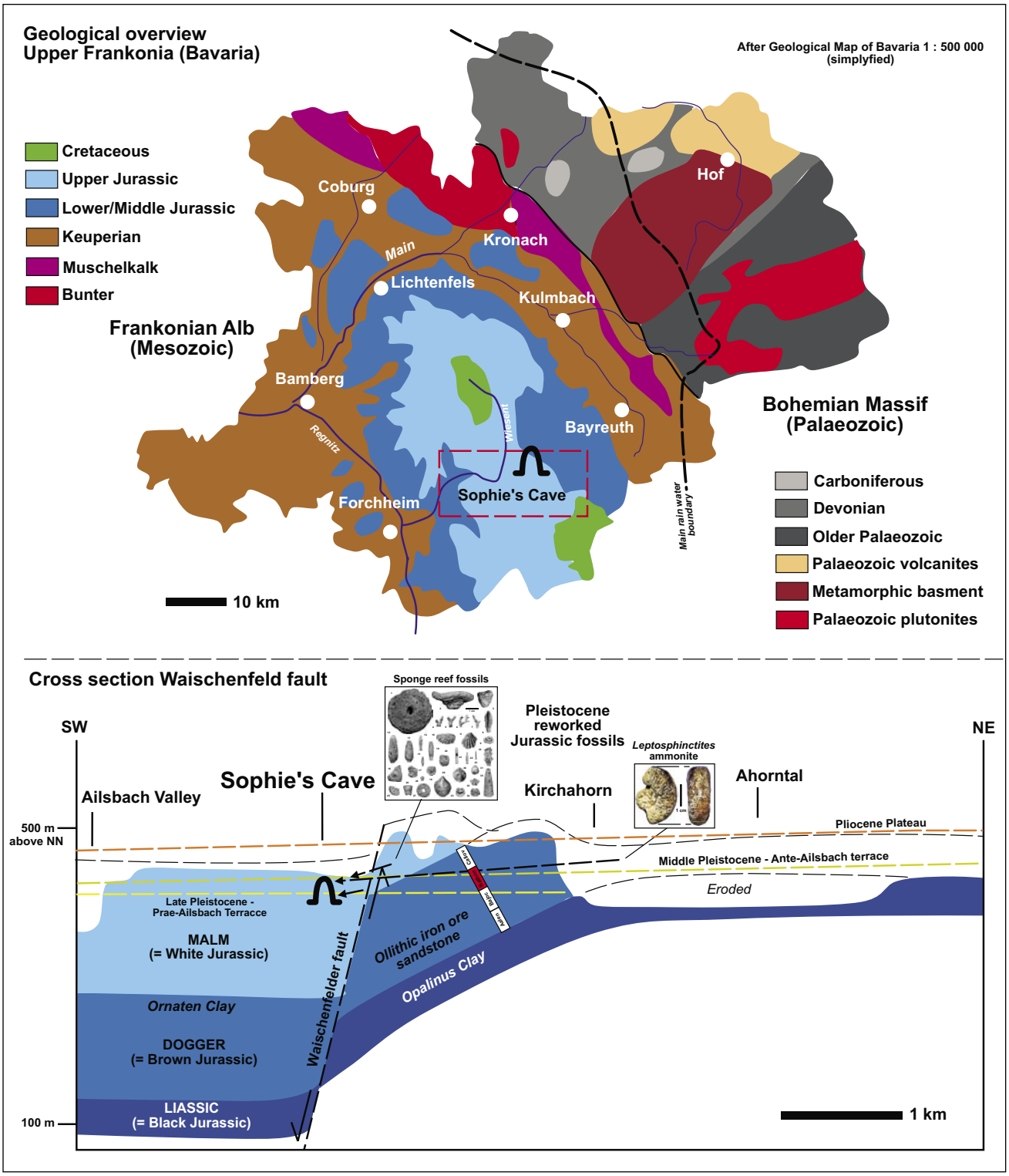

Fig. 2: Geological overview of Upper Franconia and cross section along the Kirchahorn Depression and Ahorn Valley and fault, and former elevations of the river terraces. The fossils found in the Pleistocene sediments of the Sophie's Cave are from the surrounding Brown and White Jurassic, whereas quartz pebbles are from nearby Lower Cretaceous sandstones (geology modified and simplified after Meyer & Schmidt-Kaler 1992 and Geological Map of Bavaria 1 : 500.000).

Abb. 2: Geologische Übersicht von Oberfranken und Querschnitt entlang der Kirchahorn-Depression und Ahorntal-Störung sowie ehemaligen Flussterrassen-Höhlenlagen. Die Fossilien aus den Pleistozän-Sedimenten der Sophienhöhle stammen aus den umgebenden Braun- und Weißjura-Schichten, wobei Quarz-Kiesel von wenig weiter entfernten Unter-Kreide-Sandsteinen aus der Umgebung herrühren (Geologie verändert umgezeichnet nach Meyer & Schmidt-Kaler 1992 und Geologische Karte von Bayern 1 : 500.000).

river in the Plio-Early Pleistocene consisting of „coloured series" of about 1–4 meters thickness: black manganese, red iron (minerals are used for palaeomagnetic anlyses) and orange limonite clays, silts and yellow dolomite ash sand layers (Fig. 4). Within the Early Pleistocene, the upper wide extended initial river valley must have developed in elevations starting below 450 m a.s.l. (with unclear depth of erosion at end of Early Pleistocene) but terrace sediments were impossible at that time to have been washed into the not opened Sophie's Cave branches. The cave was cut by the Ante-Ailsbach River not before the Middle Pleistocene.

B. Middle Pleistocene: During the further valley genesis

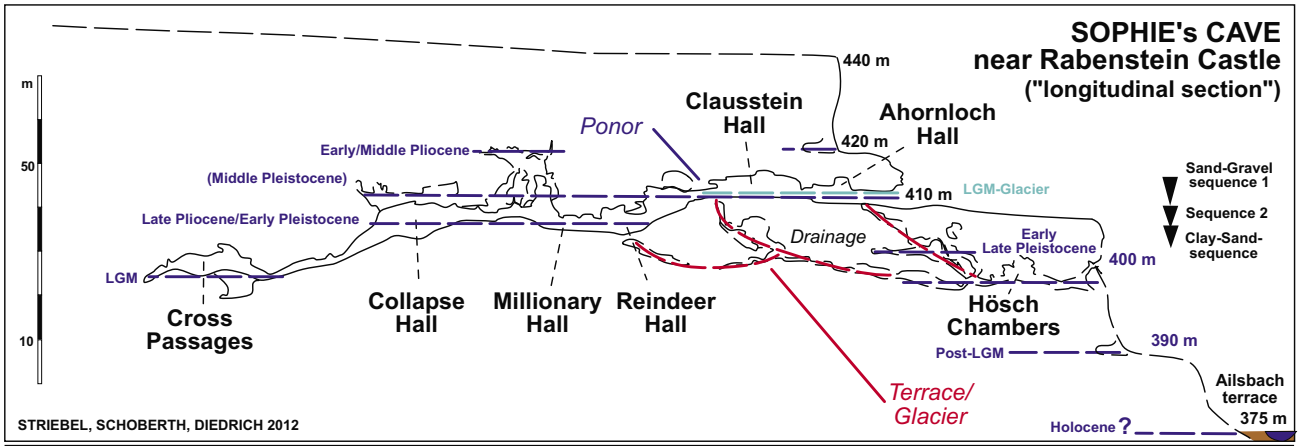

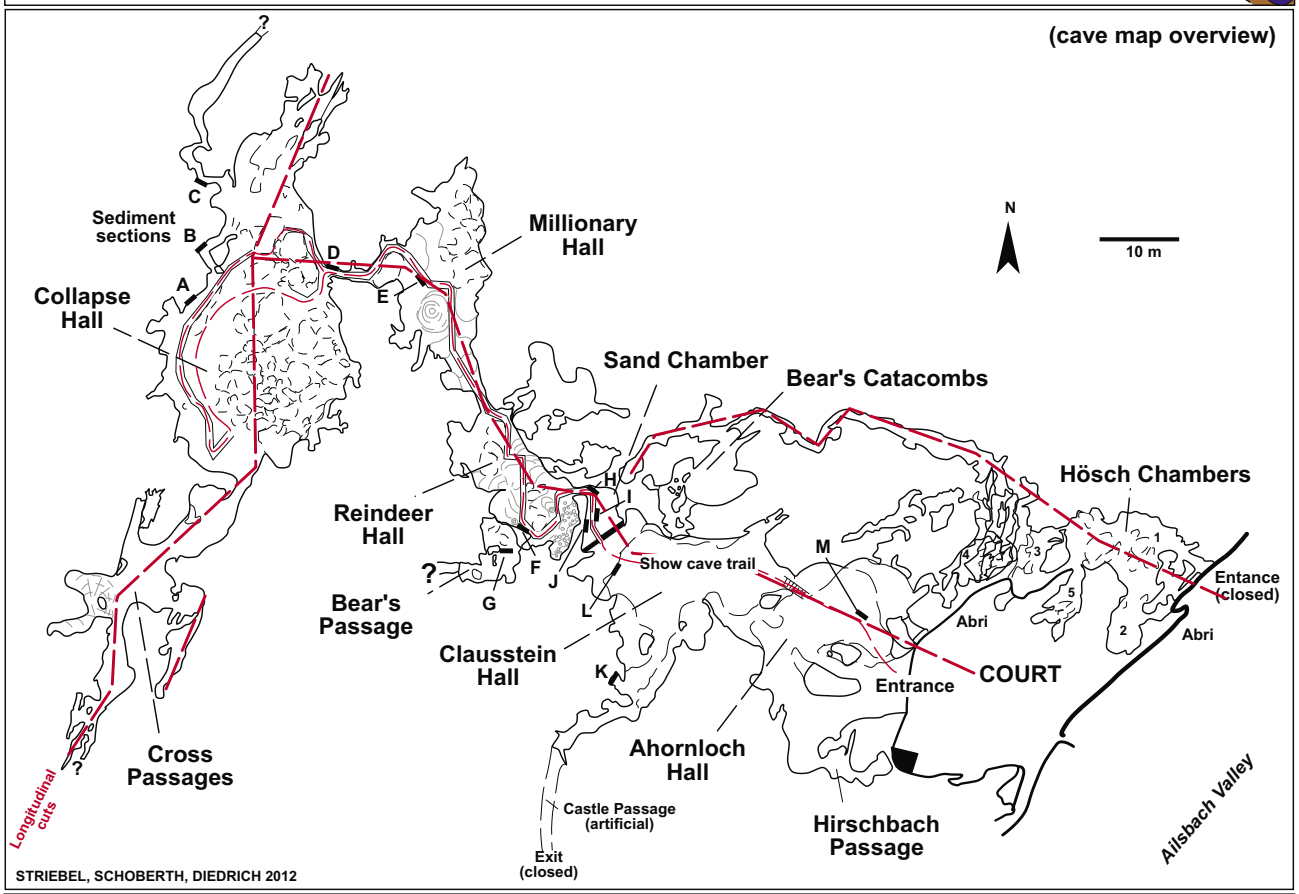

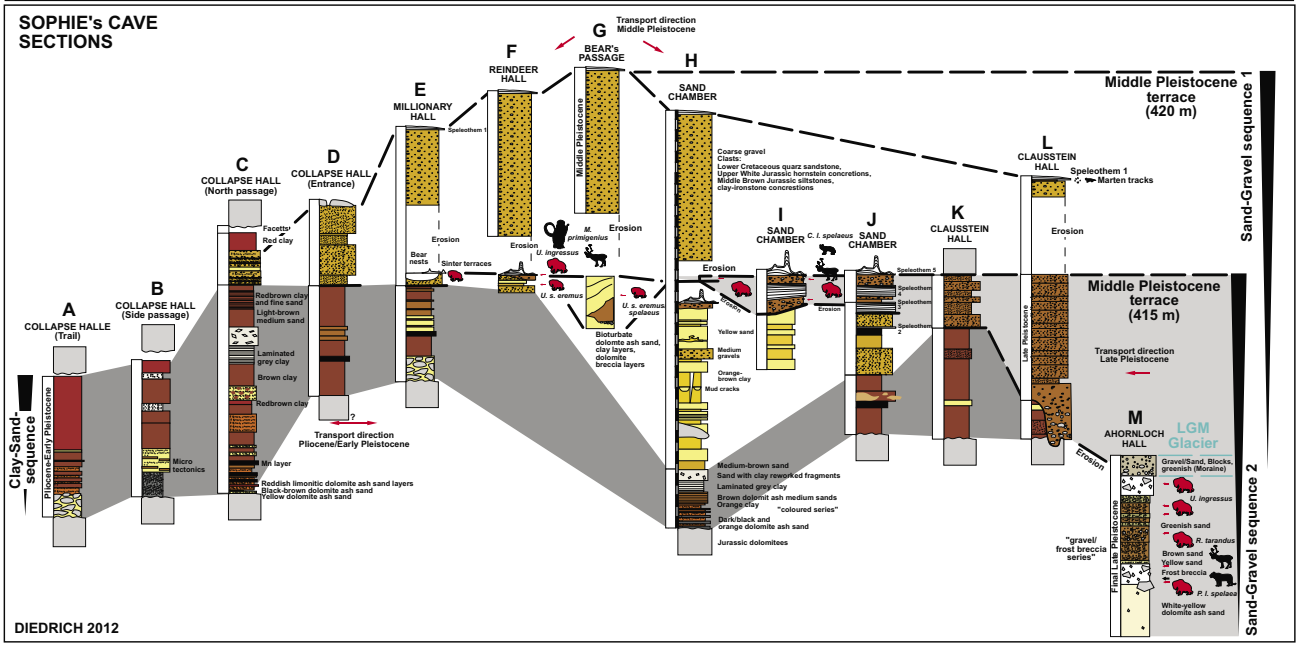

E&G / Vol. 62 / No. 2 / 2013 / 162–174 / DOI 10.3285/eg.61.2.07 / © Authors / Creative Commons Attribution License

(continuing wide valley morphology) and river terrace deepening of the Ante-Ailsbach River, parts of the cave fell dry time by time, others (valley close related parts) were flooded and filled (transitional cave stage, Fig. 5B). The oldest Ante-Ailsbach River terrace (elevation about 420 m a.s.l) left a first larger sedimentary fluvial sequence („yellow series", Fig. 4) of up to 8 meters thick limonitic, yellow clay/sand (high flood deposits) which end in some meters thick massive coarse gravel layer (terrace maximum high). The water did clearly not went too deep into the cave system (preserved bonebeds and cave bear nests in the Millionary Hall). The water did not produce a classical underground river system again, most probably due to vadose changed cave morphology and vertical shafts. Waters clearly disappeared vertically in the Reindeer Hall, and the Clausstein-Halls, which have larger vertical shafts to lower elevated systems, in which most probably the water was drained (Fig. 3). Those Middle Pleistocene gravels which maximum thickness in the Reindeer Hall contain Middle/Upper Jurassic non-dolimitic rock pebbles (even Middle Jurassic ammonites: *Leptosphinctites* – Fig. 2, and many metasomatic silicatic replaced and calcitic reef fossils) but also up to 1 cm small well-rounded clear quartz pebbles, which latter were transported twice and originate from surrounding eroded Lower Cretaceous fluvial deposits. The sediments were washed over an open vertical/diagonal shaft above the Clausstein Hall into the cave, and filled up nearly half of the Reindeer Hall and most of the Millionary Hall and were finally covered in some areas by a first undated speleothem layer (first speleothem genesis period, Fig. 3, compared to other Frankonian Caves: cf. Nordhoff 2005). Below this, in the Clausstein Hall, marten tracks on originally mud-cracked clay surfaces (preserved now as hyporeliefs below speleothem layer) (Fig. 5B) indicate the first use as a marten den of the Clausstein Hall cave part at least.

C. Early Late Pleistocene: The terrace lowered only few meters to an elevation of about 415 a.s.l. (Fig. 5C). In the early-middle Late Pleistocene only small cave bears used the cave over a new opened entrance (not today's entrance) even deep for hibernation purposes to protect against carnivore predators (lions, hyenas, and wolves). Many bite damaged and cracked cave bear bones, and scavenged disarticulated carcasses were found deep in the cave (Millionary Hall, Reindeer Hall and Bear's Passage). Wolf (*Canis lupus spelaeus*) and small weasel (*Mustela erminea*) remains were also found there. Porcupines (*Hystrix (A.) brachyura*) are indirectly proven by two chewed (typical 4-5 mm wide rodent bite marks) cave bear cub humeri. Many wolf excrements were found in the Bear's Passage mainly, and few also in the Reindeer Hall and Millionary Hall in which coprolites partly digested cave bear bones are cemented.

D. Middle Late Pleistocene: In the middle Late Pleistocene a first slight ceiling collapse and new speleogenesis (second speleothem genesis) changed the cave morphology few which resulted the blocking of the Bear's Passage to the Reindeer Hall and in general to the deeper hibernation areas. Further 5 meters the river terrace lowered deeper (410 m a.s.l.) (Fig. 3, 5D) possibly during a warmer period (third speleothem genesis period), which finally opened the today's valley-sided large portal entrance, but closed the former one. The youngest Pre-Ailsbach River terrace started with another coarsening up terrace sequence and started to grow again indicating increasing valley terraces (?glaciers) (Fig. 4). This time, quarz-rich sands (brown to greenish colored, warmer period) do not contain clay layers and are intercalated with frost brekzia layers (colder period). Large cave bear remains of *U. ingressus* date all those layers of the anterior cave area into the final Middle Late Pleistocene (32.000–24.000 BP, cf. Münzel et al. 2011; Fig. 4), where large cave bear types used the today's entrance and side chambers over many generations (rich bonebeds, and many cub remains). Ice Age spotted hyenas and wolves used this cave part periodically as a den, and scavenged on the bears too. Finally climatic cold interstadial indicators are arctic fox remains from the anterior cave area (Ahornloch Hall).

E. Final middle Late Pleistocene (Late Palaeolithic Gravettian, around 25.000 BP): The terraces seem to have been eroded fluvial (or ?by glaciers); the ponor cave was the Hösch Chambers elevation, whereas the deposits in the Clausstein Hall increased about 2 meters in a short time of a cold period (Fig. 5E). This is the time, when Gravettian humans used the Reindeer Hall as sanctuary place only (see cave use by humans), and large *U. ingressus* cave bears the anterior cave parts.

F. Last Glacial Maximum (= LGM, around 19.000 BP): Floods of melting large snow field (e.g. large depression area in soft Middle Jurassic sediments around Kirchahorn) or ?glacier surfaces washed in events the side moraine/kames material (unsorted sediments with local dolomitic non-well rounded blocks in the uppermost layers into the Ahornloch Hall (see glauconitic till: Figs. 3-4) and the large cave bear *U. ingressus* bones downwards into the Bear's Catacombs and other side branches (Fig. 5E), which bones are in "non-stratified" dolomite gravel layers (semi-rounded pebbles) and are in non-rounded well conditions. The some meters higher elevated gravels in the Clausstein Hall, which replaced the bone layers, and contain itself only very few bone remains. Those sediments seem to represent LGM side moraine/kames reworked gravels, when the ?terrace increased on elevation of about 410 a.s.l. (if not transported from glacier surface waters).

G. Final Late Pleistocene – Meiendorf, Alleröd to early Holocene: When the snow field (or ?Valley glacier) was melting post LGM lowering from 412 m a.s.l. to the ground (?ground moraine) the former river terrace eroded from an unknown level to 385 m a.s.l. (or even deeper, Fig. 5F). Again braided rivers and its coarse gravels must have formed the steep margins of the narrow valley morphology, where no terrace sediments were left on the wall margins before (?due to the glaciers); which lateral moraine sediments (till) mainly

Fig. 3: Correlation of the sections in the Sophie's Cave, and dating of the two river terrace sequences using mainly cave bear species/subspecies (cave map according to Schoberth et al. 1997, and longitudinal cuts composed by Dr. T. Striebel).

Abb. 3: Korrelationen der Profile in der Sophienhöhle und Datierung der beiden Flussterrassen-Sequenzen mit Hilfe der unterschiedlichen Höhlenbären-Arten/Unterarten (Höhlenplangrundlage nach Schoberth et al. 1997, Längsschnitte zusammengestellt von Dr. T. Striebel).

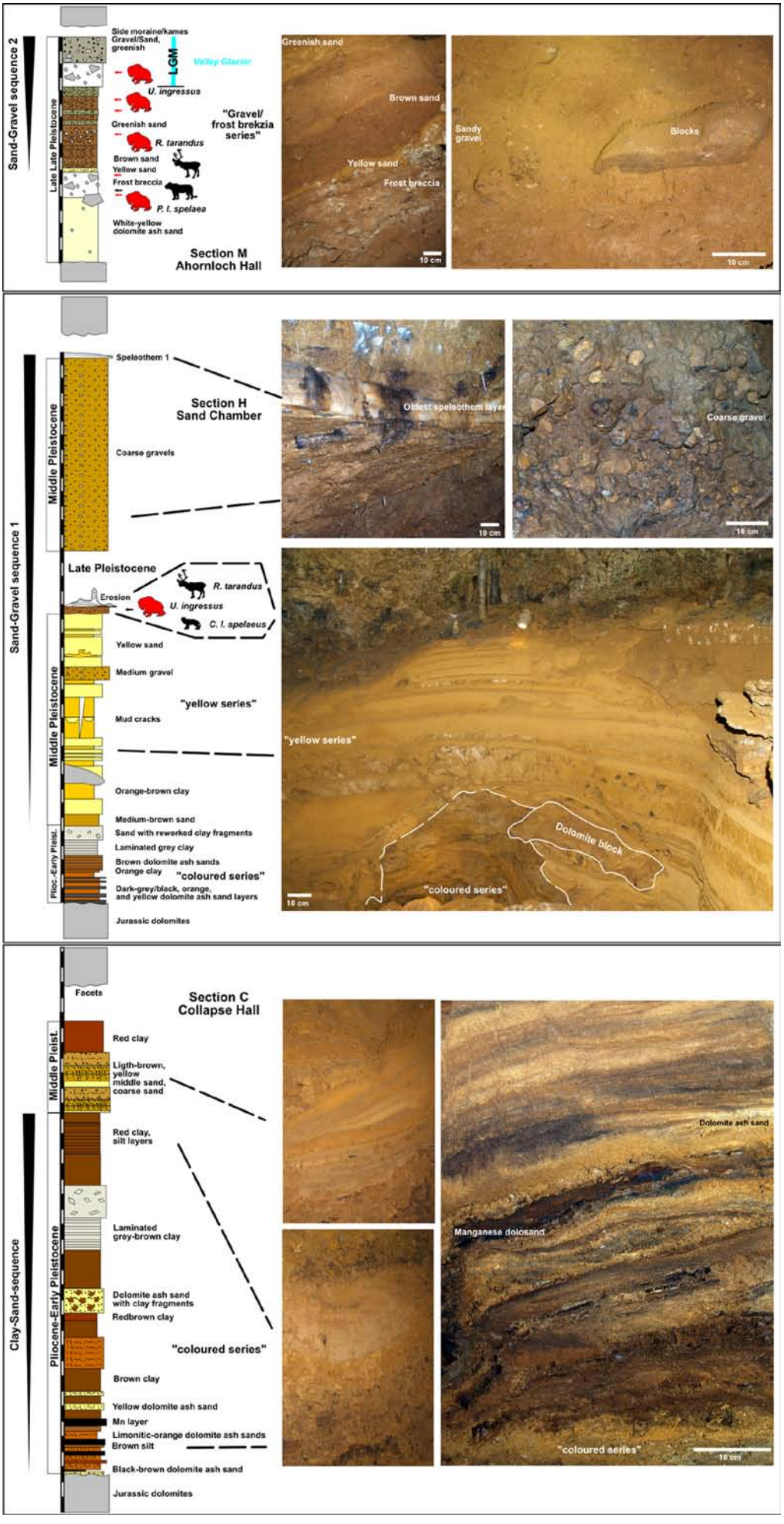

Fig. 4: Sophie's Cave main sedimentary series types and composed generalized Pliocene to Late Pleistocene section.

Abb. 4: Hauptsedimentär-Serientypen der Sophienhöhle und zusammengestelltes generalisiertes Pliozän-Spät-Pleistozän-Profil

E&G / Vol. 62 / No. 2 / 2013 / 162–174 / DOI 10.3285/eg.61.2.07 / © Authors / Creative Commons Attribution License

were left only in caves or cavities, such as found in the upper layers of the Sophie's Cave (Fig. 4). In the cave changing conditions caused massive event-ceiling collapse changed the cave morphology drastically, which blocks are mainly in the chambers covering their floors (Fig. 5F). Their age can be dated indirectly by two facts, first the reindeer antler remains partly are "below" those dropped blocks, whereas the last speleothem layer and candle stalagmites grew all over those large blocks, which are comparable in age to absolute dated candle stalagmites from other Frankonian caves (Nordhoff 2005: dated around 10.513 and 10.227 cal. a B.P.). During this again humid interglacial period the terrace still lowered some meters (today 375 m a.s.l., Fig. 5G) under more humid climates, that also caused the fourth and final speleothem genesis (continuing into the Holocene). Most of the speleothems such as typical "candle stalagmites" also developed on the large ceiling drop-blocks. At this ending Ice Age time, finally the access to the Reindeer Hall over the Sand Chamber was closed by a speleothem layer (that was opened again in 1833 when the cave was "discovered" twice – first by Gravettians).

The Ahorn Valley terrace stages and dating

The 550 meters elevated Moggaster Cave of Upper Frankonia was refilled with sediments during the Early to Middle Palaeogene (Palaeocen-Eocene: Groiss 2000). The 455 meters elevated Zoolithen Cave (close to the Moggaster Cave, Fig. 1) was refilled very few with sediments (clay layers) not before the Neogene (most probably Miocene: Diedrich 2013a). The Sophie's Cave in elevation of 410 meters must have been eroded and refilled correlating the cave level elevations only (south few higher as in the north, see Fig. 1) in younger Tertiary times, which Pliocene age is expected, not being confirmed by fauna or absolute dating. Typical first refills not only in the Sophie's Cave are the dolomite ash sands (yellow or dark-manganese or reddish-limonite layers = coloured series, Fig. 4), products of dolomite weathering (cf. Burger 1989). Whereas the Zoolithen Cave repesents a cave system in elevation between 460–430 meters in about three different levels (Diedrich 2013a) with early to maximum middle Middle Pleistocene refill, and finally latest Late Pleistocene flood event and terrace infill with medium to coarse dolomite gravels, the Sophie's Cave is more north and in lower elevation of 415–385 meters and has mainly a Middle to Late Pleistocene terrace refill (Figs. 4–5). The Ahorn Valley was eroded between the Pliocene and late Middle Pleistocene between 450–420 meters (Fig. 5). In the upper first 10 meters, the valley was wide, and started about 440 meters to become narrower. In the late Middle Pleistocene, the Ante-Ailsbach was already one third deep eroded of the today's Ahorn Valley elevation (375 m) on 420 meters. Possibly in this stage and first speleothem genesis time that covered the first terrace sedimentary sequence in the Sophie's Cave correlates more or less with the first speleothem genesis in the Zoolithen Cave (cf. Diedrich 2013a). There are few speleothem data available from the Franconian Alb caves, which can be used for correlations of the Sophie's Cave speleothem ages preliminary. Oldest speleothem data delivered the Zoolithen Cave 342.050 ± a 71.400 BP (Middle Pleistocene, Holsteinian interglacial, MIS 9) with its largest and oldest speleothems (Kempe et al. 2002). Those speleothems in the Zoolithen Cave developed on an elevation of about 445–435 meters in some parts of the cave system only (Diedrich 2013a). At Hunas Cave ruin the first and older speleothem is represented by a dated flowstone sample (HU-i) bearing a single age of 270.593 ± 24379 BP (Middle Pleistocene, Middle Saalian, MIS 7, Nordhoff 2005). The younger Hunas Cave ruin stalagmite has been dated between 79.373 ± 8237 and 76.872 ± 9686 BP (Late Pleistocene, MIS 5d) during the warm interstadial around 79 ka BP (Nordhoff 2005). This seems to be the time period, where the larger older speleothems (Large and Small Millionary) of the Sophie's Cave also started to grow. The Mühlbach Cave candle stalagmite reveal some analogy to the candle stalagmites of the Sophie's Cave including the transitions from the post-LGM (Boelling/Alleroed Interstadial and Younger Dryas cold phase) to the Early Holocene between 10.513 and and 10.227 BP (Nordhoff 2005). During the early/middle Late Pleistocene small cave bears (*Ursus spelaeus eremus/spelaeus*) date an unknown river terrace elevation at that time below 410 meters, and indicate dry cave conditions (no more flooded). The final Late Pleistocene and LGM has at least two deposit levels or series in the cave on elevations of 410 and 412 meters, dated by *Ursus ingressus* cave bear teeth which appeared in general in central Europe between 32.000-24.000 BP (Stiller et al. 2010). The Pre-Ailsbach River terrace grew first slowly and finally postglacially after the LGM at least two meters. The post-LGM replacement of bonebeds in the Sophie's Cave is similar to the replacements of bone layers in the Zoolithen Cave or Große Teufels Cave, which is also dated into the post-LGM (Diedrich 2013a). Although so far there is no geomorphological and for hard rock areas (here those are soft sedimentary rocks) typical evidence of a (valley) glaciation in the Franconian Alb during the LGM a minor glaciation of some elevated valleys in the study area could be a matter of debate. In this case sedimentary remnants of the glaciers have been eroded or remained undetected so far in the valleys but may have been preserved in caves (see Fig. 5 F and Diedrich 2013b). After 19.000 BP, the terraces must have eroded (probably even by ?glaciers) in some Frankonian valleys (Wiesent Valley, Ahorn Valley) whereas massive melting waters (which originate from larger snow fields or ?glaciers) replaced the "bonebed layers" of the anterior cave areas and mixed them with non-rounded and reworked tilt material. A questionable glaciation in 500 a.s.l. elevations and valley glacier development would have had massive impact of the Palaeolithic settlement of Upper Frankonia, because the natural quick landscape change explain the absence of Late Palaeolithics such as Late Solutréeans to Middle Magdalénians (= around LGM time). This is similar as recently described for the Harz Mountain Range and its caves in northern Germany (Diedrich 2013b).

Finally, there is the discussion about the extreme high elevation of the Zoolithen Cave gravel relicts of LGM times times compared to the today's Wiesent elevation (140 meters deeper), which dolomite gravels are found also in other caves around Muggendorf in elevations between 455-435 meters (Diedrich 2013a) which can be explained at the moment only by the presence of large snow fields in depressions or ?glaciers (ice caps or filled depressions) at least on the highest Frankonian areas and branching valleys (over 500 a.s.l.), especially around Muggendorf (Diedrich 2013a). The directions of the postglacial drainage (or LGM-valley gla-

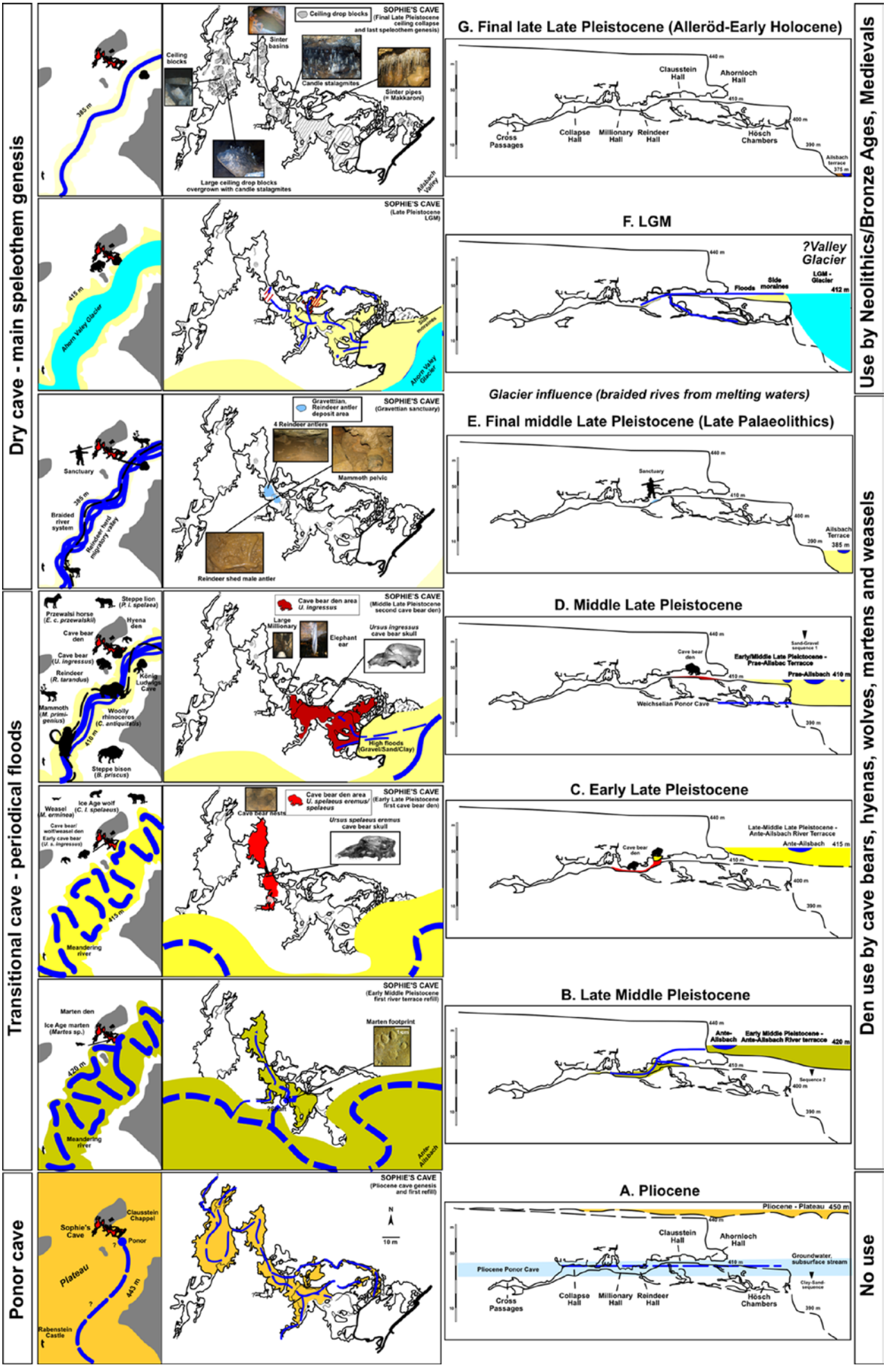

E&G / Vol. 62 / No. 2 / 2013 / 162–174 / DOI 10.3285/eg.61.2.07 / © Authors / Creative Commons Attribution License

ciers) reconstructions is still vague and a first model (Diedrich 2013a) under further study. This theme has to be discussed much further (e.g. at Große Teufels Cave), but much more cave relict sediments have to be studied and interdisciplinary cave research in Upper Franconia are of need. However, those LGM sediments in the Zoolithen Cave or Sophie's Cave such as Große Teufels Cave seem to be reworked moraine tilt sediments (including glauconite or loess sands). Glaciers would have been over 80 meters thick in the Muggendorf Wiesent Valley region (after present estimations of the Zoolithen Cave sediments: Diedrich 2013a), but only 30–40 meters in the Ahorn Valley near the Sophie's Cave. Glacial signs outside caves in lowlands or glacier valleys (e.g. moraines, drumlins, ice scratch marks on dolomite rocks) would not have survived outside the caves, because dolomites weathered quickly (to dolomite ash sands), also the post-LGM fluvial valley erosion was that rapid caused by climatic changes in the Meiendorf-Younger Dryas stadials/interstadials and must have destroyed those typical glacial signs within the valleys. Possibly relicts and signs are present, but have not been described or identified yet. This is different in "hard rock" middle high mountain regions of central Europe such as the Krkonoše Mountains (CZ, Pl: Engel et al. 2010), the Bohemian Forest Mountains (Mentlík et al. 2010), or northern German Harz Mountain Range (Diedrich 2013b), where all typical glacial structures and deposit types are still preserved in several valleys or also only as relic sediments in caves (cf. Diedrich 2013b). At least the deep valleys would fit to a glacier landscape. The early Postglacial was the main "hazard time" in Upper Frankonia, when caves collapsed due to climate changes in the Bölling/Alleröd times (see last speleothem genesis phases of Frankonian Alb in Nordhoff 2005) when the valley formed quickly (?and glaciers melt rapidly).

Cave use by mammals

Ice Age mammals were able to use the Sophie's Cave when it was cut during the valley genesis not before the late Middle Pleistocene.

Middle Pleistocene: After the first river terrace material was washed into the cave, when it fell dry before the first speleothem generation grew, martens used a part of the cave (Clausstein Hall) as den (only track records, Fig. 5B).

Early-Middle Late Pleistocene: The further erosion opened an entrance to the Bear's Passage which was used in the early and middle Late Pleistocene by small cave bear subspecies mainly with still primitive cave bear dentition and enamel morphology (P4 are three-coned, dated after methods of Rabeder 1999), which went deep into the cave for hibernation. About nine cave bear nests are still preserved in the Millionary Hall (Diedrich 2012a). Also weasels (*Mustela erminea*) used the same cave area as a den (also Zoolithen Cave, Diedrich 2013a), whereas porcupines (*Hystrix* (*Atherurus*) *brachyura*) went into the cave via the former entrance (into Bear's Passage) for bone chewing (possibly also short den use there). In Upper Frankonia such Ice Age porcupines are not only indirectly proven in the Sophie's Cave (Diedrich 2012a), those were already found in the Hasenloch Cave, and the Fuchsloch Cave in the Franconian Alb with original bones, and additionally with typical rodent-chewed bones (Ranke 1879, Nehring 1891, Brunner 1954, Heller 1955). Also lions must have penetrated the cave for bear hunting (especially cubs) similar as demonstrated not only for the Zoolithen Cave (Diedrich 2011, 2012a). Lion remains are not directly present yet of the Sophie's Cave from the early-middle late Pleistocene, but from the final Late Pleistocene (Diedrich 2013a). Wolves also consumed the bear carcasses in the Sophie's Cave similar as documented for the Zoolithen Cave (Diedrich 2011, 2012b, 2013a), especially in the Bear's Passage somehow during the middle Late Pleistocene, when there was a block (large dropped ceiling block) between the Bear's Passage and the Reindeer Hall, a time where cave bears had to hibernate at the end of the Bear's Passage way too close to the entrance. There the bones show strongest carnivore damage caused by of all four, lions, hyenas, wolves and porcupines (Diedrich 2011, 2012a-b, 2013a).

Latest Middle Late Pleistocene: In this time, the largest cave bears species *Ursus ingressus* replaced the smaller and older cave bear subspecies (*U. spelaeus eremus/spelaeus*; cf. cave bear evolution and dating: Rabeder 1999, Stiller et al. 2010) which used the new opened today's entrance and anterior Sophie's Cave areas (Ahornloch, and Clausstein Halls, or Sand Chamber). A hyena den was present (early *U. ingressus* time) not only at the opposite König-Ludwigs Cave (Fig. 1), which pioneer work there started with the beginning of the "hyena den cave research" by Buckland (1823). He worked against Esper's (1774) biblical flood theories, explaining at least "non-cave bear bone assemblages in caves" to be of Ice Age hyena origin. Hyenas imported also in the Sophie's Cave few mammoth steppe animal prey remains (*Mammuthus primigenius*, *Coelodonta antiquitatis*, *Equus caballus przewalskii*, *Rangifer tarandus,* even *Panthera leo spelaea* juvenile remains, Diedrich 2014) into the short-term used den. Also similar few mammoth steppe prey was imported into the large hyena den of the Zoolithen Cave entrance, which is typical in boreal forest mountainous regions, and explains the "cave bear scavenging and hunt specialization" in those habitats (Diedrich 2011, 2013a).

LGM: Already before the last glaciation maximum in the final Late Pleistocene cave bears (last large species) and top predators (steppe lions, Ice Age spotted hyenas, Ice Age wolves) disappeared/became extinct with most species of the "mammoth steppe megafauna" from northern Germany and also from Upper Franconia (e.g. Diedrich 2013a).

Neanderthal camp sites

Dense populations of hyena clans, wolf packs and cave bear families in Upper Frankonia might have been a good reason, why Middle Palaeolothic (Neanderthals) humans did not oc-

Fig. 5: Sophie's Cave genesis during the Pliocene to final late Pleistocene, river terrace relicts and cave use by animals (marten, hyena, wolf, cave bear dens) and by humans (Late Palaeolithic, Gravettian).

Abb. 5: Genese der Sophienhöhle während des Pliozäns bis zum ausgehenden Spät-Pleistozän, Flussterrassen-relikte und Höhlennutzung durch Höhlenbären und andere Tieren (Marder-, Hyänen-, Wolfs-, Höhlenbären-Horste) und durch Menschen (Spät-Paläolithikum, Grevettian).

cupy the large portal cave entrance of the Sophie's Cave or other caves nearby (similar at e.g. Zoolithen Cave or Große Teufels Cave). The killing of cave bears by Neanderthals is not proven yet in Europe, and the only site where a camp site was possibly present is the Hasenloch cavity near Pottenstein.

Cave use by Gravettians-Solutréens (middle Late Palaeolithic)

In the final middle Late Pleistocene Gravettians used the Reindeer Hall only for shamanic purposes. They left there a "reindeer antler depot", similar as reported for the Magdalénian culture layers of the Oeger Cave (Sauerland Karst, Westphalia: Bleicher 1993), or at the unclear dated Westeregeln open air site (Diedrich 2012c). The origin of the Sophie's Cave antler accumulation will be discussed with comparisons of other caves in Northern Germany (Sauerland Karst) in future in more detail to be of human origin. The antlers (estimated about 100 using the new documented finds and historically mentioned ones in Sternberg 1835) are nearly all "shed male antlers", and are clearly not of "carnivore - hyena, wolf" selective origin (Diedrich 2012a-b, 2014). Additionally, those are found only limited in the Reindeer Hall, close to the "Elephant Ear" and "Bee Basket" speleothems (map in Diedrich 2014). After comparisons to other caves (Zoolithen Cave, Mühlbach Cave), the speleothems Elephant Ear and Bee Basket have not existed that large within the Late Palaeolithic Gravettian period (compared to dated ones in Mühlbach Cave: Nordhoff 2005). The only large reindeer antlers, of which one shed male antler was dated C14 to 25.750±130 BP, were found in a "sanctuary hall", the Reindeer Hall of the Sophie's Cave. A different shamanic use is found in the Mäander Cave, which is also in Upper Frankonia. There only engravings on speleothems (abstract feminine symbols) were left by Late Magdalénians (Bosinski 2011). The absence of artifacts at both shamanic used cave sites in the caves is not unusual and also typical at sites with "cave paintings and engravings" of SW-France (e.g. Lumley et al. 1984). At both Upper Franconian cave sites, the Late Palaeolithic ritual places are deeper in the caves, where "camp site rubbish" is anyway not expected.

Cave use by Late Magdalénians/Epipalaeolithics (final Late Palaeolithic)

Late Magdalénians had a settlement rock shelter site very close to the Sophie's Cave situated close to the Neumühle (between Kirchahorn and Oberailsfeld) at the historically discovered and excavated Rennerfels rock shelter which includes some cavities (Gumpert 1931). There, the Late Paleolithic (deeper layer, "Madeleine" = herein Late Magdalénian VI) and Early Mesolithic (upper layer, "Tardenoisian" = herein: Epipalaeolithic and not Mesolithic) material was excavated (Gumpert 1981) being housed at the Museum in Tüchersfeld. The Late Palaeolithic artefacts can be identified herein as belonging to the today's so-called Late Magdalénian VI and Epipalaeolithic based on two typical projectiles figured by Gumpert (1981). This hunting camp rock shelter site in nearly today's river terrace elevation includes a fire place and artifacts and less bones (Gumpert 1981).

The König-Ludwigs Cave (opposite to the Sophie's Cave) would have been a perfect Late Magdalénian/Epipalaeolithic settlement or hunting camp cave site, too. It was also accessible for the humans at that time (14.000–12.000 BP) after (terrace elevation was below the entrance, Fig. 5F). It is known there, the archaeological layers have been removed already during the 19th century (Sommer 2006) and were moved in front of the cave (still dumped there), similar as at the Sophie's Cave entrance area, where also the upper layers of the first halls have been scooped in front of the cave (or Ahornloch Hall branching areas). The final Late Paleolithic reindeer hunter groups (Late Magdalénians/Epipalaeolithics) were possibly present at further rock shelters similar to the Rennerfels (Gumpert 1981) and not in the caves. At that time entrances were already collapsed or closed by speleothems (e.g. Sophie's Cave) or were not used (no art in caves anymore) as known from other cave-rich regions of Europe). The rock shelter cavities instead were used along the Upper Franconian valleys, because seasonally reindeer herd migration took place and allowed the hunt on those. It seems that the absence of further archaeological sites of those cultures is only a lack of research knowledge and cave history damage or non prosecutions of rock shelters. This is demonstrated at the Sophie's Cave and Mäander Cave with their presence of at least shamanic sanctuaries. Their camp sites along the river valleys (on the plateau margins or caves) must be prospected systematically in future. A further Epipalaeolithic site was described also not far in Upper Frankonia at the site Plankenfels (Schönweiss & Sticht 1968).

Conclusions

The Sophie's Cave can be used as a model for the cave evolution from a ponor cave, to transitional cave with floods and refills of river terrace and glacial (?valley glacier) sediments, which became a dry cave that collapsed and built finally its main speleothems at the end of the Ice Age and during the Holocene. Animals started to use the cave as a den within the Middle Pleistocene (marten den). In the Late Pleistocene mainly small cave bear subspecies (*Ursus spelaeus eremus/spelaeus*) denned in the cave, but those had to change the entrances and areas of denning due to lowering of the river terraces, and collapse of the older entrance (transitional cave stage). Those were hunted by lions and scavenged by hyenas and wolves also deeper in the cave. This is the reason why several of their hibernation nests (9) are still preserved in the deepest reachable part, the Millionary Hall. The closing of the Bear's Passage did not allow bears to hibernate there furthermore. Later, at the late Middle Pleistocene (32.000–24.000 BP) new larger *Ursus ingressus* cave bears appeared, which were able to use the new opened today's entrance. *U. ingressus* populations inhabited several caves along the Wiesent and branching valleys, and also still hyenas, wolves and lions which all disappeared already before the LGM (= before 19.000 BP). Hyenas and wolves also denned periodically in the Sophie's Cave entrance area. At this time of final Middle Late Pleistocene Late Palaeolithic Gravettians left a reindeer antler accumulation within the Reindeer Hall of the Sophie's cave. This depot counts more then 100 mainly shed antlers, which are all or dominated male antlers of which one was C14 dated with 25.750±130 BP. Possibly to this shamanic antler/bone deposition also two mammoth pelvis remains belong to, one being dated with an C14 age of 24.150

±130 BP. With few increase of the terrace, and tentative presence of a LGM valley glacier, all their bones were washed post-LGM into deeper and side-branched Sophie's Cave areas, mainly into the Bear's Catacombs. Possible glaciation models with larger snow fields (or ? small glaciers) of the Upper Franconian region could explain both, the absence of humans around the LGM (22.000–16.000 BP: Late Solutréens to Middle Magdalenians), and the strong and deep erosion of the river valleys, and even extremely high elevated young river terraces, such as tilt or glauconite sand relict sediments in valley sided caves. The massive erosion of the steep valleys must have happened directly post–LGM and may tentatively also be explained by smaller glaciation forms in which form however remains unclear with first models being under construction. First new human appearance in this study area are the Late Magdalénians within the end of the Ice Age when the climate allowed the resettlement of the middle high mountainous region. Whereas in the Ahorn Valley at the Rennerfels rock shelter a camp site is known of those Late Magdalénians/Epipalaeolithics. Whereas in the Mäander Cave feminine engravings are present (Magdalénian), in the Sophie's Cave an antler depot was left (Gravettian) – both indicating a shamanic use of medium-deep cave areas within the Upper Frankonian cave-rich region. Late Magdalénians/Epipalaeolithics reindeer hunter groups found the valley already deeply eroded similar as today, which were used by reindeer herds for seasonal migrations to the boreal forests. Epipalaeolithics have left at least one (or two) camp sites (Plankenfels, Rennerfels) in the Upper Frankonian region, with the end of the Ice Age.

The valley and cave genesis of the Upper Frankonian river valleys started mainly in the Pliocene when the region was still a plateau. Most of the caves evolved within the Pliocene to early Pleistocene in the "ground water level" (ponor caves) due to climatic changes which caused the erosion of the plateau – the time of the beginning of the landscape change. Caves in different elevations were then opened time by time by rivers along the valleys. Those were partly refilled and contain different elevated river terrace relict sediments between 450 to 375 meters a.s.l. The natural weathering and erosion such as river terrace lowering changed the accessibility of caves (for humans and animals) of the Upper Frankonian valleys. Some entrances were blocked by collapses, other were closed by terrace sediments or even speleothem layers. In general, caves in the study area above 410 meters a.s.l. contain Late Pleistocene to Middle Pleistocene megafauna remains. Below 410 meters, caves have only final Late Pleistocene (Late Magdalenian to Epipalaelithics) human settlement or shamanic sites, or even Holocene Early Mesolithic (Rennerfels rock shelter) and younger epoch sites. In the Hasenloch Cave near Pottenstein Neanderthals used a smaller cave (also porcupines there) also in higher elevation as camp site, which was at the branching Püttlach Valley of another strongly frequented cave bear, wolf and hyena den cave, the Große Teufels Cave in the branching Weiherbach Valley. Also at this den site no human artifacts are known. At the time of the Neanderthals, the river valleys were about half to two-third deep eroded, as today and much less in its geomorphology relief. It seems, the larger cave systems where large mammal bone amounts were found, Neanderthals were unable to occupy due to dangerous competitions with denning cave bears and hyena clans or dwelling wolves and lions.

Acknowledgements

The paper is dedicated in memorial to Mr. W. Dess, who died unexpected during a car race accident in 2013. The author gratefully acknowledges funding by Mr W. and Ms. S. Dess, the Sophie's Cave owners. Mrs W. Wedewardt and R. Moosdorf supported the work in the cave. Sieving and bone recovery work was carried out by S. and J. Uhl, I. and P. Heubes, N. Hedler, N. Niedling, M. Zistl, D. Zistl, K. Zistl and C. Moosdorf. M. and M. Conrad helped with the exploration of those parts of the cave system that were difficult to access. R. Rittinger assisted much in the sedimentological work. Dr. T. Striebel provided important information on the Sophie's Cave and about cave and archaeological literature, supported with a new longitudinal cut map, and made a critical review of the first manuscript draft. The C14 analyses were thankfully made by D. Hood from the Beta Analytic Laboratory, Florida, USA (www.radiocarbon.com). Prof. Dr. W. Schirmer made a helpful second review. Additionally, Dr. H. Schabdach and R. Schoberth allowed the use of the new maps of the cave. Finally I thank Prof. Dr. L. Zöller for helpful critical remarks.

References

Bleicher, W. (1993): Die Oeger-Höhle – eine Kultstätte altsteinzeitlicher Rentierjägergruppen. – Hohenlimburger Heimatblätter 9: 309–323.

Bosinski, G. (2011): Les figurations féminines de la fin des temps glaciaires. – In: Musée National Préhistoire Les Eyzies de Tayac (Ed.), Mille et une femme(s) de la fin de temps glaciaires, 50–67.

Bretz, J.H. (1942): Vadose and phreatic features of limestone caverns. – The Journal of Geology 50: 675–811.

Bridgland, D.R., Maddy, D. & Bates, M. (2004): River terrace sequences: templates for quaternary geochronology and marine-terrestrial correlation. – Journal of Quaternary Science 19(2): 203–218.

Brunner, G. (1954): Das Fuchsloch bei Siegmannsbrunn (Oberfr.), eine mediterrane Riss-Würm-Fauna. – Neues Jahrbuch für Geologie und Paläontologie, Abhandlungen 100: 83–118.

Buckland, W. (1823): Reliquiae Diluvianae, or observations on the organic remains contained in caves, fissures, and diluvial gravel, and other geological phenomena, attesting the action of an universal deluge. – 303 pp., Murray, London.

Burger, D. (1989): Dolomite weathering and micromorphology of paleosoils in the Frankonian Jura. – Catena Supplementaria 15: 261–267.

Diedrich, C. (2011): The Late Pleistocene spotted hyena *Crocuta crocuta spelaea* (Goldfuss 1823) population from the Zoolithen Cave at Gailenreuth (Bavaria, South Germany) – a hyena cub raising den of specialized cave bear scavengers in Boreal Forest environments of Central Europe. – Historical Biology 23(4): 335–367.

Diedrich, C. (2012a): Late Ice Age wolves as cave bear scavengers in the Sophie's Cave of Germany – extinctions of cave bears as result of climate/habitat change and large carnivore predation stress in Europe. – ISRN Zoology 2013, 1-25.

Diedrich, C. (2012b): Cave bear killers and scavengers from the last ice age of central Europe: Feeding specializations in response to the absence of mammoth steppe fauna from mountainous regions. – Quaternary International, 255, 59-78.

Diedrich, C. (2012c): Late Pleistocene *Crocuta crocuta spelaea* (Goldfuss 1823) clans as prezewalski horse hunters and woolly rhinoceros scavengers at the open air commuting den and contemporary Neanderthal camp site Westeregeln (central Germany) – Journal of Archaeological Science 39(6): 1749–1767.

Diedrich, C. (2013a): Quaternary bone taphonomy and stratigraphy in the Zoolithen Cave – and new theory about Esper's "biblic flood" with a first geomorphological Wiesent Valley and river terrace evolution model – ?glaciers and postglacial flood events in Upper Frankonia. – E&G Quaternary Science Journal, 62/2 (in press).

Diedrich, C. (2013b): Impact of the German Harz Mountain Weichselian ice-shield and valley glacier development onto Palaeolithics and megafauna disappearance. – Quaternary Science Reviews (in press).
Diedrich, C. (2014): Sophie's Cave – in the dangerous dark kingdom of the cave bears. – Springer-Verlag (accepted for press).
Dogwiler, T. & Wicks, C.M. (2004): Sediment entrainment and transport in fluviokarst systems. – Journal of Hydrology 295: 163–172.
Engel, Z., Nyvlt, D., Křižek, M., Treml, V., Jankovská, V., Lisá, L (2010): Sedimentary evidence of landscape and climate history since the end of MIS3 in the Krkonoše Mts., Czech Republic. – Quaternary Science Reviews 29, 913–927.
Esper, J.F. (1774): Ausführliche Nachricht von neuentdeckten Zoolithen unbekannter vierfüssiger Thiere und denen sie enthaltenden, so wie verschiedenen andern, denkwürdigen Grüften der Obergebürgischen Lande des Marggrafthums Bayreuth. – 148 pp., Nürnberg.
Ford, D.C. & Williams, P.W. (1989): Karst geomorphology and hydrology. – 601 pp., Unwin-Hyman, London.
Gibbard, P.L. & Cohen, K.M. (2009): Global Chronostratigraphical correlation table for the last 2.7 million years. – Episodes 31(2): 243–247.
Groiss, J.T. (2000): Paläontologische Funde und strati-grapische Aussagen. – In: Erono , J. & Stein, G. (Eds.): Die Moggasterhöhle. Eine der bedeutendsten Höhlen der Fränkischen Schweiz. – Karst und Höhle 10: 31–49.
Groiss, J.T., Kamphausen, D, Michel, U. (1998): Höhlen der nördlichen Fränkischen Alb: Entwicklung, Fauna, Karst-Hydrologie. – Erlanger geologische Abhandlungen, Sonderband 2: 161–168.
Gumpert, K. (1931/32): Der Rennerfels - eine neue Madeleine Station in der Fränkischen Schweiz. – Bayrische Vorgeschichtsblätter 10, 60–66.
Gumpert, K. (1981): Der Madeleinzeitliche „Rennerfels" in der Fränkischen Schweiz. – Praehistorische Zeitschrift 22: 1–77.
Habbe, K.-A. (1989): Der Karst der Fränkischen Alb – Formen, Prozesse, Datierungsprobleme. Die Fränkische Alb. – Schriften des Zentralen Institutes für fränkische Landeskunde Universität Erlangen 28: 35–69.
Heller, F. (1955): Zur Diluvialfauna des Fuchsloches bei Siegmansbrunn, Landkr. Pegnitz. – Geologische Blätter von NO-Bayern 5: 49–70.
Holle, J.W. (1833): Die neu entdeckte Kochshöhle oder die Höhlenkönigin im königlichen Landgerichte Hollfeld-Waischenfeld. – Bayerische Annalen 26: 197–198.
Jennings, J.N. (1985): Karst Geomorphology. – 293 pp., Blackwell, Oxford.
Kaiser, K. (1961): Gliederung und Formenschatz des Pliozäns und Quartärs am Mittel- und Niederrhein sowie in den angrenzenden Niederlanden unter besonderer Berücksichtigung der Rheinterrassen. – Festschrift Deutscher Geographen-Tag, Köln, 236–278.
Kempe, S., Rosendahl, W., Wiegand, B. & Eisenhauer, A. (2002): New speleothem dates from caves in Germany and their importance fort the Middle and Upper Pleistocene climate reconstruction. – Acta Geologica Polonica 52(1): 55–61.
Lumley, H., Couraud, C., Delloc, B., Delluc, G., Delporte, H., Leroy-Prost, C., Lumley, M.-A., Perpère, M. & Vialou, D. (1984): Art et civilisations des chasseurs de la préhistore. 34000–8000 ans av. J.-C. – 415 pp., Laboratoire de Préhistoire du Muséum National d`Histoire Naturelle Musée de l`Homme, Imprimerie Louis-Jean, Paris.
Mentlík, P., Minár, J., Břízová, E., Lisa´, L., Tábořík, P. Stacke, V. (2010): Glaciation in the surroundings of Prášilské Lake (Bohemian Forest, Czech Republic). – Geomorphology 117(1–2), 181–194.
Meyer, R.K.F. & Schmidt-Kaler, H. (1992): Wanderungen in die Erdgeschichte (5), Durch die Fränkische Schweiz. – 167 pp., Pfeil-Verlag, München.
Münzel, S.C & Conard, N.J. (2004): Cave bear hunting in the Hohle Fels, a cave site in the Ach valley, Swabian Jura. – Revue de Paléobiologie 23, 877–885.
Münzel, S.C., Stiller, M., Hofreiter, M. Mittnik, A., Conard, N.J. & Bocherens, H. (2011): Pleistocene bears in the Swabian Jura (Germany): Genetic replacement, ecological displacement, extinctions and survival. – Quaternary International 245, 225–237.
Nehring, A. (1891): Über diluviale *Hystrix*-Reste aus bayrisch Oberfranken. – Sitzungsberichte der Gesellschaft der Naturfreunde Berlin 1892: 10.
Neischl, A. (1904): Die Höhlen der Fränkischen Schweiz und ihre Bedeutung für die Entstehung der dortigen Täler. – 95 pp., Schrag, Nürnberg.
Nordhoff, P. (2005): Stable isotope investigations on speleothems from different cave systems in Germany. – 149 pp., Unpublished Dissertation, Georg-August-Universität Göttingen.
Rabeder, G. (1999): Die Evolution des Höhlenbärgebisses. Mitteilung der Kommission für Quartärforschung der Österreichischen Akademie der Wissenschaften 11: 1–102.
Ranke, J. (1879): Das Zwergloch und Hasenloch bei Pottenstein in Oberfranken. – Beiträge zur Anthropologie und Urgeschichte Bayerns 2: 209–210.
Sasowsky, I.D. & Mylroie, J. (2007): Studies of Cave Sediments Physical and Chemical Records of Paleoclimate. – 329 pp., 2nd ed., Springer.
Schabdach, H. (1998): Die Sophienhöhle im Ailsbachtal. Wunderwelt unter Tage. – 47 pp., Verlag Reinhold Lippert, Ebermannstadt.
Schönweiss, W. & Sticht, E. (1968): Das Endpaläolithikum von Plankenfels/Ofr. – Archiv für Geschichte von Oberfranken 48: 71–86.
Sommer, C.S. (2006): Archäologie in Bayern – Fenster zur Vergangenheit; 2006 zusammengestellt von der Gesellschaft für Archäologie in Bayern 25 Jahre nach Gründung. – 336 pp., Verlag Friedrich Pustet.
Spöcker, R.G. (1952): Zur Landschafts-Entwicklung im Karst des oberen und mittleren Pegnitz-Gebietes. – 60 pp. Verlag des Amtes für Landeskunde, Remagen.
Sternberg, K. (1835): Vortrag des Präsidenten Grafen Kaspar Sternberg in der allgemeinen Versammlung des böhmischen Museums in Prag. – Verhandlungen der Gesellschaft des vaterländischen Museums in Böhmen Prag, 1835, 12–30.
Stiller, M., Baryshnikov, G., Bocherens, H., Grandal d'Anglade, A., Hilpert, B., Munzel, S.C., Pinhasi, R, Rabeder, G., Rosendahl, W., Trinkaus, E., Hofreiter, M. & Knapp, M. (2010): Withering away – 25,000 years of genetic decline preceded cave bear extinction. – Molecular Biology and Evolution 27(5): 975–978.
Wagner, R. (1833): Ueber die neu entdeckte Zoolithenhöhle bey Rabenstein. – Bayerische Annalen 47: 313–315.
White, W.B. (2007): Cave sediments and paleoclimate. – Journal of Cave and Karst Studies 69(1): 76–93.

Instruction to Authors

Basically the manuscript shall be submitted in electronic form and has to include the name and the address of the first author. Please use a standard word processor in .rtf, .odt or .doc-format (LaTeX files on request). As character set please use the standard fonts Times Roman, Helvetica or Courier with 1.5 line spacing.

For the submission please use our online system at *www.quaternary-science.net*. After the login you can upload your manuscript as well as separate figures and tables.

Manuscript style

The acceptable languages are English and German. Manuscripts in German have to contain an English subtitle, an abstract in English and English keywords. The rules of the new German spelling reform apply to German texts.

Manuscripts should be arranged in the following order:

I Short but concise title
II Full names, full address and e-mail
III 5 to 10 keywords that describe the contents of your paper
VI An abstract of up to 200 words in German and English. The translated abstract should carry the translated titel in square brackets,
V Clearly structured text. For chapter numbering use Arabic numerals.
VI The reference list has to be arranged alphabetically and should be conform to the examples given below.

References have to be insert in the text as brief quotations, the name of the author has to be set in small Capitals, the year of publication in brackets e.g. Müller (2006). If more than one publication of the same author in the same year is cited, identify each citation as follows: Müller (2006a, 2006b). Where three or more authors are listed in the reference list, please cite in the text as Müller et al. (2006). Papers with up to three authors should be cited as Müller & Meyer (2006) or Müller, Meyer & Schulz (2006). If a special page or figure of a paper should be cited, use following citation style: Müller (2006: 14) or Müller (2006, Fig. 14).

Scientific names of flora and fauna (*gender, sub-gender, species, sub-species*) have to be written in *italics*. Use small Capitals for the author (*Armeria maritima* Willd.)

Do not justify your text, use a ragged left alignment.
Do not use automatic hyphenation.
Do not use any automatic formatting.
Do not use pagination.

Do not insert images, tables and photos into the text, it should be added as separate files. Captions of figures and tables in German and English should be placed at the end of the manuscript.

Illustrations

Supply each figure as a separate file with the name of the author. Illustrations should be reducible to a column width (8.4 cm) or type area (17.2 x 26 cm). The lettering has to be easy readable after reduction. Where a key of symbols is required, include this in the figure, not in the caption of the figure. Avoid fine lines (hairlines) and grey-shading/halftones. All figures may be colored. There are no additional costs.

For printing all illustrations have to be supplied electronically. Please use for pixel-based images (photos) the .tif-format with a resolution of at least 450 dpi and for vector-based illustrations (graphs, maps, tables) the .eps-format. Greatly reduced .jpg-files or .pdf-files or figures included in word-documents are not accepted.

References (examples)

Papers:
Schwarzbach, M. (1968): Neue Eiszeithypothesen. – Eiszeitalter und Gegenwart, 19: 250–261.
Eissmann, L. & Müller, A. (1979): Leitlinien der Quartärentwicklung im norddeutschen Tiefland. – Zeitschrift für Geologische Wissenschaften, 7: 451–462.
Zagwijn, W.H. (1996): The Cromerian Complex Stage of the Netherlands and correlation with other areas in Europe. – In: Turner, C. (ed.): The Middle Pleistocene in Europe: 145–172; Rotterdam (Balkema).
Magny, M. & Haas, J.N. (2004): A major widespread climatic change around 5300 cal. yr BP at the time of the Alpine Iceman. – Journal of Quaternary Science, 19: 423–430. DOI: 10.1002/jqs.850

Books:
Ehlers, J. (1994): Allgemeine und historische Quartärgeologie. – 358 S.; Stuttgart (Enke).

Please do not use abbreviations of the journal names.

Specimen copies

Authors receive no printed specimen copies. The electronic version is available as download free.

For further questions about the submission of manuscripts please contact the production editor (imprint).

Autorenhinweise

Das Manuskript ist grundsätzlich in elektronischer Form einzureichen und muss mit Namen und Adresse des Erstautoren versehen sein. Bitte benutzen Sie eine Standard-Textverarbeitung im .rtf, .odt oder .doc-Format (LaTeX-Dateien auf Anfrage). Als Zeichensatz verwenden Sie bitte die Standard-Fonts Times Roman, Helvetica oder Courier mit einem 1,5-fachen Zeilenabstand.

Zur Einreichung nutzen Sie bitte unser Online Submission System unter *www.quaternary-science.net.* Nach dem Login steht Ihnen hier eine Upload-Funktion für das Manuskript und die Abbildungs-Dateien zur Verfügung.

Manuskriptform

Als Publikationssprachen sind Englisch und Deutsch zugelassen. Manuskripte in deutscher Sprache müssen einen englischen Untertitel tragen sowie eine englische Kurzfassung und englische Keywords beinhalten. Für die deutschen Texte gelten die Regeln der neuen Rechtschreibreform.

Die Manuskripte sollen folgendem Aufbau entsprechen:

I Kurze, aber prägnante Überschrift
II Ausgeschriebener Vor- und Nachname, Post- und E-Mail-Adresse
III 5 bis 10 englische Keywords, die den Inhalt des Manuskriptes widerspiegeln.
IV Deutsche und englische Kurzfassung des Textes mit einer Länge von bis zu 200 Wörtern. Der englische Untertitel des Manuskriptes ist der englischen Kurzfassung in eckigen Klammern voranzustellen.
V Klar gegliederter Text. Kapitelnummerierungen sind mit arabischen Ziffern zu versehen.
VI Alphabetisch geordnete Literaturliste. Die Zitierweise muss der unten angegebenen Form entsprechen.

Im fortlaufenden Text sind Literaturhinweise als Kurzzitate einzufügen, der oder die Autorennamen sind in Kapitälchen-Schrift zu setzen, das Erscheinungsjahr in Klammern, z. B. Müller (2006). Werden von einem Autor mehrere Arbeiten aus einem Jahr zitiert, so sind diese durch Buchstaben zu unterscheiden: Müller (2006a, 2006b). Bei mehr als drei Autoren kann et al. verwendet werden: Müller et al. (2006). Arbeiten mit bis zu drei Autoren werden folgendermaßen zitiert: Müller & Meyer (2006) oder Müller, Meyer & Schulz (2006). Sind mit der Zitierung bestimmte Seiten oder Abbildungen gemeint, müssen diese genau angegeben werden: Müller (2006: 14) oder Müller (2006: Fig. 14).

Die wissenschaftlichen Namen von Pflanzen und Tieren (*Gattungen*, *Untergattungen*, *Arten*, *Unterarten*) sind kursiv zu schreiben. Die den biologischen Namen folgenden Autoren werden in Kapitälchen gesetzt (*Armeria maritima* Willd.).

Bitte keinen Blocksatz verwenden, sondern linksbündigen Satz.
Bitte keine automatische Silbentrennung verwenden.
Bitte alle automatischen Formatierungen in Ihrer Textbearbeitung deaktivieren.
Bitte keine Seitenzählung.

Abbildungen, Tabellen und Fotos nicht in den Text einbauen, sondern separat als Datei beifügen. Abbildungsunterschriften in Deutsch und Englisch am Ende des Manuskripttextes platzieren.

Abbildungen

Bitte fügen Sie jede Abbildung als separate Datei mit einem eindeutigen Namen bei. Alle Grafiken müssen eine Verkleinerung auf Spaltenbreite (= 8,4 cm) oder Satzspiegel (= 17,2 x 26 cm) zulassen. Die Beschriftung muss nach der Verkleinerung noch gut lesbar sein. Sollte eine Legende nötig sein, so binden Sie diese in die Abbildung ein. Bitte vermeiden Sie Haarlinien oder Grauwerte. Alle Abbildungen können farbig sein. Es entstehen keine Mehrkosten.

Für die Drucklegung müssen alle Abbildungen in elektronischer Form eingereicht werden. Bitte verwenden Sie für pixelbasierte Abbildungen (Fotos) das .tif-Format mit einer Auflösung von mindestens 450 dpi und für vektorbasierte Abbildungen (Diagramme, Maps, Tabellen) das .eps-Format. Stark reduzierte .jpg oder .pdf-Dateien sowie in Text-Dokumente eingebundene Abbildungen werden nicht akzeptiert.

Zitierweise (Beispiele)

Aufsätze:

Schwarzbach, M. (1968): Neue Eiszeithypothesen. – Eiszeitalter und Gegenwart, 19: 250–261.

Eissmann, L. & Müller, A. (1979): Leitlinien der Quartärentwicklung im norddeutschen Tiefland. – Zeitschrift für Geologische Wissenschaften, 7: 451–462.

Zagwijn, W.H. (1996): The Cromerian Complex Stage of the Netherlands and correlation with other areas in Europe. – In: Turner, C. (ed.): The Middle Pleistocene in Europe: 145–172; Rotterdam (Balkema).

Magny, M. & Haas, J.N. (2004): A major widespread climatic change around 5300 cal. yr BP at the time of the Alpine Iceman. – Journal of Quaternary Science, 19: 423–430. DOI: 10.1002/jqs.850

Monographische Werke, Bücher:

Ehlers, J. (1994): Allgemeine und historische Quartärgeologie. – 358 S.; Stuttgart (Enke).

Bitte keine Abkürzungen der Zeitschriftentitel verwenden.

Belegexemplare

Es werden keine gedruckten Belegexemplare verschickt. Die elektronische Version steht zum kostenlosen Download zur Verfügung.

Bei weiteren Fragen zur Manuskripteinreichung wenden Sie sich bitte an die technische Redaktion (s. Impressum)

DEUQUA

German Quaternary Association

The German Quaternary Association (DEUQUA) eV is an association of German-speaking Quaternary Scientists. The aim of the association is to promote the Quaternary Science, to represent it in public, to intensify the contact to applied science as well as to advice public and political boards in quatarnary issues.

Furthermore, the association has set itself the task of operating the contacts between the Quaternary Scientists and related organizations at home and abroad.

The DEUQUA published annually several editions of "E&G – Quaternary Science Journal". In that journal research results from the field of Quaternary Science are published. In addition, developments in the DEUQUA are announced in the "Geoscience messages" (GMIT). GMIT is published quarterly.

Every two years, the German Quaternary Association held the DEUQUA-Conference. At this conference the latest research results of the Quaternary Science are presented and discussed.

Deutsche Quartärvereinigung

Die Deutsche Quartärvereinigung (DEUQUA) e.V. ist ein Zusammenschluss deutschsprachiger Quartärwissenschaftler und wurde 1949 gegründet. Der Verein hat zum Ziel, die Quartärwissenschaft zu fördern, sie in der Öffentlichkeit zu vertreten, den Kontakt zu angewandter Wissenschaft zu intensivieren sowie öffentliche und politische Gremien in quartärwissenschaftlichen Fragestellungen zu beraten. Des Weiteren hat der Verein sich zur Aufgabe gemacht, die Kontaktpflege der Quartärforscher untereinander und zu verwandten Organisationen im In- und Ausland zu betreiben.

Die DEUQUA veröffentlicht jährlich mehrere Ausgaben von „E&G – Quaternary Science Journal". Dort werden Forschungserkenntnisse aus dem Bereich der Quartärwissenschaft publiziert. Zusätzlich werden Entwicklungen in der DEUQUA vierteljährlich in den Geowissenschaftlichen Mitteilungen (GMIT) bekannt gemacht.

Im zweijährigen Turnus veranstaltet die Deutsche Quartärvereinigung e.V. die DEUQUA-Tagung. Diese bietet ein Forum, in welchem aktuelle Forschungsergebnisse aus dem Bereich der Quartärwissenschaften vorgestellt und diskutiert werden.

Committee / Vorstand

PRESIDENT / PRÄSIDENTIN
MARGOT BÖSE
Freie Universität Berlin
Malteserstr. 74–100
D-12249 Berlin, Germany
Tel.: +49 (0)30-838-70 37 3
E-Mail: m.boese (at) fu-berlin.de

VICE PRESIDENTS / VIZEPRÄSIDENTEN
CHRISTOPH SPÖTL
Institut für Geologie und Paläontologie
Universität Innsbruck
Innrain 52
A-6020 Innsbruck, Austria
Tel.: +43 (0)512-507-5593
Fax: +43 (0)512-507-2914
E-Mail: christoph.spoetl (at) uibk.ac.at

LUDWIG ZÖLLER
Fakultät II – Lehrstuhl für Geomorphologie
Universität Bayreuth
Universitätsstraße 30
D-95440 Bayreuth, Germany
Tel.: +49 (0)921-55 2266
Fax: +49 (0)921-55 2314
E-Mail: ludwig.zoeller (at) uni-bayreuth.de

TREASURER / SCHATZMEISTER
JÖRG ELBRACHT
Landesamt für Bergbau, Energie und Geologie
Stilleweg 2
D-30655 Hannover, Germany
Tel.:+49 (0)511-643-36 13
E-Mail: joerg.elbracht (at) lbeg.niedersachsen.de

EDITOR-IN-CHIEF / SCHRIFTLEITUNG (E&G)
HOLGER FREUND
ICBM – Geoecology
Carl-von-Ossietzky Universitaet Oldenburg
Schleusenstr. 1
D-26382 Wilhelmshaven, Germany
Tel.: +49 (0)4421-94 42 00
E-Mail: holger.freund (at) uni-oldenburg.de

ARCHIVIST / ARCHIVAR
STEFAN WANSA
Landesamt für Geologie und Bergwesen
Sachsen-Anhalt
Postfach 156
D- 06035 Halle, Germany
Tel. +49 (0)345-5212-12 7
E-Mail: wansa (at) lagb.mw.sachsen-anhalt.de

ADVISORY BOARD / BEIRAT
CHRISTIAN HOSELMANN
Hessisches Landesamt für Umwelt und Geologie
Postfach 3209
D-65022 Wiesbaden, Germany
Tel.: +49 (0)611-69 39 92 8
E-Mail: christian.hoselmann (at) hlug.hessen.de

DANIELA SAUER
Institut für Bodenkunde und Standortslehre
Universität Hohenheim
Emil-Wolff-Str. 27
D-70593 Stuttgart, Germany
Tel.: +49 (0)711-459-22 93 5
E-Mail: d-sauer (at) uni-hohenheim.de

FRANK PREUSSER
Department of Physical Geography and
Quaternary Geology
Stockholm University
10961 Stockholm, Sweden
Tel. +46 8 674 7590
E-Mail: frank.preusser@natgeo.su.se

REINHARD LAMPE
Institut für Geographie und Geologie
Ernst-Moritz-Arndt-Universität Greifwald
Friedrich-Ludwig-Jahn-Straße 16
D-17487 Greifswald, Germany
Tel: +49 (0)3834-86-45 21
E-Mail: lampe (at) uni-greifswald.de

BIRGIT TERHORST
Geographisches Institut
Universität Würzburg
Am Hubland
D-97074 Würzburg, Germany
Deutschland
Tel. +49 (0)931-88 85 58 5
E-Mail: birgit.terhorst (at) uni-wuerzburg.de

Reorder / Nachbestellung

The volumes 6–7, 11–17, 19–28 and 30–58 are currently available. All other volumes are sold out. A reduced special price of 10,– ☐ per edition is up to and including volume 55. The regular retail price applies from vol. 56/1–2. The prices are understood plus shipping costs. VAT is included. The complete content is searchable at *www.quaternary-science.net*.

1951–2006

Vol. 6–7, 11–17, 19–28, 30–55	each volume 10,– ☐

2007	Topics	Price
Vol. 56 No 1–2	Special issue: Stratigraphie von Deutschland – Quartär	54,– ☐
Vol. 56 No 3	Pfälzerwald, pollen types and taxa, Oberösterreich, Riß-Iller, Schatthausen	27,– ☐
Vol. 56 No 4	Nußloch, Rangsdorfer See, Lieth/Elmshorn, Gardno Endmoräne/Debina Cliff	27,– ☐

2008	Topics	Price
Vol. 57 No 1–2	Special issue: Recent progress in Quaternary dating methods	54,– ☐
Vol. 57 No 3–4	Special issue: The Heidelberg Basin Drilling Project	54,– ☐

2009	Topics	Price
Vol. 58 No 1	Surface Exposure Dating, Bodensee, Living Fossil, Hochgebirgsböden	27,– ☐
Vol. 58 No 2	Special issue: Changing environments – Yesterday, Today, Tomorrow	27,– ☐

2010	Topics	Price
Vol. 59 No 1–2	Baltic Sea Coast, Rodderberg Crater, Geiseltal, Wettersteingebirge, Møn, Argentina	54,– ☐

2011	Topics	Price
Vol. 60 No 1	Special issue: Loess in Europe	27,– ☐
Vol. 60 No 2–3	Special issue: Glaciations and periglacial features in Central Europe	54,– ☐
Vol. 60 No 4	Special issue: Quaternary landscape evolution in the Peribaltic region	27,– ☐

2012	Topics	Price
Vol. 61 No 1	Calcareous Alps Austria, Löss, Holzreste Schweiz, Rinnen-Strukturen, Permafrost carbon	27,– ☐
Vol. 61 No 2	Rivers, Lakes and Peatlands NE Germany, Lavrado Region Brazil, Terna River Basin India	27,– ☐

Subscription / Abonnement

Title: E&G – Quaternary Science Journal
Print-ISSN: 0424-7116
Issues per volume: 2

Prices (EUR) print per volume

End customers: 50,46 ☐ (Free for DEUQUA-Members)
Wholesalers, booksellers: 32,80 ☐
Scientific libraries: 47,94 €
VAT is not included.

Postage (EUR) per volume

within Germany: 2,50 ☐
World (Surface): 6,80 ☐
World (Airmail): 7,70 ☐

Special offer

Libraries which subscribe our journal can receive the volumes 1951–2006 for free. Only shipping costs have to be paid.

Order address

Geozon Science Media
P.O. Box 3245
D-17462 Greifswald
Germany

tel.: +49 (0)3834-80 40 80
fax: +49 (0)3834-80 40 81
e-mail: info (at) geozon.net
web: www.geozon.net

E&G Quaternary Science Journal
Volume 62 / Number 2 / 2013 / ISSN 0424-7116 / DOI 10.3285/eg.62.2
www.quaternary-science.net

Contents

GEOZON SCIENCE MEDIA
www.geozon.net